A Study of Infrasound Signals in Mesopause OH* Emissions Using a Ground-Based Three-Element Array at Maynooth (53.3 °N, 6.6 °W)

National University of Ireland, Maynooth

A thesis submitted in fulfillment of the requirements for the degree of Doctor of Philosophy by

Julianne Kealy

Department of Experimental Physics

Faculty of Science and Engineering

Research Supervisor: Dr. Frank Mulligan

Head of Department: Dr. Créidhe O'Sullivan

September 2021

Contents

Acronyms

Acronym	Name	Note
AIM-CIPS	Aeronomy of the Ice in the Mesophere – Cloud Imaging and Particle Size experiment	Experiment present on the AIM satellite, used for monitoring polar mesospheric clouds and ice water content
ARISE	Atmospheric dynamics Research InfraStructure in Europe	Major research project this thesis is part is under
BV	Brunt-Väisälä	Frequency limit of gravity waves
CCD	Charge-Coupled Device	Type of camera
CCN	Cloud Condensation Nuclei	
CNEOS	Centre for Near Earth Object Studies	Dataset used for source determination
CTBTO	Comprehensive nuclear Test Ban Treaty Organisation	
ECMWF	European Centre for Medium-Range Weather Forecasts	
EUV	Extreme Ultraviolet	
FOV	Field-of-View	
GLONASS	GLObal NAvigation Satellite System	
GNSS	Global Navigation Satellite System	
GPS	Global Positioning System	
GRIPS	Ground-based Infrared P-branch Spectrometer	Instrument used by (*Bittner et al.*, 2010) among others
GVP	Global Volcanism Program	Dataset used for source determination
GW	Gravity Wave	
HWMF	Horizontal Wind Model Forecast	
IMS	International Monitoring System	Global Infrasound Monitoring Network
LED	Light Emitting Diode	
LIDAR	LIght Detection And Ranging	
MAW	Mountain Associated Waves	Type of infrasound
MFR	Maynooth Fixed Radiometer	Instrument used in this thesis
MSIS	Mass Spectrometer and Incoherent Scatter	Thermospheric model of temperature and density
NLC	NoctiLucent Cloud	

NLCNET	NLC Network	Amateur Observation Database for NLCs
NOAA	National Oceanic and Atmospheric Administration	
OHP	Observatoire de Haute-Provence	
PMC	Polar Mesospheric Cloud	
PMSE	Polar Mesospheric Summer Echoes	
PMWE	Polar Mesospheric Winter Echoes	
POC	Proof-Of-Concept	
SNR	Signal-to-Noise Ratio	Instrumentation parameter
TEC	Total Electron Content	Used in ionospheric studies for various purposes
TIA	Trans-Impedance Amplifier	
USGS	United States Geological Survey	Dataset used for source determination
UTC	Coordinated Universal Time	
UV	UltraViolet	
UWO	University of Western Ontario	
UWOSCR	University of Western Ontario SCanning Radiometer	Instrument used in this thesis
vDEC	virtual Data Exploitation Centre	Database of signals detected by IMS networks
VHF	Very High Frequency	

Abstract

This thesis describes the development and testing of a three-element array of ground-based infrared radiometers for the purpose of detecting infrasonic (acoustic-gravity) waves propagating through the mesopause region of Earth's atmosphere. The individual radiometers are based on an earlier generation of scanning radiometers developed at the University of Western Ontario for the study of gravity waves in the upper atmosphere by observing infrared emissions from vibrationally excited OH* radicals. These devices provided a low-resolution ($16° \times 16°$) image of a small portion of the zenith sky once per minute. The main modification of the earlier instruments has been to change the mode of observation from two-dimensional scanning to fixed viewing in order to increase the time sampling from once per minute to approximately five samples per second. The trade-off for this increase in cadence was the loss of imaging capability of each radiometer. The formation of a three-element array of fixed viewing radiometers was the method chosen to compensate for this loss of imaging capacity. While the three-element array does not produce an image of the sky, it does allow the possibility of assigning a speed and a direction to waves that are detected in all three radiometers through the use of correlation techniques. Current alternatives to the method adopted here involve the use of sensitive CCD cameras to record an image of a section of the sky. These have the advantage of facilitating immediate recognition of any wave pattern in the field-of-view, without the need to apply correlation techniques. The very low light levels available require integration times of the order of 500 ms even in the most sensitive devices available, and these are very costly devices compared with the relatively inexpensive approach of the three-element array.

The remainder of the thesis describes the experience of operating the three-element array over a number of years at Maynooth together with the interpretation of the recorded data. Infrared radiation from the flashing beacons on pedestrian crossings, reflected from low level clouds provided valuable confirmation of the ability of each

radiometer to accurately detect infrasonic signals. Gravity waves were frequently observed throughout clear nights. Infrasound signals were detected by all three elements in the network on many occasions, but the attribution of these signals to specific events has proven difficult. Sources of infrasonic signals, such as earthquakes, volcanos, tsunamis and large meteor showers are by their nature transient events. A number of case studies of strong infrasound signals (with one specific signal tentatively connected to a large meteor event) are included to illustrate the possibilities and the limitations of the technique. The one known source of infrasound that is consistently present at ground level are the pressure variations associated with microbaroms. Reports from modelling studies show that the magnitude of these signals is expected to be extremely weak at mesopause levels, but like other observers in this field we have resorted to searching for these signals. While there is some evidence of their presence at certain times of the year, it is difficult to say that these signals have been observed with absolute certainty. The clearest infrasound signals that have been obtained appear to be associated sunlight scattered from noctilucent clouds, examples of which are presented.

Acknowledgments

"Coming back to where you started is not the same as never leaving."

- Terry Pratchett

I have been fortunate enough to start and finish my college experience in Maynooth. However, this was not always a sure thing and I am immensely grateful to the people who got me to where I am today. There have been many hiccups on my journey to complete this PhD and accompanying thesis, where it has sometimes felt I had to go back to the beginning and hadn't achieved much. I have learned these past few years that, as Mr. Pratchett alludes to above, that's not always a bad thing. Sometimes we require perspective, and you need to find the best vantage point to get it. For me, that was the starting point.

I want to first thank Dr. Frank Mulligan for his constant encouragement, enthusiasm and the scourge of his red pen. He has been a source of inspiration during both my undergraduate and postgraduate. If it weren't for him, I wouldn't have been afforded some amazing opportunities. His commitment to teaching and research has driven me to become a better teacher and student. I will envy the drive he embodies, and that so many wish for, for the rest of my life. His honesty and support is something I will always appreciate.

To the staff of the Experimental Physics department, thank you for being so approachable and kind. I have told this story many times, but I was not considering a path in physics when I first arrived in college, initially I had my heart set on other sciences. However, by the end of the first year in undergraduate, I had a decision to make, where in the end I chose to keep on physics. Part of this decision was due to the helpfulness of the department. Thank you to Dr. Créidhe O'Sullivan, Prof. J. Anthony Murphy, Dr. Marcin Gradziel, Dr. Peter van der Burgt, Dr. Michael Cawley, Dr. Neil Trappe, Dr. Emma Whelan, Dr. Dan Nickström, Dr.

Colm Bracken, Dr. Ian McAuley, Ms. Grainne Roche, Mr. Derek Gleeson, Mr. John Kelly, Ms. Marie Galligan, Mr Pat Seery and Mr. David Watson. I would also like to thank the wonderful maintenance staff with whom I always had lovely chats when I was working late. I also extend a thank you to the staff of the Graduate Studies Department who have been very kind with their time over the last few years. Maynooth University have made this thesis possible through their funding and for that I am forever grateful. I would also like to acknowledge and thank my fellow researchers who have helped get this thesis to where it is today.

To the postgraduates, both past and present, who have made this whole experience so lovely, who would always knock on my door and ask me to go for a cup of tea, I say "thanks for all the good nights out, and all of the wonderful chats". A huge thank you to Daithí Byrne, Jack Graham, James Murphy, Dave Burke, Donnacha Gayer, Eimantė Kalinauskaitė, Eoin Cahill, Mark Deegan, Adam Byrne, Andrew Miller, Aisling Murphy, Michael Brown, Melissa Dunne, Andrew Wilson (especially for all his work on the LabVIEW programming) and Darren Cashin.

To Sharon Rourke - where do I begin with such a wonderful person. Thank you so much for being my office mate, for the memes, and for the good jobs. I have always appreciated our walks together and you are so kind for proof-reading my thesis (you are incredibly fast and meticulous!). To Joe Brennan – thank you for being so kind since I've known you, you have made being a PhD student bearable, and have also always stood up for me and pushed me to get those opportunities that had felt so out of reach. Thank you to both of you.

To my fantastic friends, especially Shauna who is not shy of a deep chat into the early hours and who has always been there no matter the hour, Laoise (sorry about the ham glaze, I wanted to immortalise it here so I could publish my shame (But also you're a big legend who will always tell me straight up, ham glaze included)), Juxhin, Rory, Caoimhe, Muireann, Becky (who collectively are some of the most supportive people I've ever come to know, in this last year I don't know what I would have done

without you), Christine and Alison (two parts of a triplet, but a lifetime of friendship), Caroline (Keep hissing! Thank you for being so lovely and not afraid to be yourself), Aoife (the Queen of Postcards and will never be usurped) and to Megan for all her advice. A shoutout to the Irish mammies, where Collette and Essie get a special mention (Kevin, you are included).

To the coffee crew, especially Jack, thank you for keeping me sane through both my undergraduate and postgraduate years with your great coffee and crazy discussions. Thanks to Ellie, Siofra, Ryan and to Aoife and Avril too. To the teaching crew: you absolute nerds helped me not to fear teaching, and taught me how to face public speaking, while also enjoying myself. My thanks go out to Naoise, Alex, Shannon and Chris.

To my parents: thank you for raising me to question my surroundings, to always acknowledge that different isn't bad even if you haven't grown up around it, and also if you didn't know it when you were younger. We have disagreed, but the arguments we have had have always made us stronger. Thank you to my siblings: Caroline, Susan and Richard, for being the people that I can always come back to. Thank you to my aunts and uncles: Justin and Justina (especially for the wonderful chats during our times in Galway and Wexford, as well as taking care of me while I was in the Gaeltacht [also special mention to Justina for the advice she gave me at 3 a.m. only 2 years ago, that I will always remember]), Paula and Russell (for letting a very naïve teenager spend the summer and to understand her, as well as teaching her about their wonderful love of art and cats), and Aileen (who always makes time to have a conversation). A thank you also to Charlie and Max, my lone cousins who are excellent and wonderful to always have a laugh with. A thank you to Anne, who let me believe that physics is for people who have a curiosity, including and especially women. I would also like to thank my god-father Nicky, who has always thought I could achieve something even if I didn't think I could. I would also like to thank him for all his encouragement and kind letters throughout the years.

Chelsey, my partner in crime, you have been the single greatest thing to happen to me, I can't express what you mean to me. Thank you for everything, thank you for attempting to understand my point of view, and not be afraid to question it. Soon we will be back sitting in an old man pub, in one of the snugs, discussing morality and the meaning of everything, while you tell me I sound like a character out of a John B. Keane novel who is attending a funeral. I hope you'll stay with me on the journey through this life, and that we learn together, wherever and however it may be. As someone once said, you're my woman.

Finally, a note to those who I have lost, but who will make an impact on me as I venture through this life that is sure to be unpredictable: thank you to my god-mother Mairead, my Nana Mary and my Granny Muriel. Thank you for believing in me, and thank you for making this thread of life possible.

1. Introduction, Background Theory and Literature Review

1.1. Project Overview

Infrasonic waves (or infrasound) are sound waves with frequencies between **20** Hz (the lower end of the audible frequency range (for humans)) down to around **0.003** Hz (the acoustic cut-off frequency of Earth's atmosphere, which defines the point where gravity effects become non-negligible (*Artru et al.*, 2004, *Jones* and *Bedard*, 2018)). They have been the subject of ongoing study in both geophysics and atmospheric research due to their potential use for tracing atmospheric disturbances back to their origin event. Sources of infrasound include events such as earthquakes, volcanic eruptions, tornadoes, meteors, mining explosions, aircraft wake vortices, and nuclear detonations. This last source, nuclear detonations, caused a revival of interest in infrasonic research during the Cold War years, especially during the 1950s (*Bedard* and *Georges*, 2000).

Just as Cold War era scientists used infrasound during this time to detect nuclear explosions, this same method of detection is also in use today by the Comprehensive Nuclear Test Ban Treaty Organisation (CTBTO) (*Bedard* and *Georges*, 2000) to detect illicit nuclear explosions. Infrasound monitoring employed by the CTBTO is used as a verification technique to detect these events. Sensors in the form of microphone arrays are used to pick up infrasonic signals, and are managed by the International Monitoring System (IMS) (*Christie* and *Campus*, 2010). Ground microphones detect not only nuclear activity, but also infrasound from all other sources, like those mentioned above. Ground-based microphone arrays have been the dominant detection method for the investigation of atmospheric infrasound until the past decade or so. More recently, however, researchers have begun to measure infrasound at different altitudes in the atmosphere as illustrated by the high-altitude calibration experiments described by

Herrin et al. (2008) and free-flying acoustic arrays (composed of differential pressure transducers) which have been used to measure infrasound in the middle atmosphere by *Bowman* and *Lees* (2015).

Another method of infrasound detection at even higher altitudes, employed by *Bittner et al.* (2010) and *Pilger et al.* (2013c), has been the use of optical emissions from the hydroxyl layer (a layer of infrared emissions located at approximately 87 km altitude) using ground-based spectrometers. Both studies used these instruments to examine how infrasound affects hydroxyl layer temperatures, where *Pilger et al.* (2013c), for instance, found that infrasound can vary the hydroxyl layer temperatures by different amounts based on the origin source of the signal. Volcanic activity and explosions appear to have the greatest impact on the temperature of the layer, while orographic infrasound (due to airflow over mountainous regions, also known as mountain-associated waves (MAWs)) produces the weakest temperature variations. *Hannawald et al.* (2016) and *Le Dû et al.* (2020) have investigated infrasonic signatures in this same layer through the use of fast camera systems that have the required temporal resolution to study transient features in the hydroxyl layer.

The work of *Bittner et al.* (2010) and *Pilger et al.* (2013c) use infrasound monitoring to investigate the possibility of its use as an early warning system for natural hazards. Demonstrations of how volcanic eruptions could be detected through infrasound monitoring have been shown by authors like *Garcés et al.* (1999). Other natural hazards that have been detected through infrasonic monitoring include earthquakes (*Afraimovich et al.*, 2002, *Arrowsmith et al.*, 2009) and meteors (*Revelle*, 1976, *Revelle* and *Whitaker*, 1999, *de Groot-Hedlin* and *Hedlin*, 2014).

If such applications are to be understood and implemented, a broader knowledge of how atmospheric conditions affect the long-range detection of infrasound must be considered. Although infrasound is not subject to large amounts of attenuation in the atmosphere, its propagation is greatly affected by variations in temperature and wind. *de Groot-Hedlin et al.* (2010) and references therein discuss how strong infrasonic source signals can be affected as such and can lead to the weak detection of otherwise substantive infrasonic

events. Thus, a knowledge of the atmosphere plays an important part in source determination of signals. Due to the potentially weak nature of signals originating from strong sources, enhancement of the infrasound network's coverage is essential for signal detection.

The aim of this project is primarily an attempt to demonstrate that optical emissions from the hydroxyl layer can be used to study infrasound propagation at mesopause altitudes ($80-100$ km). A secondary objective is to enhance the infrasound network through observations of infrasound at mid-latitudes as part of the Horizon 2020 ARISE 2 project (*ARISE*, 2019). One of the goals of ARISE 2 is to investigate the potential of infrasound to study parts of the atmosphere that are poorly understood, such as the mesopause. Optical emissions from the hydroxyl layer, which is embedded in the mesopause, can be used as a probe for the atmospheric dynamics of this layer.

Monitoring of infrasound at mesopause altitudes by using optical emissions from the hydroxyl layer has been reported recently by a number of groups (*Hannawald et al.*, 2016, *Sedlak et al.*, 2016, *Le Dû et al.*, 2020). All of these studies employ a high-speed CCD camera as the detector in an optical system with a wide field-of-view. These are very elegant instruments, but the cost of the CCD is very substantial. Even with this investment, the cadence of sampling is no greater than two samples per second. As an attempt at proof-of-concept, the main aim of this study was to achieve infrasonic monitoring capability using a detector array deployed at Maynooth with a sampling capability of at least four samples per second. A significant aspect of the work, therefore, has been the design of the instrumentation which is described in detail in Chapter 2 but is outlined briefly here.

The final configuration of the instrumentation used is a three-element array of radiometers, each of which uses fast optics together with a large light-collecting area, a small field-of-view and a sensitive detector to capture small-scale infrasonic waves in the hydroxyl layer. This type of design is needed to both capture the waves, due to their speed (these waves travel at the speed of sound) and to ensure that the wave amplitudes are not averaged out over the field-of-view. Another consideration that must be taken

into account is the low level of light emitted by the hydroxyl layer. Although the hydroxyl infrared bands are some of the brightest emissions in the night sky (*i.e.*, in the near-infrared), they still are relatively dim compared to moonlight and scattered streetlight. The general radiance levels and calibration of the instruments is described in Chapter 3.

The results obtained with the three-element array are presented in Chapters 4 and 5. Chapter 4 outlines some of the challenges of differentiating between infrasound that originates from modulation of the hydroxyl emissions that are the subject of investigation from that of other sources that contribute in the same infrared wavelength range. One such source that proved to be both problematic, and yet interesting in its own right, was sunlight scattered from very thin noctilucent clouds.

Having eliminated "false" infrasound detections as far as has been possible, Chapter 5 presents initial results of infrasound modulations of hydroxyl emissions obtained during the project. Two classes of signals are considered; episodic and regularly recurring signals. The regularly occurring signals are interpreted to arise from microbaroms – infrasonic waves generated by non-linear interaction of ocean surface waves with the atmosphere. Identifying the origin of episodic signals, even though they tend to be much larger in amplitude, is a much more difficult task.

Chapter 6 concludes with a discussion of the future of the approach adopted in this work, the lessons learned, and includes suggestions for further development of the technique.

1.2. History of Infrasound Detection

Infrasound detection began with ground-based microphone-array observations of sound waves emanating from Krakatoa (lithograph shown in Figure 1-1) in 1883 with investigations regarding the eruption and the characteristics of the event first documented by *Verbeek* (1885). The intensity of these sounds emanating from the

volcanic eruption reached its peak on the 26 August 1883, as described by *Sturdy* (1884) in the *Atlantic Monthly* magazine, who noted that the eruption was heard in nearby Batavia (located around modern-day Jakarta, Indonesia), around **130** km away. *Verbeek* (1885) went into greater detail and found that the eruptions caused barographic (pressure) deviations, observed as far away as Sydney, Australia.

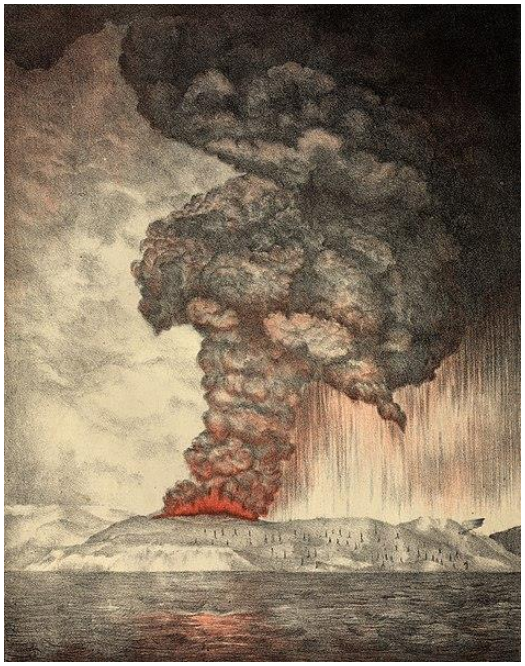

Figure 1-1: Lithograph by Parker and Coward of the ejected materials from Krakatoa on the 27 May 1883 (*Symons*, 1888)

Verbeek (1885) took the average of **4** readings detected at Sydney and found an air wave speed of **314** m/s. Waves that travelled straight to Sydney from Krakatoa were not the only waves detected from the eruptions as *Verbeek* (1885) notes, as some waves travelled around the globe before arriving at Sydney. Such extensive propagation was also observed by *Symons* (1888), who reported on the detection of air waves associated with Krakatoa, as far away as Scotland and Canada.

Atmospheric conditions based on the propagation characteristics were noted by both *Verbeek* (1885) and *Symons* (1888), where the temperature and wind were considered as factors in the detection of the air waves. Not only were these characteristics of the

atmosphere considered, but the effects of the volcanic event on the atmosphere regarding twilight effects and the expulsion of dust into the higher atmospheric layers were detailed. Due to the material ejected, the eruption of Krakatoa is also suspected to be the origin behind the first appearance of noctilucent clouds in the upper atmosphere (*Schröder*, 2001), which were documented by Otto Jesse a number of years after the eruption (Figure 1-2).

The eruption of Krakatoa represented the first major infrasonic source identified by scientists, with the Great Siberian Meteor of 1908 (the so-called Tunguska event) being the second notable explosion, before the advent of the nuclear era, that made an impact on the future of infrasonic monitoring. *Whipple* (1930) detailed the event of the meteor, giving the first demonstration of microbarographs (pressure variations) as a method of infrasound detection.

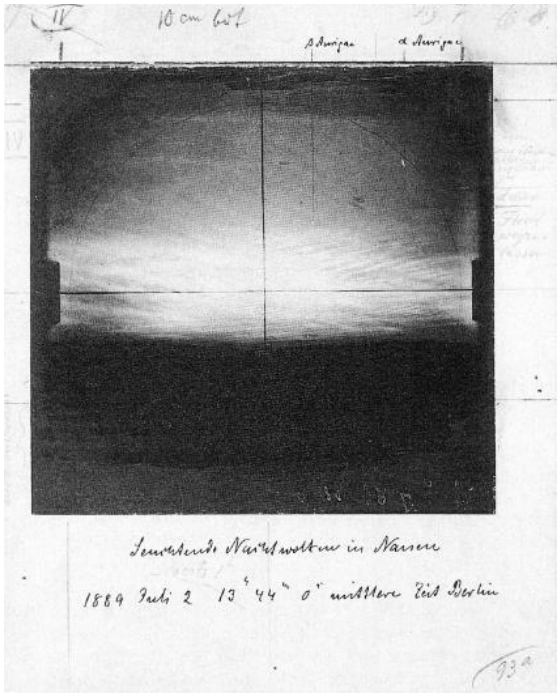

Figure 1-2: One of the earliest surviving photographs of Noctilucent clouds as taken by Otto Jesse in 1889 (Schröder, 2001*)*

Small advances were made in the area of infrasound detection up until the Cold War, when nuclear testing became common, and with it the detection of nuclear infrasound.

Nuclear explosions served as a clear and strong source of infrasound during the Cold War and enabled scientists to establish the sources of infrasonic signals. Along with the detection of this infrasound came advances in better testing methods and the use of raytracing in determining acoustic propagation paths in the atmosphere (*Rothwell*, 1947). This increase in nuclear infrasound monitoring also led to increased detection of other infrasonic sources such as earthquakes and microbaroms as outlined by *Donn* and *Posmentier* (1964) and *Posmentier* (1967) respectively.

The development of infrasound monitoring capacity arising from the Cold War era came to an end with the Limited Test Ban Treaty in 1963. Instead, greater focus was given to seismic observations of nuclear testing (*Bedard* and *Georges*, 2000). The recent advances in infrasonic observations and monitoring have their origin in the signing of the Comprehensive Nuclear Test Ban Treaty during the 1990s, where the CTBTO utilised infrasound as one of its four verification techniques to monitor illicit nuclear activity. The other three verification techniques are seismic, hydroacoustic, and radionuclide. These verification techniques are managed by the International Monitoring System (IMS) and have led to greater interest into how infrasound propagates in the atmosphere (*Le Pichon et al.*, 2010).

Donn and *Rind* (1971) and *Rind et al.* (1975) used infrasound, and specifically microbaroms, to probe the upper atmosphere. The detection of infrasound also allowed for scientists to investigate the state of the atmosphere (*Drob et al.*, 2003, *de Groot-Hedlin et al.*, 2010), in a manner similar to the method used by *Verbeek* (1885) to determine the theoretical temperature that waves from Krakatoa would have travelled through to reach the observing station in Sydney.

The upper atmosphere has attracted greater research interest in recent years due to the need to understand the dynamics of higher altitudes, thereby stimulating renewed interest in infrasound as an atmospheric probe. The next sections seek to give a general overview of the atmosphere, and includes the discussion of the regions of interest for this thesis.

1.3. Structure of the Earth's Atmosphere

Detection of infrasound signatures in the variations of hydroxyl emissions is the main aim of this project. These emissions emanate from a chemiluminescent layer located in the vicinity of the mesopause and result from the excitation of hydroxyl radicals (an unstable species).

Before embarking on a full explanation of the method, a knowledge of chemical composition and thermal structure of the atmosphere is required. The structure of the atmosphere is primarily defined by the atmospheric layers, based upon the variation of temperature as a function of altitude. The laws of thermodynamics govern the atmosphere as the molecular gases move about in random motion, where they can be described by statistical mechanics (*Fleagle* and *Businger*, 1980). Chemical reactions between the gases drive the dynamics of different layers that will be described later in this section.

The layers themselves are defined by the temperature gradient and also the chemical makeup, with the dry atmosphere defined by three main molecules - molecular nitrogen, molecular oxygen and argon (Table 1-1) (where dry refers to the exclusion of water from the composition). Nitrogen is the most abundant molecule of the dry atmosphere as shown in Table 1-1 with oxygen the second most common. Water is not considered part of the dry atmosphere but, if taken into account, the ranking shown in this table can change substantially.

Component	*Symbol*	*Volume %*	*Weight %*
Nitrogen	N_2	78.08	75.51
Oxygen	O_2	20.95	23.15
Argon	Ar	0.93	1.28

Table 1-1: Composition of the dry atmosphere below 80 km altitude (*Thompson*, 2002)

Although water vapour concentrations are highly variable and reside mainly in the lower atmosphere, concentrations can reach levels of 3% (*Seinfeld* and *Pandis*, 1998). The remaining constituents (*i.e.* the trace gases) that mainly compose the atmosphere are listed in Table 1-2. Trace gases play important roles in the behaviour of the atmosphere despite their low relative abundances. Such gases are an essential component to the determination of the planet's radiative budget (*Seinfeld* and *Pandis*, 1998). Ozone and so-called "greenhouse gases" such as carbon dioxide and methane are just some examples of these low concentration gases. Although not on the same scale of importance as ozone and methane, the chemical constituent of primary importance in this thesis, namely the hydroxyl radical (OH*), also has a very low abundance but plays a vital role at all latitudes (*Summers et al.*, 1997) in the destruction of ozone.

Gas (and particles)	*Symbol*	*Volume %*	*Concentration/parts per million (ppm)*
Water vapour	H_2O	0 to 4	
Carbon dioxide	CO_2	0.035	355
Methane	CH_4	0.00017	1.7
Nitrous oxide	N_2O	0.00003	0.3
Ozone	O_3	0.000004	0.04
Particles/aerosols (dust, sulphates, etc.)		0.000001	0.01
Chlorofluorocarbons	CFCs	0.00000001	0.0001

Table 1-2: Traces gases of the entire atmosphere, showing the variability of water vapour volume (Thompson (2002) *after Ahrens* (1991)*).*

Abundances of lighter gases increase with height, particularly above 90 km (*Fleagle* and *Businger*, 1980), *i.e.* the heterosphere, which is dominated by the process of molecular diffusion.

1.3.1. Atmospheric Layers

The atmosphere, in terms of mass, is unevenly distributed in the vertical direction. This contributes, in part, to differences in the thermal makeup of the atmosphere, which is used to categorise the atmosphere into individual layers. The thermal composition affects the dynamics of each region (*Salby*, 2012) and induces various unique processes. Up to 100 km in height, the atmosphere is known as the homosphere, because of constant mixing of the atmospheric components due to turbulence. Mixing of the components leads to the fact that the chemical composition in the homosphere region is independent of atmospheric height.

The distribution of radiant energy absorption in the atmosphere offers another description of the structure of the atmosphere. Radiation from the sun is absorbed in one of two main areas below 60 km, either at the surface of the Earth or in the ozone layer. This radiation is redistributed through the three main heat transfer processes: conduction, convection and radiation (*White et al.*, 1992). Areas of absorption lead to two temperature maxima, forming the basis of the thermal structure of the atmosphere, at the surface and around 50 km. These maxima are within the homosphere, as illustrated from Figure 1-3 below. Two minima are seen in the atmosphere's thermal structure, occurring at around 10 km and 85 km. These thermal extremes indicate the boundaries of the various layers in the thermal atmosphere.

The first layer with respect to the Earth's surface is named the troposphere, and extends from 0 km at the surface to the first minimum which can vary from 16 km in altitude at the equator, to as low as 8 km at the poles (*Seinfeld* and *Pandis*, 1998). The height of the troposphere depends both on the latitude (*White et al.*, 1992) and the season (*Sturman* and *Tapper*, 1996). Vertical mixing of this layer results in phenomena unique to the troposphere such as the Earth's weather, and is mainly a result of surface heating (*Salby*, 2012). The temperature of this layer plays a key role in the dynamics of the region and the temperature is seen to decrease with respect to altitude (Figure 1-3). The lapse rate describes the relationship between temperature and altitude, and is defined as

the negative of the rate of temperature change with altitude ($\Gamma = -\frac{dT}{dz}$) (so in the case of the troposphere, the layer exhibits a positive lapse rate due to the decreasing temperature with altitude). The height of the troposphere is marked by a sharp change in lapse rate, indicating that the temperature begins to increase with altitude. This upper boundary, where a change in lapse rate occurs, is known as the tropopause.

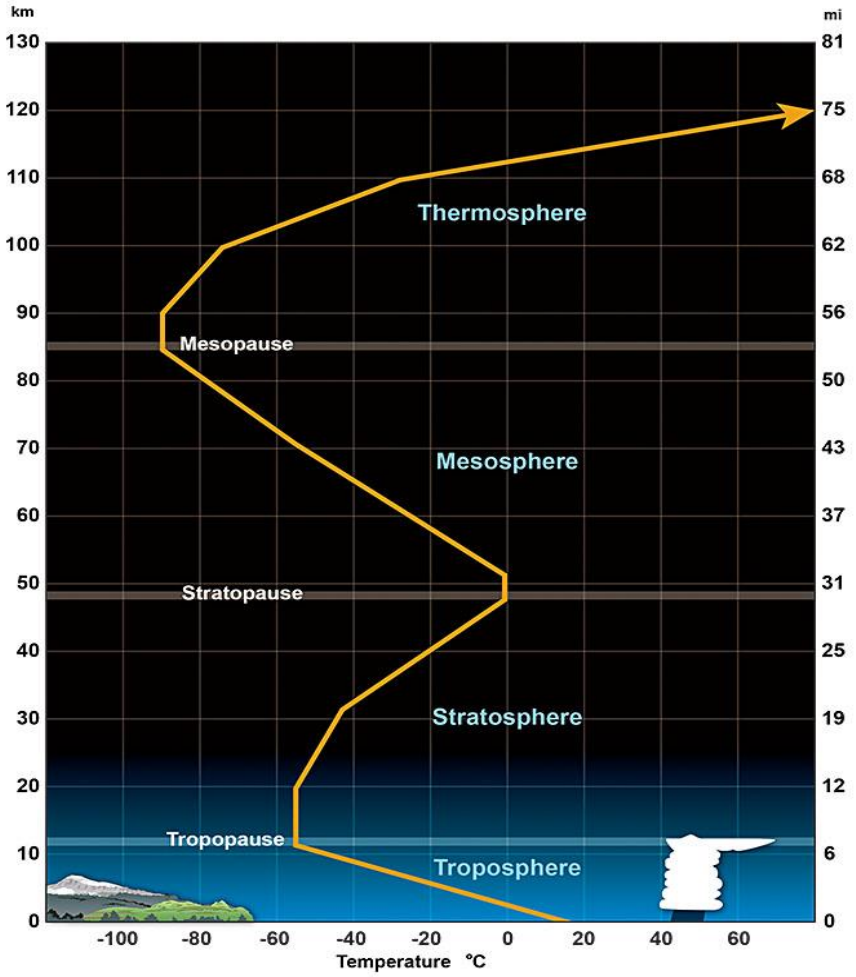

Figure 1-3: Temperature profile of the atmosphere up to 130 km (*NWS*, 2017).

Immediately above the tropopause is the layer known as the stratosphere. This layer is primarily known for the large ozone concentration that is present, which results in a warmer temperature for the layer (*Andrews*, 2010). Ozone molecules absorb solar UV radiation, causing a heating of this layer and resulting in a negative lapse rate (Figure 1-3 shows this temperature increase with respect to height). However, this ozone heating cannot fully explain the magnitude of the temperature increase. A lack of vertical

mixing within the stratosphere due to increase in temperature, as opposed to the convective overturning in the troposphere, also contributes to the large negative lapse rate seen in the layer. The stratosphere is a layer of little mixing between two layers of a large amount of mixing, which leads to a stratified (stable) region (*White et al.*, 1992). A change in lapse rate occurs again at the stratopause, located at around 50 km in altitude, and defines the upper boundary of the layer. The middle atmosphere is made of two parts, the stratosphere and the mesosphere (*Salby*, 2012). In terms of range, the mesosphere is distributed between the stratopause (at around 50 km in altitude) and the mesopause (occurring close to 85 km in altitude, but is subject to change). The mesosphere is separated from the stratosphere by the stratopause, where the temperature reaches a maximum with respect to the stratosphere. This temperature maximum does not sustain and there exists a positive lapse in the mesosphere. This contributes to the mesosphere being one of the coldest regions on the planet, with a number of factors contributing to the positive lapse rate, including a decrease in molecular density compared to lower layers (due to atmospheric density decreasing with height). UV radiation has little influence over the mesosphere due to the low molecular density and convective motion, where instead radiative processes are the main influencers of the region. The mesosphere is bounded above by the mesopause, where the second thermal minimum of the homosphere occurs. This area of the atmosphere is shown to be the coldest naturally occurring place on Earth and is critical for this thesis as it exhibits a particular type of radiative process in the form of hydroxyl emissions. These emissions come from the hydroxyl layer that is centred near ~ 87 km (*Pilger et al.*, 2013b) in the vicinity of the mesopause.

Above the region of the mesopause, there exists a layer known as the thermosphere. This layer of the atmosphere stands starkly opposed to the layer immediately below, as it is defined as the hottest layer of the atmosphere. The high temperature of the region is driven by UV radiation and high-energy x-rays, and indicates the amount of energy absorbed by the molecules present (which are present in very low densities). Due to this high temperature, which only increases in height, the thermosphere exhibits a negative

lapse rate. Importantly, the definition of the homosphere as mentioned earlier cannot be applied to this region (*Salby*, 2012). The thermosphere constitutes part of the atmosphere considered to be the heterosphere, where the atmosphere is not regarded as a continuous medium and is instead dominated by molecular diffusion processes. Gases in this region are distributed according to their weights as the region is subject to diffusive equilibrium rather than hydrostatic equilibrium (discussed later in Section 1.6.2), and results in heavier species at lower altitudes compared to lighter species.

Above this region, there occurs a very diffuse layer of the atmosphere known as the exosphere which merges with interplanetary space. This section of the atmosphere is tenuous and some atoms (mainly hydrogen and helium) which are normally gravitationally bound to Earth, may have sufficient speed to escape to the space (*Taylor*, 2010) (due to their low mass).

1.4. Upper Atmospheric Dynamics

The layers of the atmosphere already discussed are primarily heated by sunlight, however, other processes such as charged particle precipitation can also heat the upper atmosphere of a planet (*Lissauer* and *de Pater*, 2013). This precipitation can result from the solar wind incident on the planet. In Earth's case, this leads to several upper atmospheric phenomena, including the ionosphere (discussed in Section 1.4.1) and the aurora (borealis and australis) (Section 1.4.3).

1.4.1. The Ionosphere

Up to this point, the layers described constitute the neutral atmosphere. Extreme UV (EUV) radiation dominates in the ionosphere along with cosmic rays, causing photo-ionisation. This is a different characteristic compared to the layers already discussed, as

photo-ionisation in this region implies that the layer cannot be treated as electrically neutral. Ions and free electrons (plasma) are caused by solar radiation and interact with the Earth's electrical and magnetic fields (*Salby*, 2012), creating a section of the atmosphere that is ionised and overlaps with part of the neutral gas atmosphere (Figure 1-4). The classification of this region is based on plasma density rather than temperature.

The region that consists of plasma and free electrons is known as the ionosphere, consisting of four main layers – D, E, F1 and F2 illustrated in Figure 1-5 with each layer defined by its electron density (*Hargreaves*, 1992). The free electrons are key to the behaviour of the layer and they respond easily to electrical and magnetic fields because of their much lower mass compared with the ions, which explains why the ionosphere is often thought of in terms of total electron content (TEC).

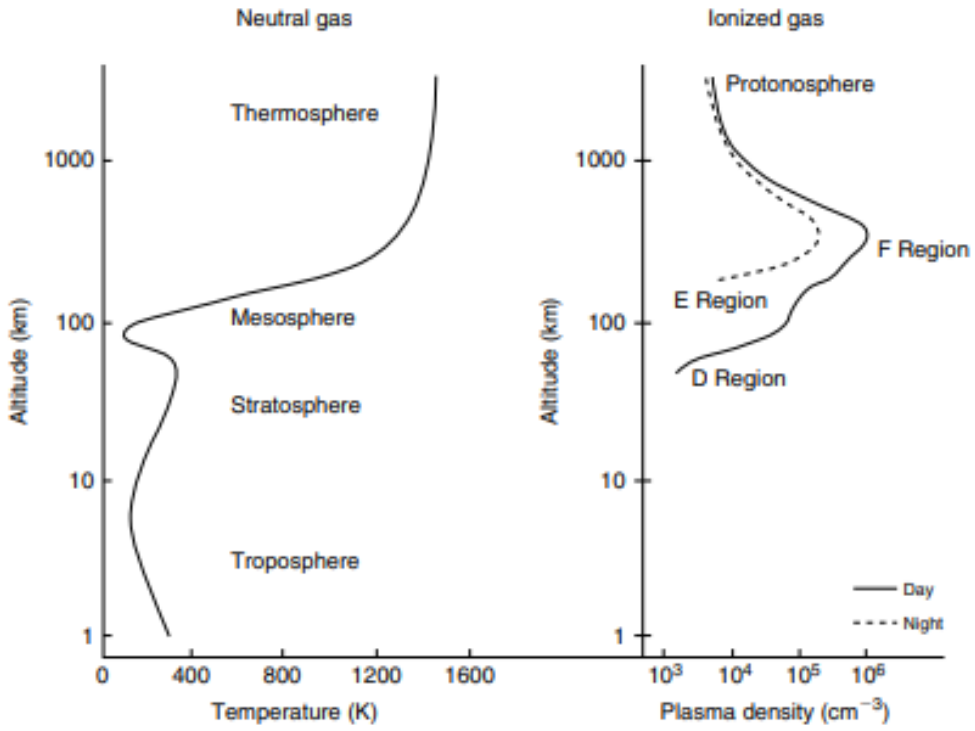

Figure 1-4: The altitude profile of the neutral atmosphere and the ionosphere (Kelley, 2009)

TEC is defined as the number of free electrons in a $1\,m^2$ column (along line of sight) (*Leick et al.*, 2015) and is used in GNSS (Global Navigation Satellite Systems) systems

such as GPS (USA) and GLONASS (Russia) for navigation and mapping. The value for TEC for any area of the ionosphere is constantly changing over periods of hours to seasons and decades (*Scharroo* and *Smith*, 2010). Some authors have noted that irregularities in TEC can be attributed to earthquakes (*Otsuka et al.*, 2006, *Afraimovich*, 2008), with many irregularities arising from coronal mass ejections and changes in UV radiation (*Leick et al.*, 2015). Other authors have stated that irregularities in TEC could be caused by acoustic gravity waves (*Kotake et al.*, 2007).

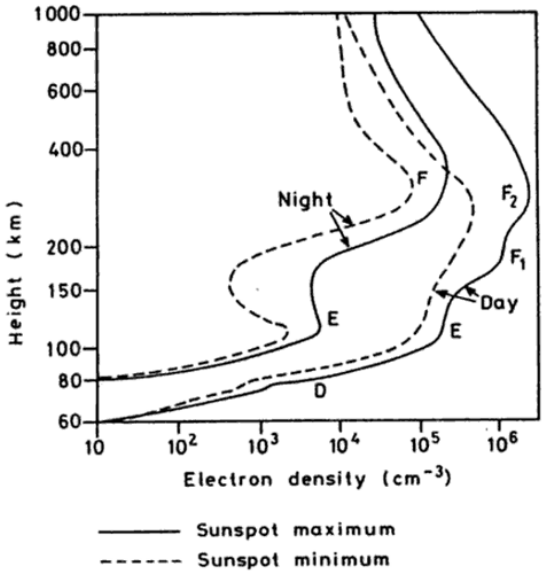

Figure 1-5: Ionospheric layers depicting the electron density of each. Scintillation measurements (explained in text) are usually made in the higher electron density areas (Hargreaves, 1992*)*

These TEC irregularities can cause a phenomenon known as scintillation, which is the rapid variation in amplitude and phase of signals propagating through the ionosphere, such as radio and GPS signals. This implies that if a radio signal undergoes scintillation due to TEC irregularities, the source of the irregularities could theoretically be detected. Such measurements could serve as supporting evidence for waves in other parts of the atmosphere. The technique has maximum sensitivity in the altitude region where the electron density has its maximum (~300 km). Unfortunately, this means that it is relatively insensitive in the region of the hydroxyl layer (*Verhulst* (2018), *private communication*).

1.4.2. The Magnetosphere

The magnetosphere of the Earth is defined as the region of space where the dominant magnetic field is that of the Earth (*SWPC*, 2021), and results from the interaction of the solar wind with the Earth's magnetic field. The regions of the magnetosphere are shown below in Figure 1-6. This sketch shows the Sun on the left-hand side, from which the solar wind originates, with the night-side of the Earth indicated by the dark-side of the planet in the sketch (right-hand side). As noted by *Moldwin* (2008), the Earth's inner magnetic field lines resemble that of a dipole, where the magnetic field lines originate in the south pole and flow to the north pole, shown in Figure 1-6. The sketch also demonstrates the radiation belts, which are now known as the Van Allen belts, and the ring current (*Lissauer* and *de Pater*, 2013), which is the electric current in the magnetosphere caused by charged particles in the Van Allen Belts.

Due to the high speed of the solar wind, a bow shock wave is produced upwind of the magnetosphere, towards the Sun (known as the dayside of the Earth). The solar wind still affects the Earth's magnetic field by compressing the field on the dayside of the Earth (*Strangeway*, 2008). The solar wind also acts to stretch out the Earth's magnetic field on the night-side, creating a geomagnetic 'tail' as seen in Figure 1-6.

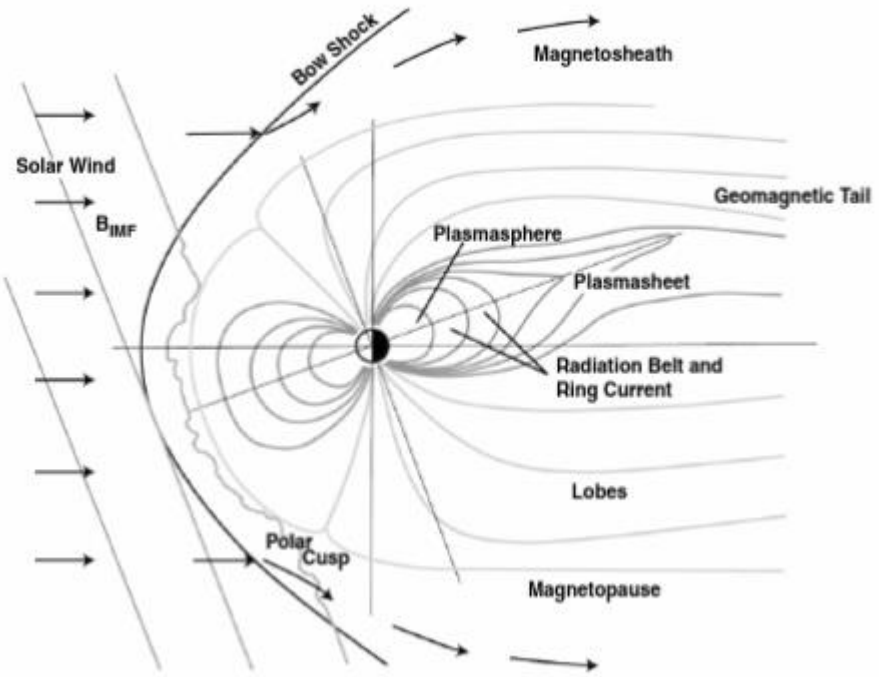

Figure 1-6: Sketch of the Earth's magnetosphere (*Moldwin*, 2008)

One of the processes that can take place is that of the magnetic field lines brought in by the solar wind connecting to the field lines of the Earth. This depends on the orientation of the magnetic field in the solar wind to the Earth's field lines. Reconnection can result from this process, leading to one of the most well-known phenomena in the upper atmosphere at polar latitudes: the aurorae.

1.4.3. Aurorae

The main cause of the aurorae, both in the Northern and Southern hemispheres, results from the precipitation of energetic charged particles from the solar wind into the atmosphere (*Strangeway*, 2008). These charged particles (electrons and protons) are retained within the Van Allen belts, and can spiral into the Earth's atmosphere, colliding with atoms, molecules and ions. This influx of precipitating particles excites the atoms and ions, and upon de-excitation, result in the optical display known as the aurorae.

Strong auroral displays can result from the reconnection process, first mentioned in the previous section (Section 1.4.2). This reconnection of the Earth's magnetic field lines can occur on the dayside or the nightside of the magnetopause (Figure 1-7).

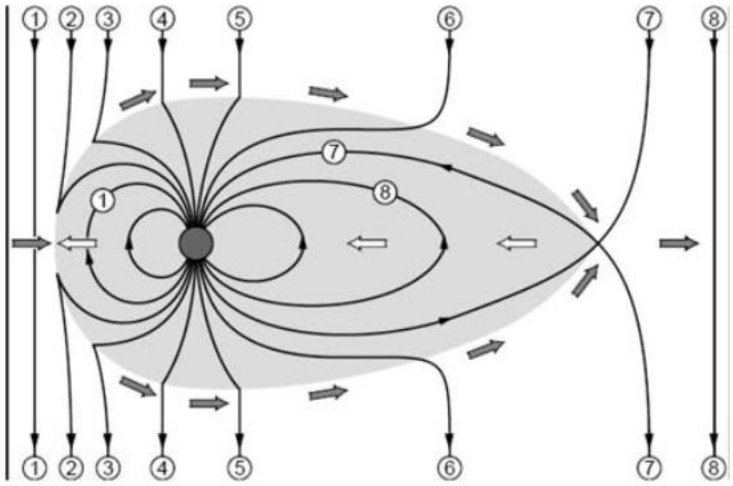

Figure 1-7: Reconnection areas (where white and grey arrows meet) for Earth's magnetic field lines which lead to an influx of charged particles into the Earth's atmosphere (*Fujimoto et al.*, 2008).

Reconnection can lead to substorms in the magnetosphere, resulting in aurora intensifications (*Strangeway*, 2008). The colour of the aurora depends on the energy of the precipitating particles originating from the magnetosphere, as well as the subsequent molecules/ions that the particles encounter. The precipitating particles have energies between $\sim 1 - 10$ keV (*Zhou et al.*, 2003), where particles with energies around 1 keV penetrate to lower altitudes, colliding with oxygen, to produce the recognisable green aurorae (*Strangeway*, 2008). Particles with energies of around 10 keV can penetrate deeper into the atmosphere and create purple/red auroral displays associated with nitrogen (*Hallinan*, 1991).

1.4.4. Airglow

The aurora are not the only optical emissions present in the confines of the upper atmosphere. As mentioned earlier, there exist optical emissions due to airglow in the upper/middle atmosphere. Photochemical reactions resulting in the emission of light lead to the creation of phenomena known as airglow, a constant source of electromagnetic radiation in the sky (*Fleagle* and *Businger*, 1980). Several reactions exist which lead to multiple airglow layers, such as the oxygen green line layer (557.7 nm), oxygen red line layer (630 nm), the sodium layer and the hydroxyl layer. These layers are normally confined to relatively narrow regions of the atmosphere, as shown for the oxygen red and green lines in Figure 1-8, rendering them useful for the study of dynamics within the given region. Figure 1-8 also shows that the narrow regions that the layers occupy can vary depending on the time (night or day), where the dynamics of the area around **100** km can more easily be obtained at night using the green oxygen line, compared to the same airglow layer present in the day.

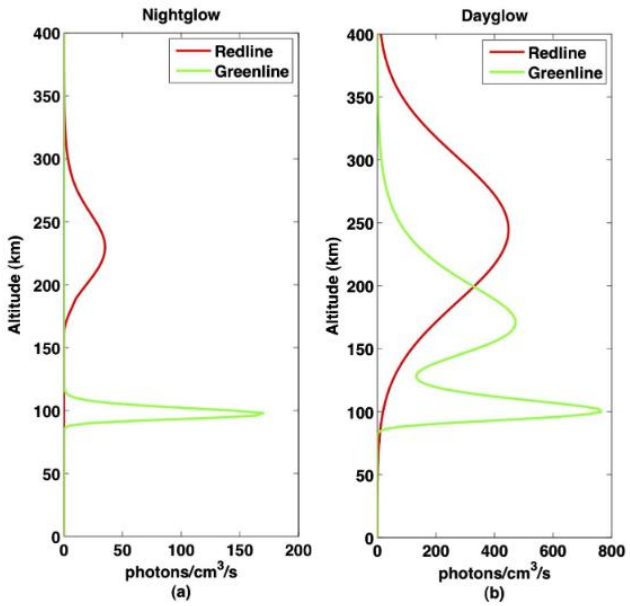

Figure 1-8: Altitudinal distribution of the Oxygen lines (green and red) during the night and day (*Huang et al.*, 2012)

As these emission layers result from the process of chemical reactions, they are said to be chemiluminescent in nature. The same process holds true for the main layer of focus: the hydroxyl layer. Many studies (e.g. *Hecht et al.* (2007), *Snively* (2013) and *Gumbel et al.* (2020)) have used the hydroxyl layer as a tracer for upper atmospheric dynamics due to the narrow region it occupies.

1.5. The Hydroxyl Layer

The region known as the mesopause (~90 km altitude) has become an active area of research as less is understood about the region due to its inaccessibility to satellites and *in-situ* instruments like rockets and weather balloons. The region is too high for balloons to reach and too low for measurements by satellites (*Kelley*, 2009). Rockets, particularly sounding rockets, have been used to obtain data from the region (*Baker* and *Stair*, 1988). These expeditions are expensive and infrequent, leading to remote sensing to become a prominent method for probing the mesopause. Measurements have been made of mesopause temperatures (*Ortland et al.*, 1998) and gravity wave activity (*Taylor* and *Hill*, 1991, *Liu* and *Swenson*, 2003) through remote sensing.

Such measurements are achieved through the use of radiative processes in the mesosphere, namely emissions resulting from excitation of hydroxyl. Hydroxyl is the combination of atomic oxygen and hydrogen, and comes in two types, ground state hydroxyl (OH) and hydroxyl radicals (OH*). The hydroxyl radical, which is the species at play in the hydroxyl layer, is highly reactive due to the presence of an unpaired valence electron in the outer shell. Hydroxyl is not only present within the mesopause region, but is also present in lower layers (*Seinfeld* and *Pandis*, 1998), and acts to destroy ozone within the stratosphere and mesosphere (*Summers et al.*, 1997). The hydroxyl layer near the mesopause, however, incorporates the largest abundance of hydroxyl radicals in the atmosphere, concentrated in a narrow layer, making it useful for the study of this region.

Hydroxyl emissions are also known as the Meinel bands (after *Meinel* (1950) and (*Meinel*, 1950b)) and emit primarily in the infrared part of the electromagnetic spectrum. *Meinel* (1950) first attributed the emissions of these bands to arise from the rotation-vibration spectrum of hydroxyl (OH*). Many studies have used the OH* bands as a probe to determine and investigate the chemistry and dynamics of the poorly understood region (*Marsh et al.*, 2006). *Xu et al.* (2012) conducted studies to investigate the mechanisms of the OH Meinel bands, furthering knowledge of how this hydroxyl layer arises. Transient features that affect the chemistry and dynamics of the hydroxyl layer have been investigated (*Peterson*, 1979, *Sedlak et al.*, 2016, *Chadney et al.*, 2017, *Hannawald et al.*, 2019). Many investigations have studied gravity wave propagation through the hydroxyl layer both on a climatological (*Rourke et al.*, 2017) and case-by-case (*Taylor et al.*, 1995) basis.

To fully understand the dynamics and uses of the hydroxyl layer, a basic knowledge of the chemistry of the hydroxyl radical is required. The hydroxyl radical can either be found in the atmosphere in its ground state or vibrationally excited state, and this thesis focuses on the excited state. *Pickett et al.* (2006) estimate that near 90 km, the amount of excited OH* is around 20% of all OH present at that altitude. These excited OH* radicals (molecules with an unpaired electron) are highly reactive and are the species that give rise to the emissions in the near infrared.

Oxygen, through a covalent bond, is combined with atomic hydrogen to produce a hydroxyl molecule. This radical is highly reactive due to the presence of an unpaired valence electron and is created in the mesopause by the following reaction (*von Savigny et al.*, 2012):

$$O_3 + H \rightarrow OH^* (v' \leq 9) + O_2 + 3.34\,eV \qquad (1\text{-}1)$$

Equation (1-1) shows an exothermic reaction (one that emits heat) involving atomic hydrogen and ozone to create OH* radicals in vibrationally excited states. These vibrationally excited states are from $v' = 1$ to $v' = 9$, where 9 is given as the highest

vibrational level. OH* radicals are unstable resulting in short lifetimes (on the order of milliseconds), where the radicals de-excite according to various processes. Processes which can cause this de-excitation include spontaneous emission, quenching and reaction with other species such as atomic oxygen. The photoemissions of these vibrational levels occupy a wavelength range from around $0.4 - 5$ μm, as shown through the diagram in Figure 1-9 from *Roach* and *Gordon* (1973). It is noted here that the vibrational bands are not the only bands of interest for studying the hydroxyl layer, as rotational bands are also produced, which are investigated to obtain the temperature of the mesopause.

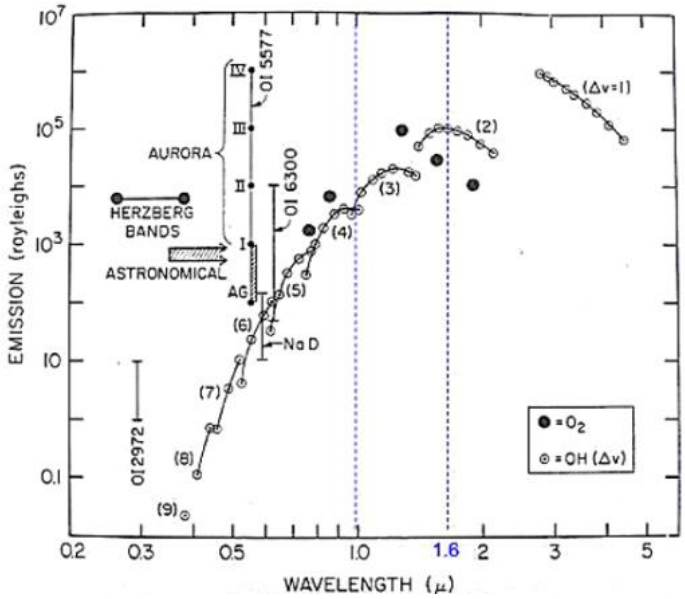

Figure 1-9: Wavelengths of the vibrational bands of hydroxyl. Wavelengths for the aurorae emissions coincide with many of these bands. The region between 1 - 1.6 μm is highlighted as it will be of special interest to sections leading forward (*Roach* and *Gordon*, 1973)

The mechanism in Equation (1-1) is widely accepted to be the main contributor to the presence of the hydroxyl layer (*Bates* and *Nicolet*, 1965, *Xu et al.*, 2012). This mechanism results in the formation of the layer centred around 87 km, with a full-width half-maximum of about 8 km (*Baker* and *Stair*, 1988). The hydroxyl layer, which emits primarily in the infrared region, was first identified and described by *Meinel* (1950) as noted above. More recent studies (*von Savigny*, 2015, *Wüst et al.*, 2017) have reported that the altitude of the layer can change, as well as the shape of the layer's distribution. *Grygalashvyly et al.* (2014) have explored this question while calculating the mean trends

of the hydroxyl layer at various altitudes. It is of note here that *Krassovsky et al.* (1962) and *Nicolet* (1970) have proposed another reaction which can give rise to excited OH* radicals, called the per-hydroxyl reaction. The mechanism given by *Xu et al.* (2012) describing the reaction is given in Equation (1-2) below:

$$HO_2 + O \rightarrow OH^*(v <= 6) + O_2 \tag{1-2}$$

The importance of this mechanism in the formation and continued source of hydroxyl molecules in the layer have been a subject of detailed research as outlined by *Xu et al.* (2012) and references therein. Some argue the mechanism only gains importance in the generation of low vibrational states (*Makhlouf et al.*, 1995) and others (*McDade* and *Llewellyn*, 1987) have argued that the contribution of hydroxyl to the layer by way of this mechanism is minimal. In the context of this report, it will not be examined as a substantial contributor.

Of importance to this thesis are the production and loss mechanisms leading to varying concentrations of hydroxyl molecules in this layer. As the observation of pressure waves relies on this concentration variation, these mechanisms are discussed in detail next.

1.5.1. Processes Leading to the Hydroxyl Layer

Equation (1-1) produces vibrationally excited OH* vibrational states up to $v' = 9$. De-excitation from these states can occur through spontaneous emission (*Grygalashvyly et al.*, 2014), which results in the phenomenon known as the airglow layer. The mechanisms that result in the production and excitation of hydroxyl radicals are dependent on the concentrations of the reactants.

As noted in the previous section (Section 1.5), only Equation (1-1) will be considered when discussing the production of hydroxyl. The presence of the hydroxyl layer is driven by the concentration of atomic oxygen, with the production of hydroxyl radicals being linearly dependent on it. Equation (1-1) shows that OH* is dependent on the

concentration of ozone (O_3) in particular, where the main mechanism of ozone production in the upper atmosphere is given by *Melo et al.* (2000):

$$O + O_2 + M \rightarrow O_3 + M \tag{1-3}$$

where, the value of M is defined a "third-body" and represents O_2 and N_2 (*Marsh et al.*, 2001). As a result, these constituents drive the production of ozone, which leads to the hydroxyl layer in the upper atmosphere, a process shown by Figure 1-10. The plot shows the theoretical night-time concentrations of atomic oxygen and M molecules, where they intersect at the top of the mesosphere, representing a point of maximum concentration for ozone, and thus hydroxyl.

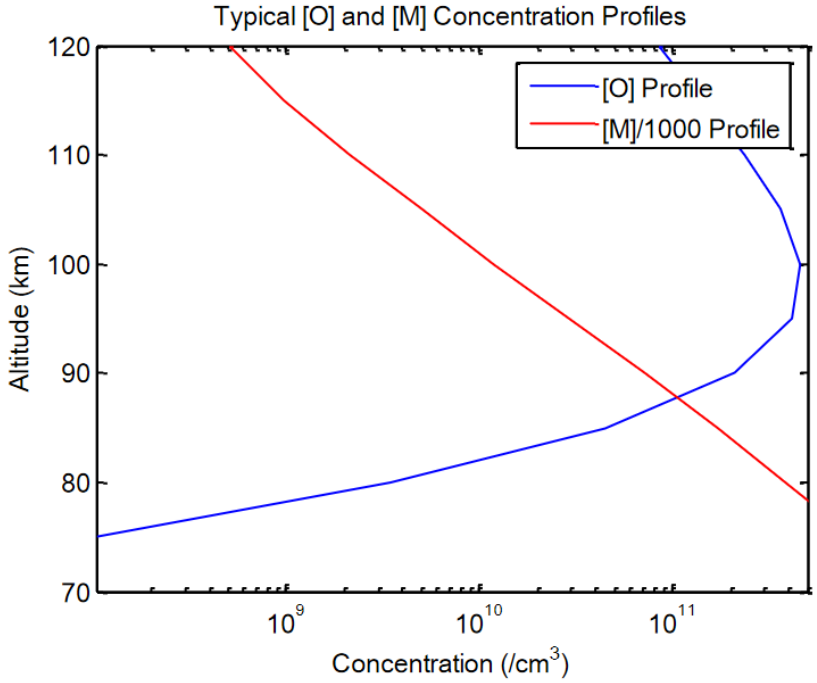

Figure 1-10: Concentration profiles of the reactants in the ozone production mechanism. The intersection of the concentration curves show the optimal region for ozone production and thus hydroxyl production (leading to the hydroxyl layer) (*McCarthy*, 2015)

The general production term is given by *Grygalashvyly et al.* (2014) for Equation (1-1) as:

$$P_{OH*} = k_1[H][O_3] \tag{1-4}$$

where $k_1 = 1.4 \times 10^{-10} e^{(-470/T)}$ is the reaction rate and T is the temperature (in Kelvin) (*Sander et al.*, 2006) and the square brackets denote the concentration of the species. Equation (1-4) only considers the production of hydroxyl through the main equation rather than the per-hydroxyl reaction in Equation (1-2).

The production of hydroxyl through this main reaction in Equation (1-1) is deemed to be a simpler process than that of the loss mechanism, which mainly results from quenching with M (O_2 and N_2) and a chemical reaction with atomic oxygen (*Melo et al.*, 2000), however other loss mechanisms exist and are described below.

1.5.2. Loss/Relaxation Processes

Before infrasound is discussed, it is important to note the relaxation processes of the OH* radicals, as these give rise to the measurable quantity of infrared emissions. Relaxation plays an important role in the overall project, allowing for visual confirmation of $O_3 - H$ interactions. Relaxation processes can occur in three main ways as referred to in Section 1.5.1, above, where vibrational relaxation is the focus in this thesis. As noted by *Khomich et al.* (2008), vibrational relaxation involving collisions with molecules surrounding the species in question is important for relaxation processes in the case of OH*. These authors go further and discuss the transition probabilities of the vibrational levels, also discussed by *Turnbull* and *Lowe* (1989). In terms of loss processes of OH* radicals, this is discussed in *Makhlouf et al.* (1995) and *Xu et al.* (2012). Spontaneous emission occurs when a photon is released from, in this case, an unstable molecule. Quenching occurs when the radical collides with another molecule or atom – usually by collisions with O_2, N_2 and O. In general, quenching will cause the OH* radical to de-excite to another vibrational level. In certain cases, 'sudden death' can occur (*Xu et al.*, 2012) where the radical is quenched to the lowest vibrational state, $OH_{v=0}$. The last case to consider is de-excitation by chemical reaction such as can be seen in Equation (1-5) (*Bates* and *Nicolet*, 1965):

$$OH^*(v) + O \rightarrow H + O_2 \quad (1\text{-}5)$$

All three cases must be considered when discussing de-excitation of OH*. These deactivation processes are relevant to how OH* radicals are viewed using various instruments. However, each mechanism results in the eventual emission of light, the basic process of which is shown in Figure 1-11.

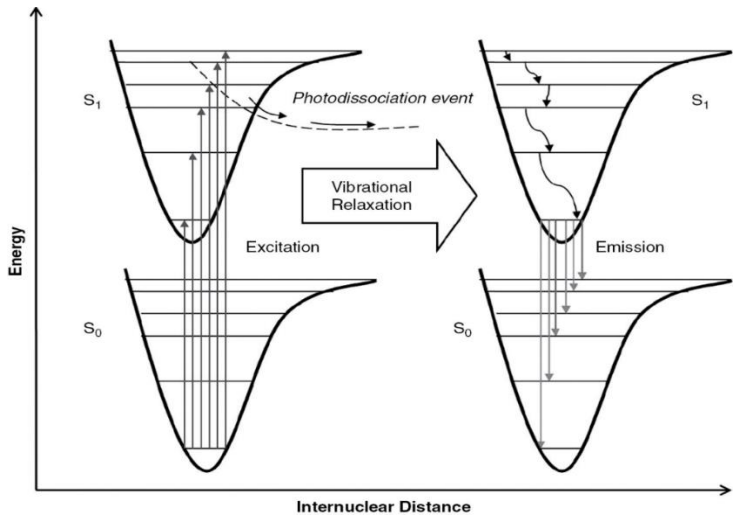

Figure 1-11: Diagram showing the excitation and eventual emission of a diatomic molecule by vibrational relaxation (*Coble et al.*, 2014)

The emission rate of OH* depends on the concentration of atomic oxygen and other constituents (O_2 and N_2), but not on the concentration of ozone (*Melo et al.*, 2000). Equation (1-1) is the main destruction mechanism of ozone, and for ozone to be in equilibrium, creating hydroxyl, the rate of destruction of ozone by Equation (1-1) must equal the rate of creation of ozone by Equation (1-2).

1.5.3. OH* Lifetimes

The chemical lifetime of the hydroxyl radical is an important parameter in the determination of whether acoustic waves can affect the hydroxyl layer in such a way that

they can be observed. As well, these lifetimes also give an idea of the basic dynamics of the region. An assumption that is made throughout the current project is that the hydroxyl layer is in photochemical equilibrium. This assumption can only hold true if the relaxation of hydroxyl is smaller than that of the photochemical lifetimes between molecules that result in the formation and destruction of OH* (*Grygalashvyly et al.,* 2014). Given that the hydroxyl radical is an unstable molecule, the expected lifetime would be extremely short (seconds or less) and thus the layer would be in a steady-state equilibrium (*Le Texier et al.*, 1987, *Belikovich et al.*, 2018). *Grygalashvyly et al.* (2014) use this assumption of the photochemical equilibrium, noting that the lifetimes of the relaxation stage of OH* are small compared to its production rate. The radiative lifetimes of OH* radicals (vibrationally excited) are given in the range of milliseconds (*van de Meerakker et al.*, 2005). *Sivjee* and *Hamwey* (1987) go further and state that the radiative lifetimes of hydroxyl are on the order of about $4-6$ milliseconds at 87 km. However, these values are only defined for the vibrationally excited states of $v'=8$ and $v'=6$, and as such, *Xu et al.* (2012) gives the most comprehensive account of these lifetimes. *Xu et al.* (2012) give lifetimes of $t=1$ ms for $v'=9$ and $t=30$ ms for $v'=1$ at an altitude of ~ 85 km, supporting the lifetime estimates by other studies.

Perhaps the most significant discussion on the values for lifetimes in relation to this study is that of *Tarasick* and *Shepherd* (1992). The authors note within their study that the concentrations of species such as hydroxyl would not be greatly affected by waves with periods longer than that of the chemical lifetimes. Although the authors only analyse gravity wave dynamics, they elaborate that the given analysis is also applicable to situations of acoustic perturbations, which are waves of shorter periods. These statements and results show that for acoustic waves travelling through the airglow layer, the OH* lifetimes are sufficient to allow signatures of such disturbances to be theoretically observable, coupled with the short lifetimes of the hydroxyl excitations.

1.5.4. OH* and pressure

Focus on the production and loss of [OH*] allows for a derivation to obtain the dependency of OH* concentration on pressure. Assuming a photochemical equilibrium of O_3, and quenching by predominantly atomic oxygen (*Adler-Golden*, 1997) the following is obtained:

$$[OH^*] = \frac{6 \times 10^{-34}(300/T)^{2.4}[O][O_2][M]}{Q[O_2]} \tag{1-6}$$

This equation is as quoted in *Grygalashvyly et al.* (2014). $[M]$ is the number density of air (synonymous with concentration), and Q is the rate of quenching by molecular oxygen, while T is temperature. Allowing the number density of air to be represented by an ideal gas, the following is obtained:

$$[OH^*] = \frac{6 \times 10^{-34} 300^{2.4}}{\kappa Q} p T^{-3.4}[O] \tag{1-7}$$

Equation (1-7) draws a direct relation between the concentration of OH* and pressure. This relation is important in terms of the effect that acoustic waves will have on the mesopause. Acoustic waves are pressure variations of a medium (a series of compressions and expansions of the air) and will be discussed further in Section 1.7.4.

1.6. Dynamics of the Atmosphere

Atmospheric motion is primarily driven by radiation from the Sun (*Taylor*, 2010). This heat (radiation) is distributed across the globe, flowing from equator to pole, governed by three fundamental laws (*Kalnay*, 2003, *Brasseur* and *Solomon*, 2006):

a. The conservation of mass

b. The conservation of momentum

c. The conservation of energy

Kalnay (2003) also discusses the importance of the equation of state, as well as another conservation equation regarding water mass. The main principles governing atmospheric motion can be applied to obtain the main governing equations, namely Newton's second law, the continuity equation and the first law of thermodynamics. All three equations are introduced in the next section, where the fundamental forces influencing circulation and the associated variables are discussed first.

1.6.1. Fundamental Forces

Before the forces are introduced, the variables at play are noted. *Bjerknes* (1904) discussed how the state of the atmosphere at any given point in time can be described by seven variables: density, pressure, temperature, humidity and the three components of velocity (v_x, v_y, v_z). *Holton* (2004) notes the main forces affecting these variables include the pressure gradient force, the force due to gravity and the frictional force. These forces can be applied both to the static frame of reference and a rotating frame of reference. In a rotating frame of reference, additional apparent forces apply, including the Coriolis and centrifugal forces.

Pressure is described as the momentum transfer per unit time per unit area exerted on an infinitesimal volume of air (*Holton*, 2004). The net force applied to such a volume by this momentum transfer is known as the pressure gradient force, which is proportional to the gradient of the pressure applied. The force due to gravity is based on Newton's Universal law of gravitation, while viscosity (friction force) causes the atmosphere to resist flow. The two apparent forces noted occur in the non-inertial reference frame of the Earth (rotating). For the main laws to function on a non-inertial reference frame, acceleration of the frame must be considered, which leads to the creation of these fictitious forces.

The centrifugal force arises due to the rotation of the Earth. It is the apparent outward force exerted on an object when rotated, where the force acts opposite in direction to the force of gravity. The centrifugal force, however, is not sufficient to explain the total force acting on an object when in motion on the Earth's surface. An additional fictitious force called the Coriolis force is required to explain the forces acting on an object. The Coriolis force acts to deflect objects in motion when these objects are viewed from a non-inertial frame of reference (this motion is shown in Figure 1-12 below).

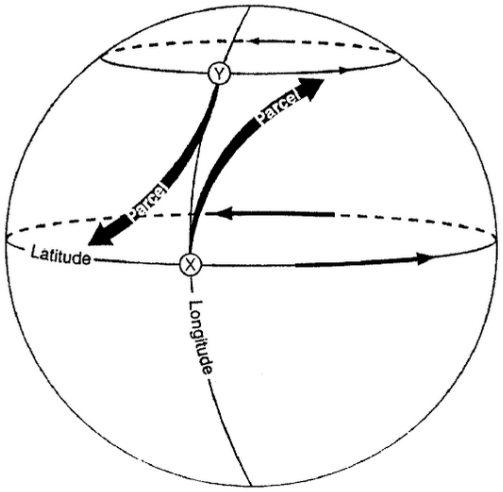

Figure 1-12: The concept of Coriolis induced deflection of winds on Earth. On the rotating sphere of the Earth, as a parcel of air moves south from Y to X, X is traveling at a higher velocity compared to Y and the parcel appears to an observer to deflect the parcel to the left. The same is said for a parcel travelling from X to Y, but instead the parcel appears to gain speed and deflect to the right (*Seinfeld* and *Pandis*, 1998)

The Coriolis and centrifugal forces are only relevant for motions on larger time scales, and are important for longer scale phenomena like the Earth's macro-circulation. For instance, when the sun heats the equator, circulation occurs, and extends from equator to pole, in what is known as a Hadley cell (*Taylor*, 2010, *Lissauer* and *de Pater*, 2013). As the Earth rotates, a single Hadley cell stretching from equator to pole is not stable and so multiple circulatory regime cells form between the equator and the pole. For the Earth's rotation, three separate cells form – the Hadley cell, the Ferrel cell and the Polar

cell (Figure 1-13). As the Coriolis force acts to deflect winds, it completes the circulation for the cells.

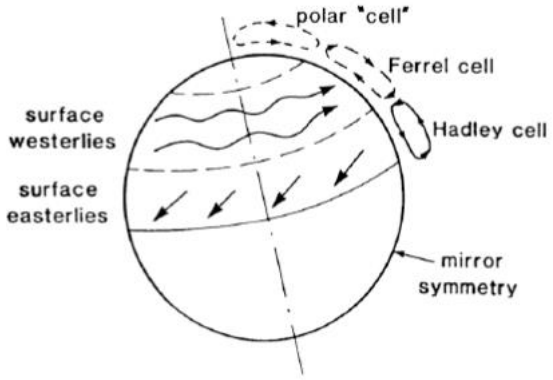

Figure 1-13: Overturning circulatory cells present in the Earth's Northern Hemisphere. These same three cells are found in the Southern Hemisphere (mirror image) (*Lissauer* and *de Pater*, 2013)

Importantly, the Coriolis force does not change the speed of the winds - only the direction of the winds are changed. The Coriolis force is not the only force acting on these cells, as the pressure gradient force also acts, directing winds from areas of high pressure to areas of low pressure. This pressure gradient force thus moves the atmosphere from high to low pressure areas until the force balances with the Coriolis force (*Kivelson* and *Schubert*, 1986). This leads to areas of constant pressure called isobars (where *iso-* is the Greek for equal). Isobars are areas where the pressure gradient force and Coriolis force balance in a situation known as geostrophic balance, with winds flowing along these lines (*Lissauer* and *de Pater*, 2013).

Geostrophic balance describes the forces acting in the horizontal, but the balancing of forces also occurs in the vertical direction. In this vertical direction, where the change in temperature has already been discussed (Section 1.3), a variation in pressure/density also occurs as a function of atmospheric height. As height from the ground increases, both atmospheric pressure and density decrease, due to the Earth's gravity. Situations arise where both the pressure gradient force and gravity balance, a process known as

hydrostatic equilibrium. This situation is described by the hydrostatic equation (*Holton*, 2004, *Lissauer* and *de Pater*, 2013):

$$\frac{dp}{dz} = -\rho g \tag{1-8}$$

Equation (1-8) describes how the change in pressure with respect to height is equal to the negative product of density and gravity. *Holton* (2004) notes that the concept of hydrostatic equilibrium fits well to observations and has been used as an approximation for simple global circulation models (*Jacobson*, 1999). A full derivation of the hydrostatic equation is given in Appendix A.

So far, the real and fictitious forces at play have been discussed, as well as situations where these forces balance in the horizontal plane (geostrophic balance) and vertical plane (hydrostatic balance). These forces are governed by three main conservation laws which are described in the following section.

1.6.2. Governing Laws

Brasseur and *Solomon* (2006) describe how the three basic principles of Earth's circulation are given by the conservation laws. For the atmosphere, as it is modelled as a fluid, these conservation laws are known in different forms. The conservation of momentum is demonstrated through Newton's Second law, while the conservation of energy is normally given in the form of the First Law of Thermodynamics. The final conservation law, the conservation of mass is represented by the continuity equation.

1.6.2.1. Equation of State

The equation of state is a fundamental equation, showing the relationship between variables that describe the atmosphere, which normally include pressure, temperature, and volume, among others (*Sanchez-Lavega*, 2010). As the atmosphere can be described as an ideal gas (it is mainly composed of nitrogen and oxygen, which both behave closely to ideal gases), the equation of state is given as:

$$PV = nRT \tag{1-9}$$

where P denotes the pressure, V the volume, T the absolute temperature. The value of R is the ideal gas constant ($= 8.314$ J/(K·mol)) and n is the number of moles of the substance/gas in the volume V. This relation arises from a combination of the following thermodynamic laws: Boyle's Law, Charles's Law, Avogadro's Law and Gay-Lussac's Law, and can also be expressed using the Boltzmann constant (k) as $PV = NkT$, where k is the Boltzmann constant and N is the number of molecules of gas in the volume V. The ideal gas equation underpins the main relations governing the atmosphere.

1.6.2.2. Conservation of Momentum

In a rotating frame of reference, *Holton* (2004) gives Newton's Second law as follows:

$$\frac{dv}{dt} = -2\Omega \times v - \frac{1}{\rho}\nabla p + \boldsymbol{g} + F_r \tag{1-10}$$

This equation follows the same logic as Newton's Second law, where the acceleration is equal to the sum of forces. Equation (1-10) shows the derivative of velocity. The left-hand side denotes the change in velocity (acceleration) for a small infinitesimal volume of atmosphere. The right-hand side is the sum of the following forces – the Coriolis force (Ω), the pressure gradient force, the force of gravity (effective gravity – which considers

the centrifugal force) and the force due to friction. This conservation law represents an equation of motion on the Earth's frame of reference, and can be simplified to:

$$\frac{dv}{dt} = \frac{\boldsymbol{F}}{\rho} \tag{1-11}$$

where **F** is the sum of all the aforementioned forces.

1.6.2.3. Conservation of Energy

As the atmosphere is modelled as a fluid, but is fundamentally a gas, the First Law of Thermodynamics represents the starting point for conservation of energy. For the atmosphere, *Holton* (2004) remarks that the first law shows that '*the change in internal energy of the system is equal to the difference between the heat added to the system and the work done by the system".*

This is given in equation form by *Gossard* and *Hooke* (1975) as:

$$dE = dH - dW \tag{1-12}$$

Equation (1-12) demonstrates the statement of *Holton* (2004), where E is the internal energy of the system, H the heat added to the system, and W the work done by the system. This equation represents the simplest version of the first law, but for applicability to the atmosphere, the law can be rewritten as:

$$\frac{c_p dT}{dt} - \frac{1}{\rho}\frac{dP}{dt} = Q \tag{1-13}$$

where c_p is the specific heat at constant pressure, and Q is the net heating rate per unit mass (*Brasseur* and *Solomon*, 2006). The left-hand side of Equation (1-13) shows the effect of compression and rarefaction of a fluid associated with adiabatic (where energy is

conserved) processes in a compressible fluid. The right-hand side instead represents the diabatic processes occurring (net heating/cooling effects).

1.6.2.4. Conservation of Mass

Conservation of mass within a fluid is given by the continuity equation (*Brasseur* and *Solomon*, 2006; *Andrews*, 2010). The continuity equation is best described using the Eulerian description of a small element of volume, where the Eulerian description is applied to a concentration of particles rather than the individual particles (which would be known as the Lagrangian description). More specifically, a Eulerian approach involves looking at the fluid flow at a given location and how this fluid flows through this space per unit time. The Lagrangian description, on the other hand, focuses on individual particles in a fluid and how they move in time and space.

A small volume with sides $\Delta x, \Delta y, \Delta z$ is considered, suspended in the atmosphere, where the fluid can flow through the volume (seen in Figure 1-14). The velocity of the fluid moving through this volume is given by the fluid velocity:

$$\boldsymbol{v} = (v, u, w) \tag{1-14}$$

The density of the flow is given by ρ. As the fluid passes through this volume element, a certain mass of the fluid will be present in the element. To determine this amount, it is clear that the net fluid inflow into the volume is equal to the difference of the inflow into the volume on the left of Figure 1-14 to the outflow on the right in the same figure (*Andrews*, 2010).

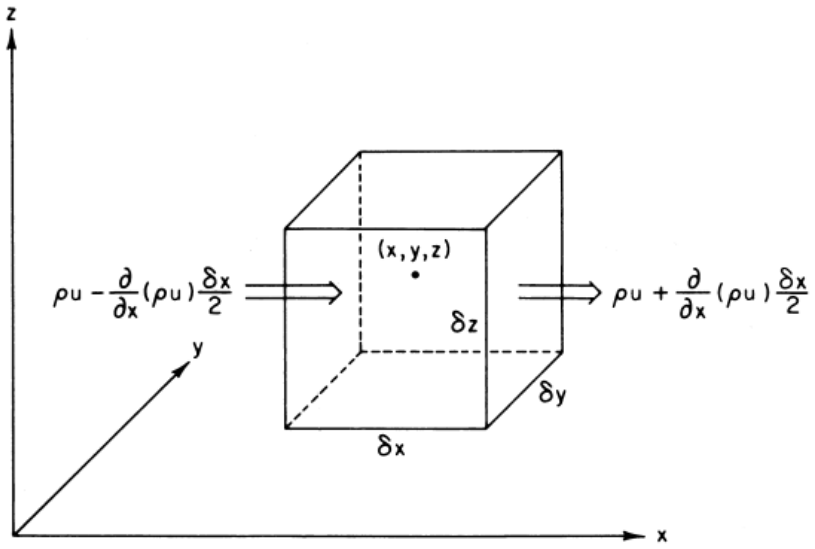

Figure 1-14: Small volume of atmosphere with fluid flow allowed through. This volume element is the basis behind the Eulerian description of the continuity equation. (*Holton*, 2004)

For the x direction, this difference in inflow and outflow is represented as the following:

$$\rho(x)v(x) - \rho(x + \Delta x)v(x + \Delta x) \tag{1-15}$$

This follows for both the y and z directions.

$$\rho(y)v(y) - \rho(y + \Delta y)v(y + \Delta y) \tag{1-16}$$

$$\rho(z)v(z) - \rho(z + \Delta z)v(z + \Delta z) \tag{1-17}$$

Equations (1-15), (1-16) and (1-17) represent the partial derivatives of the density and velocity of the fluid and are given by $\frac{\delta}{\delta x}(pv)\Delta x$ and so on. The total mass net inflow [MNI] is thus equal to the sum of these terms, each multiplied by the area through which the fluid is flowing (for instance $\Delta y \Delta z$ in the x-direction etc.):

$$MNI = \left(-\frac{\delta}{\delta x}(\rho v)\Delta x \Delta y \Delta z\right) + \left(-\frac{\delta}{\delta y}(\rho v)\Delta y \Delta x \Delta z\right) + \left(-\frac{\delta}{\delta z}(\rho v)\Delta z \Delta x \Delta y\right) \tag{1-18}$$

$$= -\left[\frac{\delta}{\delta x} + \frac{\delta}{\delta y} + \frac{\delta}{\delta z}\right](\rho v)(\Delta x \Delta y \Delta z)$$

Since the volume, $\Delta V = \Delta x \Delta y \Delta z$ and the product of the three derivatives is the divergence, then the mass net inflow is given as:

$$Mass\ net\ inflow = -\nabla \cdot (\rho v)(\Delta V) \tag{1-19}$$

The amount of fluid in the volume at any one time must thus equal the additional mass introduced by the fluid into the volume element. The mass increase is obtained through the mass, density, volume relation:

$$\Delta m = \frac{\delta}{\delta t}(\rho \Delta V) \tag{1-20}$$

Thus, bringing Equations (1-19) and (1-20) together:

$$-\nabla \cdot (\rho v)(\Delta V) = \frac{\delta}{\delta t}(\rho \Delta V) \tag{1-21}$$

$$-\nabla \cdot (\rho v) = \frac{\delta}{\delta t}(\rho) \tag{1-22}$$

$$\frac{\delta}{\delta t} + \nabla \cdot (\rho v)(\Delta V) = 0 \tag{1-23}$$

Equation (1-23) is known as the continuity equation.

The laws shown above are applied to stationary volumes of air, and thus are given in their Euclidian form. If such volumes are considered to be moving, they would then be discussed in their Lagrangian form where individual particles are considered. The Lagrangian form of the conservation of momentum law for instance is known as the Navier-Stokes equation. This equation represents an accurate description of fluid motion. Not only does it govern atmospheric motion - it has led to the modern inventions of passenger jets and fast submarines (*Stewart*, 2012).

The general principles of atmospheric motion have been introduced and discussed. However, the motion of the atmosphere is not confined to just the major atmospheric

circulation discussed, but it is subject to various wavelike phenomenon. Such waves can be of various scales and include larger scale waves such as Rossby (planetary) waves and smaller wavelike phenomena like turbulence. Figure 1-15 shows the various atmospheric phenomena and their general scales in the atmosphere. The grey box present at the top right of the figure shows the phenomena that are resolvable in atmospheric models.

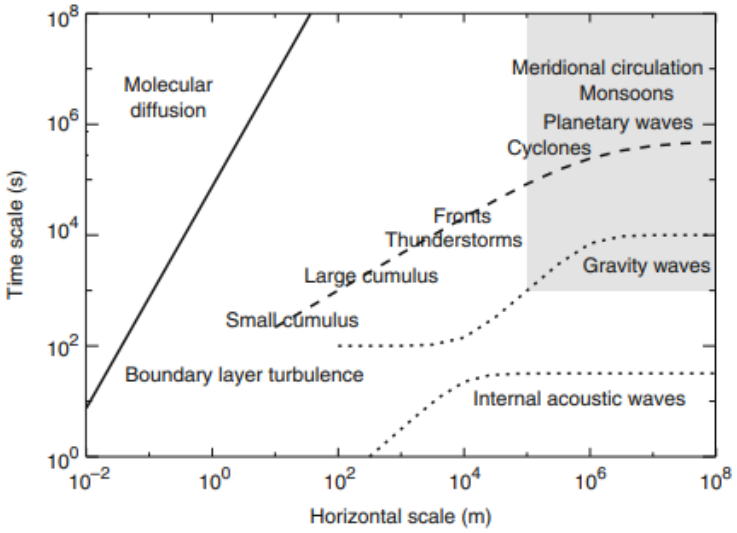

Figure 1-15: Horizontal scales and time scales of various atmospheric phenomena (*Thuburn*, 2011)

1.7. Atmospheric Waves

Four types of waves are introduced and discussed here – Rossby waves, tides, gravity waves and acoustic waves. Each of these waves affect the atmosphere in different ways. According to Figure 1-15, Rossby waves and gravity waves (implemented in parametrised form) can be resolved through atmospheric models, while acoustic waves are currently unresolvable. However, progress has been made ins this area as shown by *Le Pichon et al.* (2018) and refererences therein, in recent years.

1.7.1. Planetary Waves

Planetary waves, also known as Rossby waves, are large-scale transverse waves on the order of 10^4 km (*Thuburn*, 2011) which are important in the context of large-scale meteorological phenomena (*Holton*, 2004). For instance, Rossby waves are known to be associated with undulations in the jet stream (*Thuburn*, 2011), which have a large effect on the weather in mid-latitude regions such as Ireland, causing persistent weather patterns. These Rossby waves arise due to the variation of the Coriolis effect with latitude in a rotating atmosphere, where the Coriolis force acts as a restoring force for the waves (*Salby*, 1996). This results in Rossby waves propagating westward in the atmosphere, and are generally considered slow-moving, with speeds less than that of gravity waves. An example of a Rossby wave over the Northern Hemisphere is shown in Figure 1-16.

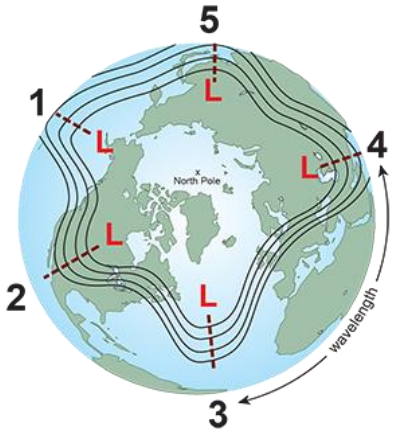

Figure 1-16: Rossby wave over the Northern Hemisphere showing areas of low pressure - these waves tend to trace out the jet stream (*NOAA*, 2019)

1.7.2. Tides

Another type of large wavelike disturbance in the atmosphere are tides. Tides are cyclical motions which are multiples of the solar day (*Taylor*, 2010), and come in two types: gravitational and thermal. This first type, gravitational tides, result from the push

and pull of both the Sun and Moon on the Earth's atmosphere while thermal tides arise due to the solar radiation incident on the Earth (*Chapman* and *Lindzen*, 2012). Gravitational tides due to the Sun are half as strong compared to similar tides resulting from the effect of the Moon, but both exert little influence on the atmosphere compared to thermal tides (*Taylor*, 2010). As thermal tides follow the heating of the atmosphere in response to solar radiation, these tides tend to be in diurnal or semi-diurnal cycles (where diurnal tides experience a single high and single low tide each day). This is shown in Table 1-3, where the wavelengths of tides are on the scale of the Earth's radius and have periods of multiples of a solar day. The general motion and characteristics of Rossby waves and gravity waves are also shown in Table 1-3. As *Taylor* (2010) points out, tides can be classified as a type of gravity wave, which are discussed in the next section.

Wave	**Horizontal Wavelength (λ)**	**Period (τ)**	**Horizontal Wave Phase Speed (λ/τ)**	**Motion**	**Source Mechanisms**
Rossby-planetary waves	$\sim R_E$	$\sim 5\tau_E$	$\ll R_E/\tau_E$	Geostrophic Hydrostatic	Instability Topographical forcing Differential heating
Tides	$\sim \frac{2\pi R_E}{n}, n = 1,2,\ldots$	$\sim \frac{\tau_E}{n}, n = 1,2,\ldots$	$\sim \frac{2\pi R_E}{\tau_E}$	Non-geostrophic Hydrostatic	Solar, lunar gravitational fields Solar heating
Gravity waves	$\ll R_E$	$\ll \tau_E$	$< C_0$	Non-geostrophic Non-hydrostatic (except for largest τ)	Instability Topographical forcing Differential heating Wave-wave interaction

R_E = radius of the Earth

τ_E = solar day

$\frac{2\pi R_E}{\tau_E} = 460$ m sec^{-1}

C_0 = speed of sound (~ 300 m sec^{-1} at altitudes < 100 km, increasing to 10^2 m sec^{-1} above)

Table 1-3: Characteristics of various transverse waves in the atmosphere. Tides for instance have periods following multiples of the solar day (*National Research Council*, 1977)

1.7.3. Gravity Waves

Gravity waves are transverse waves in the atmosphere where the restoring force is the buoyancy force (*Taylor*, 2010). These waves exist in any part of the atmosphere which can be described as a stably stratified fluid, as such a fluid can support these wave motions. Gravity waves are of a smaller scale than both planetary waves and tides, and thus the effects of the Earth's rotation and radius are negligible in the characteristics of these waves. Although this is true, they are nevertheless notable for their effect on the atmosphere, because they are associated with the transport of energy and momentum around the globe. The type of gravity waves present in the atmosphere are known as internal gravity waves as opposed to gravity waves on shallow water (*Holton*, 2004), also known as surface waves (*Nappo*, 2013). Surface waves propagate along the boundary interface of two layers, where the most common example cited are water waves and wind waves along the water-air boundary. Internal gravity waves exist in the atmosphere (example shown in Figure 1-17 below) due to the decreasing density of the atmosphere with height (stably stratified, except at the Earth's surface), thus giving a vertical gradient. As a result, unlike surface waves which can only propagate horizontally, internal gravity waves can propagate vertically through the atmosphere.

Figure 1-17: Example of internal gravity waves propagating in the troposphere above Maynooth University's observing station. Here, the gravity wave signature is visible in the cloud base (Credit: J. Kealy)

A parcel of air can be considered, which has been displaced from its equilibrium position, upwards, towards a region of lower density. Such a parcel of air obtaining the same density as it had originally would then be surrounded by areas of less dense air. Due to this density difference, the parcel of air decelerates and reverses direction to return to its original position (equilibrium). However, like a pendulum, the parcel of air overshoots the equilibrium position and once again is in a field of density difference to its own. The parcel of air would now be surrounded by air denser than the parcel of air, decelerating once again. This leads to the parcel of air oscillating about its equilibrium position. This oscillation has a characteristic frequency known as the Brunt-Väisälä frequency (N_A) (*Rehm* and *Radt*, 1975), which is dependent both on the density of the air and the acceleration due to gravity:

$$N_A^2 = -\frac{\mathrm{g}}{\rho}\frac{d\rho}{dz} \tag{1-24}$$

where $\frac{d\rho}{dz}$ represents the change of density with altitude in the atmosphere. Equation (1-24) represents the Brunt-Väisälä frequency in an incompressible atmosphere where acoustic waves cannot exist (known as the Boussinesq approximation (*National Research Council*, 1977)).

The Brunt-Väisälä (BV) frequency can change depending on the altitude at which gravity waves occur, but normally has a period of around $5-10$ minutes (*Holton*, 2004, *Nappo*, 2013). One notable aspect of the BV frequency is that as it increases, the stability of the given wave decreases (*Fleagle* and *Businger*, 1980). Although gravity waves do not necessarily have to oscillate at this frequency, the BV frequency has increased importance with respect to gravity waves as it represents the upper boundary of gravity wave frequencies. At higher frequencies, the force due to gravity becomes less important and ceases to be the dominant force on the waves.

Gravity waves can be described two-dimensionally by the governing equations of motions for these types of perturbations. These equations lead to the following dispersion

relation (relating the frequency and wavenumber (in this case the vertical wavenumber m) of gravity waves):

$$m^2 = k^2\left(\frac{N^2}{\omega^2} - 1\right) + \frac{\omega^2 - \omega_a^2}{c_s^2} \tag{1-25}$$

The values of $c_s^2 = \gamma RT$ and $\omega_a = \frac{c_s}{2H}$ in Equation (1-25) indicate the square of the speed of sound and acoustic cut-off frequency respectively. The variable H refers to the scale height of the atmosphere ($H = \frac{kT}{Mg}$, where k is Boltzmann constant, T is the temperature, g is the acceleration due to gravity, and M is the mass of one mole of atmospheric particles (~ 0.029 kg)). Equation (1-25) represents the dispersion relation for acoustic-gravity waves in the atmosphere (*Salby*, 1996), a category of waves whose observations were pioneered by *Hines* (1960). When the value of $m^2 > 0$, waves can oscillate vertically and are known as internal waves, which include both internal gravity waves and acoustic waves (*Fleagle* and *Businger*, 1980). In the case where $m^2 < 0$, the waves that do propagate vertically will decay exponentially. Waves of this variety are known as evanescent or non-propagating waves, which include Lamb waves (*Gossard* and *Hooke*, 1975).

The dispersion relation of Equation (1-25) can be further broken down into two distinct branches when limiting cases are considered. These limiting cases are the following:

- Case 1: $\omega^2 \gg N^2$
- Case 2: $\omega^2 \ll \omega_a^2$
-

Case 1:

For this scenario, Equation (1-25) becomes:

$$k^2 + m^2 + \frac{1}{4H^2} \cong \left(\frac{\omega^2}{c_s^2}\right) : \frac{\omega^2}{N^2} \to \infty \tag{1-26}$$

This equation describes the vertical propagation of high-frequency acoustic waves in the atmosphere (where k is the wavenumber). This region of acoustic waves is shown in Figure 1-18 in the top-left hand corner (acoustic domain) in what is known as a frequency-wavenumber plot, showing the dispersion relation in action. In this region, $m^2 > 0$ and so these waves are, by definition, internal. This same case arises when the BV frequency approaches zero. Equation (1-25) also showcases the acoustic cut-off frequency (ω_a), which is the lower boundary of this region of waves (shown in Figure 1-18 by the blue horizontal line).

Case 2:

The second limiting behaviour describes the situation of vertically propagating gravity waves:

$$k^2 + m^2 + \frac{1}{4H^2} \cong \left(\frac{N^2}{\omega^2}k^2\right) : \frac{\omega^2}{\omega_a^2} \to 0 \qquad (1\text{-}27)$$

This case also relates to internal gravity waves, where $m^2 > 0$, and is shown by the area on the bottom right in Figure 1-18, denoted as the gravity wave region. The limiting case relates only to low frequency waves as the speed of sound (c_s) approaches infinity, resulting in incompressible behaviour of the medium through which these low-frequency gravity waves travel. The gravity wave region, as has been discussed, has an upper cut-off frequency called the BV frequency, shown by the orange line in Figure 1-18.

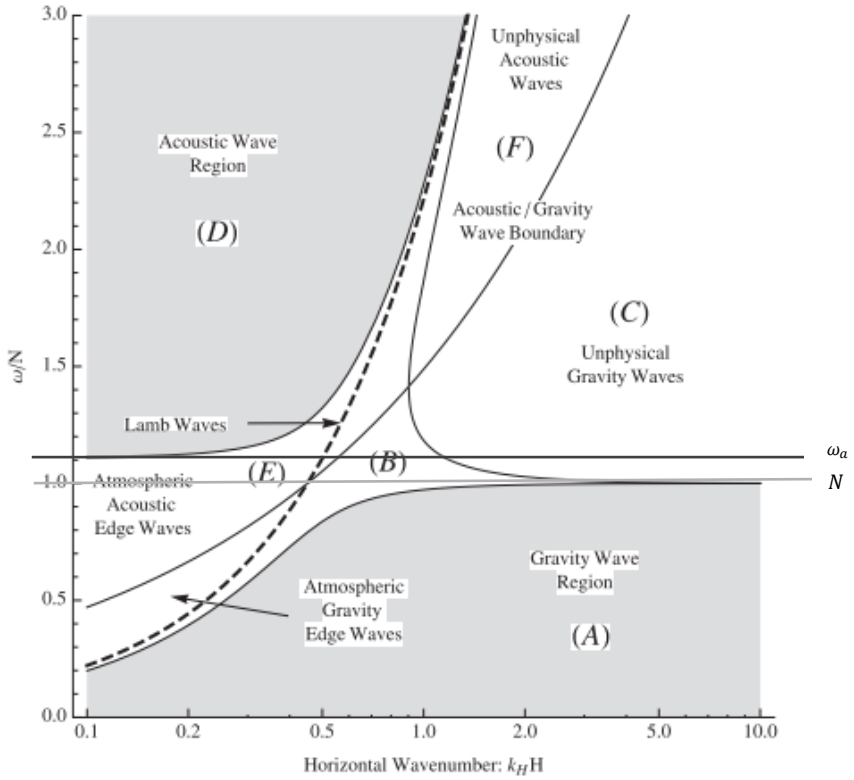

Figure 1-18: Frequency-Wavenumber plot of the dispersion relation of acoustic-gravity waves (encapsulates all waves in the diagram). Regions where the vertical wavenumber is positive are shaded in grey (*Dukowicz*, 2013). *The orange line indicates the BV frequency and the blue indicates the acoustic cut-off frequency*

Figure 1-18 also shows the region of evanescent waves where $m^2 < 0$, which includes acoustic-gravity waves which propagate horizontally and decay exponentially in terms of energy (*Salby*, 1996). Much of the theory behind the dispersion and motion of gravity waves in the atmosphere is covered comprehensively by *Fritts* and *Alexander* (2003).

The dispersion relation allows for the calculation of the group and phase velocities of the waves. The group velocity describes how energy propagates for the wave. Gravity waves are known to carry energy away from the source that they arise from and this information is contained within the group velocity of the waves. Not only do these waves carry energy away from the source, they also carry momentum, which results in gravity waves having a noticeable impact on the lower and middle atmosphere.

Sources of gravity waves are numerous and include topography, convection and wind shear (*Fritts* and *Alexander*, 2003) as well as gravity wave generation due to unbalanced flows associated with the jet stream. Waves that result from such sources can have horizontal wavelengths from tens to thousands of kilometres (*Nappo*, 2013), but are less than that of planetary waves. These sources contribute to ubiquitous gravity waves in the atmosphere which affect the circulation of the middle atmosphere (*Holton*, 1983). The process through which this occurs is well described by *Karlsson* and *Shepherd* (2018) and is briefly outlined here.

As the atmosphere decreases in density as a function of height, this allows vertically propagating internal waves (gravity and acoustic) to grow in amplitude in line with the conservation of energy. These amplitudes grow at a rate of $e^{z/2H_s}$ (where H_s is the density scale height) and thus are prone to breaking (where a large amount of the wave's energy dissipates) like that of ocean waves on the shore (*Nappo*, 2013). This occurs predominantly in the middle and upper atmosphere and thus can affect the circulation at these altitudes, through distribution of momentum into the background flow (*Andrews et al.*, 1987; *Karlsson* and *Shepherd*, 2018). Due to the background winds of the middle atmosphere, buoyancy waves can break prematurely and contribute to the directional change of circulation in these altitudes. In summer, gravity waves drive an equatorward circulation while in winter, the gravity waves instead drive a poleward flow. These gravity waves are fundamental to explaining the behaviour of the upper atmosphere (*Yiğit* and *Medvedev*, 2019).

As *Karlsson* and *Shepherd* (2018) point out, the summer mesosphere is cooled partly due to the action of gravity waves in the upper atmosphere. The gravity waves drive a poleward circulation and thus, according to the mass conservation law (continuity equation), air must ascend in the summer pole and adiabatically (*i.e.* no heat loss or gain) expand. This process of adiabatic expansion leads to cooling in the summer mesosphere, contributing to the extreme low temperatures of this layer. This process of wave breaking and the adiabatic cooling of the mesosphere (illustrated in Figure 1-19) also contributes to the formation of noctilucent clouds in the summer hemisphere

(*Karlsson et al.*, 2007). These clouds will be discussed extensively in Chapter 4 in relation to observations made locally, at the Maynooth University station.

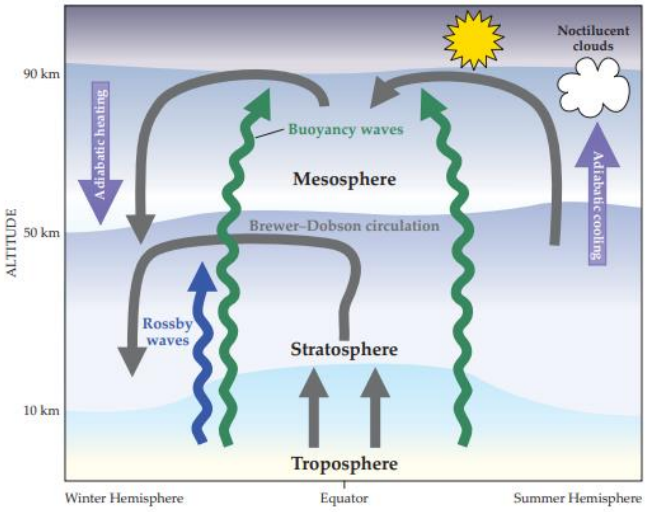

Figure 1-19: Process of gravity wave (buoyancy wave) breaking in the middle atmosphere, leading to the formation of noctilucent clouds in the summer mesopause (*Karlsson* and *Shepherd*, 2018)

1.7.4. Acoustic Waves/Infrasound

Acoustic waves, generally known as sound waves, are longitudinal waves arising from pressure variations in a medium (*Taylor*, 2010). In the atmosphere, the air acts as this medium through which acoustic waves travel, where the pressure variations consist of a repeating train of compressions and rarefactions of the medium. For the purposes of this section, the compressions and rarefactions are assumed to be adiabatic.

Acoustic waves in the atmosphere are normally modelled as linear waves with speeds equal to the speed of sound given as:

$$c_s = \sqrt{\gamma RT} \tag{1-28}$$

where $\gamma = \frac{c_p}{c_v}$ (here c_p and c_v represent the specific heat capacity of air at constant pressure and constant volume respectively). Pure acoustic waves travelling at the speed

of sound have frequencies sufficiently high so that the effect of gravity is negligible (*Gossard* and *Hooke*, 1975).

Acoustic waves involve the interactions of density, pressure and the divergence of the velocity field (*Dukowicz*, 2013). These interactions can occur through the following equations: the continuity equation, the momentum equation, and the equation of state. Following on from the discussion related to gravity waves above, acoustic waves exist above the acoustic cut-off frequency with frequencies that are larger than around 0.003 Hz (*Bittner et al.*, 2010) (a frequency of around 3.3 mHz (*Evers* and *Haak*, 2010)). The range of acoustic waves from $0.003 - 20$ Hz is normally known as infrasound, with audible frequencies (for humans) found above this range. Ultrasound constitutes very high frequency acoustic waves above 20 kHz. These acoustic ranges are shown in Figure 1-20 below, which also shows the gravity wave range. The space between the gravity range and the infrasonic range corresponds to the same range given by the frequency-wavenumber plot in Figure 1-18 in Section 1.7.3. Thus, the space between the two ranges (bounded by the BV frequency and the acoustic cut-off frequency) indicates a region of evanescent waves.

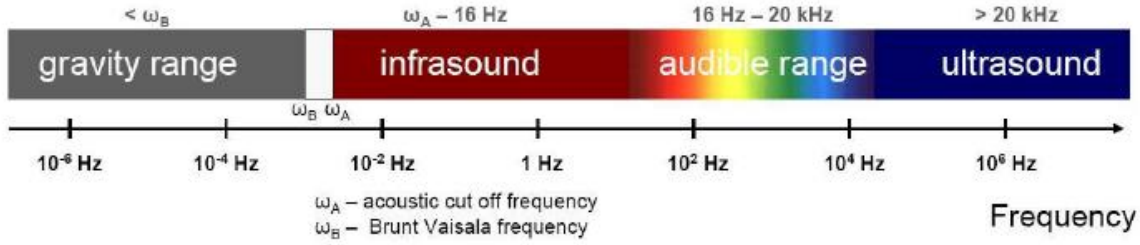

Figure 1-20: Frequency ranges of various acoustic waves. A gap is seen between the lower end of the acoustic range and the gravity range, indicating a region of evanescent waves (*Bittner et al.*, 2010)

The range of atmospheric acoustics and the related research areas are extensive, as shown in Figure 1-21, where acoustic effects and phenomena are found on the second ring from the centre circle, which includes scattering. The outer ring of Figure 1-21 shows the use of acoustic waves for atmospheric study.

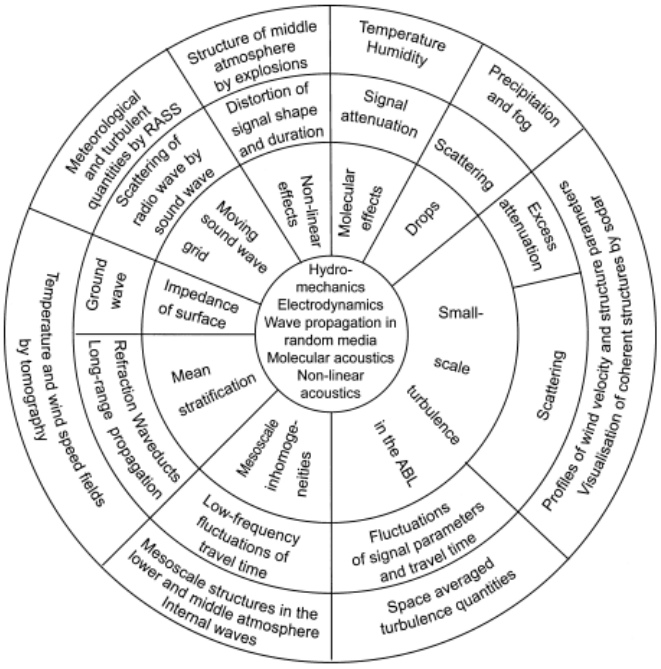

Figure 1-21: Wheel of Atmospheric Acoustics from Kallistratova (2002)*, after Lindsay's Wheel of Acoustics* (*Lindsay*, 1964)

Although all forms of acoustic waves can exist in the atmosphere, this section focuses on the lower frequency band of acoustic waves known as infrasound. A brief history has been given in Section 1.2, and the detail of infrasound and its propagation through the atmosphere is discussed here. Infrasonic waves in the atmosphere travel at the local speed of sound in accordance with the speed relation of Equation (1-28). This speed is dependent on the background conditions that are present, where the speed is proportional to the thermal structure of the atmosphere, through a factor of $\sqrt{T}$. The varying temperature of the atmosphere, as discussed in Section 1.3, results in a changing speed of sound as a function of altitude. Figure 1-22 shows that the speed of sound can vary depending on the frequency of the given acoustic wave. This same plot shows that low frequency sound waves (infrasound) encounter the least amount of dispersion in the lower atmosphere. *Sutherland* and *Bass* (2004) have demonstrated that acoustic waves undergo very little absorption in the atmosphere and an atmospheric window effectively exists for these disturbances. This allows for the long-range propagation of acoustic waves in the atmosphere (*Drob et al.*, 2003, *Kulichkov*, 2004).

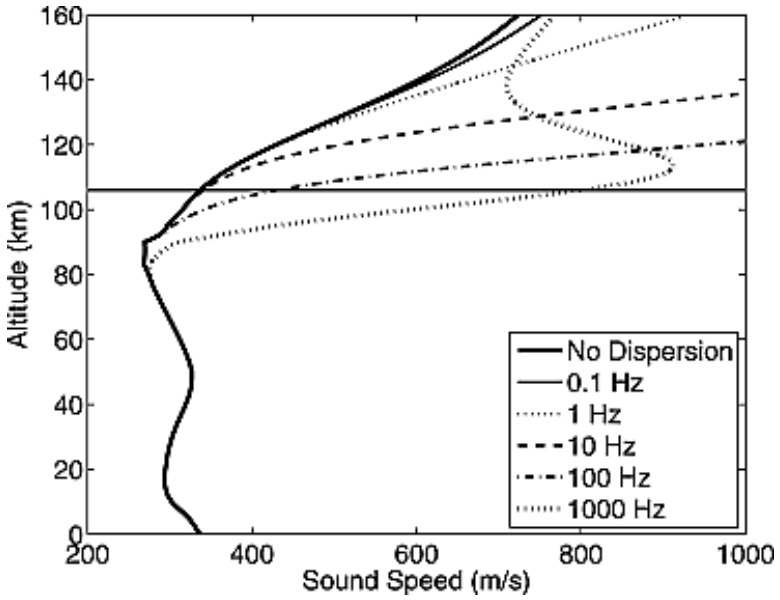

Figure 1-22: Speed of sound for varying frequencies in the atmosphere. Note that dispersion does not play a role in the majority of the homosphere (*Bass et al.*, 2007).

Infrasound propagation depends on both the temperature and wind structure of the region of atmosphere that the waves travel through. How infrasound manages to travel through the atmosphere can be fundamentally explained by the refraction of sound waves through the atmosphere. Refraction of sound waves in the atmosphere can be explained through the use of Snell's Law (*Fleagle* and *Businger*, 1980, *Mutschlecner* and *Whitaker*, 2009):

$$\frac{\sin(i_1)}{c_1} = \frac{\sin(r_1)}{c_2} = \frac{\sin(i_2)}{c_2} = \cdots \tag{1-29}$$

Here it is assumed that a simple acoustic ray propagates vertically through a series of isothermal layers that make up the atmosphere. Refraction depends on the angle of incidence of the wave and the temperature gradient (which changes the refractive index of the layer). The variables are shown in Figure 1-23 with the given acoustic ray, where it is assumed that the temperature decreases with increasing altitude. Although the acoustic ray bends (refracts) as it achieves higher altitudes, based on Equation 1-29, the speed of the wave remains constant through the isothermal layers.

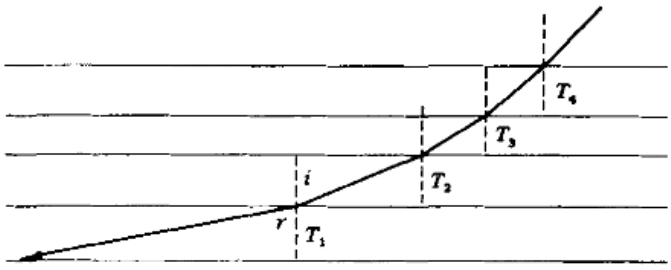

Figure 1-23: Snell's law in action for a model atmosphere made of isothermal layers (*Fleagle* and *Businger*, 1980)

Refraction can also be influenced by the wind gradient of the atmosphere, in much the same way as the temperature gradient. Returning to the thermal structure of the atmosphere, discontinuities in the temperature profile of the atmosphere, occur at the boundary of each layer. These discontinuities lead to the refraction of tropospheric-generated acoustic waves back down toward the Earth's surface. These acoustic waves have the ability to then refract back from the surface and propagate upwards again, where this whole process can be repeated. This trapping of acoustic energy in a region of the atmosphere is called ducting. Ducts occur at the atmospheric layer boundaries, leading to a tropospheric duct, stratospheric duct and thermospheric duct, while mesospheric ducts can also occur. These ducts (or wave guides) are apparent in Figure 1-24, which shows ray-tracing for acoustic waves in a summertime atmosphere. The left- and right-hand panels show the effective sound speed for westward and eastward propagation, where the effective sound speed is given as (*Evers* and *Haak*, 2010):

$$c_{eff} = \sqrt{\gamma RT} + \hat{n} \cdot \boldsymbol{u} \tag{1-30}$$

The first term of the right-hand side is the normal sound velocity, as given previously in Equation (1-28). The second term on the right-hand side ($\hat{\boldsymbol{n}} \cdot \boldsymbol{u}$) incorporates the effects of the wind structure to the speed of sound. The variable $\boldsymbol{u}$ is the directional wind component, while $\hat{\boldsymbol{n}}$ represents a unit vector in the direction of propagation of the sound wave.

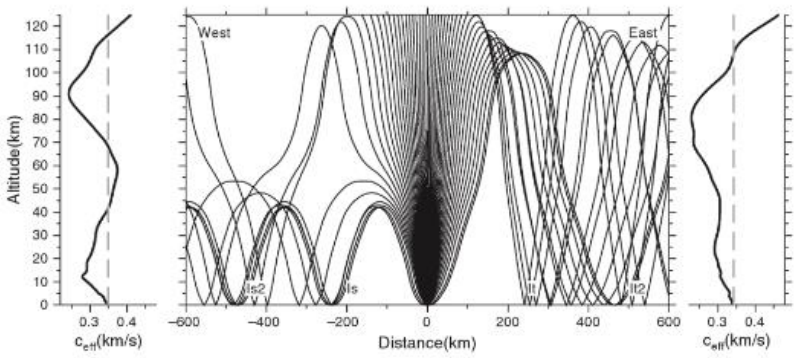

Figure 1-24: Ray-tracing of acoustic waves in the atmosphere. The right and left panels show the effective sound speeds for the eastward and westward propagating waves. These acoustic paths are plotted for summertime conditions (*Garcés et al.*, 1998, *Evers* and *Haak*, 2010)

Strong wind gradients associated with jet stream can strongly influence the propagation of waves within the atmosphere (*Evers* and *Haak*, 2010) as they affect the values of the effective sound speed. These ducts can also be localised within the atmosphere, so they do not necessarily have to form a guide between the given layer and the ground, but instead exist between natural temperature inversions or wind inversions in the atmosphere. This case was seen by *Bowman* and *Lees* (2015) when they were modelling propagation paths of infrasound in the stratosphere for balloon-borne sensors (Figure 1-25).

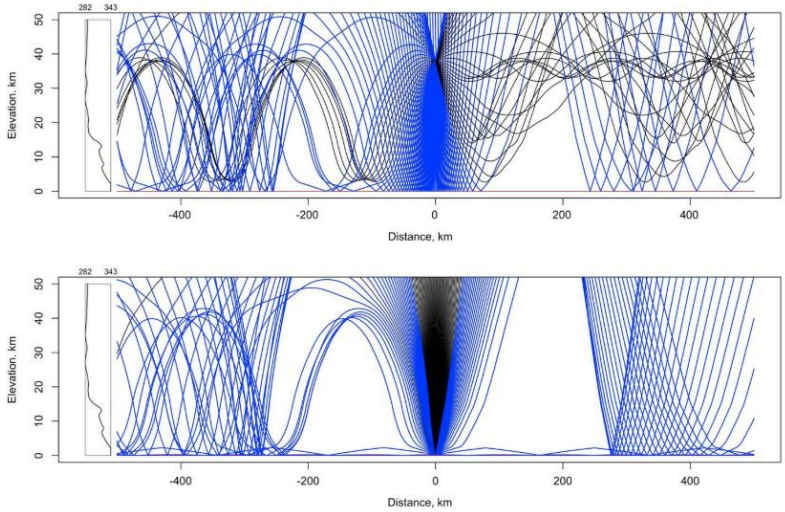

Figure 1-25: Propagation modelling completed by Bowman and *Lees* (2015), *showing localised ducting (horizontal waveguide (top), centred at 35 km) in the stratosphere for infrasound*

Ducting traps the energy of infrasound propagating through the atmosphere, as well as retaining the coherency of signals.

1.8. Infrasound Sources and its Monitoring in the Atmosphere

Section 1.7 gave a brief outline of the types of waves present within the atmosphere. These included infrasonic waves, which are the main topic of this study. Although the propagation and characteristics of infrasound have been discussed, the sources of these waves have yet to be described (a brief glimpse of the spectrum is shown in Figure 1-26). Section 1.8.1 gives a brief account of several sources that produce infrasonic waves within the atmosphere, which include ocean-ocean interactions, earthquakes, volcanic eruptions, and bolides (meteors) as well as man-made sources. Other natural sources include infrasound resulting from severe storms and lightning, auroral activity and mountain-generated infrasound (or MAWs). Monitoring of these sources and associated infrasound has become increasingly important in recent years as it may be used for future early warning systems. Knowledge of the sources and resultant propagation of their infrasound also aid in the understanding of atmospheric dynamics (*Donn* and *Rind*, 1971).

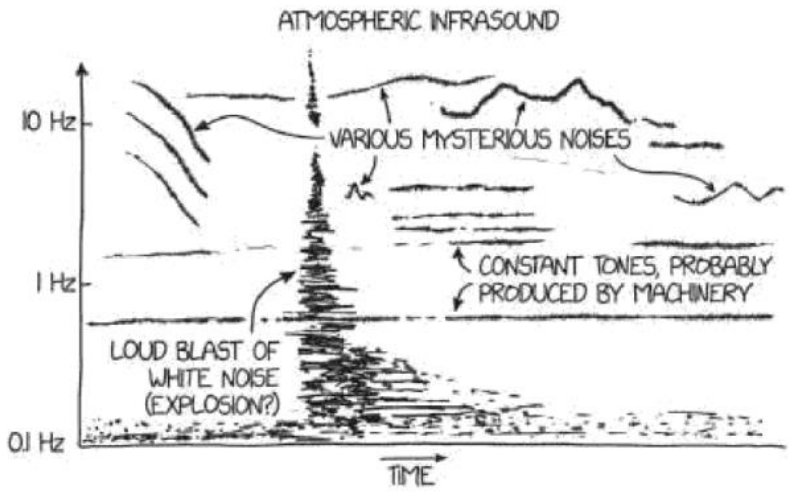

Figure 1-26: The wide spectrum of atmospheric infrasound *(Munroe, 2019)*

1.8.1. Sources

Gossard and *Hooke* (1975), *McKisic* (1997) and *Campus* and *Christie* (2010) all give detailed overviews of infrasound sources of both natural and man-made origin. These sources cover a large part of the infrasonic frequency range. Some of the major infrasonic sources are shown below in Table 1-4, with the resultant infrasonic signal characteristics shown, such as period, amplitude and duration. The amplitude values of Table 1-4 are given in Kelvin as they refer to the temperature increase of the hydroxyl layer in response to the corresponding infrasonic source waves.

Source	Period	Amplitude (K)	Duration
Severe weather	< 2 s (SP)	< 0.5	Continuous
	2–60 s (MP)	0.05–0.5	Continuous
	60–300 s (LP)	0.05–5	Continuous
	> 300 s (GW)	> 0.5	Continuous
Volcanic activity	0.1–2 s (SP)	0.05–5	Continuous
	2–190 s (MP)	> 5	Continuous
	190–300 s (LP)	> 5	Singular
	> 300 s (GW)	> 5	Singular
Orography	20–60 s (MP)	> 0.05	Continuous
	> 300 s (GW)	> 0.5	Continuous
Explosions	< 20 s (SP/MP)	0.05–5	Singular
	20–60 s (MP)	> 5	Singular
	60–300 s (LP)	> 5	Singular
Microbaroms	5 s (MP)	< 0.5	Continuous
Earthquakes	0.5–2 s (SP)	0.05–1	Continuous
Aurorae	10–60 s (MP)	< 0.5	Continuous
Meteorites	1–5 s (SP/MP)	0.05–5	Singular
Rocket starts	< 2 s (SP)	0.5–5	Singular
Thunder/Sonic boom	< 2 s (SP)	< 0.5	Singular

Table 1-4: Various infrasonic sources with their associated periods, amplitudes (in terms of temperatures induced in the hydroxyl layer) and the duration. Duration here refers to the number of wave trains that the signal is composed of where continuous signals are those consisting of more than 3 complete wave trains (*Pilger et al.*, 2013b)

Table 1-4 does not detail all infrasonic sources, and only some of these sources are shown in the next sections.

1.8.1.1. Ocean-Ocean Interactions (Microbaroms)

Microbaroms arise due to the non-linear interaction of ocean waves with the atmosphere (*Campus* and *Christie*, 2010), and have frequencies between $0.12 - 0.35$ Hz. The main peak of microbaroms occurs around 0.2 Hz (*Garcés et al.*, 2005) with a secondary peak closer to 0.15 Hz. They were first discovered by *Benioff* and *Gutenberg* (1939) using microbarographs, while their propagation from their point of origin was first explained by *Longuet-Higgins* (1950). Microbaroms are continuous signals (*Pilger et al.*, 2013b) ubiquitous in the atmosphere. Regularly described as noise, they have the ability to mask signals from sources like nuclear detonations. (*Garcés et al.*, 2010) for instance note that microbarom frequencies overlap with the frequency generated by a 1 kilo-ton nuclear explosion.

Although these signals can be a hindrance to the detection of signals from other sources, they are useful to ensure operational capabilities of instruments designed to detect infrasound. As well, microbaroms have been used as an atmospheric probe (*Donn* and *Rind.*, 1971) to determine information about the temperature and wind structure of the atmosphere. They are particularly useful due to their constant presence in the atmosphere.

1.8.1.2. Volcanoes

Infrasound associated with volcanoes is of critical importance (*Johnson*, 2003, *Fee* and *Matoza*, 2013) in the context of early warning systems and forecasting for natural hazards (*Ripepe et al.*, 2013, *Marchetti et al.*, 2018, *Ripepe* and *Marchetti*, 2019). *Marchetti et al.* (2018) for instance point out the potential of incorporating infrasonic detections of eruptions with ash advisories as an aid to civil aviation. The volcanic eruption signatures are normally considered as those arising from explosions from the crater involving discharged materials such as lava (*Campus* and *Christie*, 2010).

Volcanic infrasound is concentrated in the frequency band range $1-20$ Hz (*Johnson et al.*, 2004), where the size of volcanic eruptions can have a range between nearly 100 MT (estimated explosive yield of Krakatoa in 1883) to less than 1 kT (*Campus* and *Christie*, 2010). Explosions from volcanoes have a characteristic N-shaped signature (*Bittner et al.*, 2010) as seen in Figure 1-27, as opposed to the continuous signatures from microbaroms described in Section 1.8.1.1. The frequency of the resulting infrasound is dependent on the yield of the volcanic explosion, with higher yields producing larger ranges of frequency between $0.002-20$ Hz (*Campus* and *Christie*, 2010). Smaller explosions are defined by their high frequencies and are also normally short in duration. Mining explosions are similar to these types of signals.

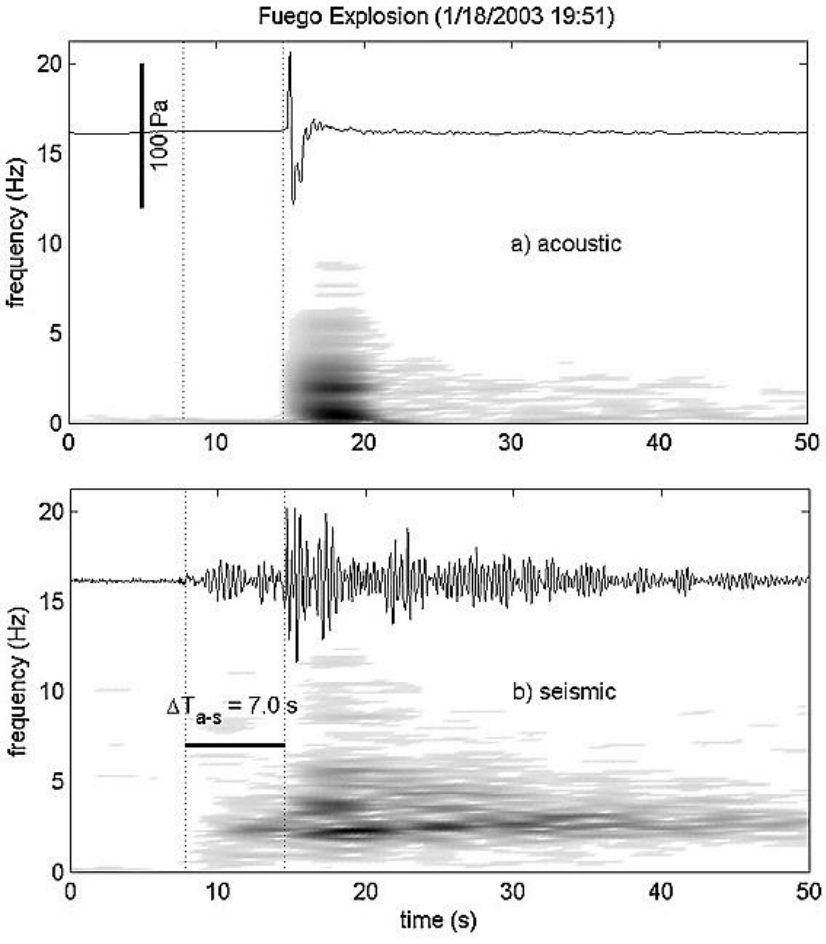

Figure 1-27: Spectrograms of volcanic explosion signatures as measured by Johnson et al. (2004). *The difference in infrasound (a) and seismic (b) traces of the same event is evident. The acoustic signal is close to 100 Pa in terms of amplitude.*

1.8.1.3. Earthquakes

Earthquakes represent another type of source producing strong infrasonic signals in the atmosphere (*Maruyama* and *Shinagawa*, 2014, *Inchin et al.*, 2020). Earthquakes can produce infrasound with frequencies between $0.005 - 10$ Hz, with amplitudes up to a few Pa in the atmosphere. These waves can travel very long distances (*Mutschlecner* and *Whitaker*, 2005) depending on the state of the atmosphere through which these signals propagate (*Mutschlecner* and *Whitaker*, 2009). Infrasound from earthquakes is associated with three mechanisms – radiation of acoustic waves away from the Earth's surface, violent ground motion associated with shallow epicentres, and seismic surface waves radiating from high mountains. These latter two mechanisms are shown by the schematic in Figure 1-28.

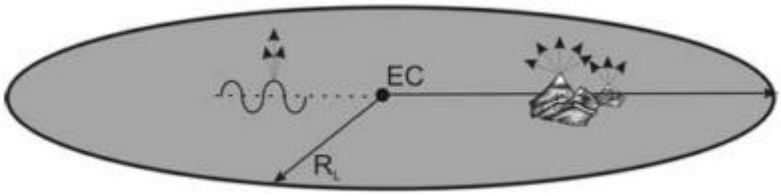

Figure 1-28: Mechanisms of infrasound production from earthquakes. The schematic from Mutschlecner and *Whitaker* (2005) *shows infrasound associated with a local epicentre source and infrasound that radiates as a result of seismic waves affecting topography.*

1.8.1.4. Bolides

Bolides are described as meteors or fireballs (particularly bright meteors) (*Revelle*, 1997) that can produce infrasound in the atmosphere. Apart from the Tunguska 1908 event mentioned in Section 1.2, perhaps the most well-known bolide to generate infrasound is that of the Chelyabinsk meteor event in February 2013 (*de Groot-Hedlin* and *Hedlin*, 2014, *Pilger et al.*, 2015, 2018). Infrasound produced by fireballs can have frequencies between $0.01 - 20$ Hz, occupying a similar frequency band to earthquakes and volcanic

eruptions. Infrasound may be produced in two ways by bolides – either through the entry of the bolide/fireball into the atmosphere (a cylindrical line source (*Edwards*, 2009)) or the subsequent fragmentation event of the object, if one occurs (*Pilger et al.*, 2020b). The Chelyabinsk meteor of 2013 produced infrasound due to this second mechanism, with the object exploding over Western Russia and producing infrasound that was observed globally. The main reason behind such a wide observation area was due to the energetic explosion of the bolide (*Edwards*, 2009). Meteor mass and overall size both play into how energetic these bodies are, and also result in a variation of the infrasound produced (frequency, amplitude). As a result, infrasound from meteors can be used to obtain information not only about the atmosphere but also about the meteor characteristics.

Infrasound from bolide entry is also of particular interest to researchers as a method of investigating the propagation of infrasound from such sources. Bolide entry and fragmentation is likely to deposit most of its energy into the middle atmosphere (specifically the stratosphere) compared to surface and tropospheric sources (*Edwards*, 2009). The signals associated with bolide infrasound have been classified by *Silber* and *Brown* (2014), where although the signals are subject to change, they do tend to keep the characteristic N-shape, as seen in Figure 1-29.

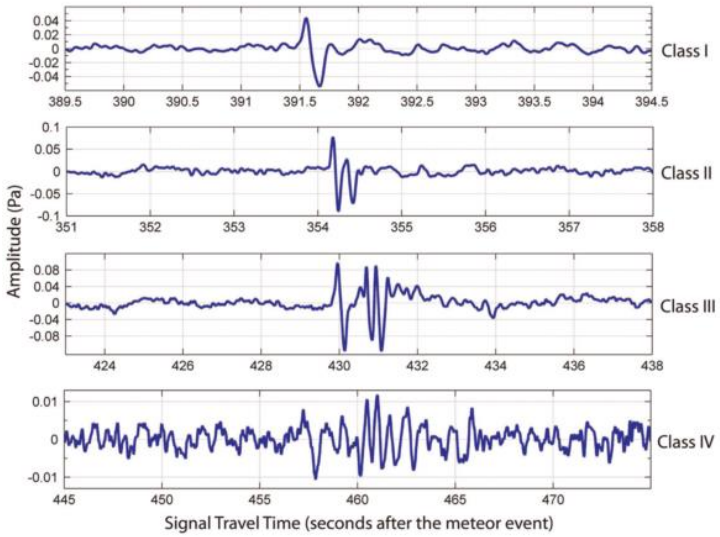

Figure 1-29: Types of infrasonic waves emanating from meteors, where the signature N-shape of meteor-generated infrasound is apparent in Class I-III (*Silber* and *Brown*, 2014)

1.8.1.5. Manmade Sources

Nuclear Detonations

A large spectrum of manmade events can result in infrasound that propagates through the atmosphere. The most well-known anthropogenic source is that of nuclear explosions, which are obviously a considerable danger to humans and are the focus of the work of the CTBTO. These sources produce sharp onset waves, similar to other impulsive sources like explosions of volcanic and chemical origin. Frequencies of infrasonic waves emanating from nuclear explosions are observed to be between $0.002 - 20$ Hz (*Campus* and *Christie*, 2010), where amplitudes of up to 20 Pa have been recorded for large events. In terms of the propagation of infrasonic signals from nuclear detonations, this depends on the same set of conditions as bolide fragmentation in the atmosphere. Long-range propagation depends on the explosive yield of the detonation itself, as well as the state of the atmosphere.

Very few nuclear detonations have occurred within the 21st century, with many incidents relegated to the Cold War era, before the signing the CTBT. Recent detonations have occurred due to tests within the Democratic People's Republic of Korea (DPRK) (North Korea), and have been successfully detected using the IMS network (*Che et al.*, 2014, *Assink et al.*, 2016). As a result, such events still pose a risk to life and infrasound monitoring ensures these detonations are tracked when visual confirmation cannot be achieved.

Chemical/Mining Explosions

Chemical and mining explosions have been observed by the IMS network, and interest researchers because they provide a clear reference event against which all measurements may be compared. As with nuclear explosions, these events produce sharp-onset waves at detectors, and can have frequencies between $0.05 - 20$ Hz (*Campus* and *Christie*, 2010). One of the key events that began research into chemical explosions was that of

the Buncefield Oil Explosion that took place on 11 December 2005 (*Green et al.*, 2011). Much more recently, the Beirut explosion of 4 August 2020 (in which approximately 2750 tons of ammonium nitrate stored in a harbour warehouse exploded) has been used as a new, large source of infrasound by way of a chemical explosion. Authors such as *Pilger et al.* (2020a) have shown the long-range propagation of this explosion as well as the determination of the source characteristics. However, detections of this specific event were not found in the datasets presented in later chapters (Chapter 5).

1.8.2. Detection Methods of Infrasound

The detection of infrasound has been achieved through a variety of means, with microphone array acting as pressure sensors having the most extensive coverage on a global scale. The main methods of detection are summarised below.

1.8.2.1. Microphone arrays

Such arrays are the main component of the infrasound monitoring hardware used by the IMS. These microphone arrays are used by the IMS to detect pressure variations produced by the propagation of infrasonic waves over the given station. The IMS uses two types of microbarometer sensors (*Christie* and *Campus*, 2010) of high sensitivity – the first is an absolute pressure microbarometer and the second is a refined differential capacitor microbarometer. Both of these microbarometers have a monitoring passband of $0.02 - 4$ Hz, which covers the range of frequencies produced by both atmospheric and underground nuclear explosions (*Campus* and *Christie*, 2010), and also includes the main frequency band produced by microbaroms. *Christie* and *Campus* (2010) note that due to the monitoring passband used, the main arrivals detected by the IMS arrays tend to be stratospheric signals, rather than thermospheric or tropospheric arrivals, as lower frequencies are typical of thermospheric infrasonic signals and are less frequent. This

monitoring is aimed primarily at nuclear detonation detection, but the microbarometers are subject to both environmental and instrument issues. This includes noise such as wind effects and microbaroms, as well as problems due to spatial aliasing and issues with signal correlations (*Christie* and *Campus*, 2010). Spatial aliasing in the array networks has led to the preference of 8-element arrays rather than 4-element arrays for IMS infrasound stations. More details regarding microbarom sensors and arrays are found in *Le Pichon et al.* (2010 and references therein).

1.8.2.2. Balloon Borne Sensors

Sensors attached to balloons have enjoyed recent exposure for their study of ground versus stratospheric infrasound (*Bowman* and *Lees*, 2017), as well as their use in detecting infrasonic waves associated with lightning (*Lamb et al.*, 2018).

One of the advantages of such sensors is that they experience little wind noise affecting a large frequency range (*Bowman et al.*, 2018) compared to the same noise experienced by the IMS network arrays (*Christie* and *Campus*, 2010). These sensors also give a perspective into the infrasound propagating at higher altitudes. As detailed by *Bowman et al.* (2018), balloon sensors have helped identify a constant presence of the microbarom frequency peak. Infrasound that has not been detectable at ground level has also be observed by these high-altitude sensors, where far-field infrasonic waves may be easier to detect (*Bowman* and *Lees*, 2017). Sensors in a region of the atmosphere where monitoring is sparse may help include more of the acoustic wavefield present in the middle atmosphere (*Lamb et al.*, 2018). Free-flying arrays have also found application to planetary atmospheric physics, with interest in these sensors for exploration of the atmosphere of Venus (*Bowman et al.*, 2018).

Although these sensors are adaptable in terms of their altitude and lack of static position, so they can cover greater range, they are subject to disadvantages like those of

ground sensors where they cannot cover the entire spectrum of waves within the atmosphere (*Bowman* and *Lees*, 2017).

1.8.2.3. Airglow

So far, only direct detection methods have been discussed. These next paragraphs detail the use of indirect methods for infrasound monitoring. The first is that of airglow, which is the main medium used in this thesis to obtain evidence of infrasound. Measurements of the layer are made either through radiance measurements or thermal measurements (both detect in the infrared (*Thorne*, 1988)), where the variations of either parameter can be used to determine the passage of infrasound through the layer.

Multiple authors (*Pilger* and *Bittner*, 2009, *Bittner et al.*, 2010, *Schmidt et al.*, 2013, *Pilger et al.*, 2013a) have made use of the hydroxyl layer for the investigation of infrasound at mesospheric altitudes. Ground-based spectrometers have been employed to obtain temperature induced perturbations in the hydroxyl layer, while fast cameras (*Hannawald et al.*, 2016, *Le Dû et al.*, 2020) are used to obtain visual evidence of these waves.

The brightest bands of the hydroxyl layer occur at infrared wavelengths, with two main band groups centred at around $1.5\ \mu\text{m}$ and $3\ \mu\text{m}$. Atmospheric studies have favoured the band at $1.5\ \mu\text{m}$ because the infrared detectors are far more sensitive at this wavelength. Spectrometers rely on the rotational bands of the hydroxyl layer to obtain temperature information, where the $\text{OH}(3-1)$ transition has been used extensively to infer thermal fluctuations (*Mulligan et al.*, 1995, *Bittner et al.*, 2010). Expected temperature fluctuations of various altitudes in the mesopause are shown in Table 1-5 below, with the signal also varying in amplitude.

	1 Pa	10 Pa	100 Pa
83 km	0.04	0.35	3.50
87 km	0.05	0.47	4.72
91 km	0.06	0.63	6.28
95 km	0.08	0.79	7.85
99 km	0.10	0.95	9.48

Table 1-5: Expected temperature perturbations (kelvin) of the mesopause in response to an infrasonic wave (pascals). The expected values differ depending both on altitude and the amplitude of the signal (*Pilger* and *Bittner*, 2009)

Other authors such as *Le Dû et al.* (2020) have used images of the sky recorded by CCD in a broad band of wavelengths from $1.0 - 1.5$ μm in an attempt to establish the passage of infrasound through the OH* layer. This thesis uses a radiometer array to investigate infrasonic signals in the hydroxyl layer, where the three radiometers return radiance amplitudes of the layer, directional information and speed of signals propagating over the observing station at Maynooth.

Both spectrometers and radiometers provide good temporal resolution, with less of a focus on the spatial resolution. Recently, fast high-sensitivity cameras have been deployed to investigate small structures in the hydroxyl layer (*Hannawald et al.*, 2016), which has been extended to infrasound detection (*Le Dû et al.*, 2020). Cameras with the level of sensitivity and response time needed are a recent development of the technology, and they are very costly. Broadband radiometers were used in this work because they are a much lower-cost option. Clearly, a system which produces a complete image of the field-of-view is preferable to one with only three sample points. On the positive side however, broadband radiometers have the possibility to sample with a far greater cadence than currently available CCD imaging systems.

1.8.2.4. Noctilucent Cloud Observations

Although not strictly a method of infrasound detection, recent reports have shown observations of small-scale structures in noctilucent clouds (*Kaifler et al.*, 2013; *Demissie et al.*, 2014), such as gravity waves (*Pautet et al.*, 2011) and turbulence (*Dalin et al.*, 2010). Evidence of gravity waves within noctilucent cloud images is shown in Figure 1-30. As infrasound wavelengths are close to that of gravity waves, noctilucent clouds could, in the future, be used as a probe of infrasound in the upper atmosphere, as they are used at present for gravity wave detection (*Pautet et al.*, 2011).

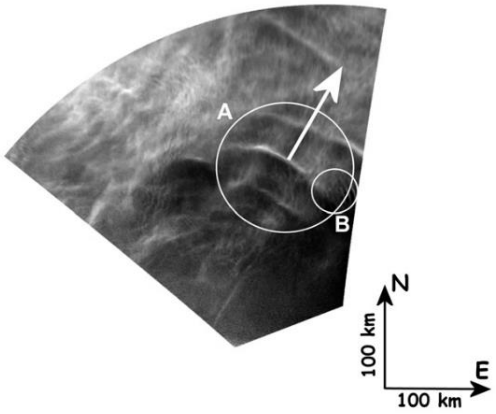

Figure 1-30: Short period gravity waves found in noctilucent cloud images as shown in Pautet et al. (2011). *These waves are shown in the circle marked A. The circle marked B shows ripples propagating. These ripples have wavelengths very similar to many acoustic waves.*

1.8.2.5. Ionospheric detection and TEC measurements

The ionosphere discussed in Section 1.4.1 has been monitored for evidence of infrasound by way of Doppler sounding and TEC measurements. *Artru et al.* (2004), *Šindelářová et al.* (2009) and *Chum et al.* (2008) have used Doppler sounding to investigate signatures of acoustic origin in the ionosphere. This method relies on measuring a frequency shift between the transmitted and received signal from the ionospheric layer. Dynamics of the ionosphere, mainly collisions of ions with neutral atmospheric components, allows for the

detection of acoustic-gravity waves with high-frequency Doppler sounding, where the frequency return can reveal evidence of these disturbances (*Chum et al.*, 2008). TEC (total electron content) measurements may also be used as a tracer of infrasound in the ionosphere, a method used by *Zettergren et al.* (2017). TEC measurements work in much the same way as airglow radiance measurements where variations in the amount of the medium occupying a fixed volume are observed. *Zettergren et al.* (2017) have found that TEC in the ionosphere does fluctuate in response to known infrasonic sources such as earthquakes. Modelling completed by *Zettergren* and *Snively* (2013) has shown that acoustic waves also have the capability of inducing dynamo-electrical currents in the ionosphere.

1.8.3. Current State of Infrasound Monitoring

The aims of contemporary infrasonic research topics are summarised in Table 1-6. The most sophisticated implementation of infrasound monitoring today is the International Monitoring System (IMS) of 60 infrasound detectors distributed all around the Earth (illustrated in Figure 1-31) and are used to monitor compliance with the Comprehensive Test Ban Treaty (CTBT).

Natural Infrasound – Potential Applications and Future Research		
Sources	**Applications**	**Areas for Research**
Avalanches	Determine location, depth, duration, occurrence statistics	Relate signature to avalanche size and type
Meteors	Determine altitude, direction, type of entry (explosive or bow shock); determine size and impact location	Estimate size and type distribution; determine ablation rates; volumetric meteor survey limits
Ocean Waves	Locate wave interaction areas; determine wave magnitudes and spectra	Monitor evolution of storms at sea; study wave-wave interactions
Severe-weather systems	Estimate storm location and energy	Study storm microphysical processes; model acoustic radiation
Tornadoes	Detection, location, and warning; estimate core radius; image funnel shape at short ranges	Study tornado formation processes; look for infrasonic precursors
Turbulence	Aircraft avoidance; estimate altitude, strength, and spatial extent	Distinguish among several generative processes; develop practical detection systems
Earthquakes	Measure Rayleigh waves; measure sound from intermediate radiation points; measure sound from the epicentre	Look for infrasonic precursors; understand seismic-acoustic coupling
Volcanoes	Estimate location and energy released	Determine relationships between infrasonic and seismic disturbances

Table 1-6: Infrasonic sources and their potential applications and associated research topics (after Bedard and Georges (2000))

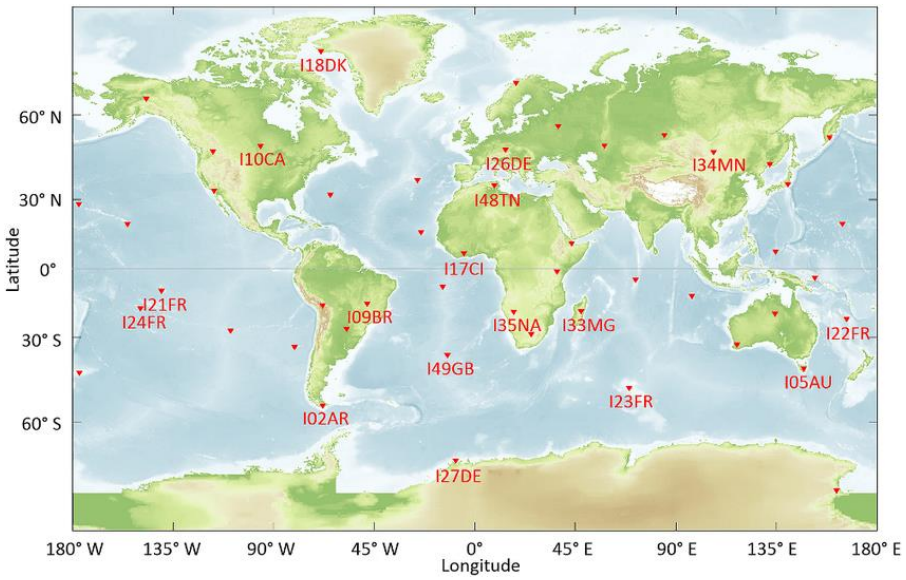

Figure 1-31: Locations of IMS stations around the globe, where some station names are labelled (Hupe et al., 2018)

A major focus of current infrasound research is the further development of early warning systems for the effects of natural hazards such as earthquakes, tsunamis and other geo-hazards (*Bittner et al.*, 2010, *Makela et al.*, 2011). A second focus is the use of infrasound propagation to monitor the state of the atmosphere between source and receiver (*Hupe et al.*, 2019, *Pilger et al.*, 2020a). *Le Pichon et al.* (2010, 2018) have detailed applications derived from infrasonic monitoring and detection. For instance, one of the top reasons to detect infrasound in the atmosphere is its use in probing the conditions of the atmosphere (*Donn* and *Rind*, 1971, *Drob et al.*, 2003), due to the continuous nature of infrasound from natural origins.

Along with the contribution of infrasound monitoring to the study of the atmosphere, this monitoring can also be used to improve global circulations models (*Lott* and *Millet*, 2009), through the detection of pressure perturbations of gravity waves in the upper atmosphere. As a result, through gravity wave detections by IMS arrays, these measurements offer an opportunity to obtain climatological information and thus improve climate and weather models (*Marlton et al.*, 2018).

Infrasound monitoring has also been used to study sudden stratospheric warmings and forecasting for such events (*Assink et al.*, 2014, *Smets et al.*, 2016). Particularly, it has been found by researchers that sudden stratospheric warmings can lead to a variation in the stratospheric wave guides that can aid in the long-range propagation of infrasound. As infrasound depends highly on the state of the atmosphere, sudden stratospheric warnings can result in increased/decreased detection of signals such as microbaroms (*Smets et al.*, 2017).

Outside of the monitoring aspect of infrasound, these waves have also been proposed as the culprits of strong polar mesospheric winter echo (PMWE) signals (*Kirkwood et al.*, 2006). Polar mesospheric echoes are strong radar returns from the vicinity of the middle atmosphere, as recorded by very high frequency (VHF) radars. The cause of such echoes, both during winter and summer has been debated in the last few years. As explained by *Kirkwood* (2007), polar mesospheric summer echoes (PMSEs) appear to be a result of neutral atmosphere turbulence combined with charged ice aerosols. However,

this same effect does not seem to explain PMWEs, as the winter mesosphere is warmer than its summer counterpart and would not support the existence of large amounts of charged ice particles. Infrasound has now been proposed as a reason for PMWEs, based on theories put forward by *Hocking et al.* (1991) and *Hocking* (2003), which explains that scattering layers in the upper atmosphere may result from highly damped viscosity waves produced by reflections of infrasonic/gravity waves. The cause of these echoes is still in debate, with other potential explanations discussed by *Kirkwood et al.* (2015).

Further, unexplained phenomena associated with auroral arcs have been suggested to be due to infrasound in a magnetic field (*Whiter*, 2018, *private communication*). Due to the interests in an early warning system as well as attributing infrasound to several atmospheric phenomena the study of infrasound has become a key research field.

New instruments (*Hannawald et al.*, 2016; *Sedlak et al.*, 2016; *Le Dû et al.*, 2020) and techniques (*Bowman* and *Lees*, 2015; *Lamb et al.*, 2018) are being developed to expand the capabilities of infrasound detection technology. This PhD thesis falls into the latter category, and it attempts a proof-of-concept technique of infrasound detection at mesopause altitudes, by monitoring the variations in hydroxyl nightglow emission using a small three-element ground based array.

1.9. Thesis Outline

Chapter 1 has dealt with some of the theory and background regarding the atmosphere, the region of the hydroxyl layer and the atmospheric waves present in the various layers. Infrasonic waves have been introduced with descriptions of their source generation, propagation, and monitoring.

This rest of this thesis is structured as follows. Chapter 2 discusses the instrumentation to be used for observation of the hydroxyl layer, with a focus on the attributes needed to investigate fast waves propagating through a low light source at mesopause altitudes.

Hardware of the main detector is outlined, and with it the software used to acquire the data. Finally, the three-element array developed during this research is introduced.

Chapter 3 describes the calibration process of the instruments described in Chapter 2, where an Oriel calibration lamp is used as a reference source. Calibration allows for the data obtained to be compared to other studies.

Chapters 4 and 5 present the initial results of this proof-of-concept experiment. The infrasound-like signals discussed in Chapter 4 have been found not to be of hydroxyl layer origin. Some of the results are due to known noise such as sunlight scattering in the atmosphere, moon effects and clouds. As clouds can affect the data considerably, there is a focus on identifying when cloudy conditions pertain. Other results are of indeterminate origin, and display considerable amplitudes in the given time-series. These signals have been attributed to the presence of noctilucent clouds in the sub-visual optical range over the station.

Chapter 5 shows results of infrasonic signals which are believed to originate in the hydroxyl layer. The description begins with the detection of gravity wave signatures (waves which also affect the hydroxyl layer (*Tarasick* and *Hines*, 1990)). These waves help to confirm clear conditions for a given night. Once gravity waves are presented, various case studies of infrasonic signals are shown, including evidence of microbaroms in the datasets, as well as infrasonic signals showing sharp onsets. Tentative source determination for one case study is laid out with supporting evidence from propagation modelling. Other case studies pertaining to infrasound detection in the hydroxyl layer are also shown.

Chapter 6 reviews the progress that has been made during the work in the thesis. It assesses the successes, the faults and failings, and the problems that remain to be overcome, and the prospects for the approach to be adopted in the future.

2. Instrumentation

2.1. Introduction

This chapter focusses on the instrumentation used in the tripartite radiometer array employed to try to prove the concept of detecting infrasound at the mesopause altitude level. Proof-of-concept (POC) systems have been studied by other teams (*Siebicke* and *Emad*, 2019, *Vasiljević et al.*, 2020) to investigate atmospheric dynamics. Systems such as these attempt to identify new ways in which to investigate different regions of the atmosphere. The array developed for this project is sensitive to the infrared portion of the light spectrum and is primarily used to study the hydroxyl layer in the mesopause. It aims to provide a relatively low-cost option, compared with high-speed CCD systems such as those described by *Sedlak et al.* (2016), *Hannawald et al.* (2016) or *Le Dû et al.* (2020), for the study of dynamical features, like gravity and acoustic waves, propagating through the hydroxyl layer. These camera systems can cost in excess of €25,000 - €30,000, leading to a cost difference between these instruments and of the current project of around €20,000.

Requirements of the instrument such as the sensitivity, field-of-view and wavelength range for successful wave detection were all considered, and are discussed in Section 2.2. In addition, the requirement of a low-cost system for the array set fundamental limits on what might be achieved, and careful choices of all parameters were required. Based on all these requirements, the choices of instrument capabilities are discussed in the first section of this chapter (Section 2.2). Discussion of instrument specification is then followed up in Section 2.3 with a description of the components of the final radiometer instrument used, along with the capabilities of this instrument for detection. Section 2.4 provides a concise description the software used to acquire the data from the three instruments which form the array. All three instruments and their use in the determination of the speed and direction of signals is discussed in Section 2.5, illustrating

the full extent of operation for the detection of signals in the hydroxyl layer. Section 2.6 describes the frequency analysis used on the signals observed by the instruments – this is an important step to determine whether a signal is infrasonic. The final section, Section 2.7, describes the method currently in use to determine when clouds are over the observing station. The passage of meteorological clouds (as distinct from noctilucent clouds) over the station has been found to produce various artefacts in the time-series signals from the radiometers (described in Section 2.7 and in Section 4.2 of Chapter 4), rendering the vast majority of such nights unusable for infrasound analysis.

2.2. Requirements to Study Infrasound in the Hydroxyl Layer

This section discusses the steps followed to ensure the detectors onsite are capable of observing infrasonic waves in the mesopause. Observation of the hydroxyl layer, described in Chapter 1, requires sensitive instrumentation because of the low level of light emitted. Instrumentation must also be able to collect information regarding variations in the light emitted from the hydroxyl layer, from which the presence of waves within the middle atmosphere can be inferred.

2.2.1. Responsivity and Wavelength Range

The first questions answered here are posed in relation to sensitivity. What is the sensitivity of the instruments at Maynooth, and what sensitivity is needed to detect waves in the hydroxyl layer? As the hydroxyl layer is a low light source, a sensitive detector is needed to carry out observations. To have the best chance of observing this low light source, the brightest bands are chosen for observation, which in this case is within the infrared part of the OH* emission spectrum. *Baker et al.* (2007) show the major OH* band system centred around 1.5 μm (as seen in Figure 2-1) which, due to

their positioning, are located in the near infrared wavelength range, outside the visible spectrum.

Several methods exist to observe these OH* bands, including the use of infrared spectrometers (*Oliva* and *Origlia*, 1992; *Rousselot et al.*, 2000) which utilise spectral gratings, infrared radiometers like that of the SABER instrument on the TIMED satellite with narrow spectral intervals (*Mlynczak*, 1997), or the use of instruments like radiometers and spectrometers with photodetectors sensitive to the wavelength range of the hydroxyl airglow (*Mulligan* and *Galligan*, 1995; *Hannawald et al.*, 2016). This project uses radiometers to observe the OH* bands centred around 1.5 μm, which are some of the brightest bands in terms of absolute intensities, and are also strongly time dependent (*Rousselot et al.*, 2000). The detectors deployed use Indium-Gallium-Arsenide (InGaAs) photodiodes to observe the hydroxyl bands shown in Figure 2-2.

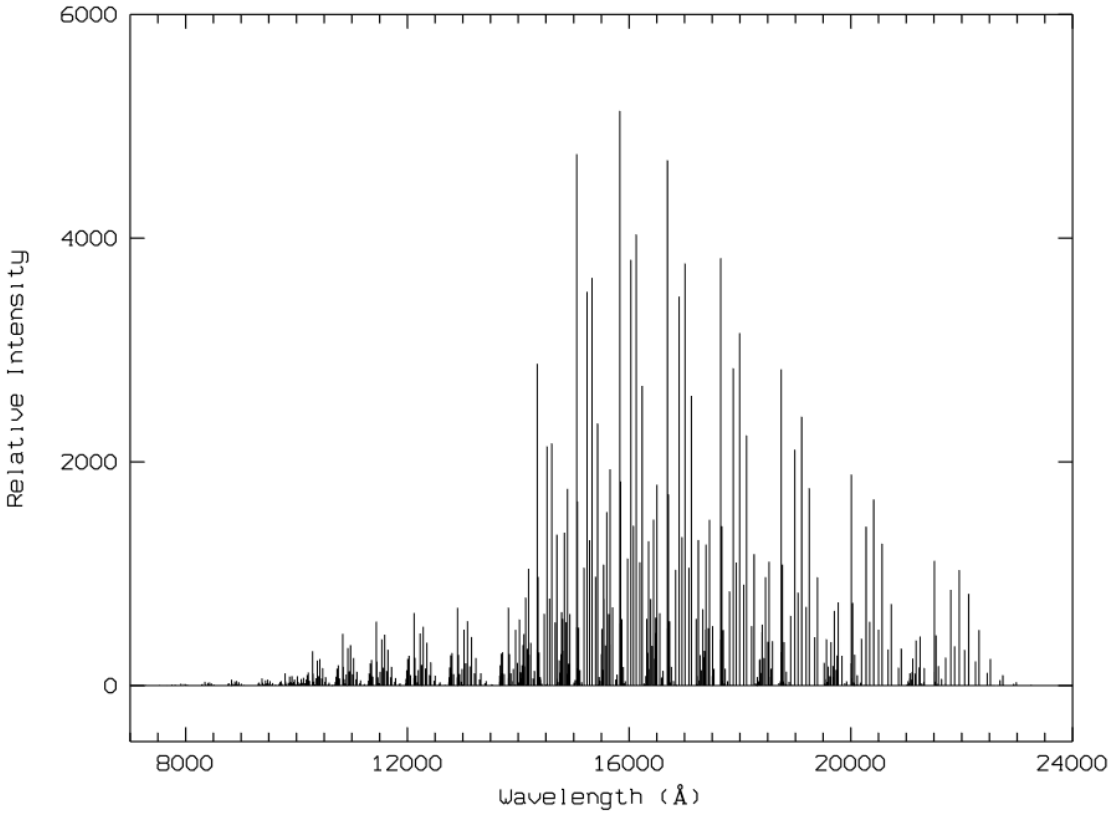

Figure 2-1: OH Bands emitted from the hydroxyl layer. The main group of emissions is seen to be centred around 1600 *nm* (*Rousselot et al.*, 2000)

Instruments containing InGaAs detectors have been used extensively to observe the hydroxyl layer (*Mulligan et al.*, 1995; *Bittner et al.*, 2010; *Schmidt et al.*, 2013; *Le Dû et al.*, 2020). These detectors are sensitive to wavelengths between $1 - 1.65\,\mu$m (*Mulligan et al.*, 1995), which include the following OH bands: $(2-0), (3-1), (4-2)$, among countless others. To describe this notation, the band $(2-0)$, for instance, represents the emission resulting from the vibrational transition of an electron from the second vibrational excited state to the ground state.

Figure 2-2 shows the response of the given detector, where the dot-dashed purple line represents the InGaAs photodiode responsivity. Also shown in Figure 2-2 is a line plot representing a silicon-window transmission. The silicon window was added to the detector, in front of the InGaAs photodiode, to hone the detector in on brighter emission bands. Bands within the InGaAs range, and outside the silicon window transmission, contribute little to the overall intensity that the InGaAs photodiode would intercept. These less intense lines do not fall under the green curve in Figure 2-2, which represents the overlapping regions of the InGaAs and silicon window curves. This green curve thus indicates the response curve of the instrument.

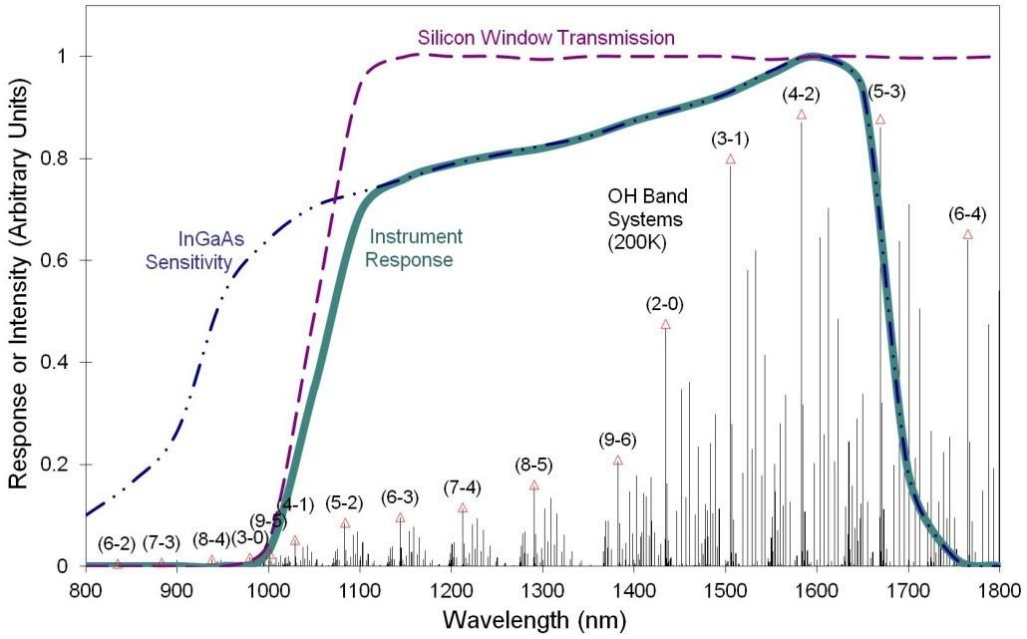

Figure 2-2: Response curve of one detector in the Maynooth array. An InGaAs photodiode and silicon window are used together to get the resulting response curve of the detector (shown in green). Courtesy of John French.

This response curve covers the majority of the brightest bands in the OH* group centred around 1.5 μm, as shown in Figure 2-2. The instrument is thus sensitive to the $(3-1), (4-2)$ and approximately half of the $(5-3)$ band as seen, along with the other bands shown. Such a response appears sufficient to detect wavelike features in the OH* layer, as shown by the observations of *Hannawald et al.* (2016) and *Bittner et al.* (2010) - studies which also use InGaAs technology. *Rourke et al.* (2017) for instance, have shown that a UWOSCR-like instrument (one of the instruments used here, also using InGaAs technology) is capable of gravity wave detection in the hydroxyl layer. This is not the only requirement for infrasound detection, as the field-of-view of the detector can also affect whether waves are detectable.

2.2.2. Field-of-View and Sampling

Along with the sensitivity of the instrument, the spatial and temporal resolution of the detector must be considered. These resolutions involve both the field-of-view and the sampling rate of the instrument, which give the spatial and temporal dimensions respectively.

For the spatial extent of the instrument, the field-of-view and fixed positioning of the detector are discussed. When choosing the field-of-view of the instrument, one must consider the wavelengths of the disturbances to be observed, which in this case are small compared to waves such as gravity waves, for instance. The expected wavelengths of infrasonic waves can be calculated using the speed of sound value (neglecting wind, and calculated from the equation $c = \sqrt{\frac{\gamma RT}{m}}$) (which follows Equation (1-28) in Chapter 1) and the frequencies of these waves (discussed later in Section 2.6). At Maynooth's latitude (~ 53 °N), the temperature in the region of the hydroxyl layer ranges from approximately 150 K in mid-summer, to 220 K in mid-winter (see Figure 7 of *Yi et al.* (2021)), translating to speeds between $240 - 300$ m/s. The frequency range of infrasound is broad, as discussed throughout Chapter 1, so a frequency corresponding to a microbarom disturbance is assumed for the purposes of this example (0.15 Hz (*Hupe et al.*, 2019)). The wavelength for such an infrasonic wave would thus be between $1.6 - 2.0$ km.

The field-of-view used for the deployed instruments at Maynooth is given as $1°$, which corresponds to a 1.5 km $\times$ 1.5 km 'footprint' on the airglow layer (at ~ 87 km in height), shown in Figure 2-3 below, where this 'footprint' is shown relative to the distance on the Earth's surface. A value of 1.5 km is close to that of the wavelengths of microbaroms, calculated above. Recent studies aimed at acoustic-gravity wave observations in the hydroxyl layer using CCD camera systems use pixel sizes which lead to fields-of-view considerably smaller than this in terms of airglow coverage.

Figure 2-3: Footprint of the instrument on the airglow layer (grey-black circle over Maynooth), where the footprint is given relative to the Earth's surface (map made by Google MyMaps). The footprint is positioned over the station.

Le Dû et al. (2020), employing such a camera system, use a pixel size of 174 m imposed on the mesopause, corresponding to a field-of-view of 2 milli-radians, similar to that of *Hannawald et al.* (2019). *Sedlak et al.* (2016), however, achieved a spatial resolution down to 17 m/pixel for zenith, with a full image size of 11.1 km× 9 km. Such spatial resolutions are small, but are used to obtain information about comparatively small structures in the mesopause. *Sedlak et al.* (2016) were able to measure turbulence in the region of the mesopause. The instrument used in this study does not achieve this kind of spatial resolution. However, the instrument used can instead attain a much better temporal resolution through a high sampling rate.

The radiometers deployed at Maynooth only collect the photons emanating from the hydroxyl layer (*i.e.* they each act like a single pixel detector, like that used in *Mackovjak et al.* (2019)) and unlike camera systems, they do not produce images of the sky. As a result, the spatial resolution for each data point taken by the instrument is the same as the field-of-view at mesospheric heights (~1.5 km). *Mackovjak et al.* (2019) in essence, achieve airglow data on this same basis. These spatial resolutions cannot compare to the

more precise resolutions of other studies, which employ camera systems. *Le Dû et al.* (2020) show, in Figure 4 of their study, that structures of the order of 1722 m are readily shown in a FOV of 8 km x 12 km. Thus, the 1.5 km FOV used within this thesis would be just sufficient enough to observe such structures as they move in and out of the FOV of the instrument. If the FOV was larger than this value of 1.5 km, then structures such as small acoustic waves may not be detectable due to averaging out of intensities over the whole FOV. *Sedlak et al.* (2016) refer to two small wavelike features that might be attributed to gravity wave instabilities, with horizontal wavelengths of 1.7 km and 550 m. The longer wavelength would be detected by the instrument described in this thesis, but the shorter structure would not because of the instrument's much larger FOV. As a result, a value of 1° appears to be capable of distinguishing wave structures that are of interest in this thesis.

Another consideration taken into account for the FOV, is that it is placed in a fixed position, rather than in scanning mode, like that of the UWOSCR (University of Western Ontario Scanning Radiometer) instrument discussed within *Rourke et al.* (2017). The reasoning here is that, as infrasonic waves are faster (have higher frequencies) compared to that of gravity waves (see Figure 1-18 of Chapter 1 (*Bittner et al.*, 2010)), their signatures would not be captured by a scanning radiometer with a cadence of one image per 60 seconds.

The temporal resolution is also considered in the observation of fluctuations and disturbances in the hydroxyl layer. The period at which the instrument samples the region determines whether disturbances like acoustic waves can be observed. Sufficient sampling is needed to observe acoustic waves. If the sampling is too slow, then 'fast' wave disturbances like acoustic waves cannot be captured as they propagate too quickly across a FOV. A high sampling rate is desirable to capture both acoustic and gravity waves passing over the station, where higher sampling rates also open up the possibility of detecting waves of higher frequencies. In the instruments deployed, the sampling rate is 0.22 s, meaning a data point is retrieved every 0.22 seconds. This is coupled with the fact that each data point is the average of 660 samples (as determined by the data

acquisition device), obtaining a snapshot of the 1.5 km × 1.5 km FOV of the airglow layer every 0.22 seconds.

Compared to other studies such as *Hannawald et al.* (2019) (who achieve a temporal resolution of 0.5 seconds) and *Le Dû et al.* (2020) (who achieve a frame rate of 0.5 seconds), the radiometers of this study have temporal resolutions twice these values (and could of course be much higher if say only 100 samples (instead of 660) were averaged for each data point recorded). *Le Dû et al.* (2020) have achieved the detection of infrasonic frequencies with their FOV, which they have attributed to the presence of microbaroms. This result confirms that the field-of-view and sampling rates of this study should be sufficient to achieve infrasonic wave observations in the hydroxyl layer.

2.3. Hardware

The requirements for infrasonic detection discussed above, along with an attempt to reduce noise, are implemented in the hardware of the instruments. The basic structure of the instrument used here, a radiometer (regularly used in remote sensing (*Rees*, 2001)), is shown in the diagram below in Figure 2-4, where all three radiometers to be described are of a similar structure. The description of the hardware will refer to the radiometer known as MFR, or the Maynooth Fixed Radiometer (this name originated from a modification of UWOSCR – University of Western Ontario Scanning Radiometer – reflecting the change from the original scanning device developed at Western Ontario to a fixed viewing configuration employed at Maynooth). Figure 2-4 shows that the main tasks of the instrument are to detect, modulate and amplify the source signal. Each part of the instrument (namely the optical chamber (shown separately in Figure 2-5), the tuning fork chopper, the InGaAs detector, and the lock-in amplifier) will be discussed in detail in the following sections. The hardware of the instrument is shown first with the software to convert the data to a user-friendly output shown in Section 2.4 and Appendix C.

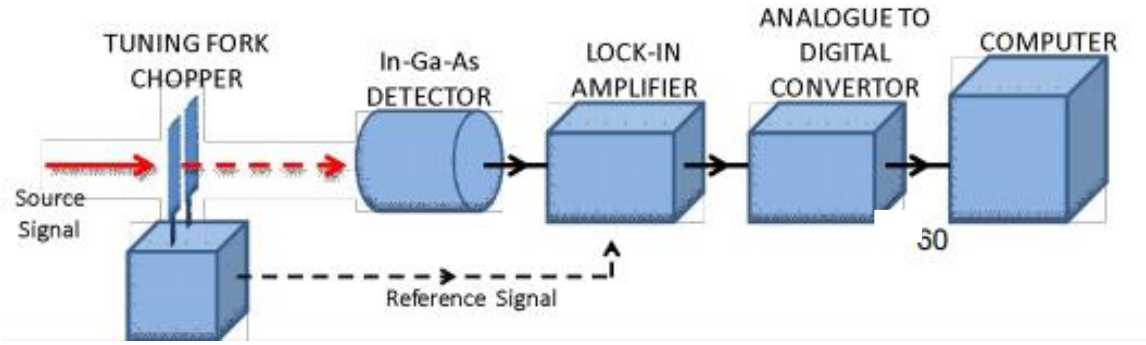

Figure 2-4: Schematic of the basic structure of radiometer's hardware

MFR, shown in Figure 2-5(a), is a specially constructed catadioptric telescope based on a US Navy searchlight and a Schmidt design (a catadioptric telescope uses elements of reflection and refraction to focus light, while a Schmidt designed telescope is a catadioptric telescope using a primary mirror and correcting lens). As shown in Figure 2-5(b), light enters through the aperture and passes through a corrector plate, correcting for spherical aberrations introduced by the primary spherical mirror where the light reflects into the InGaAs detector, located at the focus of the mirror. This light enters into the photodiode via a tuning fork chopper. Every night, all incoming light, regardless of wavelength enters through the aperture and propagates to the photodiode at the focal point of the primary spherical mirror.

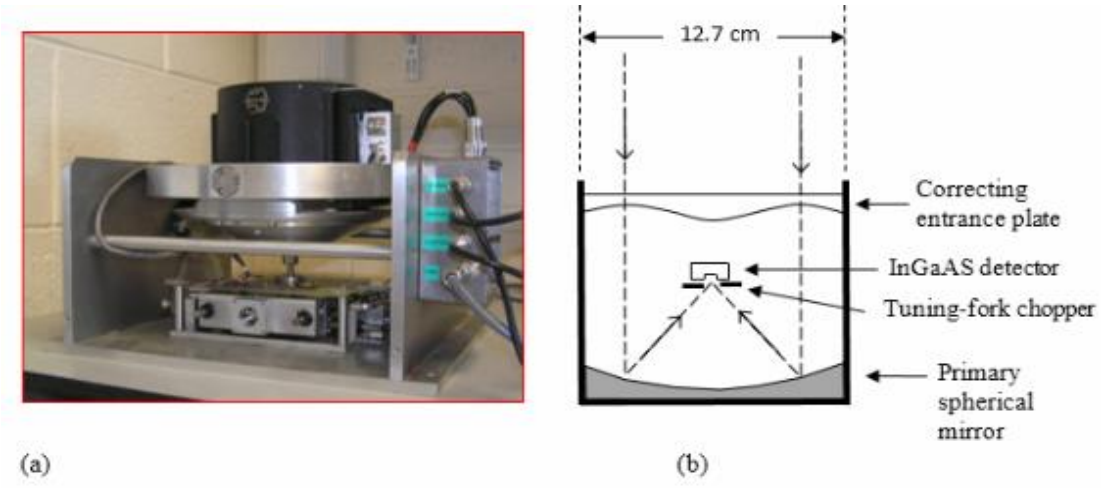

Figure 2-5: (a) Photo and (b) Schematic of the main optical design of MFR.

This operation is the beginning stage of the data acquisition process before the processes corresponding to wavelength discrimination and improvement of signal-to-noise ratio of the data take effect. The next few subsections will cover how the light entering the aperture is converted to voltage values, all whilst adhering to the requirements set forth in Section 2.2. Presentation of each part of the process will be in chronological order, following the path of light input to voltage output.

2.3.1.1. Optical Chamber

The telescope in use in Maynooth is of a catadioptric design. A catadioptric telescope is a set-up where mirrors and lenses are used in tandem to focus the light, while also correcting for aberrations (*Kingslake* and *Johnson*, 2010). The main outline of the telescope has been shown previously in Figure 2-5(b), portraying the mirror and lens set-up. Schmidt-designed telescopes are characterised by the corrector entrance plate that is placed at the aperture stop of the telescope situated at the centre of curvature of a spherical concave mirror (*Kingslake* and *Johnson*, 2010). This is all located inside the optical chamber of MFR (the instrument under discussion). As the light from the hydroxyl layer enters the aperture, a number of aspects of the optical chamber come into play. These aspects dictate how the light reaches the detector from the entrance aperture, as well as how the mechanics of the optical chamber affect the telescope operation.

One of the main questions concerns the frequency of 'images' captured by the telescope. The speed at which the telescope operates is known as the *f*-number or the focal ratio (*Winston et al.*, 2005). The smaller the focal ratio, the faster the telescope obtains images. If, however, the *f*-number is large, the image is measured over a longer period of time. The focal ratio is dependent on the diameter of the aperture and the focal length of the entrance lens, and is calculated as (*Francis* and *Yang*, 1997):

$$\text{focal ratio} = \frac{\text{focal length}}{\text{aperture diameter}} \tag{2-1}$$

The focal ratio (or *f*-number) of MFR is calculated to be $f/\# = 0.4\,(f = 2.5)$, where the aperture diameter is 12.7 cm and the focal length of the lens is 5.08 cm (as shown in Figure 2-6). Small focal numbers capture brighter images over a shorter time-span while, in the case of larger focal numbers, similar bright images take longer to capture. The *f*-number of MFR is regarded as small and so the optical system is regarded as fast. A fast optical system is needed to capture the rapidly changing state of the hydroxyl layer, where infrasonic waves are relatively fast phenomena, compared to gravity waves for instance. A small *f*-number opens up the possibility for the observation of these faster waves.

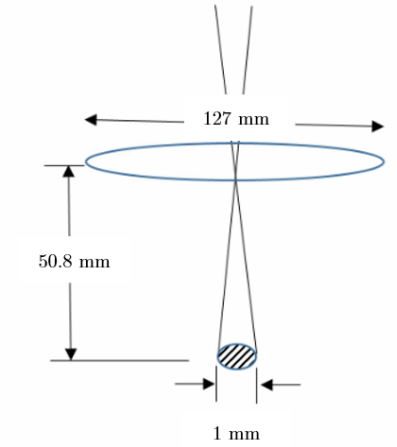

Figure 2-6: Focal ratio ($f = 2.5$) of the optical system as determined by the focal length (5.08 cm) and aperture diameter (12.7 cm)

The set-up of the optical chamber not only determines the speed at which the telescope can operate, but it is also responsible for how much light can reach the detector in the centre of the chamber. A fundamental quantity of non-imaging optics known as *étendue* or throughput, dictates the extent of the light propagating through the entrance aperture, reaching the detector. More importantly however, it contributes to how much power the detector receives.

To understand how much power the detector receives, it is necessary to outline quantities like the area of the aperture, the solid angle and the *étendue*. The area of the aperture is calculated using the area of a circle equation:

$$A = \pi r^2 = \pi\left(\frac{12.7 \times 10^{-2}}{2}\right)^2 = 1.27 \times 10^{-2}\ \mathrm{m}^2 \tag{2-2}$$

Radiation from the hydroxyl layer enters this aperture, but only a small proportion of the hydroxyl layer's extent is captured. To obtain the extent of the hydroxyl layer observed, the angle subtended by the detector is calculated using the values shown in Figure 2-6. The focal length and detector diameter represent the two quantities used in the calculation of the full angle subtended by the detector:

$$\tan(\theta) = \frac{\text{detector diameter}}{\text{focal length}} \tag{2-3}$$

$$\theta = tan^{-1}\left(\frac{1 \times 10^{-3}}{5.08 \times 10^{-2}}\right) = 1.13° \tag{2-4}$$

The full angle of $1.13°$ (Equation (2-4)) is the field-of-view of the detector, where the value is in line with the requirements discussed in Section 2.2.2 (a value of $1°$ is desired to observe wave structures). Although this represents the full angle subtended by the detector, a better representation of the angle subtended is given by the solid angle (symbol of Ω). The solid angle represents the 3D angle that the detector subtends (related to the steradian (sr) (*Smith*, 2000)), and is found by dividing the aperture area by the focal length squared:

$$\Omega = \frac{\text{aperture area}}{(\text{focal length})^2} = \frac{1.27 \times 10^{-2}}{(5.08 \times 10^{-2})^2} \tag{2-5}$$

$$\Omega = 3.05 \times 10^{-4} sr \tag{2-6}$$

Baker (1974) notes that the solid angle can also be calculated using the formula $\Omega = \pi \sin a^2$, where a is the half angle. The solid angle and the area of the aperture are multiplied to obtain the quantity known as *étendue*. *Étendue* characterises the light-gathering capacity of an instrument, *i.e.*, how spread out the beam of light entering the aperture is in both the area and the solid angle. It can sometimes be characterised as the energy throughput of the optical system and is calculated as:

$$A\Omega = (1.27 \times 10^{-2})(3.05 \times 10^{-4}) = 3.87 \times 10^{-6} sr \cdot m^2 \tag{2-7}$$

The *étendue* of the system can be combined with the radiance of the hydroxyl layer to obtain the power throughput of the optical system. According to *Baker* (1974), the power throughput of the system is independent from the distance to the source, specifically an extended source, based on the equivalence theorem. Based on this, the author notes that the unit of the rayleigh makes sense for quantifying radiance. For this reason, this concept of the rayleigh is discussed and used in Chapter 3 regarding calibration of the instruments.

The preceding discussion covers the main aim of the optical chamber: to capture light that will fall on the InGaAs detector once it has been modulated by the tuning fork chopper.

2.3.1.2. Tuning fork chopper

The tuning fork chopper acts to reduce the background fluctuations due to the atmosphere. Based on the instrument design, the chopper is present within the confines of the optical chamber. Due to the low level of light intensity emanating from the hydroxyl layer, the signal is normally obscured by background noise, but this can be

improved by the tuning fork chopper. The tuning fork chopper is situated close to the InGaAs detector, inside the optical chamber as shown in Figure 2-7 below. The schematic shown in Figure 2-7 (top right) also shows the basic structure of the tuning fork chopper. The chopper acts to modulate the light (*Duma et al.*, 2012) to obtain a better signal-to-noise ratio (SNR).

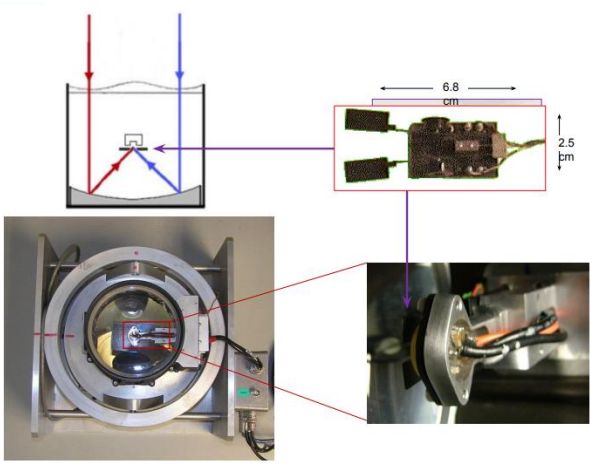

Figure 2-7: Location of the tuning fork chopper within the optical chamber of MFR

The tuning fork chopper is named as such due to its familiar structure to a tuning fork, which consists of two vanes. The vanes are attached to the end of the tines and are driven by a drive coil, which operates close to the resonant frequency of the chopper (a single sinusoidal frequency). When the drive coil is applied, the tines oscillate at the resonant frequency of the fork, causing the vanes to overlap, and modulate the light which comes through the vane gap (*Tuchman*, 1999). This chopping frequency is around 187 Hz, which was designed to not be a multiple of the mains (~ 50 Hz). This frequency of 187 Hz is approximately ten times that of the highest frequency of interest (around 18 Hz, where the infrasonic frequency range reaches to 20 Hz at the high end) – this frequency thus easily satisfies the Nyquist sampling criterion of being at least twice the highest frequency of interest.

The location of the chopper in this project (Electro-Optical Products Corporation CH10-90D, where specifications for the device are given in *EOPC* (2017)) is also important, as to ensure no spurious light enters the detector that is not modulated. The chopper is

thus placed very close to InGaAs photodiode, reducing the noise of the final signal. The chopper, while modulating the light, also provides a reference signal to the lock-in amplifier that will be discussed later in Section 2.3.1.5. These resonant choppers also offer stability whilst reducing noise such as vibrations, due to the motion of the tines (the tines of the chopper move in opposite directions, cancelling out vibrations introduced by their motion (*Tuchman*, 1999)).

By using a tuning fork chopper to modulate the light striking the detector, and using the reference signal to tune the amplifier to this frequency only, two things happen: (i) the bandwidth is moved away from the 0 Hz frequency (or d.c.), and (ii) the bandwidth includes only the frequency of the chopper. Both effects reduce noise in the output signal, and increase the SNR. *Vincent et al.* (2015) provides a detailed discussion of the operation and testing of detectors like radiometers and clearly outlines the rationale for the use of choppers in optical devices, highlighting the need for frequency specificity to obtain the required response. The output of the tuning fork chopper would be close to a square wave (*Vincent et al.*, 2015) and is used as a reference signal for the lock-in amplifier, used regularly with an optical chopper (*Lipson* and *Littler*, 1966). Chopping the signal provides a stable a.c. signal to the rest of the hardware, keeping the amplification of such a signal more stable (*Vincent et al.*, 2015). This chopped signal then enters the InGaAs photodiode immediately after exiting the tuning fork chopper.

2.3.1.3. InGaAs photodiode

The InGaAs photodiode used in this thesis is a Hamamatsu C30641E-TC (datasheet given in Appendix B) type of photovoltaic device sensitive to the near infrared range of the light spectrum. InGaAs (Indium-Gallium-Arsenide) photodiodes are sensitive to the $1.0 - 1.65$ μm wavelength range (*Mulligan et al.*, 1995, *Vincent et al.*, 2015). These devices work based on the I-V curve shown in Figure 2-8, where the short circuit current (curves) shifts lower with increasing light levels.

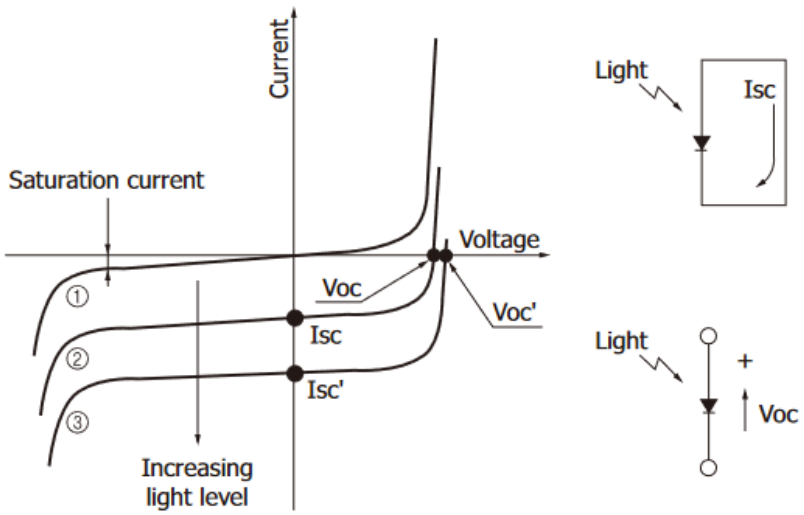

Figure 2-8: IV curve for the InGaAs photodiode and how the curve changes when the light levels increase (Hammamatsu, 2021)

The InGaAs photoconductor is thermoelectrically cooled within the detector's hardware to ensure that low-energy infrared radiation can be detected (*Budzier* and *Gerlach*, 2011). Light levels observed in the hydroxyl layer are very low and so thermal emissions in these detectors are unwanted as they are a source of noise in the signal. Thermal noise, also known as Johnson or Nyquist noise, is present in all detectors and unavoidable at non-zero temperatures, and arises due to the thermal agitation of charge carriers in the apparatus. *Moore et al.* (2009) defines this as a noise power (mean square power of the noise):

$$< i_N^2 >_{JN} = \frac{4kT\Delta f}{R} \tag{2-8}$$

Here, k is the Boltzmann constant, T is the absolute temperature, Δf is the frequency band, and R is the resistance. True variations arising from the hydroxyl layer are of the greatest interest and thus less noise and a cleaner signal are desired. One of the main advantages of this type of detector is that it cuts down on noise and is low-cost (*Schmidt et al.*, 2013).

Other groups have turned to this type of detector due to its response curve. *Hannawald et al.* (2019), for instance, use a camera based on InGaAs photodiode technology to image features in the hydroxyl layer. InGaAs technology has been used for mappers of airglow studies (*Taylor et al.*, 2010, *Pautet et al.*, 2014) to spectrometers for the measurement of airglow temperatures (*Schmidt et al.*, 2013). Use of InGaAs detectors for the study of small features like turbulence in the hydroxyl layer has also been achieved by authors like *Sedlak et al.* (2016).

The graph in Figure 2-2, shown in the first part of this chapter, shows the response curve of the photodetector. The graph, provided by John French of the Australian Antarctic Division, shows the upper and lower wavelength cut-off of the detector. Two aspects limit the observation of the detector. One, as mentioned in this section, is the InGaAs photoconductor, but a silicon window layered on top of the photoconductor also plays an important role for photon detection. In combination, the major bands of the hydroxyl layer, discussed in Chapter 1 of this thesis, can be observed in the short-wave infrared part of the spectrum. The brighter bands occur closer to the upper cut-off of the detector and only part of the $OH(5-2)$ band intensity can be captured by the instrument.

The photodiode also has an inherent gain given by the responsivity of the detector, which is dependent on the wavelength incident on the detector. The typical responsivity for this photodiode is given in Figure 2-9, where the minimum photosensitivity of the detector is 0.8 A/W (amps per watt) at 1300 nm (which occurs in the middle of the response curve). The photosensitivity of the detector only rises to around 0.85 A/W (minimum) at 1550 nm for the detector (not shown in Figure 2-9). For gain calculations, this lower value of 0.8 A/W is assumed, and is used in later sections.

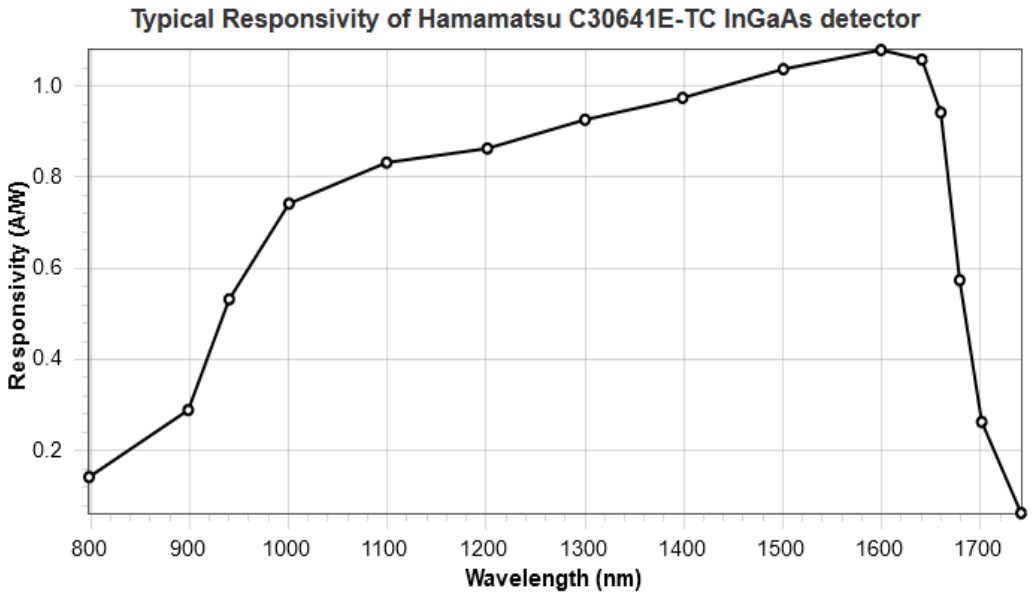

Figure 2-9: Responsivity of the InGaAs photodiode used within this project (after (Perkin-Elmer, 2000a))

Although the hydroxyl bands covered by the response of the InGaAs photodiode represent a large part of the spectra of the hydroxyl layer, the signal the layer emits is small. The next sections deal with the hardware required to both amplify this small signal from the extended source while also minimising the noise introduced and removing any spurious noise from the signal.

2.3.1.4. Trans-impedance amplifier

As photons enter the entrance window of the InGaAs PIN detector (diode with p-n junction composed of an intrinsic semi-conductor), they generate electron-hole pairs, inducing a current in the circuit. These detectors can either be operated in photovoltaic or photoconductive mode, but in either case, the current induced is very small and must be amplified. The first amplifier used within the detector circuitry is the trans-impedance amplifier (TIA), which is a current-to-voltage type of amplifier that comes

immediately after photons are registered by the InGaAs detector and converted into a current which is dependent on the photon count.

This type of amplifier, also known as a current mode pre-amplifier (*Vincent et al.*, 2015), uses a large value feedback resistor (**40** MΩ) and an operational amplifier (op-amp) to stabilise the signal. A typical setup for a trans-impedance amplifier circuit is shown below in Figure 2-10, where the circuit is connected to ground both through the detector section of the circuit and through one of the op-amp inputs (this ensures low impedance in the circuit). A high-valued feedback resistor is also needed to ensure maximum amplification of the signal while ensuring noise stays to a minimum.

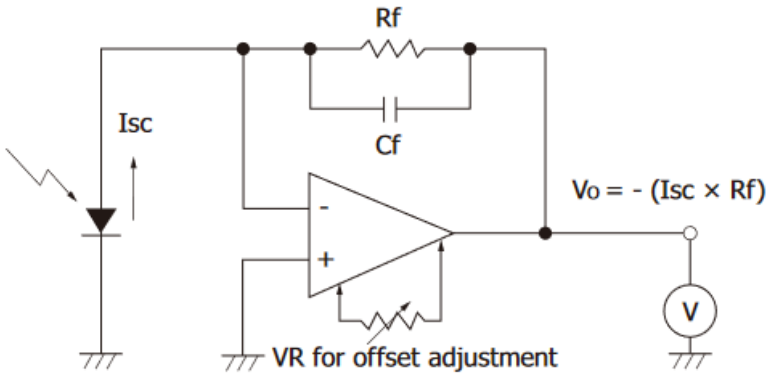

Figure 2-10: Trans-impedance amplifier set-up showing the op-amp and large feedback resistor (*Hammamatsu*, 2021)

The signal from the photodiode is multiplied by the feedback resistance to achieve the voltage conversion and amplification of the signal (*Horowitz* and *Hill*, 2015). A further advantage comes with feedback resistors such as the one shown in Figure 2-10, namely that it reduces the Johnson (thermal) noise to a point where it's below the value of the detector noise. From here, further amplification takes place along with bandwidth narrowing of the signal.

2.3.1.5. Lock-in amplifier

Further amplification of the signal occurs through a d.c. amplifier, with a multiplication factor of 200. This represents one of the larger amplifications in the process. This type of amplifier is well suited for low frequency signals, such as infrared signals, as it has very little limitation on this frequency end (*Grimnes* and *Martinsen*, 2015), and is thus ideal in the case presented here. There is little noise mitigation within the d.c. amplifier and aspects such as drift in the signal and high output noise can be apparent in the output voltage. Noise mitigation techniques are a key feature of the lock-in amplifier, the last major element in the path the signal takes from photodiode to computer.

Lock-in amplifiers are characterised by their ability to extract small signals from noisy environments. Lock-in amplifiers are used in combination with a reference signal (square wave) provided by a modulating source to extract the signals. In the case of MFR, a tuning fork chopper provides such a signal, as discussed in Section 2.3.1.2. The output signal of the previous d.c. amplifier is multiplied against the reference signal in the first part of the lock-in amplifier – which is known as the frequency mixer. A simplified version of the lock-in amplifier process is shown in Figure 2-11 below. The value of $V_r(t)$ represents the reference signal determined by the tuning fork chopper at the detector aperture, while the input signal that originates from the TIA is given by $V_s(t)$.

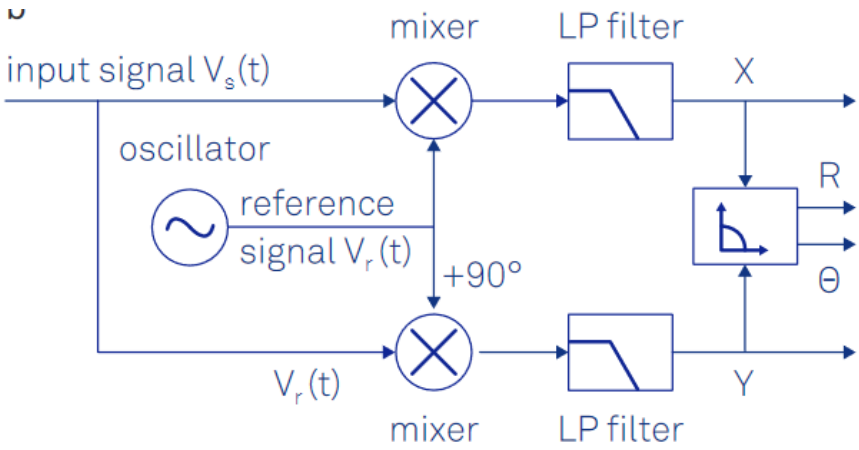

Figure 2-11: Typical lock-in amplification process (Zurich Instruments, 2016)

Assuming a perfect situation, the reference signal and main signal are both composed of sine waves. The frequency mixer multiplies the two signals together, resulting in an output of the difference of the signals and the addition of the signals. If, for instance, the main signal has a frequency f_1 and the reference signal has a frequency f_R, then the output is $(f_1 - f_R)$ and $(f_1 + f_R)$. It is obvious from this output that if the amplitudes of f_1 and f_R are equal, the output will be 0 Hz and $2f_1$ Hz. The 0 Hz value represents the d.c. component of the signal, while the sum of the two frequencies, $2f_1$ can be easily removed using a low-pass filter. The low-pass filter removes the a.c component of the signal, giving a difference frequency in terms of the d.c component, with the final signal is given as:

$$V = \frac{1}{2} V_s V_r \cos(\theta_s - \theta_r) \tag{2-9}$$

Equation (2-9), derived from *Perkin-Elmer* (2000b) shows the phases associated with the two signals (where θ_s is the phase of the main signal, and θ_r is the phase of the reference). The above equation shows that the output of the lock-in detector is a d.c signal that is proportional to the signal's original amplitude.

If the main input signal is not a perfect sine wave and instead a series of signals, a Fourier transform can be performed to deconstruct the signal into a series of sine waves. Frequencies within one bandwidth (harmonics) of the reference frequency are amplified while other frequencies are suppressed, reducing the noise far from the reference frequency.

Signal averaging can also be achieved within the lock-in amplifier, to reduce noise and drift (*Edgar*, 1989) in the signal (such noise may propagate by the previous d.c. amplifier, discussed above). Overall, the signal-to-noise ratio would be improved by this process. Once all the processes of the lock-in amplifier are complete, the output signal is sent into an A/D (analogue-to-digital) converter to be read into the software on the accompanying computer.

2.4. Software

Two main pieces of software are used to extract the data from the detectors – and they differ depending on the instrument in question. Of the three radiometers used, both MFR and MFR2 (the first and second radiometers) use in-house LabVIEW software (developed by PhD student Andrew Wilson) to complete data acquisition using National Instruments™ DAQ (data acquisition) hardware and software. UWOSCR (the third radiometer), on the other hand employs in-built software (written in the C-language by Dave Turnbull of University of Western Ontario) to complete data acquisition.

Although the two software programs differ, they both output data files containing the timestamp of each sample (or sample average) and the voltage response of the detector. This voltage response will change depending on the light incident on the detector photodiode, but is less than about 10 V, where around $1-2$ V is normal during night-time hours when sunlight or moonlight does not enter the optical chamber. The detector only records during night-time hours for this reason, and the LabVIEW software shows a conditional terminal dependent on the solar elevation angle.

The program is designed to set the conditional terminal to "True" when the Sun is below the horizon ($< 0°$) – dependent on the latitude and longitude of the instrumentation (Maynooth: $53.385°\text{N}, 6.59361°\text{W}$). The DAQ instrument collects the samples taken every 0.22 s and outputs to a waveform chart, displaying the voltage as a function of time. This process is continued until the solar elevation increases to above $0°$. The solar elevation angle is checked and once this criterion is met (positive solar elevation angle), the program exits the loop and writes the array of voltage and time stamps to a text file and outputs it to a waveform graph to be displayed on the front panel of the LabVIEW program (see description and diagrams in Appendix C)). This text file (created and saved at the end of the night) is the raw data that is analysed and interpreted. Through the use of Python programming developed throughout the course of the project, time-series graphs can be plotted and the data from the hydroxyl layer can be analysed.

Compared to the LabVIEW program used in MFR and MFR2, the software package used for the UWOSCR instrument (developed in the University of Western Ontario) begins recording during times where the solar elevation angle is below $-6°$. When the sun is below this elevation angle, less sunlight is present in the atmosphere, and thus has less of an effect on the time-series outputted by UWOSCR. Although the instruments begin recording at different times based on solar elevation angle, the time is recorded for each sample and the instruments synchronised using an internet time server available from Maynooth Computer Services Centre, thus allowing the signal from the instruments to be easily compared. An example of a time-voltage graph outputted by the LabVIEW software (in this case for MFR) is shown in Figure 2-12, and is the signal recorded during the night with 24 hours corresponding to midnight. Sunset occurs after 22 UTC and sunrise before 27 UTC (where 27 UTC corresponds to 03 UTC the next day ($24 + 3$ UTC)). Detail regarding the various features in the graph of a typical night, including the saturated signals at the beginning and end of the night (artefacts of the lock-in amplifier detection) will be discussed in Section 4.2 of Chapter 4.

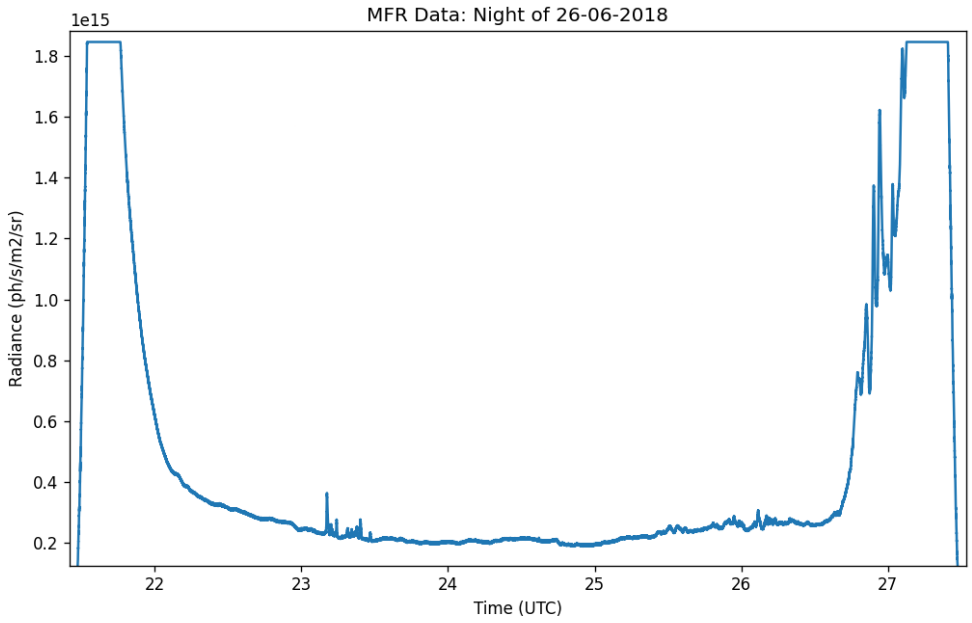

Figure 2-12: Example of the output from the LabVIEW program connected to the MFR computer (the output has been formatted through Python)

The information that these instruments can provide is limited if they are used in isolation. Each instrument can show the variations and duration of signals within the hydroxyl layer and a one-dimensional view of the period of the given signals. However, more information such as directional and speed information can only be obtained through either the use of a scanning instrument or a tripartite array. This project uses the latter, as mentioned in Chapter 1 and discussed further in the next section.

2.5. Tripartite Array

The output from a single radiometer gives no indication of the direction of propagation of the waves. Therefore two additional radiometers were constructed and deployed as a three-element array as shown in Figure 2-13. The diagram shows the basic geometry of the array, where the three instruments are co-located (Figure 2-13(left)), and are separated by approximately 15 km in terms of coverage on the hydroxyl layer. The instruments, although co-located, form a right-angled triangle on the hydroxyl layer, where MFR looks to zenith ((0,0) in Figure 2-13(right)), MFR2 looks to west $(-15,0)$ and UWOSCR views toward north $(0,15)$.

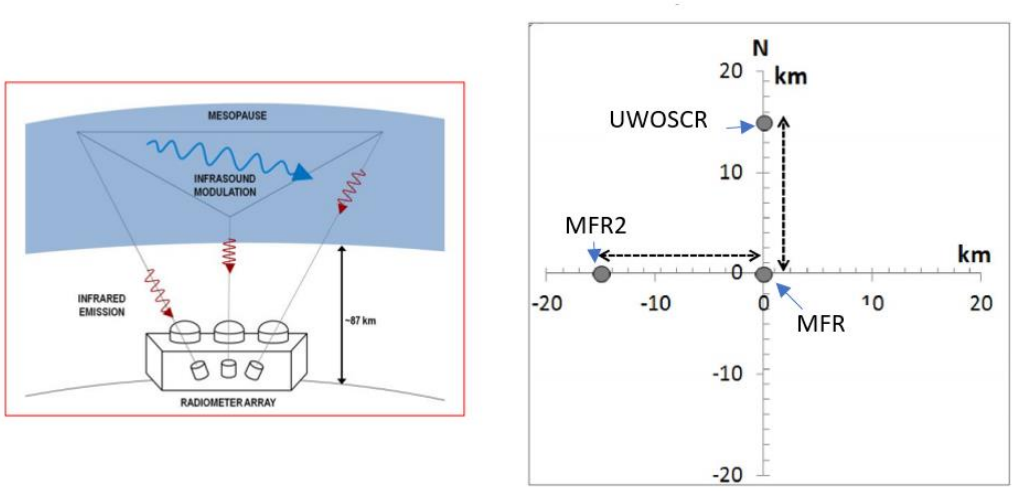

Figure 2-13: Diagram of the tripartite array and its geometry, in terms of how it views the hydroxyl layer.

The difference in the instruments' viewing conditions is attributed to their angles with respect to zenith. As mentioned already, the field-of-view of each radiometer was ~1° which translated to 1.5 km at 87 km altitude. MFR is pointed to zenith, while UWOSCR and MFR2 were set to observe 10° due north and 10° due west respectively. This combination of directions was chosen to minimise possible contamination from the nearby street lights in the town which lies to the east and south of the observatory. The choice of 10° was a compromise between wanting to detect a coherent wave, but having sufficient time difference between the three signals to obtain an accurate value of the velocity of the wave across the station. It was reasoned that relatively small values of zenith angle would increase the chance of observing a coherent wave over the radiometers. The effect on the field-of-view of these instruments arising from their different viewing angles is negligible (*i.e.* very little distortion is introduced compared to studies with larger fields of view and greater angles). The field-of-view only increases by 3% (negligible for these observations) for MFR2 and UWOSCR compared to MFR.

In terms of the instrument configurations, there exist some differences. MFR has been described in detail in Section 2.3, where the hardware of the instrument was described. MFR2 by comparison has a difference in field-of-view while UWOSCR does not contain a tuning-fork chopper or lock-in amplifier. This affects the output of each of these instruments compared to the output of MFR. MFR2 (designed at a different time) has an output averaged out compared to MFR, resulting in an instrument less sensitive to the changes in its field-of view (covered in Section 2.2.2). To improve this issue, a field-stop was inserted into the instrument hardware of MFR2 – this however, resulted in a larger amount of noise in the MFR2 signal. In the case of UWOSCR, the instrument does not contain a tuning-fork chopper or lock-in amplifier, giving a noisy and unmodulated output, giving a signal harder to analyse. Although these aforementioned points provide a disadvantage, the instrument outputs combined together still allow for analysis of signals in the hydroxyl layer.

The instruments are also time-synced, where each instrument computer (which controls the instrument's data acquisition) is synced through the use of one main computer.

Specifically each instrument computer has it's clock checked by the main computer, and the instrument clocks are re-synced if any difference occurs. The main computer is synced to the Maynooth time server, which is checked every hour to ensure all instrument clocks are correct and the time-stamps of the instrument outputs are synced. This is needed to ensure that the timing required for the direction and speed calculation of waves across the station can be calculated.

The paragraphs above show the basic geometry of the array and how it observes waves in the hydroxyl layer. However, to obtain information regarding signals passing through the layer, such as directional and speed information, an analysis method must be established. This project uses methods established by *Giers et al.* (1997), *Pignatelli et al.* (2008) and *ElGabry et al.*, (2017) to obtain this information. These methods, which follow the work by Briggs since the 1960s, are used extensively in radar determinations of wind velocities using the spaced antenna technique (*Briggs*, 1968, 1985), and have been used by studies like *Murphy et al.* (2007) to obtain information about horizontal wind velocities (for the study of long period planetary waves in the Antarctic).

The basic geometry of the array dictates that as a wave front passes over the station, it should be detected by each instrument after a given time-lag. For instance, if a signal is travelling from the north-east, then UWSOCR (facing north) should first observe the signal, followed by MFR (facing zenith), and finally by MFR2 (facing west). This triangulates the signal, giving a rough back-azimuth (direction from which the signal originated) for the signal, where the speed of the signal can also be obtained. The above assumes that the wave of interest remains coherent as it passes over the three radiometers.

The method described by *Pignatelli et al.* (2008) is followed, which is based on the cross-correlation of the signals through time-lag analysis. It is considered that a wave passes through the FOV of each detector of the array, and that the wave front is planar due to the co-located positions of the instrument, where the wave-front movement would be like that shown in Figure 2-14. The instruments, with labels S_1 (MFR – the reference

instrument), S_2 (MFR2) and S_3 (UWOSCR), can be analysed in pairs – namely (S_1, S_2) and (S_1, S_3), as S_1 is the reference.

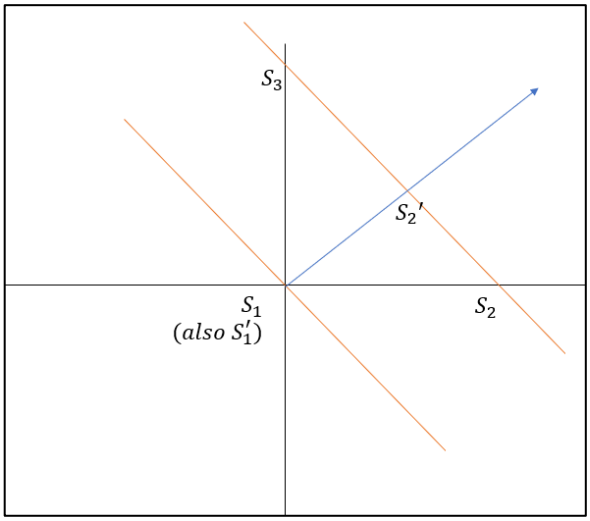

Figure 2-14: Wave front of the signal with projections of the stations on the ray

Time-lag analysis can then be computed for each pair – obtaining unknowns in the form of the direction of the wave and the speed of the wave. Figure 2-14 shows the ray representing the direction and speed of the wave (and is normally given the magnitude v_a, which represents the apparent velocity of the wave), which is perpendicular to the wave front. It is assumed here that the wave front covers the same distance between two co-located instruments, for instance, between S_1 and S_2, in the same time as that of their projections onto the ray (in this case S_1' and S_2'), shown in Figure 2-14.

Pignatelli et al. (2008) shows the evolution of the wavefront over a tripartite array in their work on seismic waves (summarised in Figure 2-15). The next paragraphs show how the time delay between signal observations is used to calculate the apparent speed and back azimuth. The time difference between arrivals at each station can be taken as the time difference between the two station projections on the ray, given by *Pignatelli et al.* (2008) as:

$$\Delta T_{12} = T_2 - T_1 = \frac{\overline{S_1' S_2'}}{V_{st}} \tag{2-10}$$

The same equation also holds true for the time difference between the second pair: S_3 and the reference S_1, and their projections onto the ray:

$$\Delta T_{13} = T_3 - T_1 = \frac{\overline{S_1' S_3'}}{V_{st}} \tag{2-11}$$

The signal's direction or azimuth and the coordinates of the station can be then related by rewriting Equation (2-10), while assuming simple plane geometry, as:

$$\Delta T_{12} = \frac{(y_2 - y_1)\cos\varphi + (x_2 - x_1)\sin\varphi}{V_{st}} \tag{2-12}$$

The angle given in Equation (2-12) represents the signal's azimuth and is normally given with respect to the origin. Equation (2-11) can also be written similarly, and when both forms are combined they give the definition of the signal azimuth:

$$\tan\varphi = \frac{\Delta T_{12}(y_3 - y_1) - \Delta T_{13}(y_2 - y_1)}{\Delta T_{12}(x_3 - x_1) - \Delta T_{13}(x_2 - x_1)} \tag{2-13}$$

This allows for the azimuth of a given signal to be easily obtained. Equation (2-13) is independent of the apparent velocity, and thus it must instead be recovered using either Equation (2-11) or Equation (2-12) once the azimuth is calculated. *Pignatelli et al.* (2008) notes that three separate estimates for the azimuth of the signal and velocity can be determined when all instruments are considered. On the basis of detector synchronisation, the time difference estimates of the signal arrivals should be similar and thus give similar estimates for azimuth and apparent velocity.

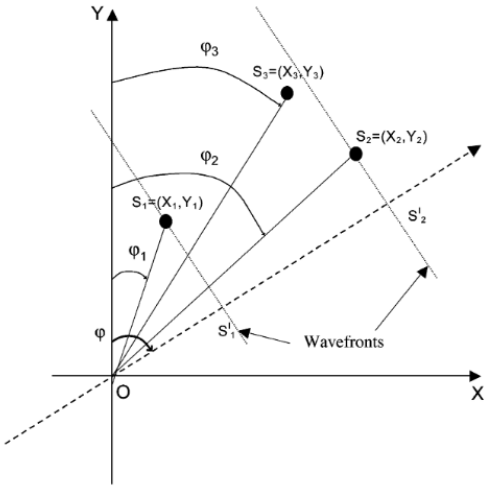

Fig. 1. Sketch of a tri-partite array. S_1, S_2 and S_3 are three elements, dashed line shows the direction of wave propagation, and φ_1, φ_2, φ_3 and φ are azimuths of the three elements and azimuth of event with respect to the origin of rectangular coordinates.

Figure 2-15: Diagram from Pignatelli et al. (2008) *showing the positions of the elements of a tripartite array. In the case of the array shown here, the wavefront velocity can be calculated based on the projections of the elements onto the wavefront ray.*

2.6. Frequency Analysis

Through time-series and time-lag analysis, basic information such as duration, period, azimuth (direction) and apparent velocity can be obtained. To determine more information about signals propagating across the array, wavelet transform analysis must be performed to extract frequency information. *Torrence* and *Compo* (1998) go through the theory of wavelet analysis in detail, and present the main wavelets used (this project uses the Morlet transform, which will be discussed in this section).

Basic information regarding the signals when in raw form are in the time domain, rather than the frequency domain. To convert from the time domain to the frequency domain, Fourier analysis is used (normally through the Fourier transform), which gives the frequency-amplitude information of the signal. Fourier analysis decomposes the signal into sinusoids of varying frequencies (phase demodulation), and determines what frequencies make up the signals. Fourier analysis decomposes the entire dataset rather than local variation, making the Fourier analysis approach a good approach when dealing

with constant (stationary) periodic signals, where the frequencies that contribute to the signals are easily obtained, but is not ideal for dealing with transient events, such as those within the atmosphere.

Cazelles et al. (2008) note another disadvantage of Fourier analysis is that is does not provide information about the time of the frequency, or in other words: although the Fourier analysis gives all the frequencies present, it does not specify when these frequencies occurred (no information can be obtained regarding the time of frequency occurrence). Wavelet analysis improves upon Fourier analysis as it provides the time dimension of frequencies during a given time-series, thus providing the local-frequency information. This analysis is also preferred for non-stationary and non-periodic waves (*Zhang et al.*, 2012), along with windowed Fourier analysis.

Windowed Fourier analysis allows for the local-frequency analysis to be obtained through windowing of a time-series instead of taking a global frequency analysis. The windowed Fourier analysis, shown in Figure 2-17(right), overcomes many of the limitations of normal Fourier analysis. However, it cannot achieve more comprehensive frequency resolution. Windowed Fourier analysis instead provides the same frequency resolution for both low and high frequency signals (*Cazelles et al.*, 2008). The frequency component of a given local signal, is of greater interest in this project and thus windowed Fourier analysis is not ideally suited for the purposes of the thesis. Wavelet analysis instead provides good time and frequency resolution for localised signals.

Wavelet analysis uses a "mother" wavelet to separate the signal into wavelet components, rather than sinusoidal components like sine and cosine signals. In this project the Morlet wavelet is used, which can be described as a plane wave modulated using a Gaussian (*Torrence* and *Compo*, 1998), which is shown in Figure 2-16, and can be described by the following wavelet function:

$$\Psi_0(\eta) = \pi^{-\frac{1}{4}} e^{i\omega_0\eta} e^{-\eta^2/2} \tag{2-14}$$

Equation (2-14) describes the Morlet transform, which depends on a "time" parameter (η) and has a non-dimensional frequency (ω_0) (*Torrence* and *Compo*, 1998). The mother wavelet chosen for analysis depends on the requirements of the analysis needs. Choices for the mother wavelet can depend on whether the analysis is needed for de-noising signals or whether a larger frequency resolution is required. In this project, a general approach to the analysis is taken, where the Morlet wavelet was chosen due to its general use and good frequency resolution. Its general shape is shown in Figure 2-16, where the time domain and frequency domain representations of the wavelet are shown.

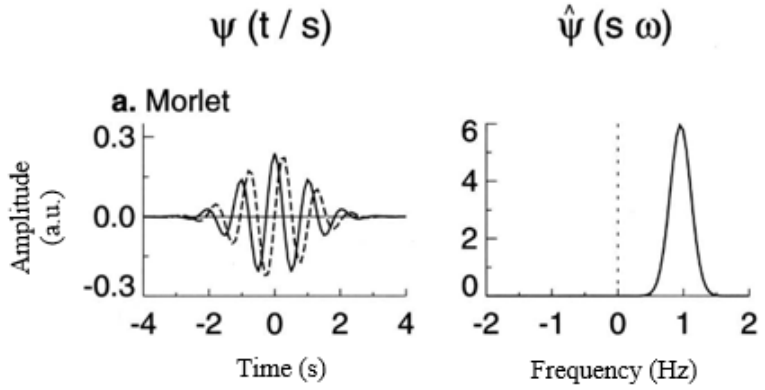

Figure 2-16: The Morlet transform as shown by Torrence and Compo (1998), where the left-hand side shows the real part of the Morlet wavelet (solid line) and the imaginary part (dotted) in the time domain. The right-hand side shows how the wavelet appears in the frequency domain.

The wavelet transform performs much the same as the windowed Fourier transform, except that it achieves the frequency resolution needed for this project. Figure 2-17 shows how the local frequency information is obtained using both wavelet transforms (left) and windowed Fourier analysis (right). Although the two types of phase demodulation appear similar, the wavelet transform method has a slight advantage with the frequency resolution. The left-hand side of the diagram shows that as the scaling of the wavelet decreases (top panel), the time resolution improves but the frequency resolution decreases. As a result, the wavelet is shifted towards higher frequencies. In the bottom panel of the left-hand diagram, the wavelet scaling increases, leading to a poorer time resolution but better frequency resolution, thus shifting the wavelet towards

lower frequencies. Other wavelets (not shown here), work in a similar manner, where a good trade-off occurs for time-frequency resolution. The study of aperiodic signals through wavelet analysis is made easier through this behaviour.

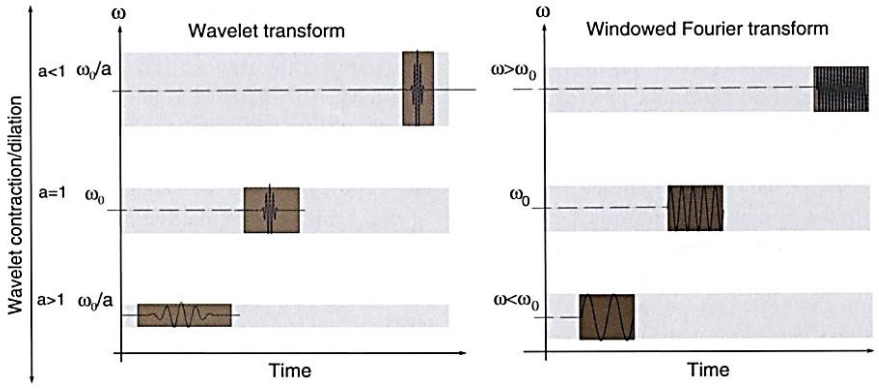

Figure 2-17: Examples of how both the wavelet transform and windowed Fourier analysis operates (Cazelles et al., 2008)

The three types of frequency analysis (Fourier analysis, windowed Fourier analysis, and wavelet analysis) are shown below in Figure 2-18.

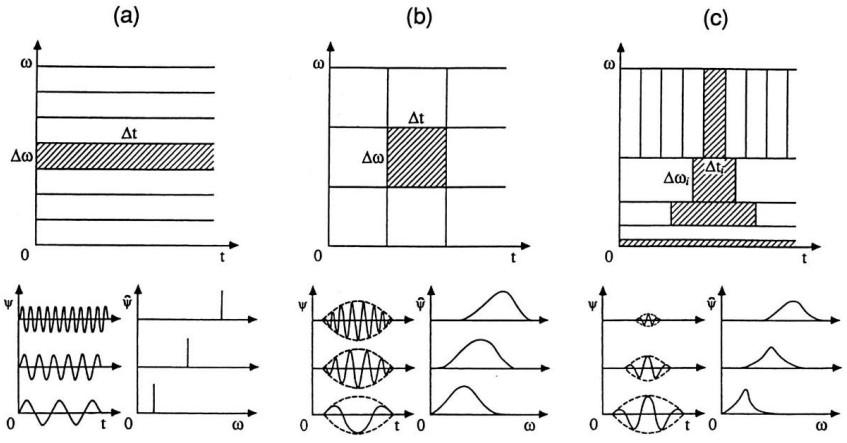

Figure 2-18: Time-frequency windows of (a) the Fourier analysis method, (b) the windowed Fourier transform, and (c) the wavelet transform (Lau and Weng, 1995). Each section shows the windows (top row), time-series and their representation in frequency and time space. The diagrams show that Fourier transforms, using sine and cosines as their base functions, give no time information, only frequency information; the windowed Fourier transforms give information based on a constant time and frequency window; the wavelet transform outputs information based on wavelets that stretch and translate and thus are variable in time and frequency.

Wavelet analysis will be used in both Chapters 4 and 5 to determine the frequencies of signals. Any further discussion of data analysis and specific methods needed to gain information will be included in the relevant sections in Chapters 4 and 5, including analysis based on other studies (such as *Le Dû et al.* (2020)) for microbarom analysis.

2.7. Cloud Detection

So far in the discussion of infrasonic wave detection, it was assumed that the night sky is clear, allowing the ground-based instrumentation to observe fluctuations in the OH* emissions at ~87 km altitude. However, this is rarely the case at the observing station, and observation of nocturnal emissions emanating from the hydroxyl layer cannot be achieved when clouds occur in the line-of-sight between the detector and the OH* layer. Thus, a cloud detector was also deployed at the Maynooth site to establish cloud conditions over the radiometric array. For data collected post-2017, a commercially available cloud detector (Aurora Eurotech Cloud Sensor III from Waddicor Associates (*Eurotech*, 2015)) identifies cloudy conditions (a photo of the detector is seen in Figure 2-19 (left)).

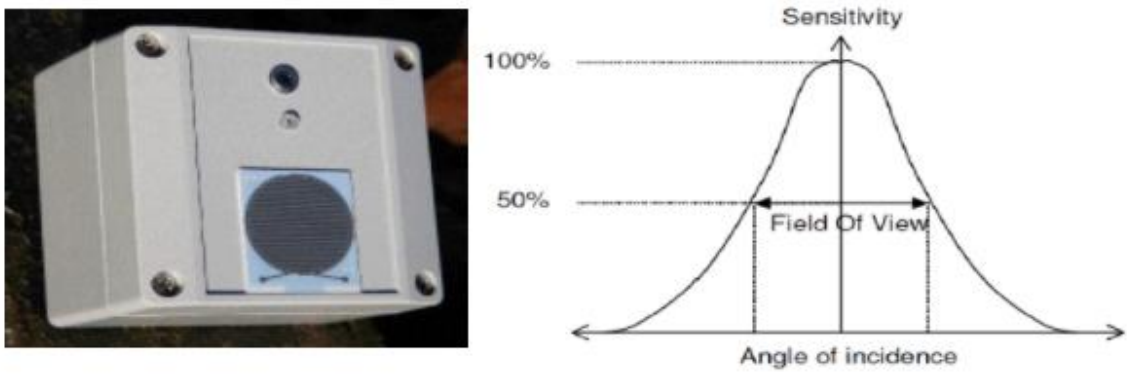

Figure 2-19: Photo of the cloud detector from Waddicor Industries (left). The field-of-view of the detector is shown on the right hand side of the figure. Sensitivity to cloud cover follows an almost normal distribution, with greatest sensitivity at zenith (Eurotech, *2015*)*, falling off to 50% at 45 degrees to zenith.*

This cloud sensor technology compares the air temperature surrounding the sensor to the sky temperature, where the difference between these temperatures results in a quantity known as "clarity". A colder sky temperature indicates a clearer sky, and results in a higher clarity value. A warmer sky temperature indicates the presence of clouds and results in a temperature closer to that of the air temperature around the sensor, leading to a low clarity value. This idea of clarity for a clear night is illustrated in Figure 2-20.

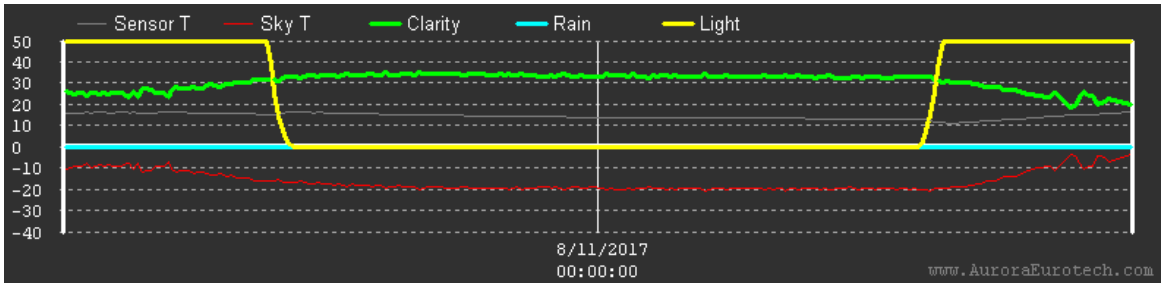

Figure 2-20: Output from the Aurora Eurotech cloud detector, with labels shown for the various variables. As noted within the text, clarity (shown in green) which indicates a lack of cloud cover, is determined by the difference in the sensor temperature to the sky temperature

Figure 2-20 shows a near-constant clarity of around 30 (arbitrary units) for the entire night of observation (7/8 November 2017) (night is indicated as areas where Light ≈ 0, as shown by the yellow line in Figure 2-20). This is deemed a high clarity value, indicating clear conditions over the station, and thus appropriate for hydroxyl emission observations. Clarity values of less than 23, are normally considered to be indicative of cloud (according to the manufacturer and experiments conducted onsite). Although the clarity value is important, the duration of a particular value also plays into clear night conditions. For the night shown in Figure 2-20, the clarity value is near constant and is preferable for analysis, compared to nights where only partial clarity occurs (which could introduce possible signals falsely attributed to hydroxyl emissions). Cloud detection is discussed further in Chapter 4.

2.8. Chapter 2 Summary

This chapter has covered the instruments used to gather information about the variation of hydroxyl emissions, including the requirements to detect infrasound (Section 2.2), as well as the hardware (Section 2.3) and software (Section 2.4) of the detectors. Basic characteristics regarding signals from the hydroxyl layer can be obtained using either a single instrument or the three instruments in tandem to achieve velocity information of disturbances (Section 2.5). In Chapters 4 and 5, the data gathered by the aforementioned instruments will be presented and analysed using these same techniques. Before this is shown, it is necessary to place voltage readings from these detectors in the context of other studies to verify the instruments are detecting similar signal levels. This process is considered in detail in Chapter 3 through calibration.

3. Calibration

3.1. Introduction

The previous chapter dealt with the instruments used in a tripartite array for the investigation of hydroxyl emissions in the mesopause region. To quantify the measurements taken as part of this thesis, calibration of the instruments is necessary (this is an approach seen in *Brändström et al.* (2012) and *Ogawa et al.* (2020), in order to create comparable scales for absolute measurements of the airglow). This allows for meaningful comparisons with other measurement campaigns as well as comparison to detailed dynamical models of the middle atmosphere (*e.g. Bellisario et al.* (2020)).

Radiometrically calibrated measurements can be used to estimate the number of emitting species within various bands, and it may be possible to reconcile the signal level received from OH* emissions with pressure changes due to infrasonic waves. A substantial effort was thus expended in the calibration of the MFR instrument, with three independent methods tested. These are (a) the use of a radiometrically-calibrated secondary standard for which a spectral irradiance output is available, (b) use of the known parameters of the instrument, such as the entrance aperture of the receiving telescope, the field-of-view subtended, the sensitivity of the detector in terms of wavelength and current output in terms of amperes per watt of input, and finally (c) taking an estimate of the known input radiance from the wavelength response of the detector together with published reports of the intensity of the bands which come within the wavelength sensitivity of the detector. Methods (b) and (c) seek to reinforce the values obtained through method (a).

It should be stated here that the use of a standard, like that of a calibration lamp, is not the only method that can be used to calibrate airglow instruments. For instance, the moon has been used as a radiance standard for earth-orbiting photometers (*Kieffer* and *Wildey*, 1996), while other authors such as *Oliva* and *Origlia* (1992) have used the brightest bands of the hydroxyl airglow for calibration purposes in astronomical studies.

There also exists the popular method of using standard stars to calibrate radiometers and cameras, a method used by *Moreels et al.* (2008). *Moreels et al.* (2008) investigate hydroxyl intensities and the variations of these intensities, whilst using standard stars to constantly calibrate the hydroxyl intensities they obtain with a CCD camera.

These stars act as very stable sources for calibration. In this thesis, standard stars were not used due to a lack of tracking capability on the part of the radiometers. Another issue that arises with the use of standard stars in the context of the hydroxyl layer is the fact that a stellar object is not an extended source, unlike the hydroxyl layer. *Muscari* (1975) makes this point by emphasising that during calibration of instruments such as radiometers, experiments should attempt to emulate realistic conditions as closely as possible. Thus, a point source being used in place of an extended source for calibration would have been undesirable. Instead, an Oriel calibration lamp and Lambertian screen were used to reproduce realistic observing conditions, creating the aforementioned extended source.

Absolute calibration of airglow instruments is notoriously difficult. The calibration source must be at a sufficient distance from the instrument to minimise errors due to multiple reflections (*Torr et al.*, 1976) and to ensure that the source is not within the hyper-focal distance of the instrument (*Muscari*, 1975). Such errors and limitations can cause uncertainties of nearly 20% in calibration experiments. As a result of this, accurate calibration is difficult to do, which is reflected in the measurements taken in this chapter. The three methods mentioned above carried out in this thesis, complement one another in determining the calibration factor. Quantification of the intensity fluctuations allows for an attempt at source identification and determination for disturbances in later sections. Analysis of any of these methods requires the use of a standard unit to compare to other studies, which in this case is the radiance unit known as the rayleigh.

3.1.1. The Rayleigh Unit

Accurately describing the emission intensity changes in the hydroxyl layer requires the quantification of the emissions using a pre-defined unit. The unit to describe these changes is the rayleigh, a radiance unit of measurement, used in calibration campaigns such as those of *Dandekar* and *Davis* (1973), to quantify the measurements taken by their instruments. *Chamberlain* (2016), *Hunten et al.* (1956) and *Baker* (1974) have all described the unit and its importance as a photometric unit in the context of airglow measurement. *Baker* and *Romick* (1976) demonstrate that the rayleigh can be defined and unambiguously applied both for column emission rate and for apparent radiance.

The unit is based on the geometry of the detector, and more specifically the field-of-view of the detector that measures the source of light. The rayleigh unit should only be used to describe extended light sources, normally having a diffuse nature (*Baker*, 1974), such as the airglow and aurora (*Chamberlain*, 2016) which emit radiation that can be captured by ground-based instrumentation. To measure the intensity variations of the airglow, and specifically the hydroxyl airglow in this case, the usual quantity used to determine such fluctuations is the surface brightness of the source (*Hunten et al.*, 1956; *Chamberlain*, 2016). These fluctuations are in the form of photon flux at the detector (in essence, how many photons are falling on the detector area per unit time). As *Hunten et al.* (1956) points out, in order to characterise how the photon rate fluctuates, the emission rate along a column of constant cross-section, between the source and detector must be known. This requires a knowledge of the solid angle of the detector, along the line-of-sight, to be known when determining the intensity fluctuations.

The solid angle of the detector has been described in Chapter 2 in relation to the hardware of the instrument. The solid angle represents the 3D angle which the detector aperture subtends, the concept of which is shown in Figure 3-1, where Ω_s represents the solid angle. In this thesis, the radiometer would take the place of the photometric receiver shown in the given figure. Based on Figure 3-1, the solid angle can be defined by the area of the detector divided by the distance to the source of light. *Chamberlain*

(2016) for instance use this definition to describe the solid angle, where the solid angle is expressed in terms of steradians (sr).

Using Figure 3-1 as a guide, the rayleigh unit can be expanded in definition using the geometry of the emission to radiometer set-up. As mentioned above and made clear in *Chamberlain* (2016), the quantity required to make sense of the radiance from the hydroxyl layer is the volume emission rate. This is related to the surface brightness of the layer by a factor of 4π, where the volume emission rate is $4\pi B$ measured in $\frac{\left(\frac{\text{photons}}{\text{cm}^3}\right)}{\text{s}}$ and B is the surface brightness of the layer. This value of $4\pi B$ represents the entire emission column along the line-of-sight of the detector, and is an integration along the line-of-sight.

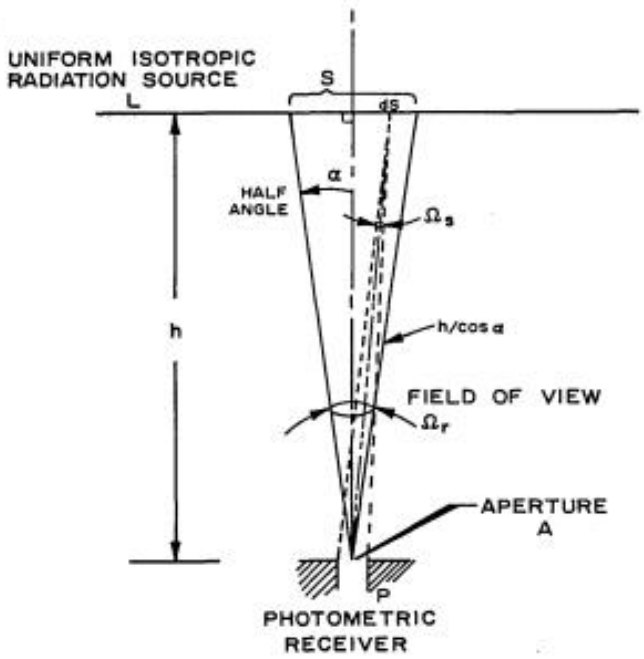

Figure 3-1: Setup showing the determination of the rayleigh unit, as given by Baker (1974), *where the object is an extended source of light.*

This value, known as the emission rate of the column, is given units of photon/cm^2 /(column/second), where column denotes the column along the line-of-sight. This is a cumbersome unit to describe the emission rate and thus *Hunten et al.* (1956) proposed the term rayleigh to describe the rate of emission from an emissive layer. *Chamberlain*

(2016) notes that the rayleigh unit gives the true emission rate of the layer and can be defined as follows, based on the $4\pi B$ value:

$$1 \text{ rayleigh} = \frac{10^6 \text{ photons}}{\text{cm}^2} \text{ /column /sec} \tag{3-1}$$

This can also be written as - 10^{10} photons/s/(m^2-column) (shown in Equation 3 of *Baker* and *Romick* (1976), where there is an added factor of 4π). This is true for the case of an isotropic surface, with no complications in terms of scattering or self-absorption of the layer (*Chamberlain*, 2016). This is the case for most of the OH* infrared bands observed here, with the exception of the OH$(9-6)$ and OH$(2-0)$ bands (*Bellisario et al.*, 2020). The definition of the rayleigh allows for an easy description of many radiative entities, such as the column emission rate, apparent surface brightness (radiance) and radiant flux density as shown by *Baker* and *Romick* (1976).

The hydroxyl airglow emission can be quantified in terms of rayleighs as seen in *Chamberlain* (2016), with the estimated total night emission of the layer calculated to be 4500 kR (or 4.5 MR) for a wavelength interval from 0.6 μm to 4.5 μm (Table 13 of *Leinert et al.* (1998)), representing the entire hydroxyl spectrum. The radiometers used in this thesis, however, only observe a portion of this spectrum. Thus, it is expected that the conversion factor that is calculated in this chapter will lead to a smaller value than 4.5 MR for the hydroxyl airglow at any time during the night. The rayleigh unit serves as one of the main units for quantifying the values obtained by the calibration of the radiometers.

It is not the only unit for quantifying the radiance measured by the detectors, where in later chapters, the radiance is quantified using photons/s/m^2/sr, a unit that describes the absolute integrated radiance. The conversion rate between this unit and megarayleighs is $1 \text{ MR} = \frac{10^{16}}{4\pi}$ photons/s/m^2/sr. The factor of 4π arises from the fact that a sphere is made up of 4π steradians (also the total solid angle for a point in space).

3.1.2. Methods used for Calibration

The main method of calibration is the use of an Oriel calibration lamp to directly quantify the relationship between input signal and voltage output from the radiometer. For calibration purposes, the MFR instrument was used as it was deemed to give the cleanest and least noisy signal (this is due to a lack of a tuning fork chopper in UWOSCR and FOV issues in MFR2). The two other instruments, MFR2 and UWOSCR are assumed to give near identical responses to MFR (in terms of radiance), based on their instrument characteristics, and are calibrated against it.

Two other calibration checks are completed, shown in Section 3.3 and Section 3.4, to ensure the calibration factor found in Section 3.2 is accurate. These checks include the use of instrument parameters (in Section 3.3) and determination through published data (in Section 3.4). A brief comparison to other studies and their calibration results/radiance results is shown in Section 3.5.

3.2. Calibration using a Known Light Source

One of the main features of the instruments used in this thesis is the ability they possess to measure the hydroxyl layer, set by the response curve of each instrument. The response curve covers a wavelength range $1.0 - 1.65\ \mu m$ (as shown in Figure 2-2 in Chapter 2).

The majority of the vibrationally excited hydroxyl emissions occur in this wavelength range between $1.0 - 3.0\ \mu$m. Figure 2-2 (in Chapter 2) gives a broad indication of the spectral response of the radiometer. In the case of the calibration, a source of known intensity and wavelength is needed to imitate the target of the radiometer, which take the form of an Oriel calibration lamp for this project.

3.2.1. Oriel Calibration Lamp

The calibration lamp used within this section is an Oriel calibration lamp, made of a 45 W tungsten filament lamp contained within a quartz envelope, filled with halogen gas (Model No: Oriel 63358). A schematic of the lamp is shown in Figure 3-2, along with the lamp mount.

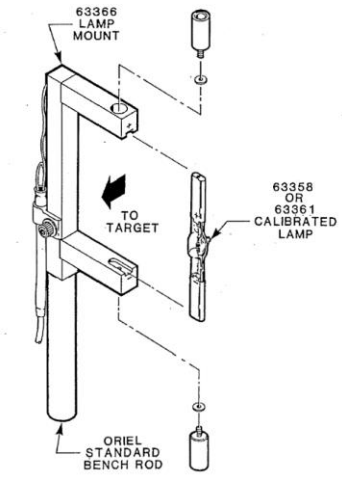

Figure 3-2: Schematic of the lamp mount and the calibrated lamp. This lamp is attached to an adjustable stand for calibration (*Oriel*, n.d.)

The spectral range of the lamp ranges from $250 - 2{,}500$ nm, peaking at around 1000 nm (or 1 μm) in wavelength (*Oriel*, n.d.), and following a curve like that shown later in Figure 3-4. The calibration curve for the Oriel lamp discussed here is based on a current of $6.5\,A$ through the filament when at a voltage of $\sim 7\,V$, corresponding to approximately 45 W. The calibration curve is specified at a distance of 50 cm from the centre of the lightbulb.

The current leading to these parameters is supplied by a high-specification power supply unit, shown in Figure 3-3. This lamp is required to provide a constant source of radiance for the radiometer to be calibrated against, which depends on the stability of the lamp's power output. To achieve stability of the lamp's output, an Oriel model 68830 power supply unit is used, which is a highly regulated power source providing a constant

current to the Oriel lamp (*Oriel*, 1991). This power supply is run at a low power to achieve the stability needed for the calibration procedure.

Figure 3-3: PSU used to provide the power to the Oriel calibration lamp.

The spectral irradiance of the lamp is shown below in Figure 3-4 (top), where it is compared with the spectral irradiance curve of a blackbody at $\sim 3000\,\mathrm{K}$. The purpose of Figure 3-4 (top) is simply to show that the Oriel lamp is similar to a black body at 3000 K, and although not identical, the figure shows the origin of the calibration curve which accompanies the calibration lamp. The theoretical spectral irradiance of the lamp with these specifications can be calculated using the intensity-power relation:

$$I = \frac{P}{4\pi r^2} \tag{3-2}$$

It is assumed that the bulb radiates into a sphere with a surface area $A = 4\pi r^2$, where r represents the radius. Based on the knowledge that $P = 45\,\mathrm{W}$ and the distance of interest is $50\,\mathrm{cm}$, then:

$$I = \frac{45}{4\pi(0.5)^2} = 14.33\,\frac{\mathrm{W}}{\mathrm{m}^2} = 1433\,\frac{\mu\mathrm{W}}{\mathrm{cm}^2} \tag{3-3}$$

The theoretical spectral irradiance of the source based on power and distance to the centre alone is thus $1433\,\frac{\mu\mathrm{W}}{\mathrm{cm}^2}$. A fraction of this value would be recorded by the detector, as the instrument is not responsive to the entire spectrum of the source (as it covers a range of $250 - 2{,}500\,\mathrm{nm}$).

The detector structure of the radiometer consists of an InGaAs photodiode, detailed in Chapter 2, and a silicon input filter placed in front of the diode, where this filter eliminates wavelengths less than $1\,\mu\text{m}$. The relative detector response, due to these two components, is shown by the red curve in Figure 3-4 (bottom panels). The green curve represents the portion of the Oriel lamp spectrum that would be captured by the radiometer. The purpose of Figure 3-4 (bottom panels) is to identify how much of the radiance from the Oriel lamp is detected by the radiometer. The green curve follows the red curve, shown clearly in Figure 3-4 (bottom right), until about $1250\,\text{nm}$, when it veers off the red curve and follows the Oriel lamp curve (blue). Based on the green curve and the area underneath it, shown as the hatched area in both Figure 3-4 (bottom right), the radiometer only captures a portion of the total lamp irradiance. The bottom panels of Figure 3-4 are for illustrative purposes only and the area where the curve between the radiometer response (red curve) and lamp emission curve (dashed black curve) intersect does not represent the actual photon flux detected by the radiometer.

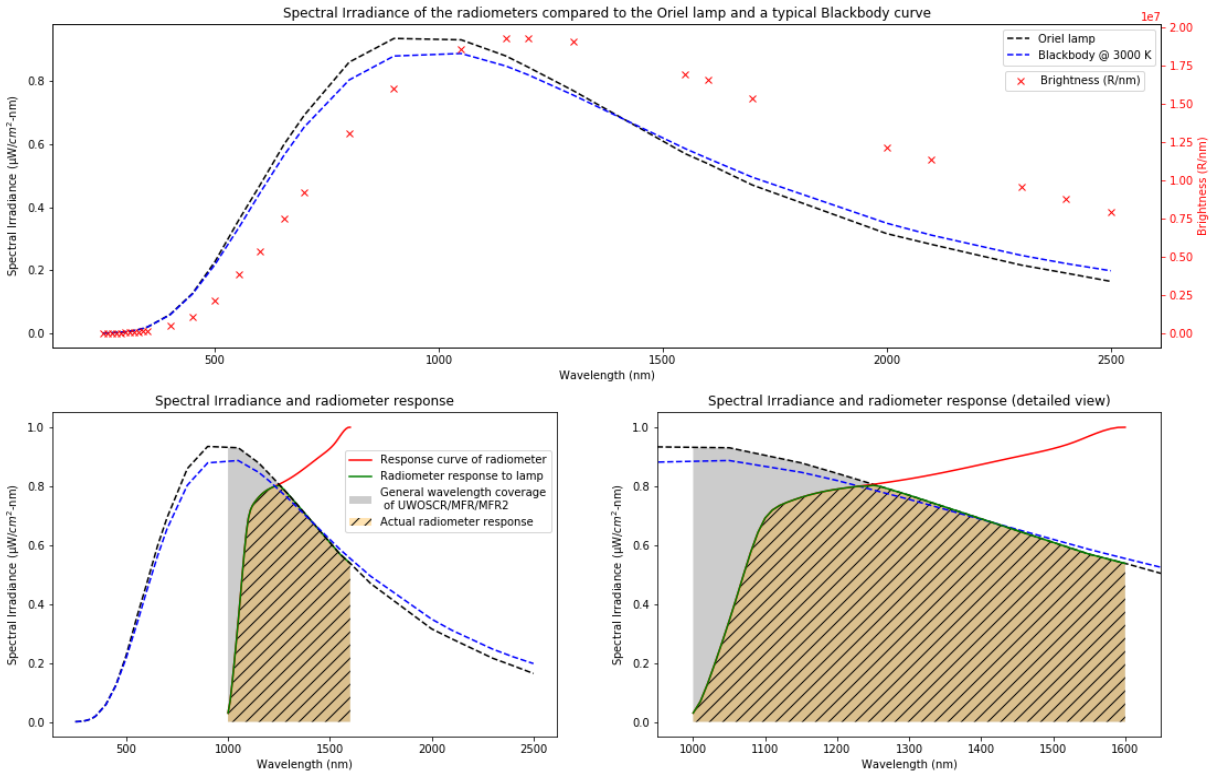

Figure 3-4: Intersection of the radiometric response and Oriel 63358 calibration lamp irradiance curve. The top plot shows the spectral irradiance of the lamp and a typical blackbody (black and blue curves respectively), while the red crosses indicate the brightness of the Oriel lamp.

The total irradiance intercepted from the lamp by the detector is calculated to be $381.44\,\frac{\mu W}{cm^2}$. This value represents the hatched area under the curve shown in Figure 3-4 (bottom panels). An estimate was made for the area under the curve, where the width of the curve is $\sim 600\,nm$ and the spectral irradiance is $\sim 0.6\,\frac{\mu W}{cm^2-nm}$, to get an approximate value for the total irradiance of:

$$(600\,nm)\left(0.6\,\frac{\mu W}{cm^2-nm}\right) = 360\,\frac{\mu W}{cm^2} \tag{3-4}$$

This approximate value for total irradiance intercepted from the lamp is in good agreement with the calculated value of $381.44\,\frac{\mu W}{cm^2}$ (through integration), and represents the intensity of the lamp received by the radiometer. To interpret this quantity more easily, it may be converted into units of rayleighs, which converts the spectral irradiance

total value into source spectral brightness. Based on the work completed by *Dandekar* and *Davis* (1973), *Baker* (1974) and *Viezee* (1960), the spectral brightness is calculated using the following formula:

$$B = (2.014 \times 10^4)(\lambda)(I)(L_R) \tag{3-5}$$

There are a number of factors that contribute to this conversion. The variable B represents the brightness in R, λ is the wavelength (in nm) calculated, while I represents the spectral irradiance in μW/(cm^2·nm·sr) and L_R is the reflectance of the Lambertian screen. The Lambertian screen is used to translate the point of the lamp into a uniform isotropic source (to emulate the hydroxyl layer). The units that each term is expressed in are as follows, where the conversion factor of 2.014×10^4 is dimensionless and L_R is a percentage:

$$[R] = [\text{nm}]\left[\frac{\mu\text{W}}{\text{cm}^2 \cdot \text{nm} \cdot \text{sr}}\right] \tag{3-6}$$

In Figure 3-4 (top) above, the brightness measured by the radiometer is shown by the red crosses, with the values represented by the secondary y-axis on the right-hand side in the same figure. The same method as above is used, where the area under the curve formed by the red-curve is calculated to obtain total brightness (again Figure 3-4 only illustrates this point). At a distance of 50 cm from the source bulb, the total brightness of the source registered by the detector was calculated to be 10.39×10^9 rayleighs [R] or 10.39×10^3 mega-rayleighs [MR].

In comparison to the estimate in Section 3.1.1 above, where the radiance of all hydroxyl emissions was quoted to be about 4.5 MR, a value of $\sim 10 \times 10^3$ MR would completely saturate the MFR detector. It is necessary to attenuate the intensity of the calibration source so that it is in the vicinity of the intensity of the actual source to be investigated (the hydroxyl nightglow). One of the most effective ways to attenuate the intensity is to increase the distance between the source and the detector, as the intensity falls off according to the well-known $1/r^2$ relationship.

3.2.2. Calibration Experiment using the Oriel lamp

Use of a source with known spectral characteristics is the first method that was carried out to calibrate the instrument (MFR). *Sigernes et al.* (2007) use this method for the calibration of their photometer located within their Svalbard laboratory. Figure 3-5 shows the set-up of the distance experiment, where the Oriel standard lamp was placed at such a distance so as to avoid saturation of the instrument (discussed above in Section 3.2.1). A Lambertian screen was placed in the path between the Oriel lamp and the aperture of MFR, as shown in Figure 3-5.

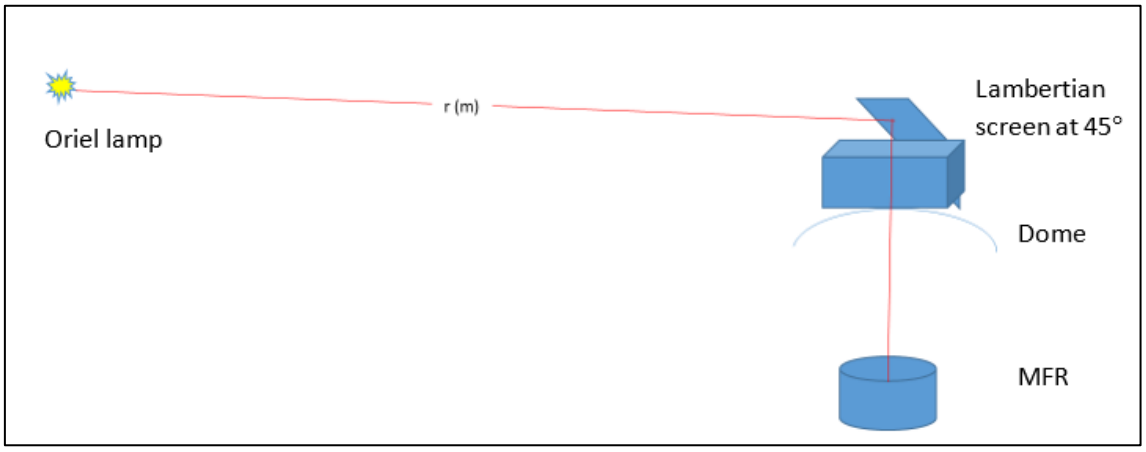

Figure 3-5: Schematic of the calibration set-up for this project.

The Lambertian screen acts as the 'source' of light for the radiometer as it uniformly fills the aperture with radiation propagating from the isotropic source of photons, which in this case is the Oriel calibration lamp (*Sigernes et al.*, 2007). The Lambertian screen acts as a proxy of the diffuse hydroxyl layer, by using the independent calibrated source. Of note within this experiment is the presence of the dome between the Lambertian screen and detector (the basis for the dome is to protect the instrument and associated devices from weather events). 100% transmission for incoming radiation was assumed through the dome, although this transmission figure may be more accurately given as ~90% (*Horgan*, 1992) due to the material of the dome.

This calibration arrangement was used three times to determine the relationship between the photon flux at the detector and the voltage output of the computer accompanying MFR. The calculations accompanying the experiment are detailed in the next section, where a conversion factor is derived.

3.2.3. Conversion

The conversion to rayleighs of the light input can be achieved through the use of the *Dandekar* and *Davis* (1973) equation or the equations provided by *Sigernes et al.* (2007) (this section uses the *Sigernes et al.* (2007) equation (Equation 15 in that paper)). The equation relies on the figure seen previously where 10.39×10^9 R (or 1.04×10^{10} R) are incident on the detector when the Oriel lamp is placed $50\ \text{cm}$ from the radiometer. The equation used for this experiment is:

$$B = 1.039 \times 10^{10}(\cos\phi)\left(\frac{r}{D}\right)^2 \tag{3-7}$$

The angle ϕ denotes the angle of the Lambertian with respect to both the MFR aperture and the light source, and is fixed at $45°$ (where the radiant intensity is proportional to the cosine of the angle normal to the Lambertian surface – Lambert's Cosine Law). The values of r and D represent the distance from the Lambertian screen to the calibration lamp (r) and the distance between the detector aperture and the calibration lamp (D). The difference between these values was determined to be $D - r = 0.84\ \text{m}$. This is a best estimate of the distance to the radiometer. As the roof laboratory was not large enough to make meaningful measurements, the lamp was moved outside the constraints of the laboratory. This presented issues as it was necessary to move the lamp to the roofs of nearby buildings to obtain useful measurements, and was made more difficult by finding a suitable place for the PSU (power supply unit) and the lamp source in relation to the radiometer. The experiments were all completed at night, to reduce the amount of background light as much as possible. The values represented by D (m) are the best

estimates of the distance between the lamp and radiometer. Absolute calibration is deemed to be difficult without such considerations and normally these procedures have $\pm 20\%$ uncertainty for the measurements. Below, Table 3-1 shows the series of measurements to determine the relationship between the calibration lamp and MFR voltage, as well as the associated Brightness calculation.

$r\ (m)$	$Error\ (m)$	$D\ (m)$	$\cos(\phi)$	$B\ (MR)$	$MFR\ (V)$
$34-35$	1.34	35.84	0.707107	1.43 ± 0.286	6.125
$30-31$	1.34	31.84	0.707107	1.81 ± 0.362	6.25
$26.5-27.5$	1.34	28.34	0.707107	2.28 ± 0.456	8.5

Table 3-1: Table of parameters of the experiment, with the response of the radiometer shown for each

The last two columns shown in Table 3-1 are graphed in Figure 3-6 below, which shows a reasonably proportional relationship between the two variables. It is clear that, with increasing brightness due to the calibration lamp (via the Lambertian screen), that larger voltage responses are induced in MFR. The graph in Figure 3-6 only contains 3 scatter plot points, giving a very large error to the subsequent calculations. However, distance experiments closer to the screen could not be performed as the lamp brightness would saturate the detector. On the other hand, the lamp could not be moved farther from the screen without obscuring the line-of-sight between the lamp and screen. These environmental concerns constrained the experiment to the values shown in Table 3-1.

The graph in Figure 3-6 still allows for the conversion factor between brightness and voltage to be determined. The slope of the best-fit line in the graph gives the direct relationship, and is calculated as 2.86 ± 1.26 V/MR or 0.29 ± 0.13 MR/V. On the basis that $1\ \text{MR} = 7.94 \times 10^{14}$ photon/m^2/s/sr, the calibration factor here of 2.86 ± 1.26 V/MR can also be expressed as a value of 2.27×10^{15} [photon/m^2/s/sr]/V.

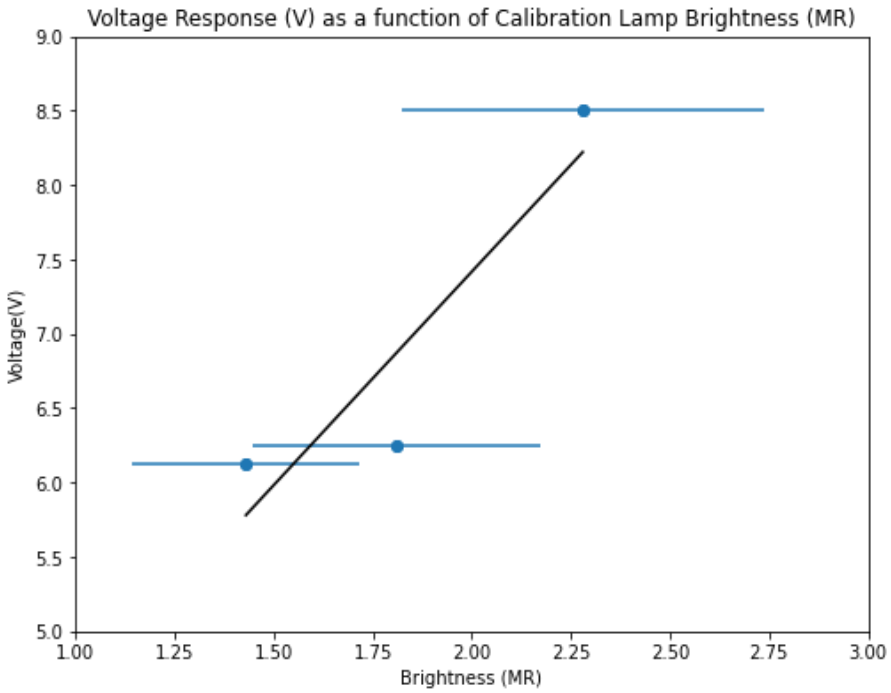

Figure 3-6: Scatter plot of the three experiments to calibrate the lamp (with error bars on the brightness measurements). The only change between the three experiments is the distance between the lamp and Lambertian screen.

3.3. Calibration using Instrument Parameters

To ensure that the calibration factor calculated in Section 3.2 is reasonable, a second method of calibrating the radiometer is performed, in order to determine the contributions of the instrument's components. If the initial photon flux at the detector is known, then a relationship between the voltage and photon flux should be determinable. *Sigernes et al.* (2007) notes this point by discussing the effects of mirrors, lenses and the sensitivity of the instrument on the signal, evolving from the initial photon flux at the detector. Further, *Sigernes et al.* (2007) notes that the process of converting the photon flux to a signal in the instrument can cause losses which may propagate to the output flux.

The majority of the components considered for their effects on the input photon flux and the resulting signal interpreted by MFR's computer are outlined in Figure 3-7 below.

Such parts have been introduced in discussions around instrumentation in Chapter 2. Each component affects the incoming signal to as to either reduce noise or amplify the signal (or perform both actions), which is reflected in the calculations in this section.

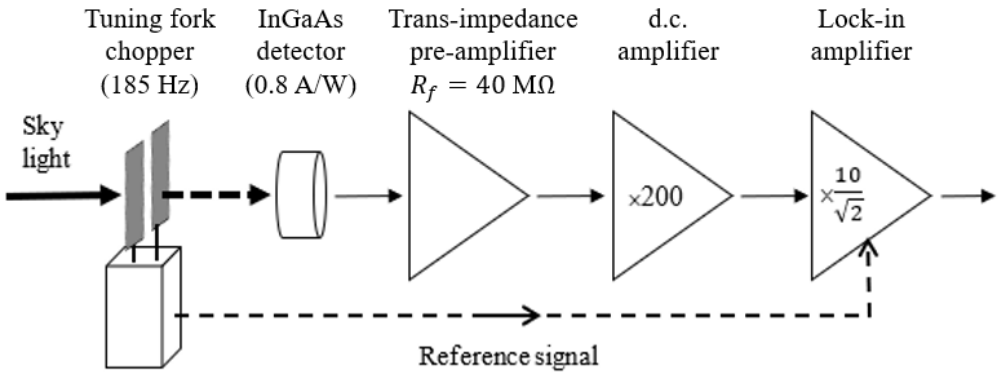

Figure 3-7: Instrument components that produce gains in the radiometer, and can be used to determine the voltage output based on a known detector input

It is assumed that the sky light referenced in Figure 3-7, or, in this case the emissions from the hydroxyl layer, are completely transmitted to the detector. Essentially, it would be assumed that the emissions as they propagate from the hydroxyl layer are not absorbed by the lower atmosphere (transmission through the dome above the instrument is also assumed as 100 %, as discussed in the previous section).

This light propagates into the instrument's aperture (via a correcting lens to correct for spherical aberrations), where the primary mirror reflects the radiation into the detector. The geometry of the optical chamber determines how many photons are received by the detector, affecting the final signal output. Geometry in the form of the *f*-number, area of the telescope, detector diameter, and the solid angle of the detector all contribute to the number of photons received by the InGaAs photodiode (discussed in Chapter 2). For calibration purposes, the *f*-number was taken as exactly $f\# = 0.4$, as specified for the primary mirror. Taking this value and the detector aperture width (12.7 cm) gives a value for the focal length of the telescope of 5.08 cm.

The main goal in the context of the optical chamber is to convert the radiance into units of energy, which allows for the successful conversion to voltage later. It is therefore necessary to convert the radiance values into the corresponding value in watts, which represents the radiance received by the InGaAs diode. Taking an example radiance value of $1\,\mathrm{MR}$, this value can be expressed in terms of photons, where $1\,MR = \frac{10^{16}}{4\pi}\,\mathrm{ph/m^2/s/sr}$ (ph refers to photons). Taking the geometry into account, this value can be reduced from $\mathrm{ph/m^2/s/sr}$ to $\mathrm{ph/s}$. First the area of the telescope is considered:

$$\frac{10^{16}}{4\pi}[\mathrm{ph/m^2/s/sr}] \cdot 0.0127[\mathrm{m^2}] = 1.01 \times 10^{13}\ [\mathrm{ph/s/sr}] \tag{3-8}$$

Once completed, the solid angle (Ω) of the telescope is taken into consideration, where the solid angle is dependent on the InGaAs detector diameter $(1\,\mathrm{mm})$, and the f-number (0.4), along with the area of the telescope:

$$\Omega = \frac{\pi\left(\frac{1 \times 10^{-3}}{2}\right)^2}{(0.4 \cdot 0.127)^2} = 3.04 \times 10^{-4}\ [sr] \tag{3-9}$$

The solid angle value is used to scale the value from Equation (3-8) to have a value expressed in units of ph/s.

$$1.01 \times 10^{13}[\mathrm{ph/s/sr}] \cdot 3.04 \times 10^{-4}\ [\mathrm{sr}] = 3.07 \times 10^{9}\ [\mathrm{ph/s}] \tag{3-10}$$

The equations are now expressed in such a way so that conversion to energy can be easily carried out. To make the conversion to watts, the value expressed in Equation (3-10) in terms of ph/s is first converted to joules/s and then to watts. The energy of one photon is given by the equation $E = \frac{hc}{\lambda}$, and assuming a value of $\lambda = 1.3\,\mu\mathrm{m}$ (centre wavelength of the response of the detector):

$$E = \frac{hc}{\lambda} = \frac{6.626 \times 10^{34} \cdot 2.998 \times 10^{8}}{1.3 \times 10^{-6}} = 1.53 \times 10^{19}\ \mathrm{J} \tag{3-11}$$

Thus:

$$3.07 \times 10^{9}\ [\text{ph/s}] \cdot 1.53 \times 10^{19}\ [\text{J}] = 4.69 \times 10^{-9}\ [\text{J/s}] \tag{3-12}$$

The result in Equation (3-12) above is expressed in terms of J/s - the definition of the watt. However, Equation (3-12) assumes that the detector takes one sample every second, but in fact, the InGaAs detector takes a sample every $0.22\ s$, as noted in Chapter 2. This time aspect is considered in Equation (3-13) below:

$$\frac{4.69 \times 10^{-9}\ [\text{J/s}]}{\left(\frac{1}{0.22}\right)[\text{Samples}]} = 1.03 \times 10^{-10}\ W \tag{3-13}$$

A radiance of 1 MR produces a miniscule amount of power from the InGaAs photodiode. This is perhaps best demonstrated by the current produced by the photodiode in response to this power (as the response of the photodiode is dependent on the detector sensitivity). The detector response curve has already been discussed and that response curve shows to which wavelengths the detector is sensitive. Another question posed by the detector is how strong of a response does the detector produce in relation to a certain amount of power?

This question is answered by the detector sensitivity (sometimes called the responsivity), which is expressed in units of A/W, and details the current produced by the detector in response to the power incident on the detector area. The detector sensitivity is a function of wavelength and thus the current produced depends on the energy of photons incident, as shown in Table 3-2 (based on values from the detector data-sheet (shown in Appendix B)):

Wavelength (μm)	**Sensitivity [Responsivity] (A/W)**
1.3	> 0.78
1.55	> 0.83

Table 3-2: Responsivity of the detector based on the wavelength incident

Due to the changing responsivity, the approach taken here was to use the average value across the response curve of the detector. Thus, an average responsivity of $0.8\ \mathrm{A/W}$ is used to determine the response of the detector. Evaluating a power of $1.03 \times 10^{-10}\ \mathrm{W}$ from Equation (3-13) based on this responsivity:

$$1.03 \times 10^{-10}\ [\mathrm{W}] \cdot 0.8\ [\mathrm{A/W}] = 8.26 \times 10^{-11}\ A \tag{3-14}$$

So, the expected current produced in response to $1\ \mathrm{MR}$ of light radiance is $8.26 \times 10^{-11}\ A$. This is a miniscule signal and thus must be amplified in order to properly analyse the signals arriving from the hydroxyl layer. Referring back to Figure 3-7, the parts that follow the InGaAs detector are amplifiers. There are three amplifiers present in the circuitry in the radiometer – the trans-impedance amplifier (TIA), the d.c. amplifier and the lock-in amplifier. Each amplifier contributes to the enlargement of the signal, where the lock-in amplifier attempts to reduce the noise of the larger signal as much as possible. This is important due to the very small signal present, as otherwise meaningful results would be difficult to analyse. These amplifiers have been discussed previously in Chapter 2.

The first amplifier, the TIA, is a current-to-voltage amplifier, where the amplification depends on a large feedback resistor, in an inverting configuration, with a value of $-R_f$ (where the value is 40 MΩ, for the TIA used). Using the result from Equation (3-14), and Ohm's law, the voltage produced through the TIA due to a radiance of 1 MR:

$$V = I(R_f) = 8.26 \times 10^{-11}(40) = 3.3\ \mathrm{mV} \tag{3-15}$$

This voltage value in Equation (3-15) represents the d.c. component of the voltage signal. This signal would then meet an amplifier with a gain of 200, resulting in a d.c voltage value of 0.661 V, until it meets a final amplifier – the lock-in amplifier (the LIA). The LIA reduces the overall noise of the signal, while also producing a gain of around $10/\sqrt{2}$, giving a final signal of around 4.67 V (d.c). This gives a conversion factor based on instrument parameters and the optical design of 4.67 V/MR (the error on this value is

much less than that of the Oriel lamp calibration value, and thus is not shown here). This process of obtaining the conversion factor, for various input radiances is shown below in Table 3-3.

			diameter (12.7 cm)	diameter			sensitivity			
			f# = 0.4	1 mm			0.8 A/W			
Input radiance	**Transmission of signal from OH* layer to instrument**	**1 MR = $10^{16}/4\pi$ photons/m^2/s/sr**	**Area of telescope (m^2)**	**C30641E-TC Detector solid angle (sr)**	**Energy of 1 photon at 1.3 µm in joules**	**Samples /s**	**C30641E-TC InGaAs(0.8 A/W)**	**Trans-impedance amplifier $R_f = 40$ x 10^6 Ω (volts d.c.)**	**Amplifier gain (x 200) output (volts d.c.)**	**Lock-in amplifier gain (x 10/√2)**
	100%	7.96E+14	1.27E-02	3.04E-04	1.53E-19	4.55	0.8	4.00E+07	200	10
								V = I R_f		
MR		**photons/m^2/s/sr**	**photons/s/sr**	**photons/s**	**joules/s (W)**	**W**	**A**	**V (d.c.)**	**V (d.c.)**	**V (d.c.)**
0.250	0.250	1.99E+14	2.52E+12	7.67E+08	1.17E-10	2.58E-11	2.06E-11	8.26E-04	0.165	1.17
0.500	0.500	3.98E+14	5.04E+12	1.53E+09	2.35E-10	5.16E-11	4.13E-11	1.65E-03	0.330	2.34
1.000	1.000	7.96E+14	1.01E+13	3.07E+09	4.69E-10	1.03E-10	8.26E-11	3.30E-03	0.661	4.67

Table 3-3: Conversion factor calculated for known values for input radiances, using known instrument parameters

3.4. Calibration using Published Data

The final method demonstrated in this thesis for the calibration of the instruments in Maynooth involves the use of published data. In particular, published data from *Harrison* and *Kendall* (1973), *Xu et al.* (2012) and other sources is used in combination with the response curve of the Maynooth radiometers to determine a conversion factor between radiance input and voltage output.

When attempting to determine the total radiance of the hydroxyl emissions, a number of studies have analysed the vibrational bands individually, like those of the studies noted above. These studies sum up the radiance contributions from each band, where this sum represents the total brightness. For instance, *Krassovsky et al.* (1962) report values for each of the OH* vibrational bands, with a total estimate of the OH* band from $\nu' = 1$ to $\nu' = 9$ of 0.5 MR, while *Khomich et al.* (2008) calculated a revised figure and found a total brightness of ~1 MR, across the entire vibrational hydroxyl spectrum.

Xu et al. (2012) have also published data with respect to the radiance emitted from the hydroxyl layer. In their study, they use SABER data from the TIMED satellite to determine the total brightness of the layer. Their results are presented in Figure 3-8,

where they compared results to the observed emissions from *Harrison* and *Kendall* (1973). *Harrison* and *Kendall* (1973) published hydroxyl airglow band intensities measured simultaneously for bands in the $\Delta v = 2, 3, 4$ and 5 sequences in the wavelength range 0.6 to 2.3 μm. The authors state that their measurements were made in particularly clear seeing conditions, and have been calibrated against a common secondary brightness standard. The intensities have also been corrected for atmospheric absorption and scattering.

Xu et al. (2012) obtain a value for total brightness close to 1 MR, for the entire spectrum considered. The individual band intensities, in units of rayleighs, are used from both the paper by *Xu et al.* (2012) and *Krassovsky et al.* (1962) to estimate the total intensity that would be received by the Maynooth radiometers. The individual band brightness values calculated by the two studies are shown in Figure 3-8, showing generally good agreement.

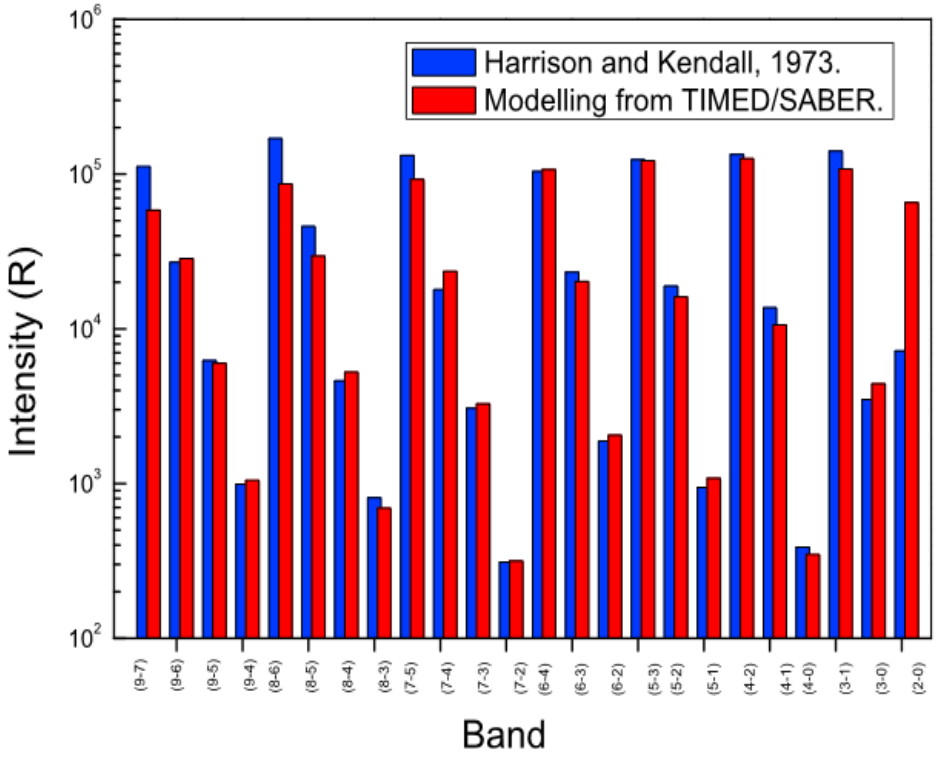

Figure 3-8: Intensities found through observation and modelling by Krassovsky et al.(1962) *and Xu et al.* (2012) *respectively, broken down by band* (*Xu et al.*, 2012)

Based on the radiometer response curve, not all of the band emissions referred to in *Xu et al.* (2012) and *Krassovsky et al.* (1962) are detected by the Maynooth radiometer, due to the wavelength response of the detector. Only emissions occurring under the response curve can be considered for their radiance contribution, where the response curve has been extensively dealt with in Chapter 2 and is shown in Figure 2-2. Using the published data within Table 3-4 below, and instrument sensitivity curve, the estimated radiance perceived in clear conditions by MFR (the instrument being calibrated) can be calculated.

OH-Band	***Xu et al (2012)* Intensity (R)**	***Krassovsky et al (1962)* Intensity (R)**	**Factor**	***MFR according to Xu et al (2012)* Intensity (R)**	***MFR according to Krassovsky (1962)* Intensity (R)**
(9-7)	57513.7	47000			
(9-6)	28300.7	16000	1	28300.7	16000
(9-5)	6066.4	3900			
(9-4)	1038.3	890			
(8-6)	87383.6	48000			
(8-5)	29380.0	14000	1	29380.0	14000
(8-4)	5205.7	3000			
(8-3)	687.2	460			
(7-5)	92300.3	63000			
(7-4)	23524.7	15000	1	23524.7	15000
(7-3)	3271.0	2500			
(7-2)	316.2	280			
(6-4)	108163.2	77000			
(6-3)	19840.5	14000	1	19840.5	14000
(6-2)	2055.3	1700			
(5-3)	122357.7	90000	0.5	122357.7	90000
(5-2)	16152.4	12000	1	16152.4	12000
(5-1)	1085.4	930			
(4-2)	126934	93000	1	126934	93000
(4-1)	10683.0	8000	1	10683.0	8000
(4-0)	347	300			
(3-1)	108850.4	92000	1	108850.4	92000
(3-0)	4427.3	3900			
(2-0)	65971.7	58000	1	65971.7	58000
				~ 0.5 MR	**~ 0.367 MR**

Table 3-4: Bands contributing to the radiance input to the detector based on values from (Xu et al., 2012) and (Krassovsky et al., 1962). If the Factor column is blank, this indicates the detector is not responsive to this band.

In Table 3-4, the *Factor* column refers to whether the radiometer can observe that particular OH* band emission. Table 3-4 indicates a value of 0 if the instrument is not sensitive to that band, while a value of 1 represents that the instrument is sensitive to that band. The value of 0.5 with respect to the $(5-3)$ band refers to the fact that the instrument observes approximately half the intensity of that band (seen in Figure 2-2).

Before a final estimate of the bands observed by the radiometer can be calculated, absorption due to atmospheric water vapour must be considered. According to *Bellisario et al.* (2020), some differences remain between the radiance seen at ground and that observed at $87\ \text{km}$ – the approximate altitude of the hydroxyl layer. Specifically, the two major effects are the depressed transmission of the hydroxyl $(9-6)$ and $(2-0)$ bands, shown in Figure 3-9, due mainly to the presence of water vapour within the atmosphere. As all experiments in this thesis are carried out at ground level, these two bands are not considered in the estimate of the total hydroxyl radiance perceived by MFR.

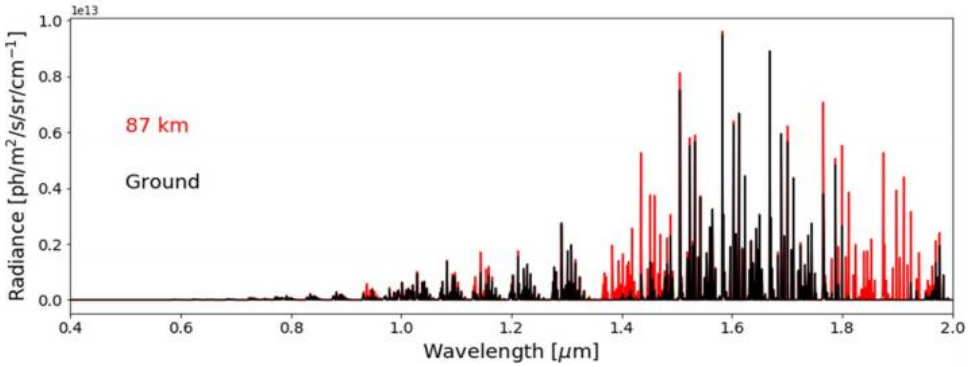

Figure 3-9: Graph showing the change in radiance observations when completed at ground and completed at around 87 km, according to Bellisario et al. (2020)*, where the effect of water vapour in the atmosphere is clearly seen around* $1.4\ \mu m$*. There is also an effect at around* $1.8-2.0\ \mu m$*, however this section is not covered by the radiometer response.*

It is estimated that the input to MFR would be in the range 0.3 – $0.4\ \text{MR}$ (taking absorption effects into consideration). The lower value is based on the data from *Krassovsky et al.* (1962), while the higher value is based on the data in *Harrison* and

Kendall (1973) and in *Xu et al.* (2012). *Maihara et al.* (1993) also find a higher value, in the range of 0.545 MR. Taking the average value, by assuming that the higher and lower estimates are the extremes, then a value of 0.35 ± 0.06 MR is obtained for a corresponding voltage of 2 V, assuming an uncertainty of 14 %. Estimates of the conversion factor, according to published data and the radiometer response, results in:

$$\text{Conversion} = \frac{2\ [\text{V}]}{0.35\ [\text{MR}]} = 5.71\ \text{V/MR} \tag{3-16}$$

3.5. Comparison to Other Studies

A summary of the calibration results is shown in Table 3-5 below. The table indicates the calibration factor resulting from each method discussed in the sections above, showing that all of the calibration factors are in reasonable agreement, bearing in mind the uncertainties in each method. This becomes clearer when the calibration factor is expressed in units of photons where $1\ MR = 7.94 \times 10^{14}$ ph/m^2/s/sr.

Method	Description	Calibration factor [V/MR]	Calibration factor [(photons/m^2/s/sr)/V]
1	Oriel Calibration Lamp	3.75 ± 1.65	2.12E+14
2	Known instrument parameters, Étendue + detector response	4.67	1.70E+14
3	Published data and wavelength response of detector	5.71 ± 1.7 V/MR	1.39E+14

Table 3-5: Summary of the calibration values calculated on the three methods shown

The values obtained in Table 3-5 can be compared to the figures of *Bellisario et al.* (2020). In that study, *Bellisario et al.* (2020) completed a ground campaign at OHP (L'Observatoire de Haute-Provence) in south-eastern France to determine the level of radiation emanating from the hydroxyl layer. Using a short-wave infrared camera with an InGaAs detector, demonstrating a very similar spectral bandwidth response range to that of Figure 2-2, the authors found the level of radiation at OHP to vary between $2 \times 10^{14} - 4 \times 10^{14}$ ph/m^2/s/sr over a single night. The authors compared this to

modelled radiances for the location, as shown in Figure 3-10, of around $1 \times 10^{14} - 2 \times 10^{14}$ ph/m^2/s/sr.

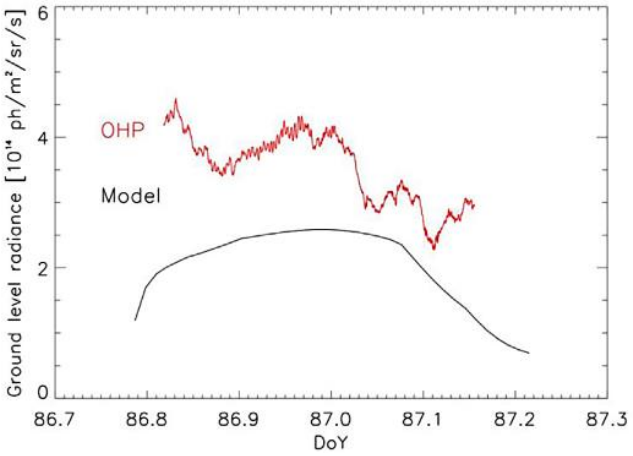

Figure 3-10: Radiances over OHP observed and modelled by Bellisario et al. (2020)

In another study, *Le Dû et al.* (2020), found similar values to the *Bellisario et al.* (2020) paper, in an experiment conducted at the same location (OHP). As shown in Figure 3-11, *Le Dû et al.* (2020) found that the radiance values fluctuated between $4 \times 10^{14} - 6 \times 10^{14}$ ph/m^2/s/sr for a night in December. These values, when compared with the conversion calculated here of $1\ \mathrm{MR} = 7.94 \times 10^{14}$ ph/m^2/s/sr, corresponds to radiances of $\sim 0.5 - 0.75$ MR. The values found by *Bellisario et al.* (2020) correspond to radiances between $0.25 - 0.5$ MR, based on the same conversion.

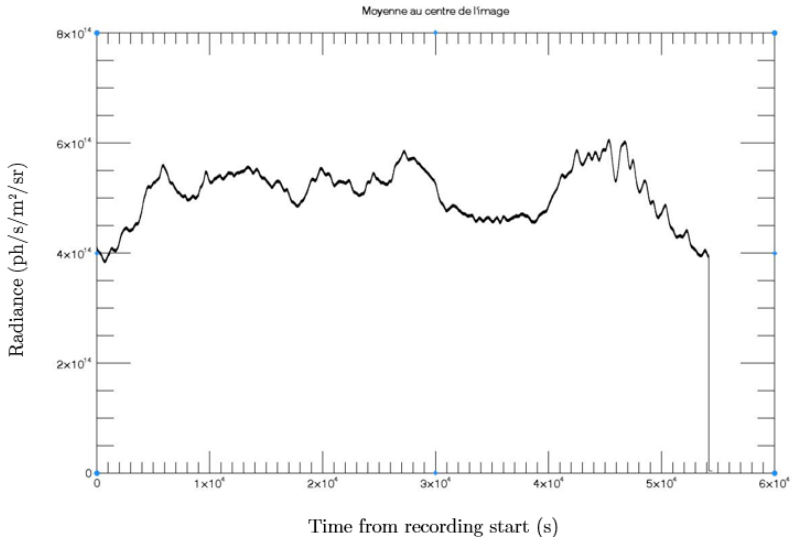

Figure 3-11: Time-series graph ("Average of the centre of the image" (translated)) showing the radiance levels seen by Le Dû et al. (2020) *(corrected values for the radiance values were provided by Simoneau* (2020, *private communication)).*

The values displayed in Table 3-5 are well within or close to these radiance ranges. Accounting for geometrical differences between the instrumentation employed in this campaign and that of *Bellisario et al.* (2020), the measurements are in good agreement for the general background radiation. The background radiance level recorded each night by MFR establishes a $1-2$ V response, which using Table 3-3 and Table 3-5 above, corresponds to a radiance of $0.25-0.5$ MR, which occurs close to the values reported by *Bellisario et al.* (2020). This confirms that the radiances found at Maynooth are equivalent to those at OHP, and are expected.

These levels of radiance only refer to the background level when no large disturbances perturb the hydroxyl layer to such an extent to decrease or increase the light measured. As *Bellisario et al.* (2020) note, the emission rate of the hydroxyl layer will change if strong gravity wave activity occurs, among other events. Chapters 4 and 5 show the radiance variation data obtained from the Maynooth radiometers, connecting the fluctuations to potential sources, where the results can be shown as a function of rayleighs rather than voltage (based on the calculations from this chapter).

3.6. Chapter 3 Summary

Chapter 3 has covered the calibration methods used to contextualise the voltage readings from all three instruments. The main calibration method involved the use of an Oriel calibration lamp in distance experiments to obtain the response of the MFR instrument to the lamp's radiance levels (Section 3.2). Method 2 calculated the expected output from the detector based on a known radiance input, which involves the use of detector components and the amplification of the signal (Section 3.3). The final method is based on using literature values to determine the expected radiance levels at the detectors (Section 3.4), and is then related to the general background voltage seen at the output.

Chapters 4 and 5 utilise the conversion factor of $1\,V = (2.12 \pm 0.93) \times 10^{14}$ ph/m2/s/sr calculated in this chapter (from the Oriel lamp experiment) to convert the time-series voltage values to radiance values. This value has been used as it was deemed the primary calibration method, while the other methods are used to ensure the calibration factor calculated is reasonable. The next two chapters show the radiance variation data obtained from the Maynooth radiometers, connecting the fluctuations to potential sources, where the results can be shown as a function of rayleighs rather than voltage (based on the calculations from this chapter).

4. Non-Hydroxyl Emission Signals

4.1. Introduction

The results in this chapter refer to radiance signals in the infrasound range that have been detected by the radiometer array, but which on subsequent evaluation have been found not to arise from hydroxyl emissions. In general, these signals are artefacts resulting from the effect of sunlight (at dusk and dawn), moonlight and noctilucent clouds.

Section 4.2 discusses the signals detected on a typical night from one of the radiometers in the 3-element array, and it establishes a baseline against which results from all nights may be compared. For the purposes of initial discussion, all nights can be categorised as either typical clear nights – discussed in Section 4.2.1, illustrating average radiance values and the effect of sunlight at dusk and dawn, or typical cloudy nights, considered in Section 4.2.2, which show the characteristic signature of clouds on the time-series. Section 4.3 describes the impact of moonlight's increase on the radiance levels above the background. Noctilucent clouds (at sub-visual levels) turned out to be the source of some large amplitude signals on otherwise clear moonless nights, and although not the primary focus of this research, the data has its own intrinsic value. Section 4.4 introduces the theory of noctilucent clouds, which are very high altitude clouds (~82 km, (*Kirkwood et al.*, 2008)) composed of ice crystals present within the mesosphere during summer months and observed regularly at mid-high latitudes ($50° - 65°$ in both hemispheres (*Dubietis et al.*, 2011)). Section 4.4 also lists the various ways these phenomena have been observed in the past while Section 4.5 discusses the potential of observing such structures over Maynooth with the radiometers.

4.2. Typical Night

A typical clear night is first considered, with the effects due to sunlight (at dusk and dawn) and other non-hydroxyl emissions discussed, which form a baseline from which hydroxyl emissions must be distinguished. Once the features of a clear night are shown, effects due to the presence of clouds (from weather systems as opposed to noctilucent clouds) are demonstrated, to distinguish the two types of nights in the dataset. Only data collected from clear nights are used for analysis.

4.2.1. Typical Clear Night Features

A typically clear night is defined as a night where no clouds persist over the observing station for at least half of a given night. Due to the geographical position of the station on the eastward edge of the North Atlantic Ocean and the temperate oceanic climate of Ireland, periods of overcast skies and rainfall are frequent, making clear nights that fall under the above definition hard to obtain (of the nights obtained, around $25-30$ % of nights are clear). In order to extract detail only from clear nights gained and to ensure noise from cloudy conditions does not interfere with clear night data, this project uses three techniques to distinguish cloudy conditions from clear conditions.

The first technique uses cloud data from the nearby army airbase located in Casement Aerodrome, Dublin (located approximately 13 kilometres south-east of Maynooth), where the data are stored by Ireland's national weather service, Met Éireann, and freely available online (at https://www.met.ie/climate/available-data/historical-data). Cloud conditions are measured on an hourly basis for all days of the year, where the measurements reflect the total sky coverage (measured in units of oktas - measurement range goes from 0 to 8 (*Stull*, 2015)). Table 4-1 shows the levels of cloud cover and how these conditions convert to oktas.

Based on Table 4-1, completely clear conditions in the Met Éireann data are indicated by 0 oktas. An okta level between 1 and 2 indicates very few clouds covering the sky, where a typical clear night in this project is between $0-3$ oktas in terms of total cloud cover and any value above 3 is considered to be a night unusable for analysis.

Sky Cover (oktas)	Sym-bol	Name	Abbr.	Sky Cover (tenths)
0	○	Sky **Clear**	SKC	0
1	◴	**Few*** Clouds	FEW*	1
2	◔			2 to 3
3	◑	**Scattered**	SCT	4
4	◑			5
5	◕	**Broken**	BKN	6
6	◕			7 to 8
7	●			9
8	●	**Overcast**	OVC	10
(9)	⊗	Sky **Obscured**	**	un-known
(/)	⊖	Not Measured		un-known

Table 4-1: Sky cover given in units of oktas (*Stull*, 2015)

The second method is the use of wavelet analysis/power spectrum to determine the cloud conditions (a method used prior to 2017 at the Maynooth University observing station). In times of cloudy conditions, two circumstances occur so that the hydroxyl layer is obscured and cannot be accurately observed. Although the hydroxyl emissions can still reach the detector, clouds along the line of sight (between the layer and detector) scatter the photons emanating from the layer. The instrument cannot distinguish between these photons and other photons that reflect or refract from the clouds, resulting in data unusable for analysis. More significantly, when cloud cover obscures the field-of-view of the detector, the clouds reflect street lights and other man-made light into the detector. The intensity of these reflected street lights far exceeds that of the light from nightglow emissions, normally resulting in large voltage values at the detector. These photons from reflected street lights allow for cloud cover analysis through a frequency spectrum, mainly as a result of pedestrian beacons on Maynooth campus that pulse at a fixed frequency of 0.78 Hz. During cloudy conditions, this fixed frequency occurs as a peak in

the power spectrum of the given time-series, shown in the red circle of Figure 4-1, where the 0.78 Hz signal is obvious in contrast to the rest of the power spectrum. The size of this 0.78 Hz peak depends on the cloudiness of the night in question, where on particularly overcast nights the 0.78 Hz peak appears larger.

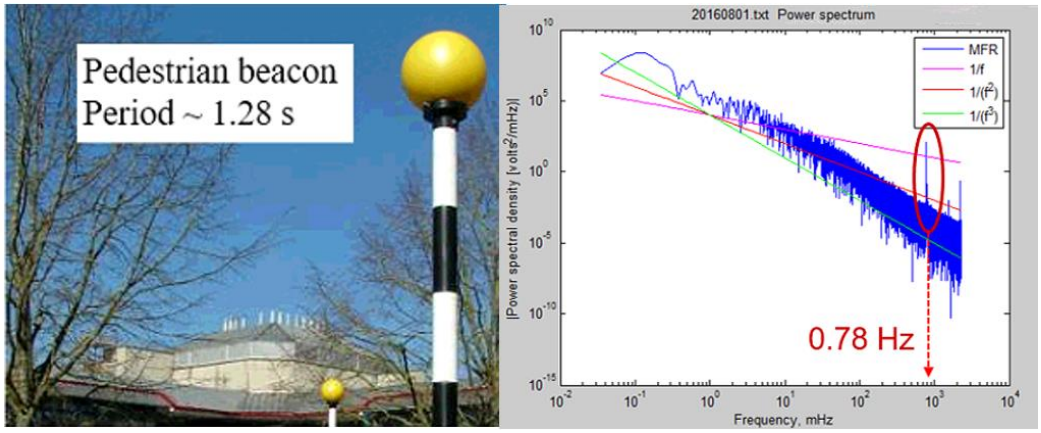

Figure 4-1: Beacon producing the fixed frequency. This beacon signal reflects off clouds during cloudy conditions and enters the detector. This leads to a stable and fixed frequency in the power spectrum (right).

The peak indicates the usability of the night, with desirable nights requiring the absence of the 0.78 Hz signal in the power spectrum (or the lack of the peak for the vast majority of the night). This technique cannot be used for nights after 2017 however, due to the replacement of the pedestrian beacon filaments, where in August 2017, the original beacons with a tungsten filament were replaced with beacons containing LEDs. The wavelength of the newer LED beacons is not within the sensitivity range of the detectors.

Due to this change of beacon filament, a new form of 'cloud detector' was required on site at Maynooth, an instrument discussed previously in Chapter 2 (the Aurora Cloud detector). The main function of the cloud detector is to compare the cloud detector temperature to that of the sky, calculating a "clarity" value which demonstrates the cloud conditions over the station (a high clarity value indicates clearer conditions). The methods noted in this section (either a single method or a combination of methods) are

all used to determine the clear/cloudy conditions on a given night. Based on these techniques, a typical clear night can now be discussed.

Figure 4-2 shows a typical clear, moonless night recorded by the MFR instrument on 10/11 August 2018 (each night is labelled with the date at the start of the night, i.e., 20180810.txt or 20180810.MAY depending on the instrument). This time-series shows a number of features, which are common to the clear nights acquired and analysed. Figure 4-2 is a manifestation of the final output of the LabVIEW software from MFR, which gives the time of the sample (averaged) and the voltage logged by the radiometer in response to hydroxyl infrared emissions. Each data point shown in the time-series is the average of 660 samples taken by the detector, giving the increased time resolution required to observe small-scale structures in the emissions (like that of acoustic waves).

The time-series shown in Figure 4-2 begins at the moment of sunset at Maynooth's latitude and ends at sunrise the following morning (given as a solar elevation angle of 0 degrees). These times follow the solar elevation angles at an altitude of 0 m above sea level, rather than the level of Maynooth, which has an approximate altitude of 60 m above sea level, but the effect on the solar elevation angle is considered negligible. A large amount of sunlight still illuminates the higher parts of the atmosphere after sunlight, explaining the effect shown by the large ($\sim$ 10.5 V) peaks seen at the beginning and end of the night in Figure 4-2 (obtained using LabVIEW software seen in Appendix C - Figure A3-5).

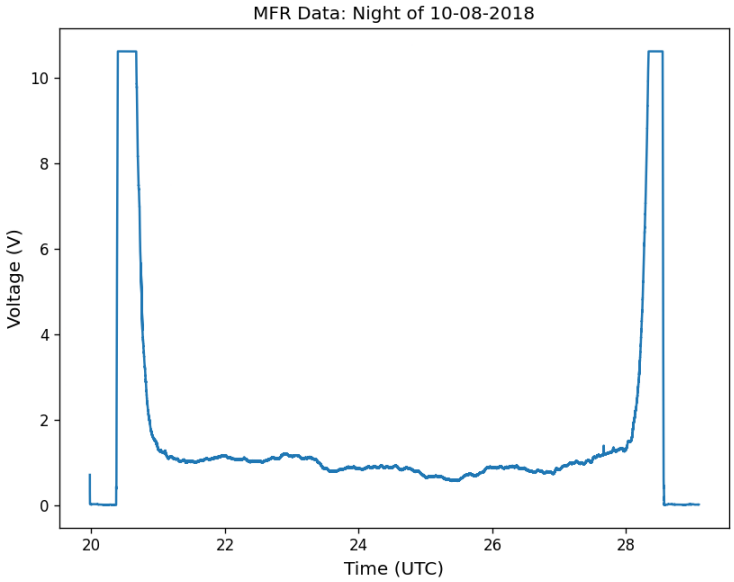

Figure 4-2: A typical clear night observed at Maynooth (midnight = 24 UTC, 2am = 26 UTC, etc.). This is the output of the MFR radiometer after acquisition and interpretation by LabVIEW and Python software

As the radiometer begins recording, a large amount of sunlight is detected due to the stray sunlight, and it would be expected that the detector would saturate and a reading like that above (10.5 V) would be recorded. However, as described in Chapter 2, the radiometer uses a lock-in amplifier and tuning fork chopper to reduce the noise on the incoming signal, which affects the final output. The lock-in amplifier works by detecting a modulated signal and comparing against a reference signal, where the parts of the signals that are correlated will be outputted with non-zero values. These signals will have some form of correlation if the input signal is modulated. However, in the case of high-intensity signals (sunlight) incident on the detector, the signal is unmodulated and essentially detected by the lock-in amplifier as random noise. Such an input signal would be uncorrelated to the reference signal and the output averages to zero volts.

Once the modulation of the chopper is detected in the input signal, the radiometers show a saturation voltage of around 10.5 V (seen in Figure 4-2), and the signal reduces as less scattered sunlight reaches the radiometer, giving way to infrared emissions from the atmosphere. However, the presence of scattered sunlight within the atmosphere is not

the only source of infrared radiation within the atmosphere during these times, as other processes also occur during dusk and dawn. Chemical processes occur in the middle atmosphere during this time, which produce emission bands from molecular oxygen in the upper atmosphere.

Although the radiometers are designed to observe the brightest OH* bands, focusing on a narrow wavelength range between $1.0\,\mu$m and $1.65\ \mu$m, they are also capable of observing other emissions in this wavelength range. Hannawald *et al.* (2016) discuss this point, where they note the contributions of the hydroxyl emissions and the $O_2(0-0)$ emission band to this wavelength range for their instruments. This O_2 emission band is centred at $1.27\ \mu$m (*Evans et al.*, 1970), and represents one of the brightest bands involving molecular oxygen in the infrared spectrum of the mesosphere (*Mulligan* and *Galligan*, 1995). After sunset, the emission of the $O_2(0-0)$ band decreases exponentially and thus contributes less to the intensities observed as the night evolves. The exponential decrease of this emission line can be seen in Figure 4-3 (as given by *Hannawald et al.* (2016)).

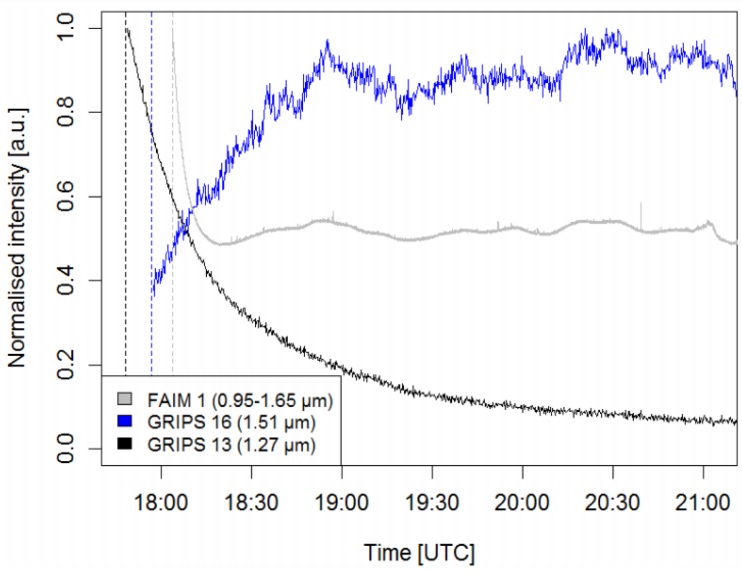

Figure 4-3: Intensity of the $O_2(0-0)$ (black line) and $OH(3-1)$ (blue) lines at twilight as seen by the GRIPS instruments (*Hannawald et al.*, 2016). *The grey line indicates the intensity as seen by the main instrument used in Hannawald et al.* (2016). *This instrument response overlaps strongly with the radiometers used in Maynooth.*

Figure 4-3 shows a grey line representing the data obtained by the fast airglow imager used by *Hannawald et al.* (2016), covering a wavelength range of $0.95 - 1.65\ \mu$m. The blue line traces the response of the GRIPS (**Gr**ound-Based **I**nfrared **P**-branch **S**pectrometer) instrument, focused around the wavelength of $1.51\ \mu$m, while the black line represents the GRIPS instrument focused around a wavelength of $1.27\ \mu$m (which primarily covers the $O_2\ (0-0)$ line). This intensity decays after sunset, whilst the blue line, primarily covering the $OH(3-1)$ branch, increases in intensity. This pattern of the $O_2(0-0)$ decaying occurs throughout the year, with a slower decay in winter and a faster decay in summer (*Mulligan* and *Galligan*, 1995).

This variation in decay rates affects the time-series by changing the contribution to the intensity variations, specifically whether the hydroxyl emissions or $O_2(0-0)$ are contributing more to the intensities. Based on the time-series from Hannawald *et al.* (2016), the contributions of the $O_2(0-0)$ emission are less than those of the OH* emission around the same time as the complete disappearance of the sun peak. This corresponds to the predictions of chemical models as noted by *Moreels et al.* (2008), where it is the sun's illumination that determines the amount of atomic oxygen in the atmosphere, mainly in the mesosphere. During the day, water vapour in the atmosphere dissociates as the Sun illuminates the molecules, creating atomic oxygen, but this process ceases once sunlight fades from the upper atmosphere.

Once the $O_2(0-0)$ emission, as first shown in Figure 4-2 (start of the night), ends (about 1 hour after sunset (*Mulligan* and *Galligan*, 1995) and levels off to a more constant radiance level, hydroxyl emissions are assumed to be the dominant intensity contributor (based on the time-series data shown in *Hannawald et al.* (2016)). The hydroxyl emission intensity is normally highest at the beginning of the night and slowly decreases through the night (*Moreels et al.*, 2008), leading to a decreasing radiance trend as the night evolves. Although not immediately obvious from Figure 4-2, the trend described by *Moreels et al.* (2008) is apparent during this same time-series. Figure 4-4, which shows a linear trend-line plotted to fit the time-series from Figure 4-2 (here, the

scattered sunlight peaks have been removed (from the beginning and end of the night) to show the decreasing linear trend-line) makes this point clearer.

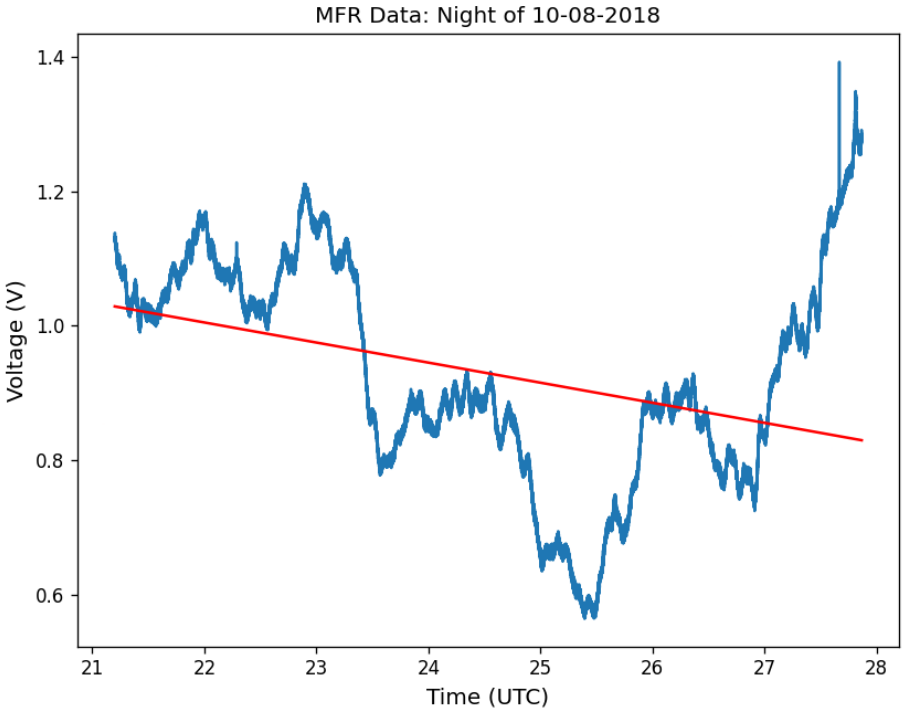

Figure 4-4: Decreasing trend of hydroxyl intensities seen on a typically clear night. The red line shows the linear trendline.

This trend holds true for the vast majority of the night in Figure 4-4, until around $27{:}00$ UTC $(03{:}00)$ when scattered sunlight begins to again illuminate the upper atmosphere with the approaching dawn. This increasing trend is as a result of increased photo-dissociation of ozone in the day-lit higher atmosphere, resulting in the mirror image of the peak due to sunset, but now due to sunrise. This known ozone increase is shown below in Figure 4-5, which demonstrates balloon radiance measurements at a mid-latitude station as described by *Lowe* and *Lytle* (1973). As a result, the increase towards the end of the night seen in Figure 4-2 is due to increased photodissociation leading to a greater contribution to the $O_2(0-0)$ emission as well as increased radiances associated with scattered sunlight. This trend is seen in most clear nights, except for nights where moonlight affects the radiance level observed by the detectors.

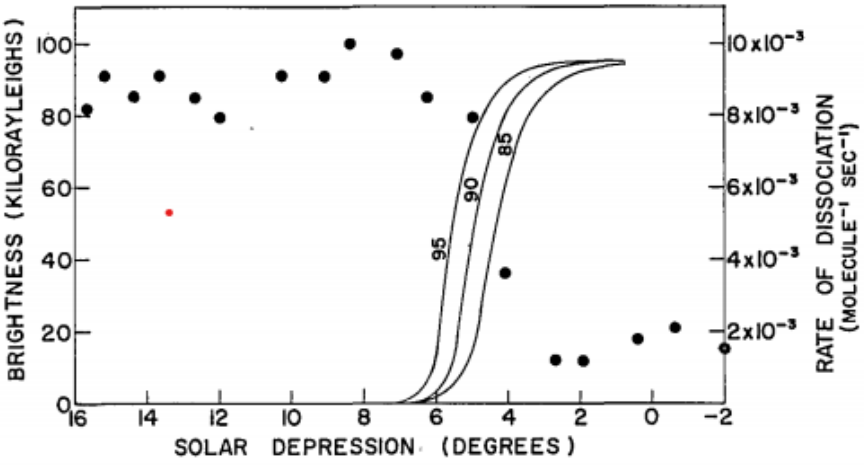

Figure 4-5: Increasing dissociation of ozone as dawn sunlight strikes the upper atmosphere. Values of 95, 90 and 85 indicate the photo-dissociation rate at these altitudes. These measurements were taken via balloon (altitude – 30 km) around a latitude of 46 degrees north (*Lowe* and *Lytle*, 1973).

The next section of the time-series to be discussed is that of the main section of the night, away from the scattered sunlight and the $O_2(0-0)$ emissions, which contains the radiance signals most likely due to hydroxyl emissions. As outlined at the beginning of this section, a typical clear night establishes a baseline with which other results can be compared in terms of amplitude and other characteristics. Before the main section is discussed however, the average radiance of a typical night is calculated (through analysis from Chapter 3), with the average radiance calculated on a monthly basis also found.

4.2.1.1. Typical Night based on calibration factor

As noted by *Schmidt et al.* (2013), the two main ways of studying atmospheric features in airglow are either by taking rotational temperatures or brightness variations. In this project, only variations in brightness are considered, a path also taken by authors such as *Le Dû et al.* (2020). In order for the values shown here to be comparable to other campaigns, calibration of the instruments was necessary.

This process of calibration was discussed in detail in Chapter 3. It is noted here that the other two instruments are normalised and scaled and so the calibration is used directly or indirectly for all instrument measurements. In Chapter 3, three different values for the calibration factor were calculated, but the calibration factor calculated from the Oriel calibration lamp distance experiments is used here:

$$1\,V = (2.12 \pm 0.93) \times 10^{14}\ \mathrm{ph/s/m^2/sr} \tag{4-1}$$

The time-series derived from the night of the 5 June 2018 is shown in Figure 4-6 demonstrating these calibrated variation measurements. The y-axis can reach values of about 1.45×10^{15} ph/s/m^2/sr, representing periods of saturation of the detector. The main part of the night, where the detector is least affected by sunlight and O_2 band excitations, shows a variation in radiance between $2 \times 10^{14} - 3.5 \times 10^{14}$ ph/s/m^2/sr.

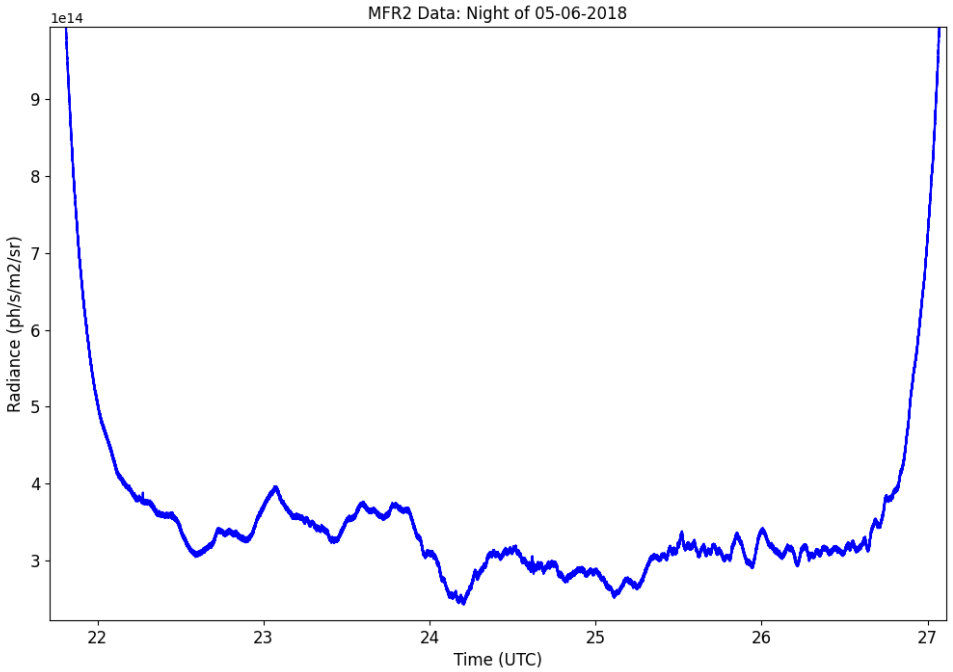

Figure 4-6: Night of the 5/6 June 2018 showing the new radiance values

This example night provides a benchmark for the normal radiance range at Maynooth. The average radiance for each month can be easily obtained through time-series analysis and is shown in Figure 4-7 below, with each month showing the average radiance from

2018 to present. Taking the calibration of the instruments into consideration from Chapter 3, the y-axis is given in kilorayleighs. If the Oriel calibration lamp calibration lamp values are considered here, it was found that $1\ \mathrm{V} = (2.12 \pm 0.93) \times 10^{14}$ photons/s/m^2/sr, while $1\,\mathrm{MR} = 7.96 \times 10^{14}$ photons/s/m^2/sr. This conversion shows a value of around $1\,\mathrm{V} = 0.266 \pm 0.117$ MR, giving the scaling for Figure 4-7 below. It appears from this plot that the average radiance is greatest during winter months ($300 - 350$ kR), while there is a smaller average radiance in summer months ($200 - 250$ kR). Based on the work by *Xu et al.* (2012), the average radiance at Maynooth (omitting the bands obscured by water absorption) should amount to $0.3 - 0.4$ MR ($300 - 400$ kR) approximately. Figure 4-7 shows a small deviation in the radiance trend for summer (although with a large amount of uncertainty ($\pm 44\%$) in some months), which has also been a feature in the work by *Espy* and *Stegman* (2002).

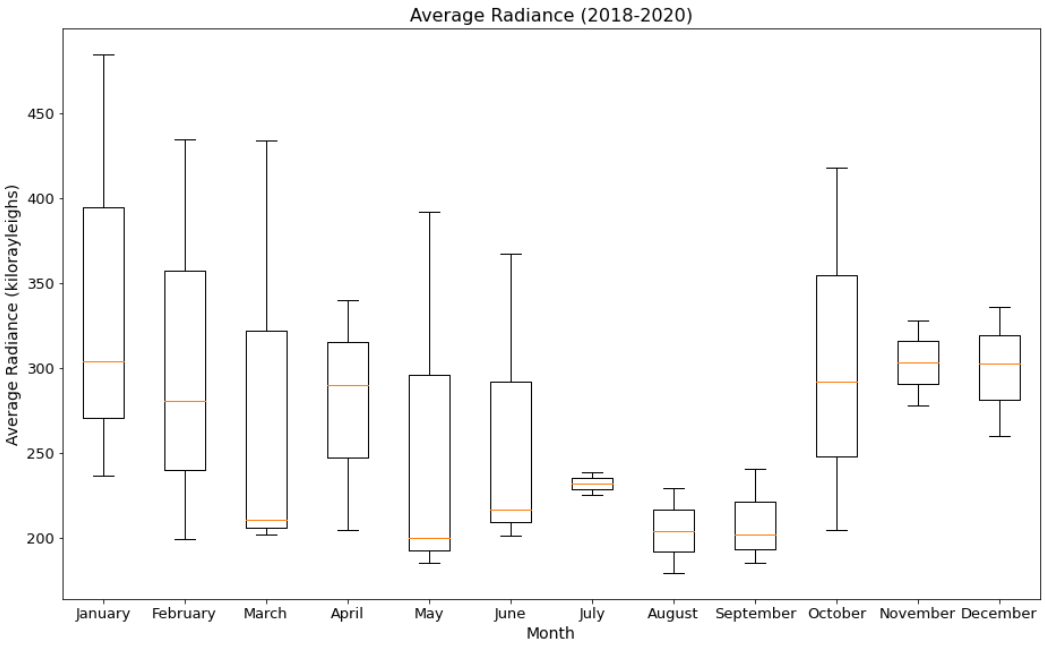

Figure 4-7: Average radiances in Maynooth as observed by MFR between the years 2018 – 2020 (covering the time frame of this thesis after calibration). The general trend is a larger average radiance in winter, with a smaller average radiance in summer.

Espy and *Stegman* (2002) in their work on OH* radiance variability above Stockholm found similar radiance enhancements during winter, with a small enhancement in summer. This trend is seen in Figure 4-8, which shows the results of *Espy* and *Stegman*

(2002), where the radiances peak at the beginning and end of the x-axis (representing winter months). The location and type of measurements taken are however different to Maynooth, as *Espy* and *Stegman* (2002) only observe at Stockholm (a high latitude), and the radiance enhancements only represent the $OH(3-1)$ radiance values. A large amount of uncertainty ($\pm 44\%$) goes with the average radiance calculated using the conversion due to the experiments performed with the Oriel calibration lamp. However, as shown by *Espy* and *Stegman* (2002), this amount of uncertainty associated with radiances from the hydroxyl layer appears to be common (the authors of the study find errors of up to $\pm 30\%$ on the average radiance ($OH(3-1)$) over 7 years in Sweden).

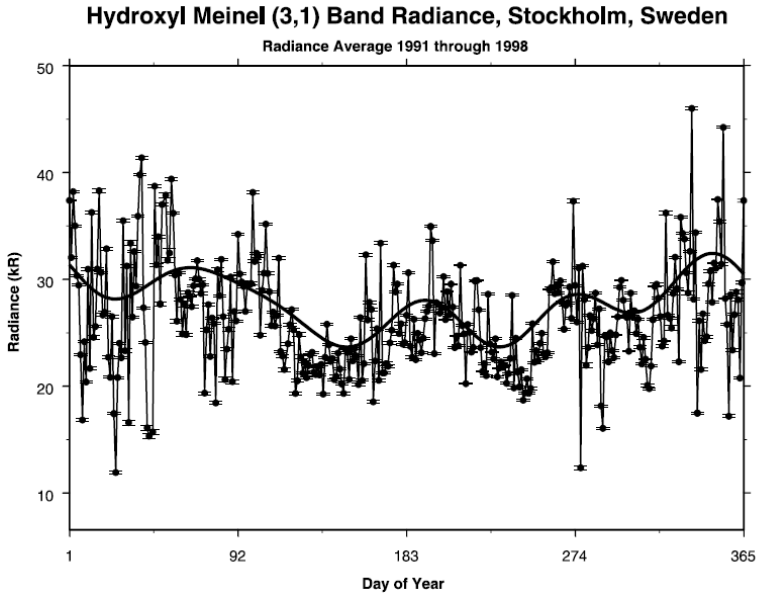

Figure 4-8: Radiance measurements by Espy and *Stegman* (2002) *showing the seasonal variation of the OH*$(3-1)$ *band over Stockholm, Sweden*

Another study that looks at how hydroxyl changes over time is that of *Sonnemann et al.* (2015). *Sonnemann et al.* (2015) have investigated the seasonal variation of the OH* species number density at various latitudes, which are shown in Figure 4-9. For a mid-latitude of 51.25 °N, shown in Figure 4-9(b), *Sonnemann et al.* (2015) show that OH* densities are generally larger in winter compared to both spring and summer. Based on the assumption that a larger number density would lead to higher radiance values (due to the abundance of the species), the higher density of OH* in the winter hemisphere

from Figure 4-9(b) would appear to explain the higher radiances seen during the season (the authors in their paper connect increased OH* density to nightglow brightness (it should be noted here that an anti-correlation exists between atmospheric density and hydroxyl radiance according to *Faivre et al.* (2003)). This trend, found in the Maynooth and *Sonnemann et al.* (2015) data, has persisted since the 1960's according to the data from Figure 4-9(b). However, the OH* variation trends at other latitudes are more complicated compared to mid-latitudes, and have been subject to change as seen in Figure 4-9 below.

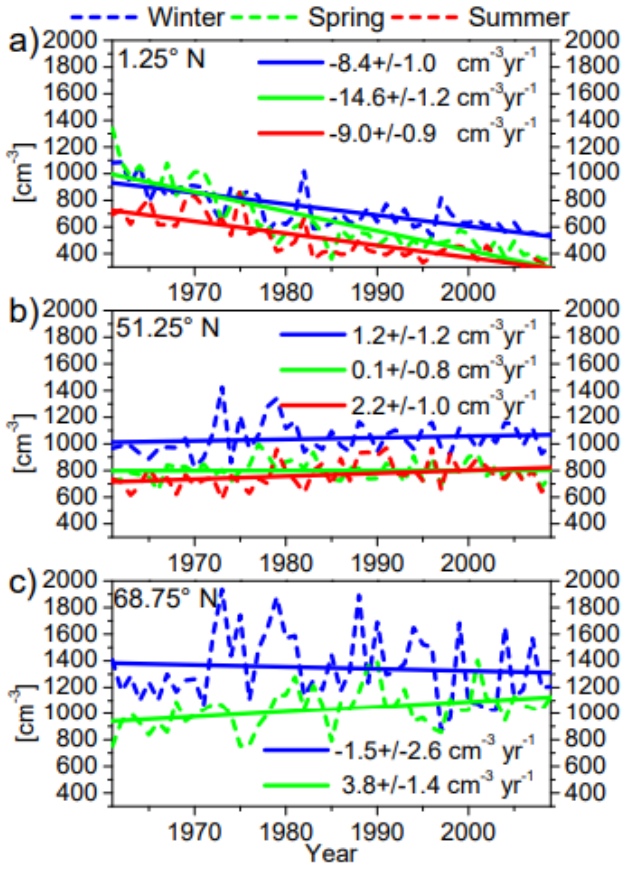

Figure 4-9: Hydroxyl number density as found by Sonnemann et al. (2015)*, showing the variation of the number density as a function of latitude and season from 1960 – 2010. From plot (b) (showing the number density variation at a mid-latitude location), it is seen that winter number densities of hydroxyl molecules are consistently higher than summer number densities.*

Average and individual radiance measurements at Maynooth are reasonable and within the expectations based on the work from *Le Dû et al.* (2020), *Bellisario et al.* (2020) and

Sonnemann et al. (2015) (the latter study was with regard to the seasonal change). These average radiances are only representative of clear nights rather than cloudy, which are discussed next.

4.2.2. Typical Cloudy Night Features

The only night dealt with so far is the that of a typical clear night. However, the typical night over Maynooth is far more likely to be cloudy than clear, an example of which is shown below in Figure 4-10. Parts of this example night show cloudy conditions while others show more clear conditions, where cloudy conditions over the station are indicated by regions of erratic radiance variations. These erratic variations are most likely due to streetlamps scattering from the cloud base (normally non-uniform). Figure 4-10 also shows clear periods, which are smoother in comparison and conform more to the general radiance patterns discussed above in Section 4.2.1.

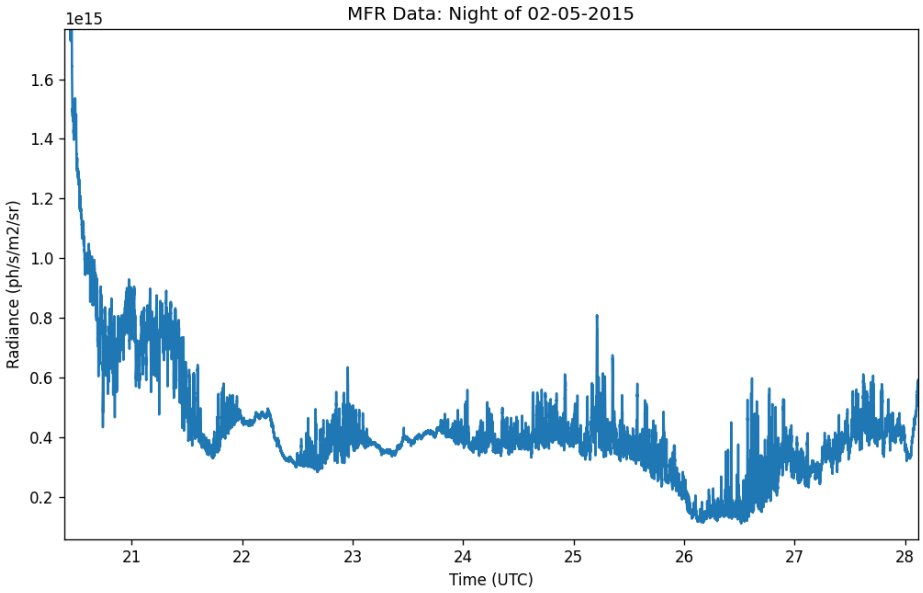

Figure 4-10: A typical cloudy night as seen by MFR from 2/3 May 2015 (the sharp drops in the baseline are due to an error introduced from the lock-in amplifier at the time of measurement).

Although Figure 4-10 shows obvious signs of cloudiness, these signatures cannot be used in isolation to confirm the weather conditions of the night. A power spectrum is taken of the night, a method discussed in Section 4.2.1, regarding cloud analysis and is given in Figure 4-11. Prior to 2017, when the pedestrian beacon was onsite and the filament spectrum overlapped with the detector response curve (the case here), the 0.78 Hz signal is obvious in both the power spectrum of the night and dominant frequency analysis. This 0.78 Hz signal (along with harmonics of this constant signal) is seen clearly in Figure 4-11, indicating cloud over the station. For the night depicted here, a harmonic of 2.3 Hz is shown, a feature common to many cloudy nights, but other harmonics on the order of 1.5 Hz are not uncommon and are seen regularly on cloudy nights.

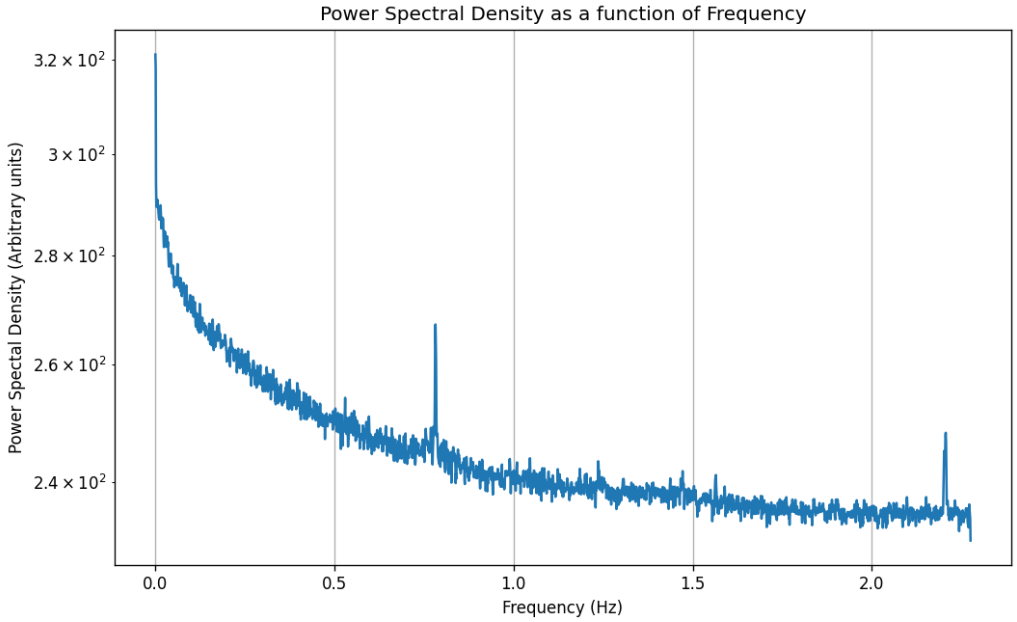

Figure 4-11: Power spectrum of Figure 4-10 above, showing a strong peak at 0.78 Hz and a second peak at ~2.3 Hz (this smaller harmonic is known as aliasing)

After 2017, when the beacon frequency is absent from any frequency analysis, the cloud detector onsite is instead relied upon to indicate cloudy conditions. The cloud detector provides localised cloud conditions at Maynooth, providing good spatial resolution of cloudy conditions compared to the beacon method. The 0.78 Hz peak cannot be relied upon in these later measurements and instead clarity measurements are used which are

provided by the cloud detector. As stated in Chapter 2 (Section 2.7), clarity defines the extent of clear conditions above the station, and is given in arbitrary units. Clarity must be above a constant value of ~23 for a night to be deemed clear of clouds above the station, while nights with values below this value are deemed to be cloudy or overcast. These clarity measurements are shown in Figure 4-12, and show regions of low light (Light $<$ 50, where a value of 50 indicates times where the Sun is above the horizon), with clarity seen to be low. If clarity is either low or intermittently low, this would indicate periods of cloud, as shown in Figure 4-12. For a night, or part of a night, to be considered usable for analysis, clarity must be both above 23 and remain relatively constant. The time-series for the night in question is shown in Figure 4-13, where cloud signatures are seen to coincide with the poor clarity of Figure 4-12.

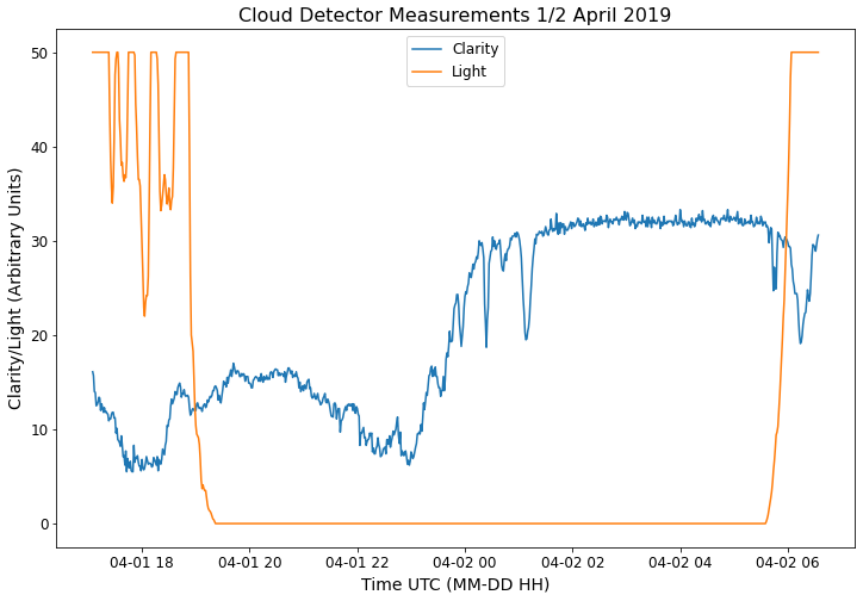

Figure 4-12: Clarity (and other measurements) as detected by the Aurora cloud detector

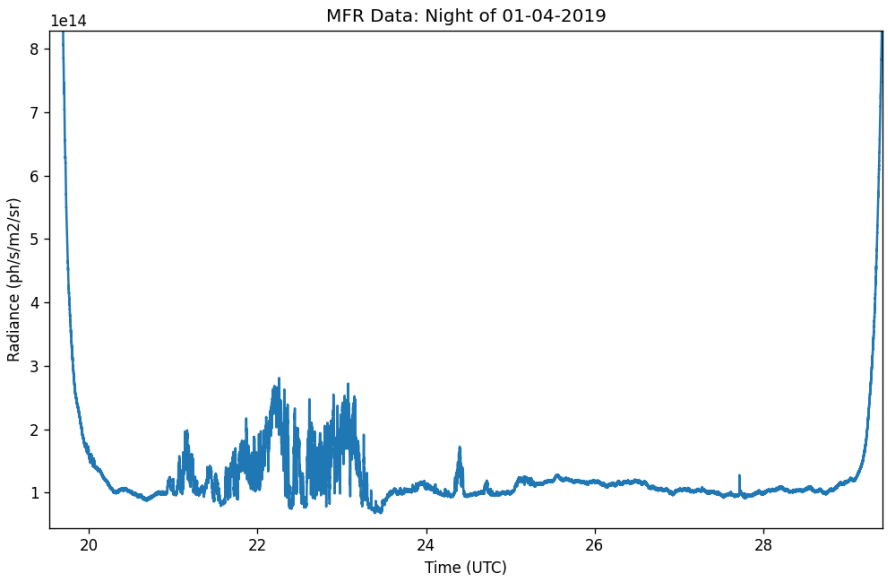

Figure 4-13: Time-series for the night of the 1/2 April 2019, showing clear and cloudy conditions

4.3. Moonlight

A noticeable change in the detector output is seen during times when the Moon is at a high azimuth and close to full even when the sky is completely clear. The main effect of a full Moon (when at a high azimuth so to be seen by the radiometers) during observing times is the increased intensities seen by the detectors. The increased intensity observations are not a result of changing hydroxyl emissions, but rather due to the reflected solar radiance from the Moon. In Section 4.2.1, the general trend-line for a clear night shows a decrease in the hydroxyl emission as the night evolves, but this same trendline is normally not seen for nights with a full Moon at high azimuth, a situation which can be seen in Figure 4-14 during the night of 20/21 January 2019. Between the hours of 20:00 – 04:00 UTC, a 'hump' of higher intensity values occurs, which, when compared to the general background intensity, is almost two times the background intensity at its maximum.

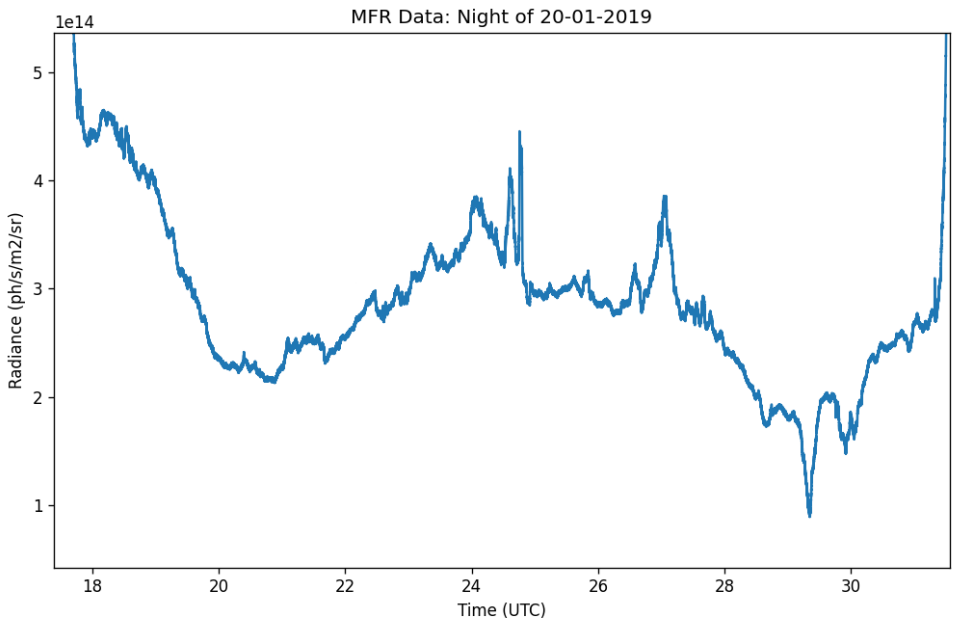

Figure 4-14: Moonlight signature as seen on the 20/21 January 2019, as indicated by the increase in radiance values.

The onset of the radiance increase occurs at ~20:00 UTC as shown in Figure 4-14, and ends just after 28:00 UTC. After 28:00 UTC, the clear conditions present were interrupted by cloud as confirmed by the Aurora cloud detector, making any other observations impossible. The peak of the hump occurred when the Moon was at an altitude of 56.26° above the horizon, and had an illumination of 99.9% (according to data from MoonCalc (*Hoffmann*, 2021)) at around 24:00 UTC. This peak appears to occur at the highest altitude of the full Moon that evening, and from around 24:25 UTC, the hump begins to decrease in radiance intensity, matching the decrease in the Moon's altitude above the horizon. This night also marked the onset of a total lunar eclipse over Maynooth, however due to cloudy conditions after 28:00 UTC (which preceded totality), it was not possible to investigate any potential radiance effects.

The non-hydroxyl signals discussed so far are due to daily or monthly radiance effects, including due to sunlight and moonlight. Other signals from intermittent sources have also been found through the dataset, the most apparent of which are signals associated with noctilucent clouds, dealt with in the next two sections: Section 4.4 and Section 4.5.

4.4. Noctilucent Clouds (NLCs)

In the search for infrasound signals in the detector data, rather large signals at sunrise and sunset were observed (and in some cases, close to midnight hours). Initially the signals at sunrise and sunset were interpreted as infrasound as a result of shock waves excited by the passage of the solar terminator. Although the theory of the solar terminator fits some aspects of these signal characteristics – such as the timing and speeds of the signals – other characteristics do not line up with the theory that the signal source is due to excitation by the solar terminator (large signal and mismatched timing of solar terminator crossing over Maynooth). An alternative explanation was sought to explain the signal characteristics. This hypothesised alternative source for the large signals observed at sunrise and sunset is that of noctilucent clouds (NLCs) (*Schmidt* (2019), *private communication*) above the station. Noctilucent clouds are an optical phenomenon primarily viewed at high-latitudes in both the Northern and Southern hemispheres, between of $50° - 65°$ in latitude (*Dubietis et al.*, 2011). These regions are shown in Figure 4-15, and are given by the cross-hatched regions. The same figure shows that these regions overlap with the location the observing station in Maynooth, Ireland, meaning that NLCs should be observable at the station.

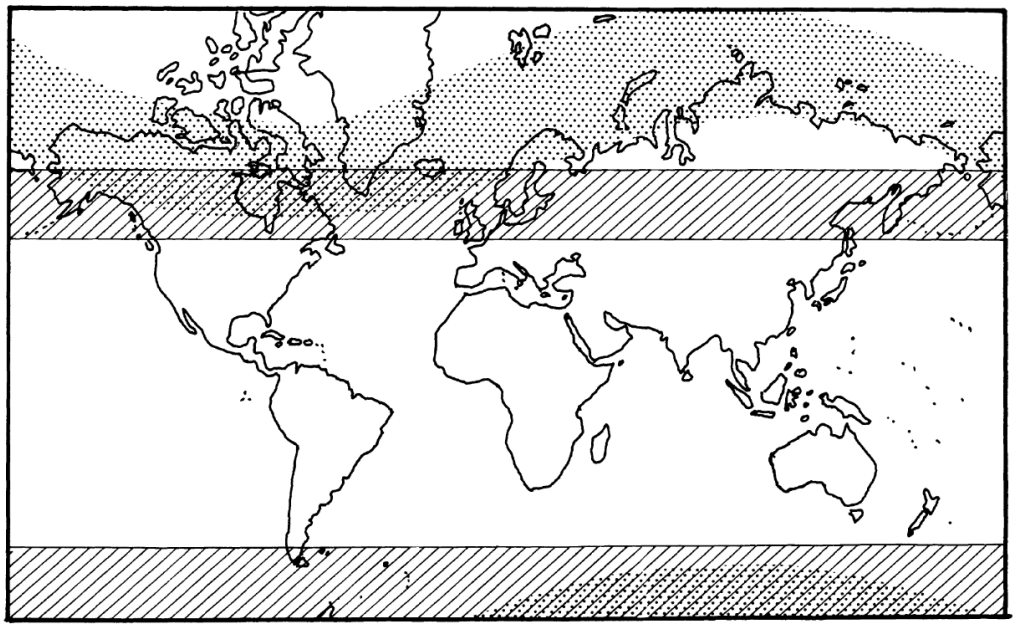

Figure 4-15: Latitudes (cross-hatched) where NLCs are primarily viewed. The location of the observing station (Ireland) is within this area (dotted bands show the auroral zones) (*Gadsden*, 1989)

These cloud structures occur near the mesopause in the vicinity of around ~82 km (*Dalin et al.*, 2018), as shown in Figure 4-16, occupying a similar region as the hydroxyl nightglow (*Bittner et al.*, 2010). These clouds are known to be the highest terrestrial clouds within the Earth's atmosphere and, to the observer with an unaided eye, are only visible in the twilight arch after civil twilight begins (this arch is seen in Figure 4-16, and is shown by the region of contrast between light and dark in the sky).

Figure 4-16: Noctilucent clouds as captured by Dubietis et al. (2011)*, showing the contrast of the illuminated clouds against the sky.*

Noctilucent clouds occur exclusively in the summer hemisphere when conditions are favourable for the clouds to form, specifically the occurrence of low temperatures in the mesosphere (more likely in the summer season) and are composed of tiny ice crystals (*Dalin et al.*, 2006) which reflect the sunlight incident upon them. Visibility of these clouds, as mentioned, is normally confined to times of twilight, and they are still relatively difficult to detect with the naked eye and cameras due to their optically thin, tenuous nature. *Gadsden* (1998) has described the requirements needed to observe NLCs in some detail, where the latitude, season, position of the observer and time of day all play a role.

The time of noctilucent cloud sightings normally occur between $22{:}00$ and $04{:}00$ local time (*Dalin et al.*, 2004), but this situation depends on the latitude of the observer as well as the season. The time period roughly corresponds to times where the solar depression angle (angle of the sun with respect to the horizon) is between $6°$ and $16°$. At these angles, the observer/station would experience either nautical or astronomical twilight, where nautical twilight occurs for solar depression angles between $6° - 12°$, and astronomical twilight is defined by solar depression angles of $12° - 18°$. Figure 4-17 shows the basic geometry for the observation of NLCs by a ground-based observer. Here, the angle α in the figure is the solar depression angle at which the NLCs are visible to the observer positioned at O, where the NLC in Figure 4-17 subtends an angle between κ and κ' (within the twilight arch).

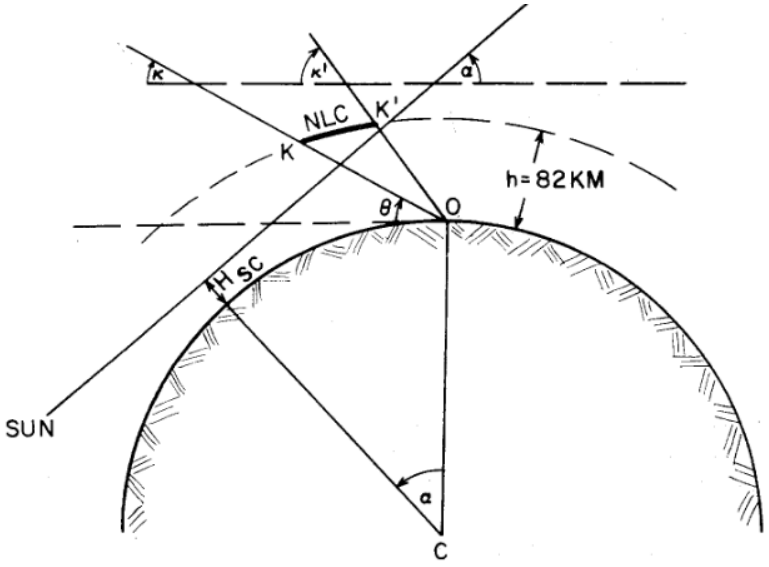

Figure 4-17: Observation geometry for NLCs in the twilight arc, showing the angle subtended by the NLC structure (between κ' and κ), and lit up by the sun, which is situated at the solar depression angle of α. H_{sc} denotes the screening height (minimum height that solar rays strike, and is subject to change) (*Fogle et al.*, 1966)

The times quoted by *Dalin et al.* (2004) above represent the main viewing times for noctilucent clouds. Figure 4-18 shows the more specific viewing times of NLCs for a latitude of 54 °N, which is close to that of the station's latitude, 53.3 °N. The figure demonstrates how the observing times (black shading) change over the course of the year for the latitude, where NLCs are viewed throughout the whole night for dates between late May and late July. These dates overlap with the noctilucent cloud season in the Northern Hemisphere, where NLC formation typically occurs between late May and early August.

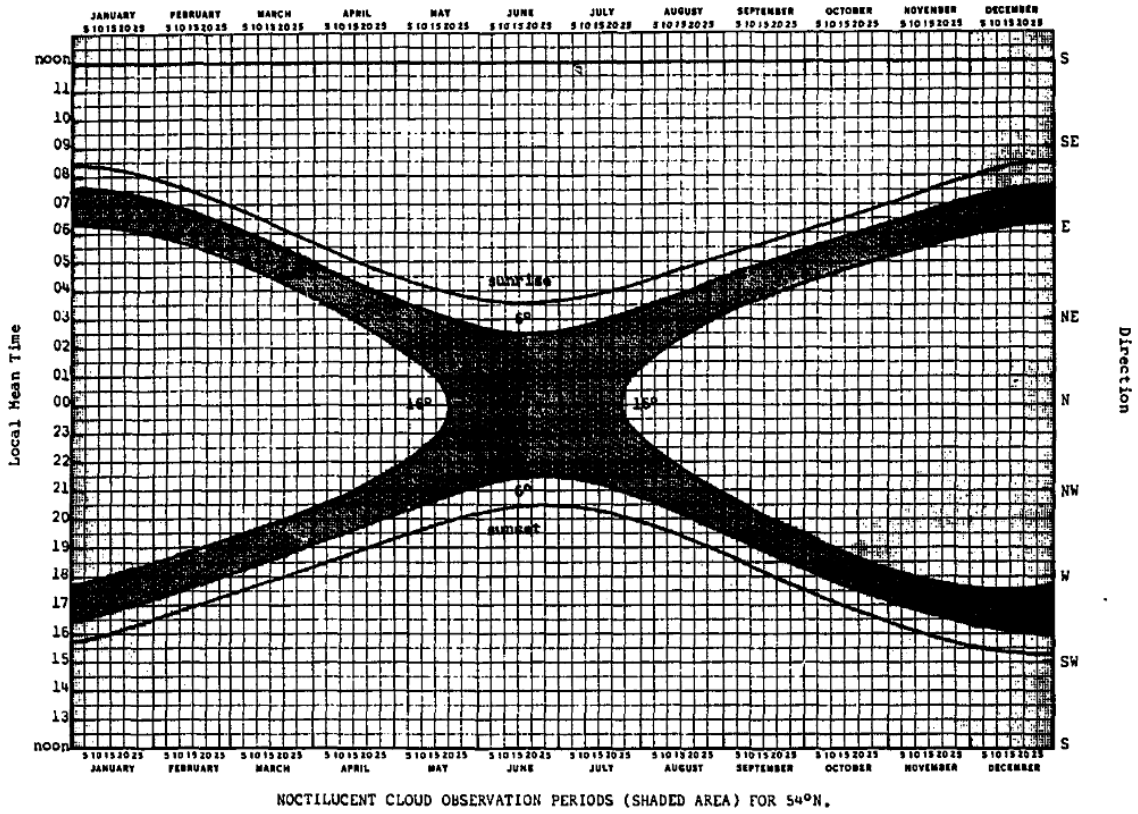

Figure 4-18: Viewing times for NLCs at 54°N, where the shaded areas indicate times when the NLCs should be visible to a ground-based observer. The viewing times are bound by the solar depression angles of 6° *and* 16° (*Fogle*, 1966)

Figure 4-18, it should be noted, shows the theoretical viewing times of NLCs in the upper atmosphere rather than the likeliest times to see these structures. The shaded region within the above figure stretches into months that are not favourable for NLC formation in the upper atmosphere due to the lack of low temperatures needed to sustain the structures. This concept of NLC formation within the mesosphere is discussed in the next section, while a brief note of how these structures have been observed in the past is also given.

4.4.1. NLC Formation

The mesopause is the coldest naturally occurring environment on Earth, with temperatures of the region dropping below 150 K during the summer months (*Rapp* and *Lübken*, 2004, *Kokhanovsky*, 2005) (for both the Northern and Southern hemispheres). These very low temperatures create the ideal conditions required for NLCs to form in the region, but are not the only conditions. For NLCs to form in the mesospheric region a number of factors must be present (*Dubietis et al.*, 2011), including low temperatures, high water vapour concentration and the presence of nuclei onto which the water vapour can condense. The two factors of low temperature and cloud condensation nuclei will be discussed first. In the scheme of the entire atmosphere, the mesosphere exhibits the lowest temperatures occurring naturally on Earth, where these extreme temperatures are due to adiabatic cooling from the summer-winter meridional circulation (*Holton*, 1983) illustrated in Figure 4-19, and which originates from critical filtering of gravity waves described in detail in the next few paragraphs.

These low temperatures meet one requirement for NLC formation but cloud condensation nuclei (CCN) are needed to produce the sites where water droplets can coalesce to produce the actual noctilucent cloud particles (a process known as seeding). Authors have generally attributed the origin of these CCN to meteoric smoke dust (*Kaifler et al.*, 2018), but other authors such as *Plane* (2000) attribute the noctilucent CCN more specifically to sodium bicarbonate, which makes up the majority of meteoric dust particles. This molecule successfully clusters, allowing water to coalesce.

Before NLCs can be successfully formed by these low temperatures and CCN, water or ice is required, which has been proposed and subsequently identified as the main component of NLC particles (*Hervig et al.*, 2001). Although this is the case, the mesosphere is a comparatively dry region of the atmosphere, where water levels within the region may only reach 1 ppm (part per million). This lack of water in the mesosphere would thus normally not support the formation of NLC structures, but only through the interaction of flows in the atmosphere does the water concentration of the

mesosphere increase while also seeking to decrease the temperature. The interaction of flows mentioned requires the explanation of several interactions beginning with the Coriolis force (covered in Section 1.6).

Coriolis forces due to the Earth's rotation act at right angles to the atmosphere's flow resulting in consequences for both the winter and summer stratosphere, through the creation of a circumpolar flow. For the winter stratosphere, this circumpolar flow is directed eastward (with a Coriolis force directed equatorward) while in the summer stratosphere, a westward circumpolar flow dominates (Coriolis force directed poleward). A geostrophic balance is achieved when the Coriolis force of the region equates to the pressure-gradient force (differences in pressure across a distance).

The winter stratosphere and mesosphere are affected by breaking Rossby waves which can affect the geostrophic balance in the region. For this balance to be restored, an eastward Coriolis force must be balanced with a weak poleward flow, which in this case is the Brewer-Dobson circulation. This circulation begins at the equator where warm air rises and flows towards the poles. The Brewer-Dobson circulation does not directly lead to noctilucent clouds, but rather, gravity waves play a central role (*Rapp* and *Lübken*, 2004). Gravity waves or buoyancy waves (discussed in Chapter 1 of this thesis) are small atmospheric waves which deposit momentum into the background flow of the atmosphere. The phase velocity of a given gravity wave determines whether the disturbance reaches mesospheric altitudes.

If the background flow in the stratosphere matches the phase velocity of the gravity waves that propagate upwards, then these waves will break prematurely before they can reach the mesosphere. The background flow thus acts as a 'critical filter' for gravity waves that have a particular phase velocity. In the confines of the summer stratosphere, due to the westward circumpolar flow owing to the Coriolis force, gravity waves with a westward phase speed will be filtered out and so only eastward gravity waves will propagate upwards to the mesosphere. The resulting eastward-propagating gravity waves cause the mesospheric flow at the summer pole to be shifted causing an equatorward flow, with a resulting ascension of air from the pole. Ascension of these air

parcels result in their cooling, due to the adiabatic expansion of the air (Figure 4-19 below). It is within these conditions that noctilucent clouds can be formed.

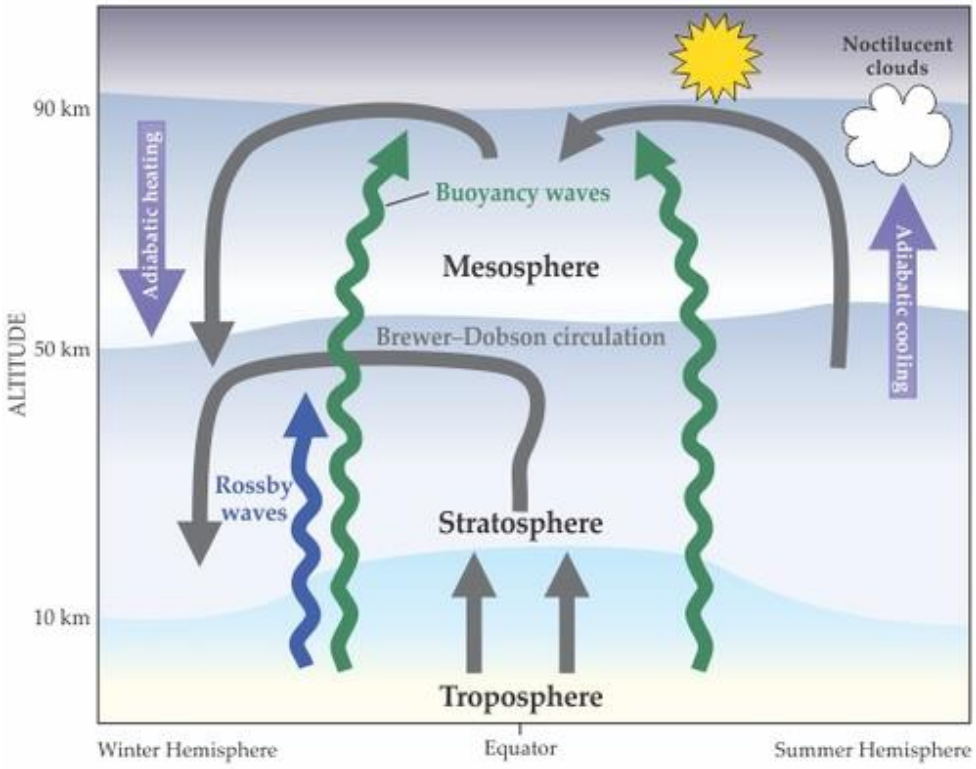

Figure 4-19: Major atmospheric motions associated with the formation of NLCs in the summer hemisphere. NLCs are formed when rising air packets in the hemisphere, reduce the temperature of the mesosphere region (*Karlsson* and *Shepherd*, 2018). *This image has been shown previously in Section 1.7, and is reproduced here for convenience.*

The introduction of air packets, which are subject to adiabatic cooling, into the mesosphere leads to a reduction of the temperature in the region, creating the temperatures necessary for the formation of NLCs. NLCs can be formed in the mesopause when the low temperatures fall below the water frost point temperature of the region (*Dubietis et al.*, 2011), which is the temperature at which water condenses to a surface (in this case the surface would be that of a CCN). This is not a stable value, constant over the atmosphere, but rather the frost-point temperature depends on the altitude as shown by *Kokhanovsky* (2005), and explains how only at mesopause heights do conditions for NLC formation occur.

Visible NLCs do not normally occur at the altitude where the frost-point temperature dips below the temperature of the environment. The ice particles that form the NLCs are normally too small at these altitudes to be seen, and instead the visible NLCs normally inhabit lower altitudes. As the nucleation sites gather more water-ice (transported by rising air), they grow larger in size and thus become more subject to Earth's gravitational pull. These larger NLC particles thus fall towards the Earth, growing larger as they descend. Once the particles reach sizes of tens of nanometres, they can scatter sunlight (*Harrison*, 1973) and thus become visible, subject to the correct viewing angles. *Ugolnikov et al.* (2017) report the largest of these particles occur around 80 km with scattering efficiency highly dependent on particle size, the idea of which is seen in Figure 4-20 below, where the visible clouds occur below the altitude of NLC formation.

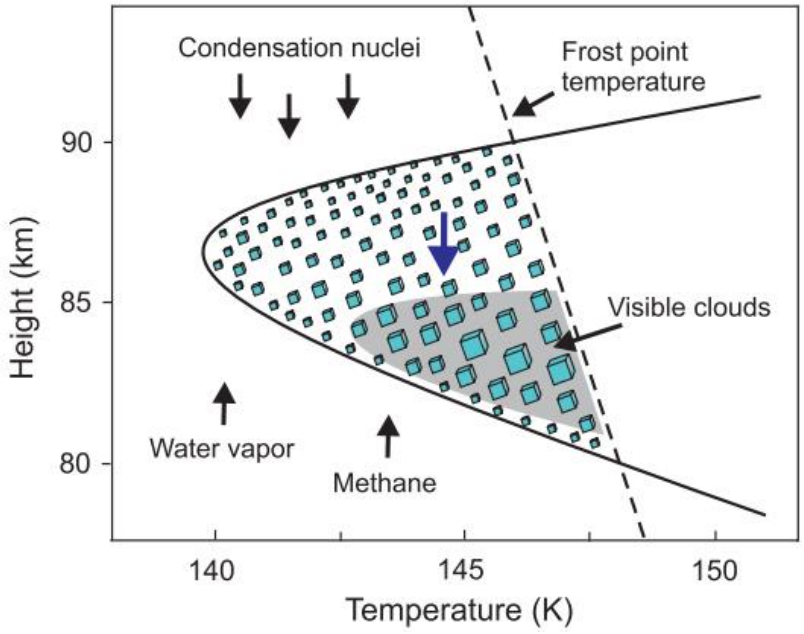

Figure 4-20: Formation of visible NLCs due to the cold temperatures, CCN and water vapour/methane (*Dubietis et al.*, 2011)

As the NLCs (and more specifically the particles that compose the clouds) descend and gain more mass, they also experience a rising temperature (*Gadsden* and *Parviainen*, 1995). The increasing temperature of the environment exceeds that of the frost-point

temperature of water, with the ice crystals of the NLC evaporating. This process eventually leads to NLC destruction (*Dubietis et al.*, 2011), and explains the lower bound of the NLC altitude range (NLCs normally do not occur below a threshold of around 80 km).

Ice particles present in NLCs have been thoroughly investigated by a number of studies (*Witt*, 1962; *Kokhanovsky*, 2005; *Kiliani et al.*, 2013; *Ugolnikov et al.*, 2017). Larger ice particles which occur at lower altitudes than the altitude of formation, as noted above, are visible as NLCs, but smaller ice particles are also capable of being detected before they grow to these sizes. These ice particle formations are a major contributor to Polar Mesospheric Summer Echoes (PMSEs), which are very strong radar echoes (*Stebel et al.*, 2000) thought to arise from a combination of turbulence and reduced electron diffusivity due to ice particles (*Rapp* and *Lübken*, 2004). Normally the two phenomena (NLCs and PMSEs) are found together (*Stebel et al.*, 2000, *Kiliani et al.*, 2013), and their different conditions and characteristics are shown in Figure 4-21.

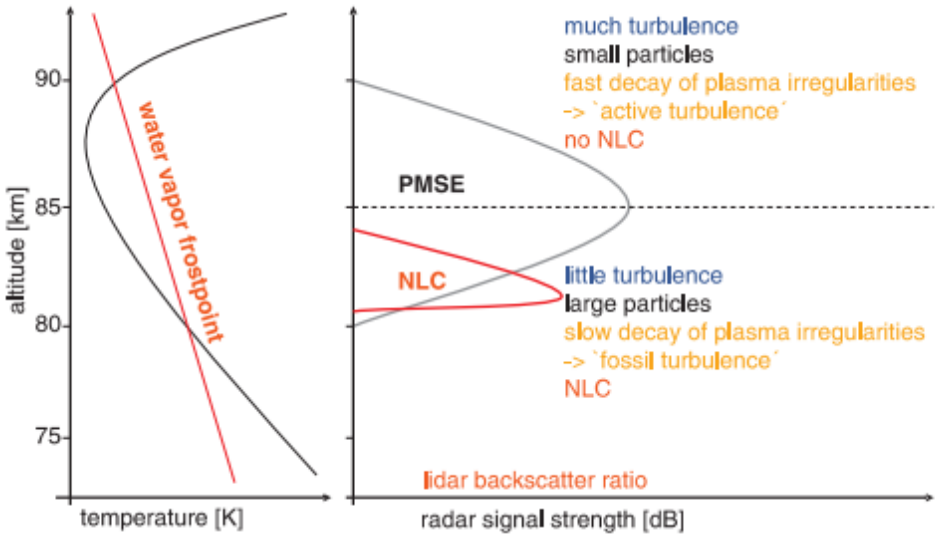

Figure 4-21: Comparison of NLCs to PMSEs. Although the two phenomena occur close together, they are composed a different material. The plot shows the LIDAR backscatter ratio, which depends on the strength of the signal as a result of increased atmospheric density (*Rapp* and *Lübken*, 2004)

Both NLCs and PMSEs are known to be good indicators of the chemical and dynamical processes that occur within the mesopause and surrounding regions. These phenomena have thus been seen as potentially good tracers for long term climate change effects in the middle atmosphere. Trends in noctilucent cloud characteristics have already been investigated by authors like *Kirkwood et al.* (2008), with debate still ongoing regarding whether the increase in methane gases present in the troposphere contribute to increased NLC cover. *Thomas et al.* (2011) for instance, argue that the cloud variability over the previous two decades shows an increase in the overall MC (mesospheric cloud: encompassing PMCs and NLCs) albedo, thus indicating a possible connection to increased greenhouse gases. On the other hand, authors like *von Zahn* (2003) argue that more research is needed into this area before a conclusion can be reached. Recent studies regarding extreme NLC events over Europe have been considered singular unusual events rather than evidence of climate change (*Gerding et al.*, 2021).

4.4.2. Methods of Observation and Analysis of NLCs

Noctilucent cloud observations have been constant since they were first reported by *Leslie* (1885). Many studies since have relied on a similar method employed by Leslie, whereby characteristics of the clouds have been investigated visually. More recently, a number of authors (*Dalin et al.*, 2008; *Pautet et al.*, 2011; *Demissie et al.*, 2014) have used automatic CCD cameras to capture noctilucent clouds in the twilight arch at various locations, particularly in the Northern Hemisphere. Other methods to investigate NLCs have included LIDAR sounding (*Kaifler et al.*, 2013, 2018; *Fritts et al.*, 2019), UV-spectroscopy (*Carbary et al.*, 2003) and polarisation methods (*Ugolnikov* and *Kozelov*, 2016), along with rocket-borne measurements (*Gumbel* and *Witt*, 2001).

More recently satellite measurements of NLCs have been obtained, investigating the phenomena from above. These measurements define the clouds as Polar Mesospheric Clouds (PMCs) (rather than NLCs) when the observations are made above the region of formation (*Carbary et al.*, 2003, *Chandran et al.*, 2009). Each of these methods have

been able to go beyond visible ground-based accounts and investigate NLCs in different perspectives, with characteristics of the clouds becoming more well-known with each advance of technology.

4.4.3. Method of NLC Observation by a 3-element Radiometer Array

The radiometers in this study rely on the emissions of the hydroxyl layer for the detection of waves and other phenomena present in the mesopause. This layer is present near a height of 87 km in altitude (the width of the profile is reported to be close to 8 km (*Baker* and *Stair*, 1988)), which overlaps with the region where NLCs form: at around 82.7 km (*Avaste et al.*, 1980).

Although not the initial primary target, it was found that the radiometer array was proficient at detecting NLCs during the summer months. These radiometers would not normally be able to detect NLCs, as these clouds clearly do not emit light (which would be needed for detection by the radiometers). However, if the clouds are illuminated by the Sun when it is positioned between 6° and 16° below the horizon (solar depression angle), it is possible that, due to the scattering efficiency of the NLC particles, scattered sunlight may enter the radiometers and thus render the NLCs detectable. In essence, the Sun in this scenario would act like a light source in a LIDAR set-up (see section above), where solar photons rather than laser photons are measured by the detectors at Maynooth. This would result in not only hydroxyl emissions being detectable by the radiometer array, but also backscattered sunlight from an optically thin layer of NLCs.

Due to the Sun acting as a blackbody, a certain amount of the sunlight reflected from these clouds is composed of infrared radiation, which has the capability of being detected by the radiometers. Referring to the detector response curve of the radiometers at Maynooth - reproduced below in Figure 4-22 for convenience, the wavelengths of the backscattered light must fall within the response curve range to be detectable. As the Sun emits across all wavelengths, the detectors would in theory be responding to

emissions across the $1.0 - 1.7\,\mu$m region defined by the curve in Figure 4-22. Unlike the normal signal found when the Sun is observed by the detector, the NLC structures would likely not always saturate the detectors, as the clouds are optically thin. However, the signal would be larger when the NLCs are denser and reflect more sunlight producing signals likely larger than that seen from gravity waves.

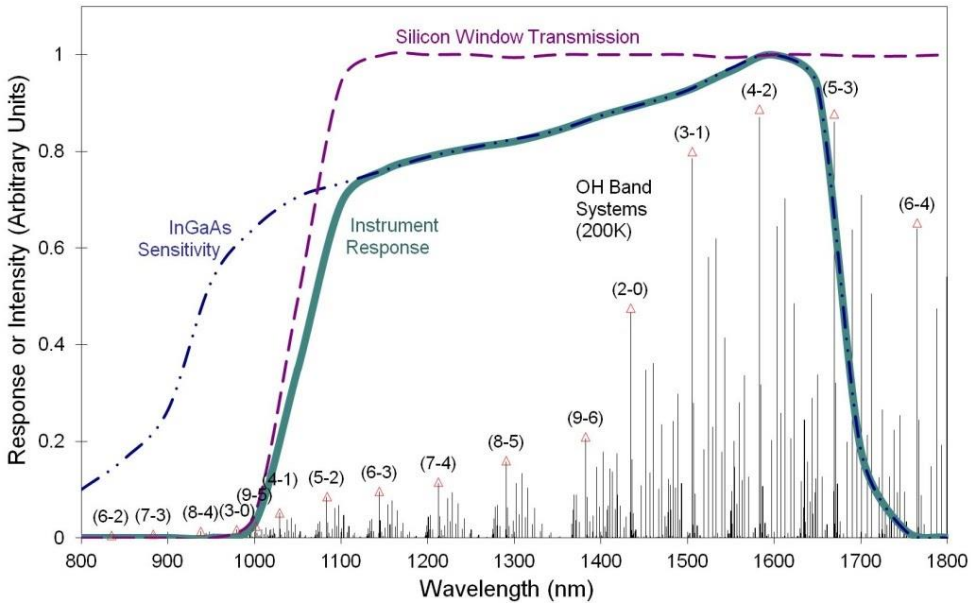

Figure 4-22: Response curve of the detector, as shown previously in Chapter 2

It is expected that due to the amount of photons that would scatter from the NLCs compared to that of the photons emitted from the hydroxyl layer, NLCs should appear substantially larger in terms of intensity in the datasets. The hydroxyl layer is a diffuse low light source which emits less than 0.5 MR (*Xu et al.*, 2012) over the entire spectrum of Meinel bands. Noctilucent clouds, on the other hand, can reflect upwards of $10 - 15$ MR (as discussed by *Carbary et al.* (2001) and *Carbary et al.* (2003)).

As mentioned above, the radiometers did not have the primary purpose of observing NLCs. However, due to their unique location and instrument response in the infrared, the detectors allow for the measurement of the NLC phenomena. The instruments set-up at Maynooth allow for the observation of NLCs from new perspectives compared to other detectors such as CCD cameras which can only observe noctilucent clouds with

sufficient density to become visible to such detectors. While CCD cameras rely on oblique viewing angles to detect NLCs within the twilight arch (*Pautet et al.*, 2011), the radiometers have the capability of detecting the clouds at zenith. This removes geometrical issues for observations and opens up the possibility of detecting less studied NLC positions. The temporal resolution of the radiometers also exceeds that of other detectors such as LIDAR, offering a certain amount of advantage over these previous methods. The next section shows the results of NLCs over the station, showcasing two particular signals that occurred in 2016 and 2018 respectively.

4.5. Case Studies of NLCs

The results reported here concern two main case studies and some smaller instances of NLC events measured by the radiometer array in Maynooth. The NLC events occurred during the Northern Hemisphere summer between the years 2013 and 2019. The two main events which occurred in 2016 and 2018 respectively, were investigated to determine whether any structure of the underlying NLC formations could be inferred. Along with these investigations, comparisons are made to visual accounts taken from NLCNET, a comprehensive visual database of NLC events, and the CIPS instrument on board the AIM satellite. The event that occurred on the 18/19 July 2016 is further compared to observations made by *Kaifler et al.* (2018) due to its relevance to an extreme NLC event that occurred over Europe on that evening.

Two separate sections (Section 4.5.1 and Section 4.5.2) will look at the two main case studies of NLC events that occurred on the night of 18/19 July 2016 and the night of 21/22 June 2018. The characteristics and background conditions for the two events are discussed in two separate sections. Potential NLC events are also shown and discussed later in this section. The theory of the signals originating from the backscatter of light from NLCs is currently the most plausible theory fitting the signal characteristics, but a

comparison will be made to whether the signals originate from the solar terminator travelling through the atmosphere.

4.5.1. Case Study 1 – Signal on 18/19 July 2016

The first case study regarding NLCs is that of the signal that occurred on the 18/19 July 2016, the time-series of which is given in Figure 4-23. This night was marked by clear conditions as confirmed by visual observations from Met Éireann and more specifically by a frequency analysis of the night, and all three instruments show a relatively quiet night. Figure 4-23 shows all three instrument datasets for the night in question (with the saturation signals at dusk and dawn removed), where MFR is regarded as the principle instrument. Before 25:00 UTC (01:00 AM), the night's data follows the general trend seen previously in this chapter (Section 4.1) where the radiance decreases as the night progresses. A large increase in radiance is seen around 25:00 UTC, where the radiance peak is marked by a sudden onset rather than by a gradual increase associated with moonlight, as was seen in Section 4.3.

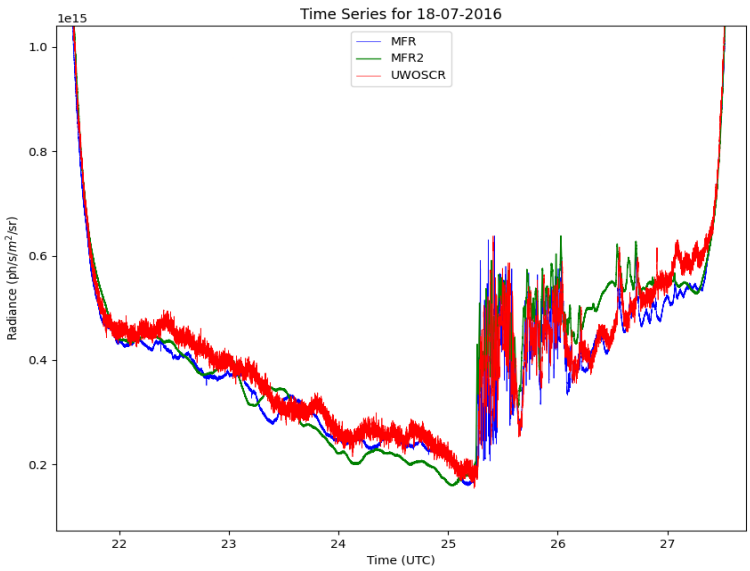

Figure 4-23: Radiance measurements of the 18/19 July 2016, showing data from all three instruments. The signal of interest occurs around 1:00 AM on the morning of 19 July 2016 (25:00 UTC).

The peak of the radiance signal in Figure 4-23 is three times larger than that of the background (where the background is taken as the radiance before the sudden onset of the signal). Before any analysis is undertaken, the weather conditions for the night must be considered and confirmed through the use of techniques outlined in the beginning of this chapter.

4.5.1.1. Weather Conditions

Based on the evidence available for the time period in question, the night was determined to be clear. Clear nights are normally quiet nights that follow the radiance trend set out in Section 4.2.1, with radiance values close to $2 \times 10^{14} - 3 \times 10^{14}$ ph/s/m^2/sr. To confirm these conditions a power spectrum of the night is taken and the Met Éireann data are consulted, as the night occurred prior to the use of the cloud detector on campus.

The power spectrum, if tropospheric clouds (as distinct from NLCs) are present, would show a 0.78 Hz signal (this night is pre-2017, when the pedestrian beacon was still in place). Based on the power spectrum taken for the whole night shown in Figure 4-24, no such signal occurs during the course of the night (no harmonics of the 0.78 Hz peak are seen either). This indicates that the night is clear of clouds, and the signal is not due to streetlight reflections from the cloud-base, but rather another source.

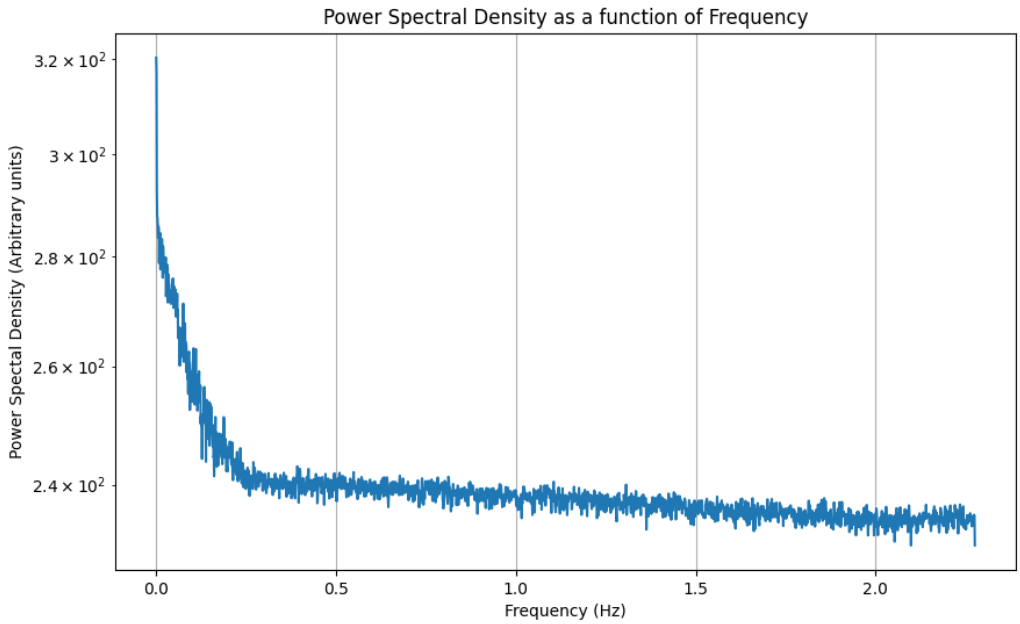

Figure 4-24: Power spectrum of the night of 18/19 July 2016. This would indicate that no clouds persisted over the station.

The power spectrum in Figure 4-24 does not deliver on the time resolution needed to determine whether clouds persisted over the station for the duration of the signal, but only for the night as a whole. Figure 4-25 shows the wavelet transform of the night (MFR signal only), which enables the dataset to be examined as a function of frequency and time components (discussed in Section 2.6 in Chapter 2). In the case of clouds above the station, the same **0.78** Hz signal would be seen as a band at around $\mathbf{10^0}$ Hz region in Figure 4-25 (bottom). This is not seen within the plot and thus it can be assumed that no clouds persisted above the station during the time of the signal. (the frequency of the signal at $\mathbf{10^{-3}}$ to $\mathbf{10^{-1}}$ Hz in Figure 4-25 occurs in the middle of the infrasound range).

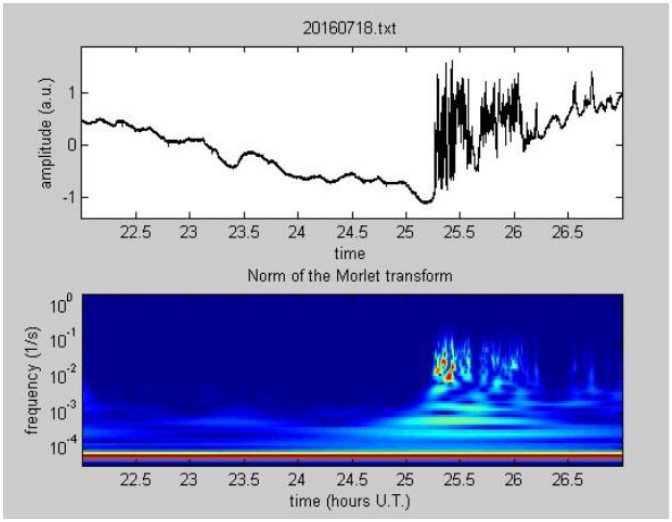

Figure 4-25: Time-series and wavelet transform of the night of 18/19 July 2016. No power is associated with larger frequencies here, normally indicative of clouds, which may show that no clouds persist above the station for the night.

Met Éireann data are also seen in Figure 4-26, showing that during the time of the signal, cloud data from Casement Aerodrome (discussed at the beginning of this chapter, in Section 4.1) show only small amounts of cloud close to the station, based on the description of cloudiness given in Section 4.1. As a result of the power spectrum, wavelet transform and cloud data from Casement, the signal was deemed to not originate from terrestrial clouds and analysis was undertaken.

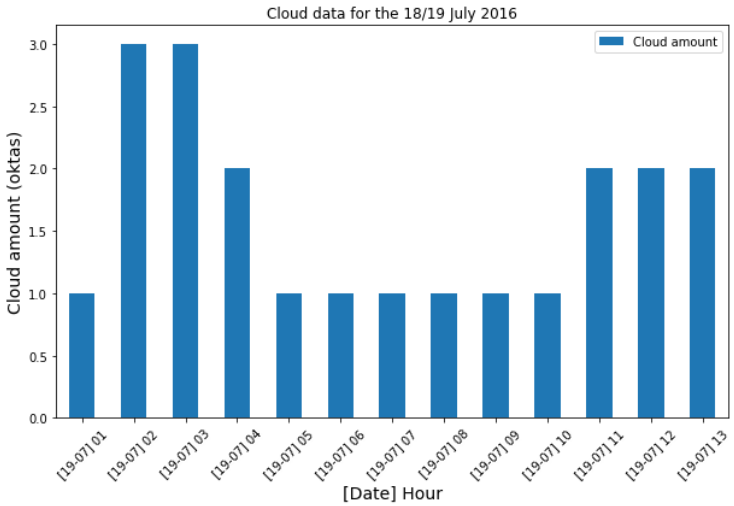

Figure 4-26: Cloud data from Casement Aerodrome during the 19 July 2016 – showing relatively clear conditions in the morning (time of signal).

4.5.1.2. Signal Characteristics

The relative intensity of the signal after 01.25 UTC (25.25 UTC in Figure 4-23) is almost 3 times the signal prior to 01.00 UTC, and reaching values of 6×10^{14} ph/s/m^2/sr, which can be written as $(2.5 \pm 0.5)I_0$ where I_0 is the intensity prior to the intensification. This large of a signal is thus comparable to clouds (already ruled out) and sunlight effects.

The basic characteristics of the signal can be extracted using a single instrument, like that of the amplitude (discussed in the above paragraph), as well as the duration, and the period and frequency. The characteristics are taken using the plots shown in Figure 4-23 (duration, amplitude and wavelength) and Figure 4-26 (period and frequency). The duration of the signal is difficult to establish due to the slow falloff of the signal radiance and whether the end of the disturbance can be rightly attributed to the same signal of interest. The best estimate for the signal duration from the MFR data is approximately one hour in length. An estimate of the wavelength can also be established manually from the time-series shown in Figure 4-23 (shown in greater detail in Figure 4-27). Using the average of the wavelengths taken from the timings of the signal peaks, a value of 5.1 ± 0.6 km was found for the wavelength of the signal.

The final basic characteristics obtained using the MFR values alone is that of the period and frequency of the signal. The time-series gives a period of $\sim 25 - 28$ seconds, translating to a frequency between $0.036 - 0.04$ Hz. Figure 4-25 shows the wavelet transform, which can be used to obtain the frequency and period of the signal, where the bottom plot of Figure 4-25 shows the power associated with various frequencies during the course of the night. The night is dominated by lower frequencies associated with the slowly varying radiance of the background (period of several hours), while the signal is dominated rather by higher frequencies where there is greater power associated. The majority of the power in the signal is associated with a frequencies between $0.01 - 0.05$ Hz, matching the frequency range estimated manually from the time-series. The period of the signal 20.5 ± 1.5 seconds based on Figure 4-25. Based on the frequency and

period of the signal, the disturbance as recorded by MFR occurs within the infrasonic range (as described in Chapter 1, Section 1.7.4). The signal in particular, occupies the infrasound range occupied by infrasound from sources such as earthquakes and volcanoes, as shown in Section 1.8.1.

Two pivotal characteristics only obtained through the use of all three instruments is the speed and back azimuth of the signal, with these parameters important to establish both the nature of and source of the signal. The attempt to determine these characteristics is summarised in Figure 4-27 below, showing how the leading edge of each signal (given in intensity – arbitrary units) was matched in time, with both the MFR2 and UWOSCR datasets matched relative to the data from MFR. Figure 4-27 shows the radiance values given in arbitrary units.

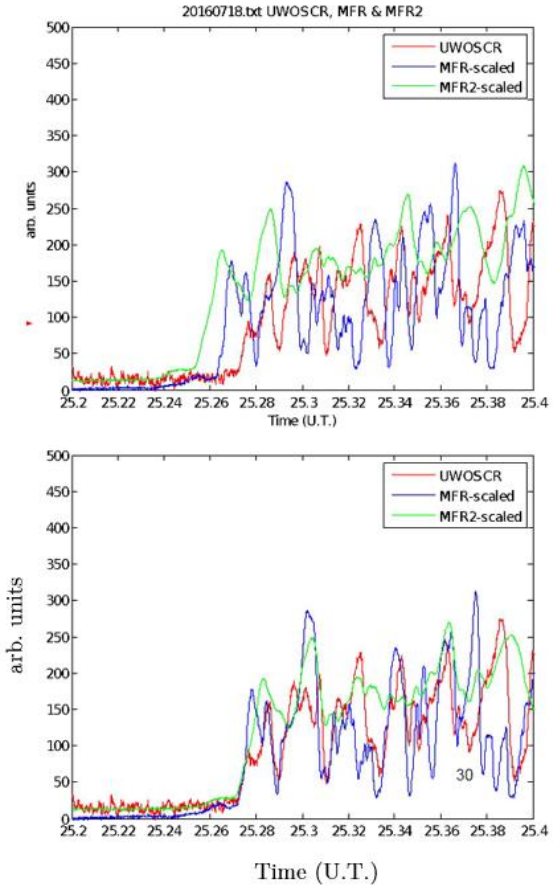

Figure 4-27: Time-lag analysis of the three signals (intensity pl , measured relative to MFR. The leading edge of the signals are matched and time-lag analysis is used to obtain the speed and azimuth. Cross-correlation could not be performed due to the disparity between signal peaks.

Chapter 2 (Section 2.5) introduced time-lag analysis as described by *Pignatelli et al.* (2008) and *ElGabry et al.* (2017) to establish the speed and back azimuth of signals. According to Figure 4-27, the signal is first registered by MFR2 (shown in green above, and pointing towards west). A signal of similar intensity is then recorded by MFR (blue, pointing toward zenith) and finally by UWOSCR (red, pointing towards north). This implies (as demonstrated in Figure 4-28) that the signal travels from south-west to north-east, and through analysis from Section 2.5, this gives a speed of 334 ± 12 m/s with an azimuth of $61° \pm 4°$ east of north. The direction (azimuth) of the signal propagation is shown below in Figure 4-28 within the frame of the detector geometry, where the letters indicate the position of the different instruments (A is MFR, B is UWOSCR and C is MFR2), where the colours mirror that of the different signals in Figure 4-27.

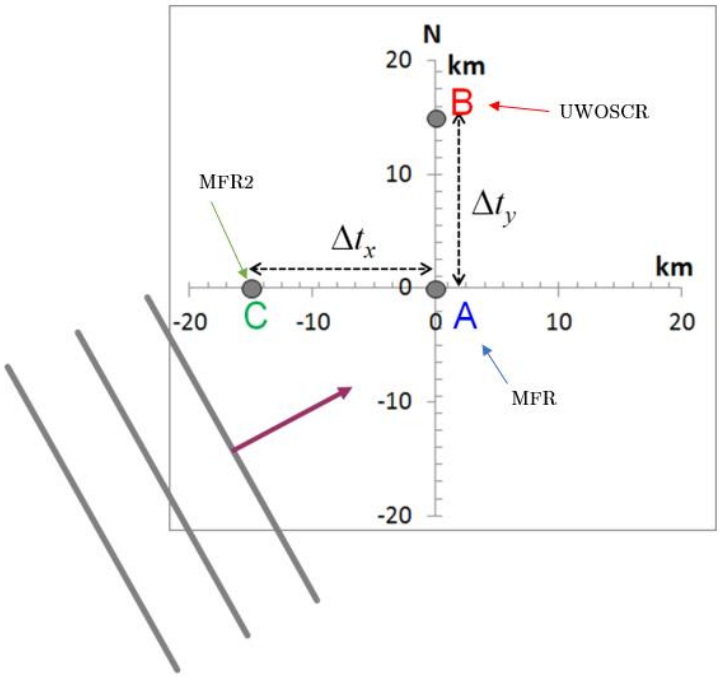

Figure 4-28: Direction of propagation of the signal on the 18/19 July 2016 over the station

Based on the speed of this signal, the value suggests that the signal is acoustic in origin, as it is close to the speed of sound in the mesosphere (which is the approximate region of

the hydroxyl layer). At the time of the signal, the general speed of sound can be determined using data from the SABER instrument on board the TIMED satellite, available from the following site: http://saber.gats-inc.com/browse_data.php. This instrument obtains the temperature data from various points on Earth based on its orbit, where the data for the time of the signal is shown below in Figure 4-29. This temperature profile represents the closest approach of the TIMED satellite to Maynooth's location ($50.9313\,°\,\mathrm{N}, 3.008\ °\mathrm{W}$, where Maynooth's coordinates are $53.38\ °\mathrm{N}$, $6.6\ °\mathrm{W}$), around 1.5 hours after the onset of the signal.

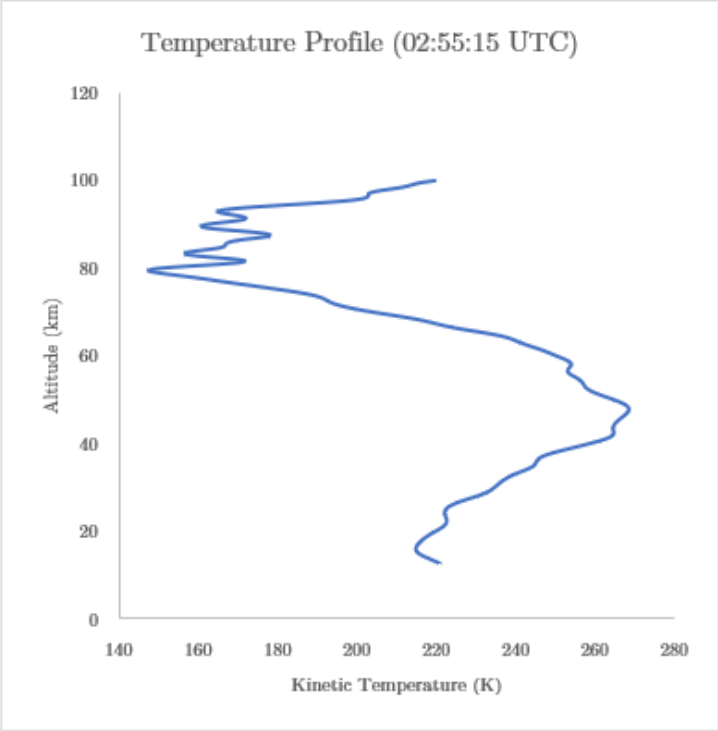

Figure 4-29: Temperature profile for the closest approach to the station of the TIMED satellite during the time of the Maynooth signal.

The speed of sound in the region of the hydroxyl layer is calculated based on the general equation found in Section 1.7.4, Equation (1-28). A more comprehensive form of this equation considers the molecular mass of the air:

$$c_T = \sqrt{\frac{\gamma R}{M} T} \tag{4-2}$$

where $\gamma = 1.4, R = 8.314\ \mathrm{J \cdot mole^{-1} \cdot K^{-1}}$ and $M = 0.02897\ \mathrm{kg \cdot mole^{-1}}$, and c_T represents the speed of sound based only on temperature. Equation (4-2) gives an average value for the speed of sound of ~ 261 m/s. Although smaller than the estimate of the signal (334 ± 12 m/s), the calculation of the speed of sound does not take the wind into account, which would likely increase the estimated value for the speed of sound in the region, bringing the two values closer in line.

This, however, cannot immediately explain the nature of the signal. Attributing this signal to infrasound, databases such as the USGS (United States Geological Survey), GVP (Global Volcanism Program) and CNEOS (Centre for Near Earth Object Studies) were examined for evidence of the source of this disturbance. However, it was determined that no source from these databases could create such a large signal within the time-series.

Another theory proposed in 2018 was the generation of shock waves emanating from the solar terminator as it crosses over the Maynooth station. The solar terminator is known to cause inhomogeneities in the atmosphere (*Somsikov* and *Ganguly*, 1995), and shock waves have been investigated and theorised previously (e.g. *Beer* (1973), *Somsikov* (1983)), and may occur when the speed of the solar terminator is less than the local speed of sound. The speed of the solar terminator at 53°N is around 270 m/s (discussed below in Section 4.5.1.3), and the speed of sound in the region of the mesosphere is also approximately 270 m/s, and thus such waves would be possible at the latitude of observation. However, such a shock wave would be unlikely to create the amplitude increase seen by the radiometers in Figure 4-23. The general increase seen by the radiometers is around 300% above the background radiance level, while waves generated by the solar terminator likely produce amplitude increases closer to ~10% above background levels (as seen by studies regarding TEC variations by the terminator (*Forbes et al.,* 2008; *Bespalova et al.,* 2016), and through GCM modelling in the mesosphere (*Miyoshi et al.*, 2009).

4.5.1.3. NLC Theory

Based on the relative intensity of the signal, with a large amount of power associated with its frequency spectrum, the apparent source appears to have a large impact on the atmosphere. The source of this signal was eventually attributed to a source of non-hydroxyl emission origin and specifically to the presence of NLCs. This reasoning was based on the relative intensity of the signal to the background radiance, as well as the time of year and the latitude of the station.

The intensity of the signal approaches that of cloud interference, moonlight and sunlight (yet the presence of these radiance sources has been excluded from contention for the source of the signal). Based on discussion with *Schmidt* (2019, *private communication*), the source may be instead more indicative of the reflection of sunlight from NLCs (theoretically possible, as sunlight is visible in the instruments), where the structure of the clouds contribute to the variation in radiance seen within the signal (Figure 4-23). Although the direction of the signal would be more likely to travel from north-east to south-west, as it would follow the movement of the sun across the sky, this apparent discrepancy may be explained by the distribution of non-uniform NLC structures.

The NLC theory may also explain the speed of the signal seen in Figure 4-23, given the speed of the Sun across the base of the NLC structure. According to *Bespalova et al.* (2016), the solar terminator travels at a speed of:

$$V_x(\varphi) = V_x(0)\cos\varphi \tag{4-3}$$

Equation (4-3) shows that the speed solar terminator V_x at a given latitude (φ) is dependent on the phase speed of the solar terminator at the equator, which is given as $\sim 450\,\frac{m}{s}$ (*Forbes et al.*, 2008). Based on this value, the solar terminator at a latitude of $53\,°\text{N}$ would be approximately equal to $270\,\frac{m}{s}$, close to that of the calculated speed of sound for the region (~ 261 m/s). Although the speed and direction may explain some

parts of the signal, the calculations are more appropriate for a plane wave travelling through the hydroxyl layer, rather than sunlight tracing across the NLC.

4.5.1.4. Comparison to concurrent data

To confirm this theory of NLCs within the night of data, concurrent data also showing the presence of these structures is needed. Unfortunately no device which is capable of measuring the presence of these phenomena exists close to the Maynooth infrasound station, so other sources of data are used to confirm the validity of NLC structures.

Comparison to data from Kaifler et al. (2018)

Through the use of LIDAR technology, *Kaifler et al.* (2018) have monitored the mesosphere above Southern Germany for the presence of noctilucent clouds. The station used by the authors represents a mid-latitude location which is less likely to observe NLCs compared to high latitude stations (*Hervig et al.*, 2009). At a latitude of 48.8 °N, this station is close to the Maynooth station in terms of mid-latitude location but also gives an indication of whether NLCs occupy latitudes as low as Maynooth.

On the 18/19 July 2016, the German station described in *Kaifler et al.* (2018) observed its only NLC structure for the night (and the season), indicated by the LIDAR system, which saw a pronounced increase in photon count. The measurements taken by the researchers are summarised in Figure 4-30, which shows a large photon count originating from an altitude centred around 81 km. The photon count results from the backscatter measured by the LIDAR system, where it represents a region of increased atmospheric density, where photon count is proportional to the density. The authors of *Kaifler et al.* (2018) note an increased backscatter (thus NLC structures) like that of Figure 4-30 for a duration of nearly 5 hours. The largest backscatter measurement that the authors took was recorded at 01:07 UTC, and is close in time to the signal onset at Maynooth, which

occurred for MFR2 at 01:15 UTC and persisted for over an hour, ending around the same time as the second backscatter observation by *Kaifler et al.* (2018) (only two backscatter observation periods displaying NLCs, between 19:51 – 20:47 UTC and between 21:55 – 01:49 UTC were available to *Kaifler et al.* (2018)).

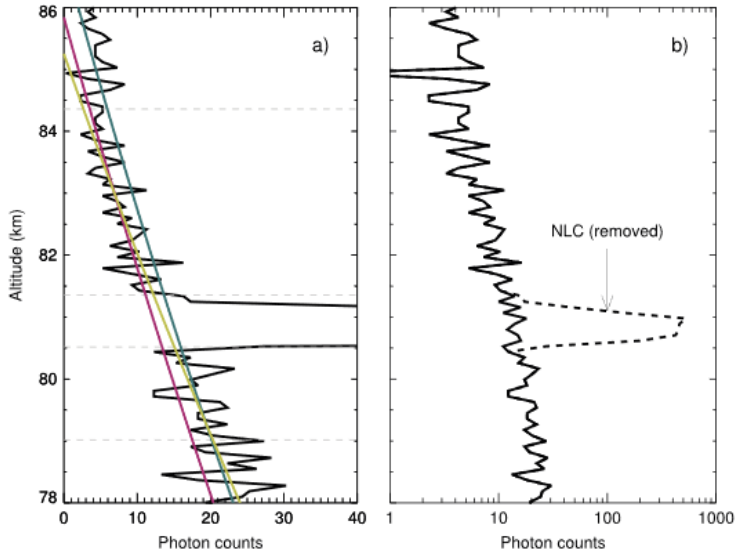

Figure 4-30: Plot from Kaifler et al. (2018) *showing the LIDAR backscatter indicating the presence of a NLC layer centred around 81 km. Plot (a) shows the backscatter with fits to the measurements (shown by the coloured lines), while plot (b) shows the profile obtained through LIDAR measurements if the NLC instance is removed. This measurement of the NLC by the LIDAR was taken between* 0:59 – 1:00 *UTC.*

Comparison to data from AIMS-CIPS satellite

In the paper by *Kaifler et al.* (2018), the researchers used data from the AIM-CIPS satellite to confirm the transport of ice particles making up NLCs to the region above the station. The data showing the albedo as measured by the satellite is shown in Figure 4-31, where the albedo is a direct measure of the reflectivity of the clouds. Figure 4-31 (in the top left of the figure) depicts a map of the Northern Hemisphere, specifically the area of the Arctic circle down to 50 °N, taking measurements in orbital strips (giving the daisy pattern). A large amount of albedo (associated with polar mesospheric clouds (also

known as NLCs)) is normally associated with the region of the Arctic circle during summer months (discussed in Section 4.4), with lesser amounts present in lower latitudes. However, Figure 4-31 (top right) shows a notable instance of albedo between the British Isles and Denmark, a feature not normally seen in the CIPS datasets. The bottom image of Figure 4-31 shows the ice water content present at these locations of albedo in the region of the British Isles, indicating the density of the NLCs present. Unfortunately, due to the orbital scan of the AIM satellite, the CIPS images do not cover the atmosphere over Ireland, but as pointed out by *Kaifler et al.* (2018) the images from the 18 July 2016 seem to add to evidence that a large outbreak of NLCs occurred over Northern and Central Europe.

One final note on these images is the method of observation that the CIPS satellite uses – reflected sunlight from the polar mesospheric clouds or NLCs (*McClintock et al.*, 2009; *Kaifler et al.*, 2018), which is the same process which is believed to produce the signature in Figure 4-23 (radiometer plot showing radiance vs. intensity).

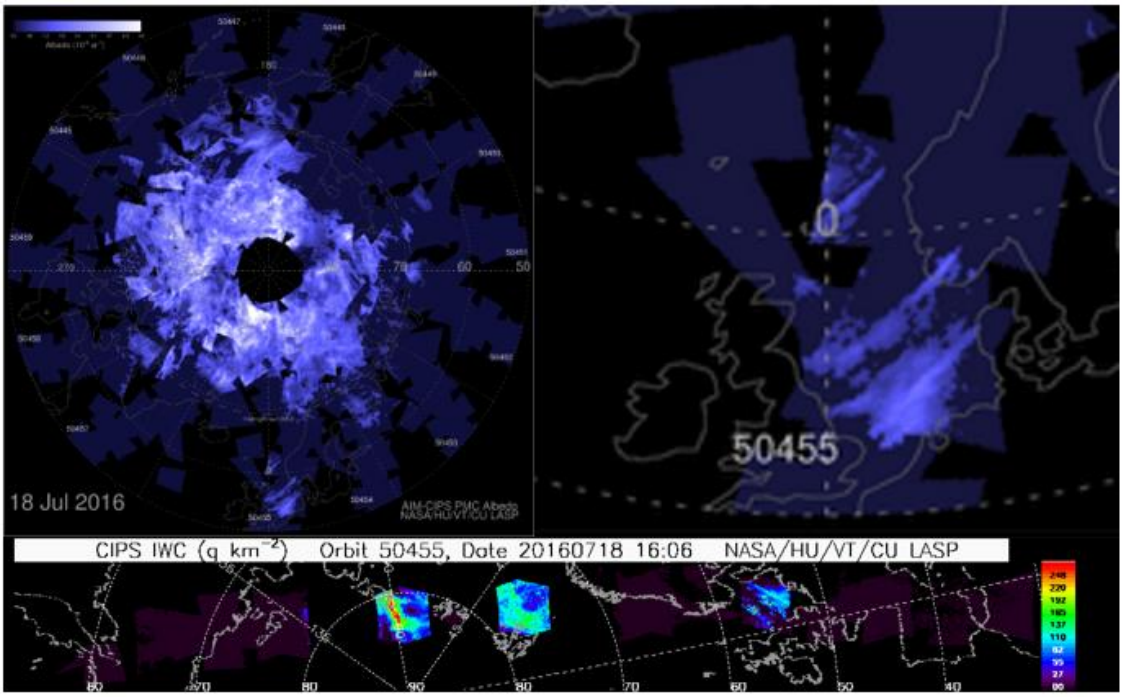

Figure 4-31: Albedo measurements (top two plots) for the 18 July 2016 showing a substantial amount of PMC albedo in lower latitudes (down to ~53°N), with some of this albedo occurring over the North Sea between the UK/Denmark/Norway. The lower plot shows the water content associated with these areas of albedo over the North Sea.

Comparison to data from NLCNET

The final piece of evidence presented here for the explanation of the radiances seen on 18/19 July 2016 are visual images amalgamated by amateur observers, and available on NLCNET (*NLCNET*, 2021). Observers mainly from Europe have recorded sightings of NLCs in various locations, with some nights having multiple entries. The night of the 18/19 July 2016 had numerous reports of visible NLCs from Wales to Estonia and Norway to Hungary, making it one of the more 'busy' nights in terms of NLC sightings (*NLCNET*, 2016). Figure 4-32 shows an example of the NLCs visible on the night above south-western Germany, where importantly the structure is photographed at a lower latitude than that shown in the CIPS imagery and the location of Maynooth. The location of the sightings over Wales (*NLCNET*, 2016) seems to indicate that NLCs were indeed in the area of the station and thus theoretically detectable.

Figure 4-32: Image of NLCs present over Freital, Germany (approximately 51 °*N) courtesy of images on NLCNET* (2016) *and photographed by Heiko Ulbricht.*

4.5.2. Case Study 2 – Signal on 21/22 June 2018

The second case study was recorded on the 21/22 June 2018 and is seen in the radiance measurements in Figure 4-33. As has been seen previously in Section 4.2.1, the majority

of the night conforms to the radiance seen on a typical night, except for a period close to sunrise. All three instruments, as shown in Figure 4-33 detect this signature at approximately 02:42 UTC (for the first instrument, in this case UWOSCR). The radiance signature is seen zoomed in in Figure 4-34, where both UWOSCR and MFR see the radiance peak in greater detail compared to that of MFR2, which although the instrument sees an increase in response, does not observe the same level of structure as that of the former two instruments. This discrepancy however may be explained by the field–of-view of the MFR2 instrument which, at the time of measurement, had a larger field-of-view. A larger field-of-view would result in a signal being averaged out and thus a smaller radiance response would be seen in that same instrument's data output (seen in Figure 4-34).

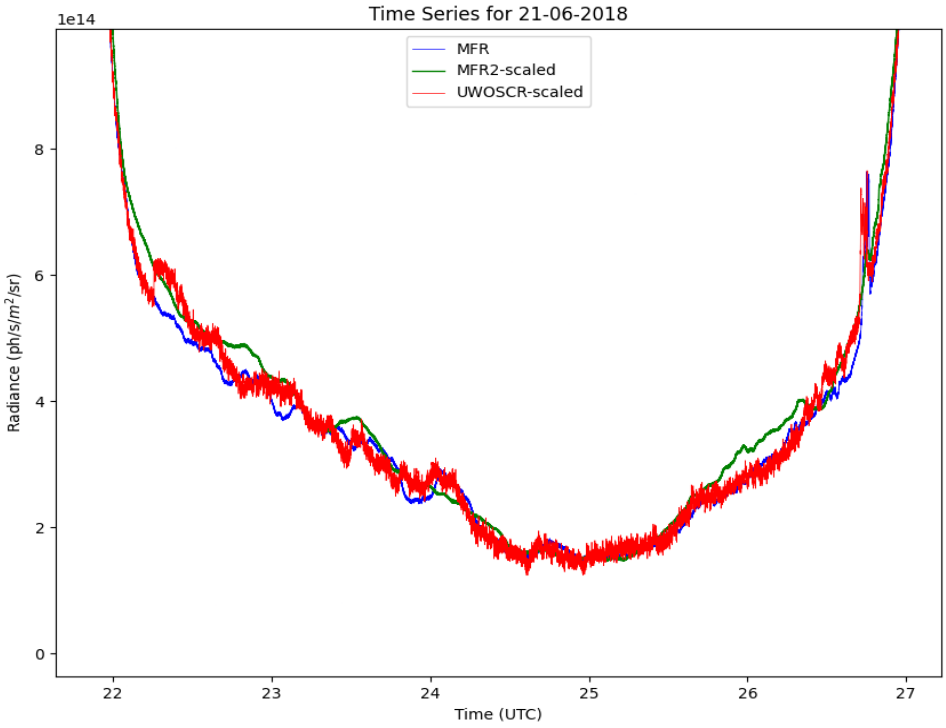

Figure 4-33: Time-series of the 21/22 June 2018, showing the signal of interest between 26.5 – 27 *UTC, which is shown in greater detail in Figure 4-34.*

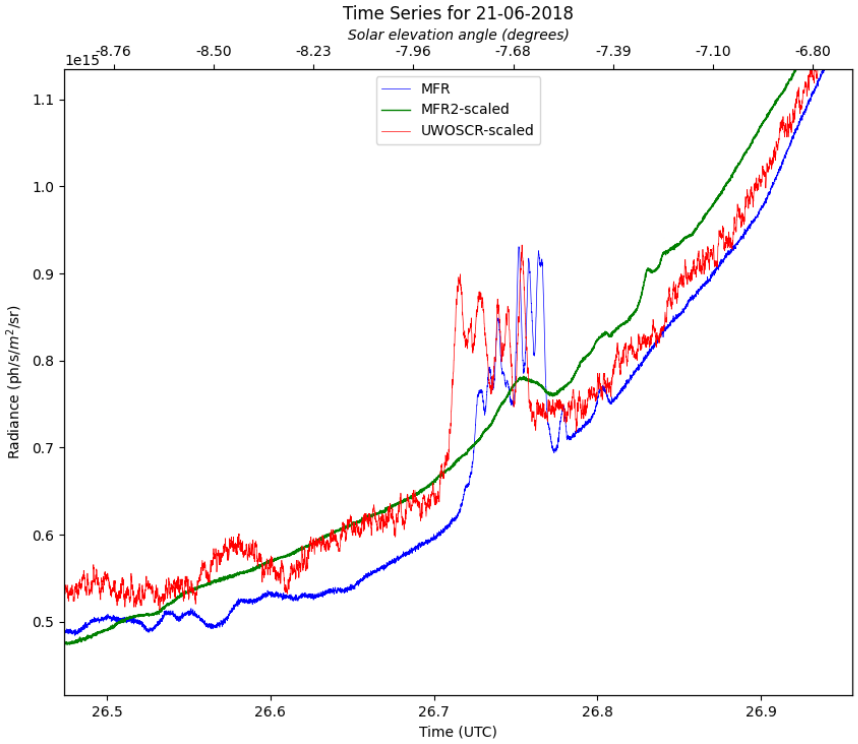

Figure 4-34: Detail of the signal seen in Figure 4-33 showing the structure observed

As seen in Figure 4-34, the increase in the radiance signal is approximately $2 \pm 0.5 I_0$ where, like before, I_0 is the background intensity immediately preceding the signal onset (see above in Section 4.5.1). The same figure shows the position of the Sun at the time of signal measurement, discussed later in relation to the source determination (Section 4.5.2.3). As before in Section 4.5.1, the weather conditions are discussed next to ensure the signal is not a result of cloud conditions.

4.5.2.1. Weather Conditions

This signal occurred after the introduction of the cloud detector to the Maynooth station and thus this instrument is relied upon rather than that of the power spectrum analysis. Figure 4-35 shows the clarity of the night, showing an approximately constant value of between 30-32, which is a requirement for a night to be considered clear and usable for analysis (Section 4.2.1 and Section 4.2.2). The most important factor regarding the

measurements in Figure 4-35 is that there is no notable dip in clarity at the time of the signal (02:42 UTC), thus indicating a clear sky over the station.

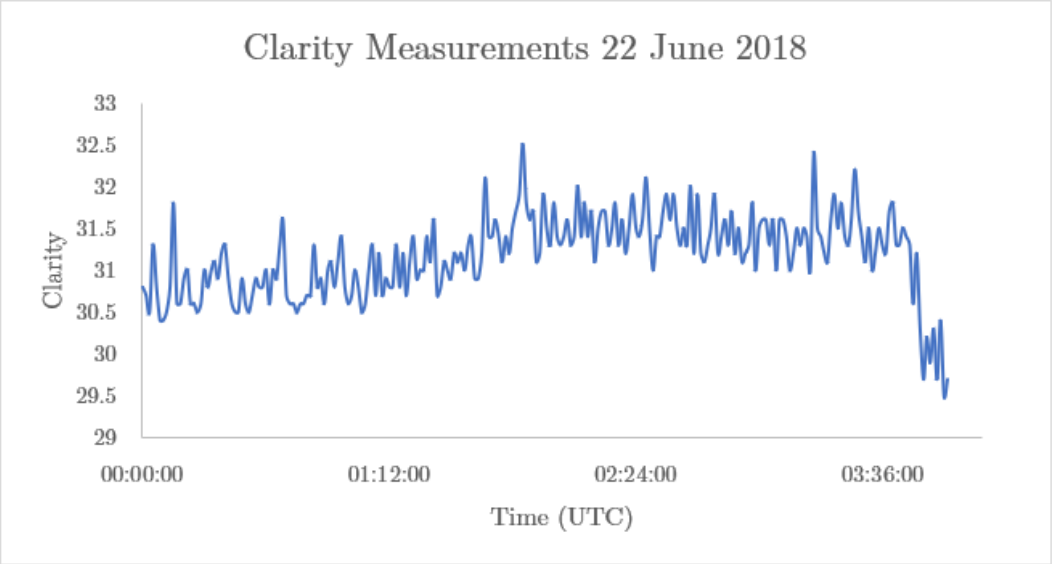

Figure 4-35: Clarity measurements on the morning of the 22 June 2018

The data shown in Figure 4-35 is bolstered by the measurements taken by Met Éireann at Casement Aerodrome, the recording of which is shown in Figure 4-36. The morning of the 22 June 2018 (when the signal occurs) shows cloudiness levels of only 1 (indicating very clear skies, with few if any clouds, as described in Section 4.2.1).

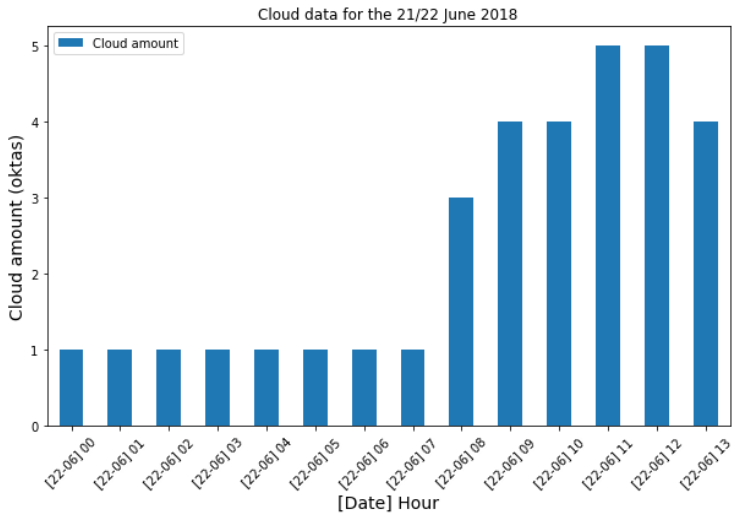

Figure 4-36: Cloudiness measurements on the 22 June 2018, showing clear skies during the approximate time of the signal (~02:42 UTC)

4.5.2.2. Signal Characteristics

Like in Section 4.5.1, describing the first case study, the basic characteristics of the signal can be extracted from a single instrument. In this case, MFR is used to obtain the amplitude, wavelength, frequency and period, where the amplitude of the signal, as stated previously, is $2 \pm 0.5I_0$.

The duration of the burst is only around 4 minutes, much shorter than the first case study, but displaying a similar structure. The variation seen in the signal is observed by both MFR and UWOSCR, but only a small increase in radiance is seen in MFR2 (the reason for which is detailed at the beginning of this section (Section 4.5.2)). Based on the variation seen in MFR, the period of the signal can be manually calculated from the time-series in Figure 4-34, giving a value between $19 - 22$ seconds and thus a frequency range of $0.046 - 0.052$ Hz (such a frequency range occurs in the infrasonic range). The wavelet transform, shown in Figure 4-37, provides more detail with regards to the frequency, where there is power associated with higher frequencies in the signal. Although less pronounced than that of Case Study 1, there is increased power compared to the background at these frequencies. Estimated frequencies associated with the signal appear to be centred around 0.05 Hz (increased brightness as seen in Figure 4-37), matching the manual calculation made from the time-series.

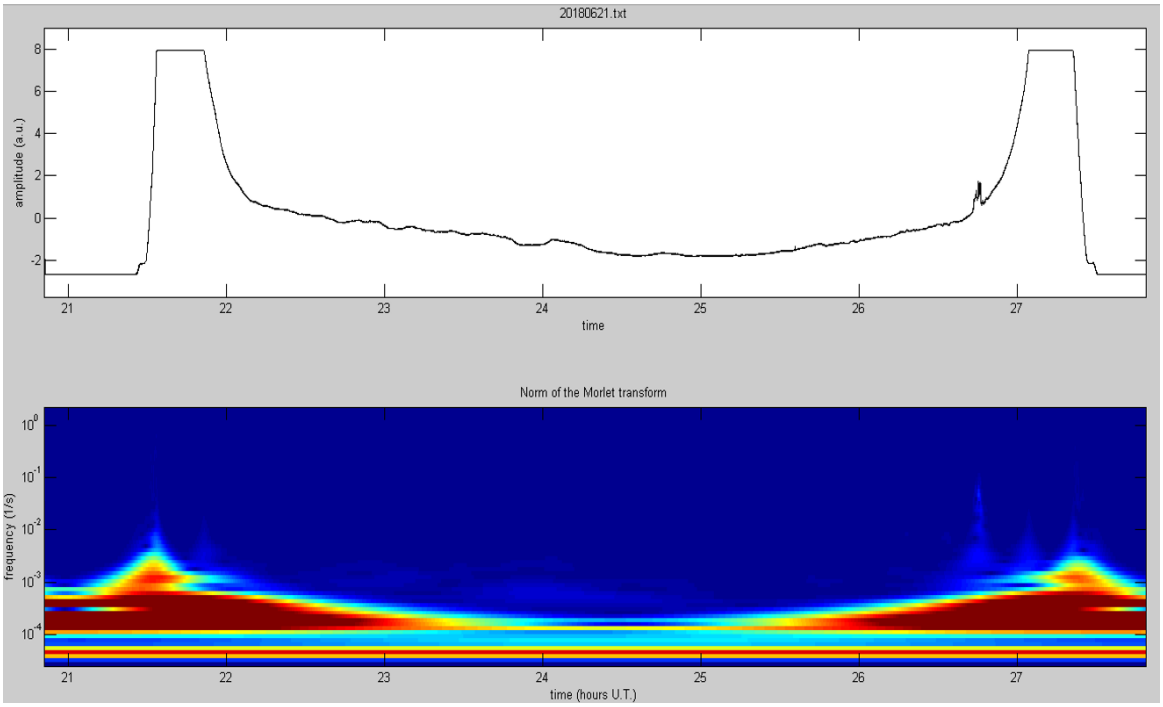

Figure 4-37: Time-series and wavelet transform of the night of 21/22 June 2018. For the time of the signal (around 26.75), a larger amount of power is associated with higher frequencies, reaching 0.1 *Hz.*

Calculation of the direction and speed of the signal proved difficult due to the averaging of the signal seen in MFR2, and thus the beginning and end of the signal in this instrument's dataset are uncertain. Based on an estimate of the signal increase across all three instruments, the speed of the signal is determined as 251 ± 25 m/s, where the large error on the value stems from the uncertainty of the signal onset in MFR2. The best estimate of the signal direction is based on the signal being first observed at UWOSCR, next by MFR and finally by MFR2, resulting in a direction of $40° \pm 19°$ (east of north), pointing from north-east to south-west (again the large error is due to the uncertainty introduced by the MFR2 measurements).

4.5.2.3. NLC Theory and comparison to other sources

As before in Case Study 1, sources that could have produced an impact in the hydroxyl layer were first investigated, including earthquakes and other high impact events. However, no large source was identified except for the presence of NLCs above the station, which may explain the sudden onset and decay of the signal in MFR and UWOSCR. The following paragraphs will discuss evidence of these structures above the station during the time of the signal.

Comparison to data from AIM-CIPS satellite

Figure 4-38 shows the CIPS data on the evening of the 21 June (top) and the morning of the 22 June 2018. On the evening of the 21 June, Figure 4-38 shows no albedo in the vicinity of Ireland, however as shown in the bottom part of the figure, which shows the data from the morning of the 22 June, instances of albedo are observed just north of the British Isles.

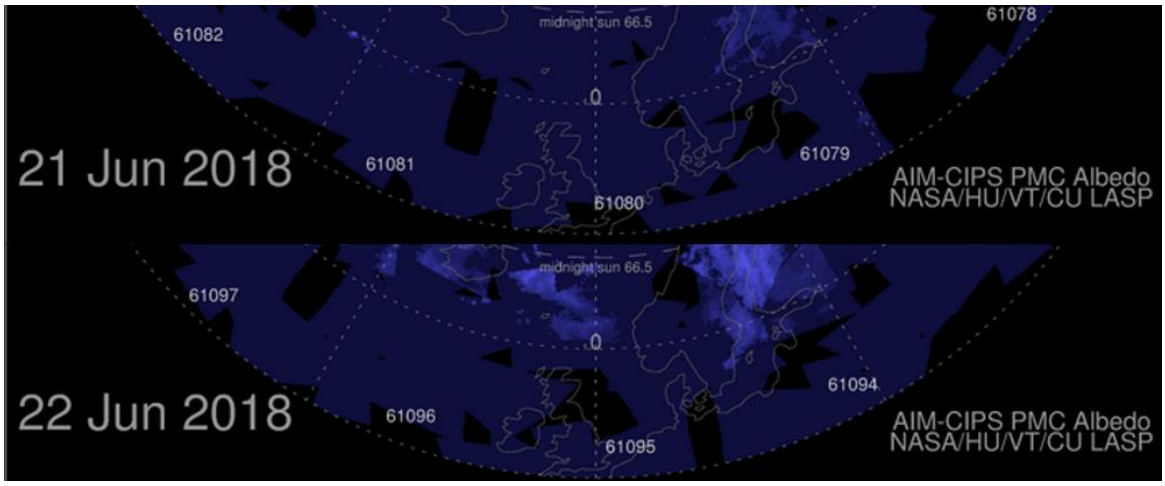

Figure 4-38: Data from CIPS showing the albedo on the day preceding the time-series and the day after. These measurements in the vicinity of Ireland were obtained throughout the day on 21/6/2018 (top) and 18:52 – 20:32 UTC (22/6/2018) (bottom)

Although the albedo during the morning hours is still north of nearly 60 °N, this may not discount the theory that the signal is due to NLCs. It may be that the density of the NLCs are too low and thus do not show up in the CIPS dataset that morning (data which is obtained nearly 3 hours after the signal onset), a fact that is supported by a smaller signal in this case compared to that of Section 4.5.1. The albedo observations do appear to reach latitudes of nearly 56 °N, as indicated by the albedo increase over Southern Sweden in Figure 4-38(bottom). Visual evidence of NLCs near the station is explored in the next section to determine the latitude extent of the structures near Ireland close to the signal time.

Comparison to data from NLCNET

As in Section 4.5.1, NLCNET (*NLCNET*, 2021) was consulted to obtain local visual evidence of NLC structures close to or over Ireland. In the section above, it was seen that although albedo measurements did occur to the north of Ireland, these same observations were not seen to extend farther south based on the CIPS imagery. Based on the data from NLCNET, NLCs were observed at several locations south of Maynooth's latitude, including Somerset, England (~51 °N) (where the photograph accompanying the report is shown in Figure 4-39) and Wokingham, England (51.42 °N), around the same time as the signal (~02:45 UTC). These NLC structures during the night were also observed in locations farther west than the locations in England, where they were observed over Anglesey, Wales. These observations indicate that NLCs were present in the area during the time of the signal, and thus the CIPS data does not represent the entire extent of the NLCs for a given night of data.

Figure 4-39: NLCs photographed by David Tate, where the structures appeared towards north in Somerset (*NLCNET*, 2018).

As well as the presence of NLCs in the area, the position of the Sun also matches with the requirement of illuminating the NLC cloud base. Section 4.4 outlines that NLCs are normally only visible when the Sun is between $6° - 16°$ below the horizon. In both case studies presented, this angle criteria was met (confirmed through code developed by *Verhulst* and *Stankov* (2017), as well as the timing of the signals compared to sunset and sunrise). The difference between the two signals presented is mainly due to their amplitude and duration rather than their structure, where the signal in the second case is much smaller than that of the first case. If it is assumed that the signal here is due to an NLC structure, the smaller signal could be a result of a more tenuous layer that reflects less light than Case Study 1.

The possibility of waves generated by the solar terminator was also considered in the case of this signal, but as before, the amplitude of the given disturbance made this source unlikely. With the available evidence currently known, the presence of an NLC is deemed to be the likeliest source of the signal seen on the 21/22 June 2018.

4.5.3. Other Possible NLC instances

The previous two subsections have considered evidence of NLC signals in the dataset that cannot be explained by tropospheric clouds. Circumstantial evidence provided by other studies (*Kaifler et al.*, 2018), satellite data and visual observations was given for the cases in an attempt to explain the source of the radiance signals as NLCs above the station. Other possible instances of NLCs in the dataset (specifically the MFR dataset) are presented in Table 4-2, which shows the approximate times of signals believed to originate from these structures. All of the instances shown have similar signal structure to Case Study 2 (presented in Section 4.5.2), where a sudden increase of radiance, followed by variation of the signal around the new radiance level established by the sudden onset, and then concluded with a sudden decrease to signal levels seen before onset is observed. The majority of the signals are seen either immediately after sunset or just before sunrise, with few instances following Case Study 1's timing (occurring closer to midnight).

As with the main two case studies, data from the AIM-CIPS satellite observations, as well as visual NLC confirmations from NLCNET are used to complement the signals found in the datasets. Much of the evidence from these data sources is sparse and cannot conclusively point to the presence of NLCs, but in other cases, Table 4-2 shows that the satellite data and the visual observations point towards the strong possibility of NLCs above the station (especially in the cases of 26 June 2018 and 27 June 2019).

Date	*Approximate time of Signal*	*0.78 Hz spike*	*CIPS (Lowest latitude of PMC albedo close to station)*	*NLCNET (Locations and (number of sightings))*
3rd June 2013	Before Sunrise	No spike	65°N	Germany, Sweden, England, Wales (9)
6th June 2013	After Sunset	No spike	64°N	No visuals
13th June 2013	After Sunset	Small spike	61°N	Wales, Scotland, Canada, England (5)
26th July 2013	Before Sunrise	No spike	67°N	Scotland, Norway (4)
5th June 2014	After Sunset and Before Sunrise	No spike	70°N	Wales, England, Canada, Ireland (7)
5th July 2014	After Sunset	No spike	57°N	No visuals
9th June 2015	After Sunset	No spike	65°N	No visuals
2nd July 2015	After Sunset	No spike	65°N	Estonia (1)
4th July 2015	After Sunset	No spike	60°N	Estonia (1)
24th June 2018	Before Sunrise	NA	59°N	Scotland, England, Canada, Wales (17)
26th June 2018	Before Sunrise	NA	50°N	Germany, Scotland, Poland, England, Hungary, Estonia, Wales (10)
8th August 2018	Before Sunrise	NA	60°N	Scotland (4)
27th June 2019	Before Sunrise	NA	58°N	Scotland, Poland, Germany, England, Netherlands, Norway, Wales, Scotland, Estonia (18)

Table 4-2: Times of possible instances of NLCs in the MFR dataset, with observations made by the AIM-CIPS satellite and NLCNET included (Case Studies 1 and 2 are not shown)

On both the 26 June 2018 and the 27 June 2019, the AIM-CIPS satellite data shows that Polar Mesospheric cloud albedo was found to inhabit latitudes only 4.5° away from the station latitude at most, with the signal found on the 27 June 2019 coinciding with evidence of PMC albedo above the station's location. Visual evidence of these structures was also numerous, with observers in locations like North Wales observing NLCs during the time in question. These smaller cases are not dealt with further however, as only a small amount of variation is seen within the signals, where meaningful frequency characteristics cannot be extracted. The strengths of the two main case studies are the variation in the signals and the observation of the cases by all three instruments, which allowed for characteristics like speed, direction and frequency to be calculated.

4.6. Chapter 4 Summary

This chapter summarised the main results found in the datasets which represent instances of radiance observations with frequencies in the infrasound regime not emanating from the hydroxyl layer. These results have included effects due to sunlight, moonlight and terrestrial clouds, but radiances associated with airglow of other species has also been observed.

The emphasis in this chapter were the results due to the likely presence of noctilucent cloud structures above the station, which produced large radiance increases in the time-series, which at times rival that of radiances produced by sunlight effects. These high radiances would be expected as the observations likely result from sunlight reflected from the cloud base of NLCs, which enter the apertures of the three detectors.

Two main case studies have been shown in Section 4.5.1 and Section 4.5.2, representing the largest and most likely cases of NLC structures in the data series. Case Study 1 provided a large signal reaching amplitudes three times larger than the preceding background radiance levels. The frequency of the signal has been estimated between $\sim 0.036 - 0.04$ Hz and travelled at a speed of almost $\sim 336 \pm 12$ m/s across the station, travelling from south-west to north-east at an angle of $\sim 61° \pm 4°$ east of north. For Case Study 2, a smaller signal was seen, but it also seen to be likely due to NLCs, based on the season and timing of the disturbance. The amplitude of the signal was found to be nearly two times the background radiance and has a frequency of around 0.05 ± 0.003 Hz, while propagating across the station at around 251 ± 25 m/s from a direction of north-east to south-east ($40° \pm 19°$ east of north). Compared to the first case study, the uncertainties associated with the second case study parameters are much larger, and are explained by the averaged signature in the MFR2 data. These values would be reasonable if the signal could be assumed to be a plane wave travelling through the hydroxyl layer. However, as the signal is from light reflecting from the NLC base, it cannot be accurately described as a plane wave and so estimates of the speed and direction are likely not appropriate to describe the signal characteristics.

Although these case studies do not represent results that directly contribute to the aim of the thesis, that is, to measure infrasound in the hydroxyl layer, they do however represent the capability of the detectors to observe signals with infrasonic frequencies. Due to the assumed speed of the solar terminator across the NLC base, signals are observed in the time-series with frequencies that would correspond to infrasonic frequencies in the acoustic domain. This aspect achieves a part of the main aim outlined, where frequencies corresponding to infrasound can be detected, indicating that

the detectors are capable of this feat. Although not the main aim of the thesis, the observation of NLCs at this mid-latitude station may help to fill the coverage gap of NLC observing stations around the world. The connection between NLCs and climate change is still under debate, but this observing station may, in future, aid in determining whether the frequency of NLCs is increasing, which in turn may be linked to a changing climate (*Lübken et al.*, 2018).

In the next chapter, signals not explained by NLC presence in the atmosphere, but possessing similar infrasonic characteristics, are presented.

5. Infrasound Modulation of Infrared Hydroxyl Emissions Detected at Maynooth

5.1. Introduction

Up to this point, signals originating from sources other than the hydroxyl layer have been discussed. This has included noise from background radiation, including scattering of sunlight, streetlights scattered from meteorological clouds, and moonlight. Another, more irregular source of infrared radiation appearing in the data is likely a result of sunlight reflected from noctilucent clouds. A number of case studies in Chapter 4 dealt with these noctilucent cloud observations and appear to provide a new way of viewing the phenomena.

This chapter explores the infrared signals emanating from the hydroxyl layer resulting from various phenomena, specifically due to two types of perturbations – gravity waves and infrasonic waves. Section 5.2 contains a brief analysis of gravity waves, which make up the clearest wave signatures in the datasets, originating from the hydroxyl layer. These waves are not the main focus of the thesis and so discussion is kept reasonably brief, but the analysis methods used to extract information about these gravity waves are also used to analyse acoustic waves which form the substance of Sections 5.4 to Section 5.7. Section 5.3 introduces the types of infrasound (whether continuous or "N-shaped") that can be theoretically detected and have been observed by the IMS network, a network previously discussed in Chapter 1 (Section 1.1 and Section 1.8). Section 5.4 expands on the general infrasound section, presenting the analysis of the main datasets for evidence of microbaroms. Sections 5.5 – 5.7 present case studies of impulsive and short-lived infrasound signatures, where the characteristics of the signal are shown and tentative connections to potential sources are provided. Although other instances of infrasonic-like disturbances are seen in the dataset, these case studies offer the best examples found of these waves.

5.2. Gravity Waves

Although the main aim of this project is to observe and analyse infrasonic waves, by way of hydroxyl emission observations, the instruments used are also capable of the detection of gravity waves (GWs) in the same layer. This capability of GW detection is also shown by *Rourke et al.* (2017) using similar instrumentation.

These buoyancy waves show the concept of wave detection by the tripartite array, examples of which are shown in this section. Gravity waves can be differentiated from infrasound based on frequency, a characteristic which has already been discussed in Chapter 1, where gravity waves occupy a lower frequency band compared to infrasound. The upper cut-off frequency for gravity waves is bounded by the Brunt-Väisälä frequency, given by $\omega_g = (\gamma - 1)^{\frac{1}{2}} g/c_s$, shown in Figure 5-1. Gravity waves are separated from acoustic waves based on frequency, where acoustic waves are bounded on the lower end by the acoustic cut-off frequency given by the equation $\omega_a = \gamma g/2c_s$. The frequencies of these two domains are connected through the dispersion relation for the waves, given in Figure 5-1 and shown in Equation (5-1) below (which describes the propagation of these disturbances):

$$(\omega^2 - \omega_a^2) + \left(\frac{\omega_g^2}{\omega^2} - 1\right) k_x^2 c_s^2 - k_z'^2 c_s^2 = 0 \tag{5-1}$$

Equation (5-1) shows the relationship between a given frequency (ω) and the acoustic cut-off and Brunt-Väisälä frequencies. The dispersion relation also demonstrates the relation between the frequencies and the horizontal (k_x) and vertical (k_z) wavenumbers, as well as the speed of sound (c_s).

Gossard and *Hooke* (1975) show this dispersion relation for such waves propagating vertically in the atmosphere, as in Figure 5-1. Although Figure 5-1 provides general information regarding the dispersion relation and acoustic and gravity domains, Figure 5-2 gives a simpler view of how the acoustic and gravity wave domains vary as a function

of altitude. Figure 5-2 shows both a dashed line representing the Brunt-Väisälä frequency (N), defining the upper end of the gravity domain on the left and another dashed line that represents the acoustic cut-off frequency (N_A), bounding the acoustic domain on the right. Within the mesopause region, where the hydroxyl layer is located, the Brunt-Väisälä frequency is approximately 3.7 mHz, but this is dependent on the stability of the atmospheric region (*Evers* and *Haak*, 2010). Above this frequency, gravity waves do not exist and the acoustic cut-off frequency takes over and gravity ceases to be the dominant force on wave propagation. The acoustic cut-off frequency occurs at around 4.5 mHz based on Figure 5-2 below. Both Figure 5-1 and Figure 5-2 show that a region separates the two domains, where neither gravity or acoustic waves exist, but where evanescent or non-propagating waves do exist. The boundaries of these domains are of greater interest here, where they dictate whether waves are in the infrasonic frequency, and will be used in later case studies to confirm this characteristic.

Dispersion relation $\left(\omega^2-\omega_a^2\right)+\left(\frac{\omega_g^2}{\omega^2}-1\right)k_x^2c_s^2-k_z'^2c_s^2=0$

$\omega_a=\gamma g/2c_s$ acoustic cut-off frequency

$\omega_g=(\gamma-1)^{1/2}g/c_s$ Brunt-Väisälä frequency

$c_s=$ sound speed

$k_z'=kz+i/2H$

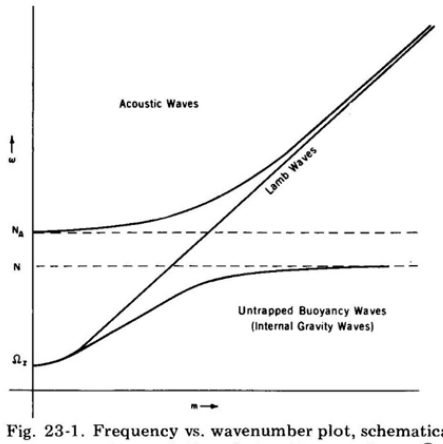

Fig. 23-1. Frequency vs. wavenumber plot, schematically illustrating domains of different wave types. At m = 0, Branch A → N_A, Branch B → Ω_z.

Figure 5-1: Equations describing the propagation of acoustic and gravity waves in the atmosphere as seen in Artru et al. (2004) *(top) and the frequency wavenumber plot from Gossard and Hooke (1975) (bottom) – a similar plot is seen in Figure 1-18 in Chapter 1.*

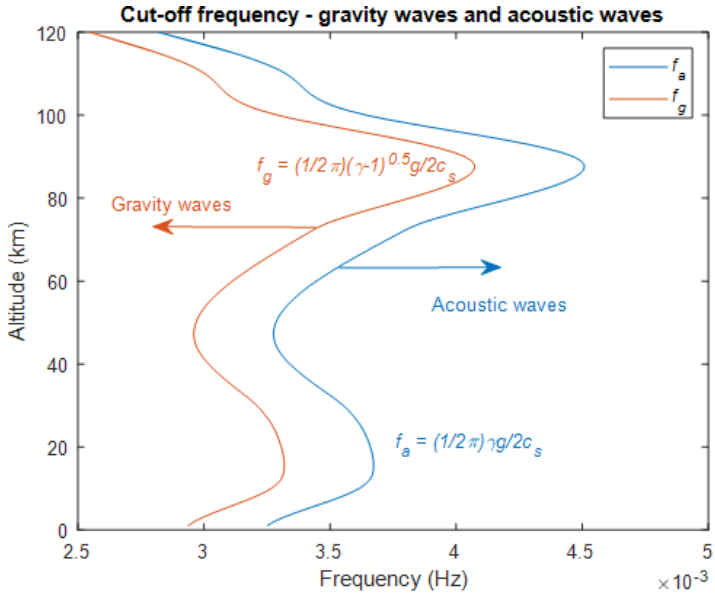

Figure 5-2: Acoustic cut-off and Brunt-Väisälä frequency limits as a function of altitude. In the region of the mesopause, the two frequencies reach an upper limit, due to the colder temperatures of the region. Gravity waves are defined up to ~4 mHz, whilst the lower bound of acoustic waves is around ~4.5 mHz in this atmospheric layer. Credit: F.J Mulligan after Jones and *Bedard* (2018)

5.2.1. Gravity Wave Determination by Manual Methods

For gravity wave observations, clear nights over Maynooth are needed, which are nights confirmed to be clear by cloud observation techniques, as outlined in Section 4.2.1. The formation of gravity waves has been discussed in Chapter 1, and is the consequence of the buoyancy force acting upon oscillating air parcels, which in turn are under the influence of the restoring force. According to *Nappo* (2013), these waves should be ubiquitous in the atmosphere. This theory seems to be borne out in the datasets recorded during this project, as gravity waves are observed in over 50% of the clear nights analysed in the dataset.

Gravity waves have a recognisable sinusoidal shape which are shown in the time-series of clear nights where they are present. Figure 5-3 demonstrates this typical shape for gravity waves observed on a clear night (16 May 2013), where the shape of the waves are used for the determination of wave characteristics such as duration and period. Gravity

wave trains are shown between $24 - 25.5$ $(00:00 - 01:30)$ UTC and after 26 $(02:00)$ UTC, with the clearest parts of these trains having durations of 54 minutes $(00:24 - 01:18$ UTC) and 24 minutes $(03:00 - 03:24$ UTC). These two trains are shown in greater detail in Figure 5-3(b) and (c), where the average period of train (b) is around 6 minutes and 14 seconds, while the second wave train shown in Figure 5-3(c) possesses an average period of 4 minutes and 45 seconds.

More detail regarding the gravity waves shown in Figure 5-3 is determined through the power spectrum for the night, which is shown in Figure 5-4. The immediate observation made from the power spectrum is the lack of peak around 780 mHz, shown by the red arrow on the right-hand side of Figure 5-4, indicating the lack of meteorological clouds over the station during the night.

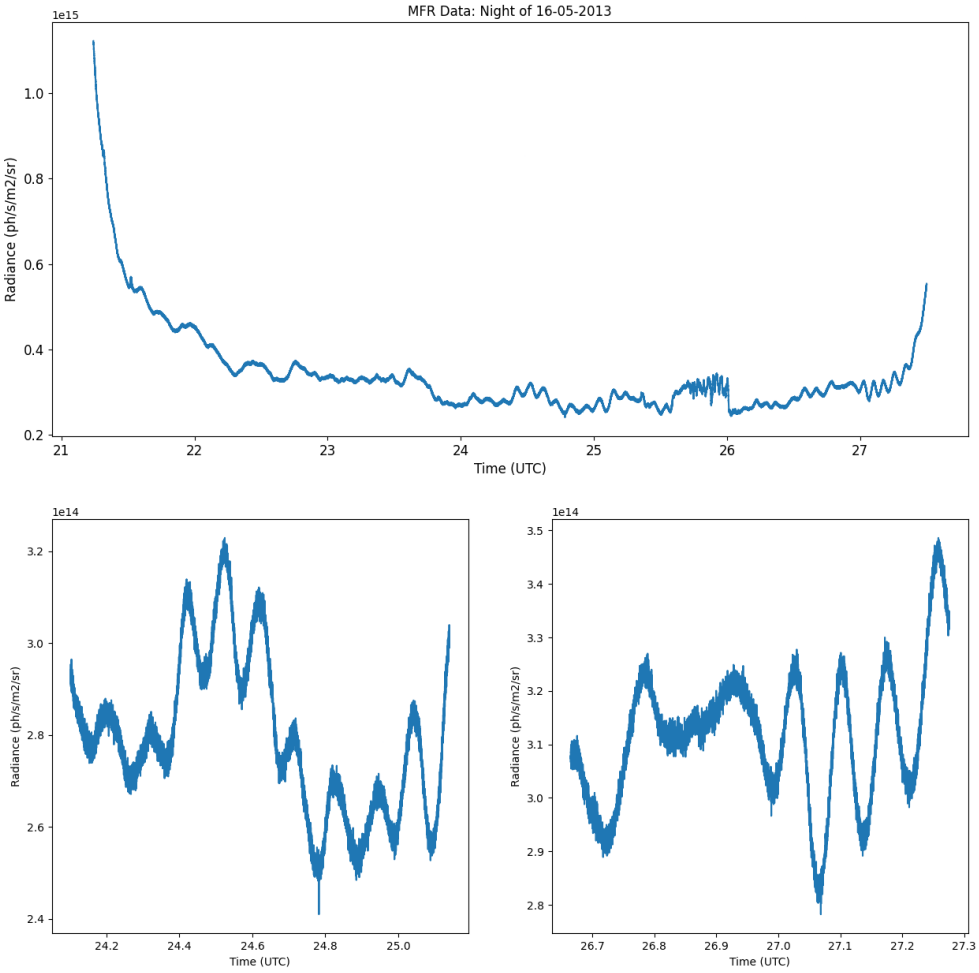

Figure 5-3: The night of 16/17 May 2013, showing multiple gravity wave trains, particularly beginning around 00:30 (24.5 UTC) and 03:00 (27 UTC).

The power spectrum also shows peaks likely associated with GW activity, with a peak around 2.67 mHz and a smaller peak around 3.46 mHz. The 2.67 mHz peak is seen in both Figure 5-4, and in more detail in Figure 5-5, while the 3.46 mHz peak is only seen in Figure 5-5. Converting these frequencies to periods, 2.67 mHz corresponds to a period of 6 minutes and 14 seconds. This is completely consistent with the period analysis undertaken manually for the first wave shown in Figure 5-3(b). The smaller peak at around 3.46 mHz corresponds to a period of around 4 minutes and 41 seconds. These periods are consistent with gravity wave periods as shown from Figure 5-2. The Brunt-Väisälä frequency in the region of the hydroxyl layer is around 4 minutes according to the orange curve shown in Figure 5-2 and so periods larger than this are within the gravity domain.

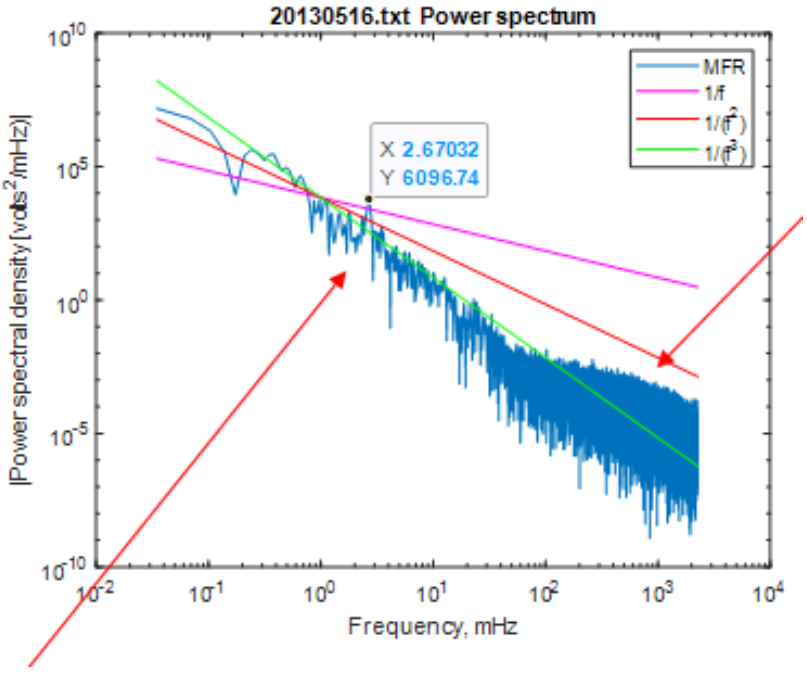

Figure 5-4: Power spectrum showing the gravity wave frequency region, with a peak indicating their presence (red arrow on the left). The power spectrum also shows the lack of the 0.78 Hz signature (red arrow on the right) that indicates the lack of cloud cover.

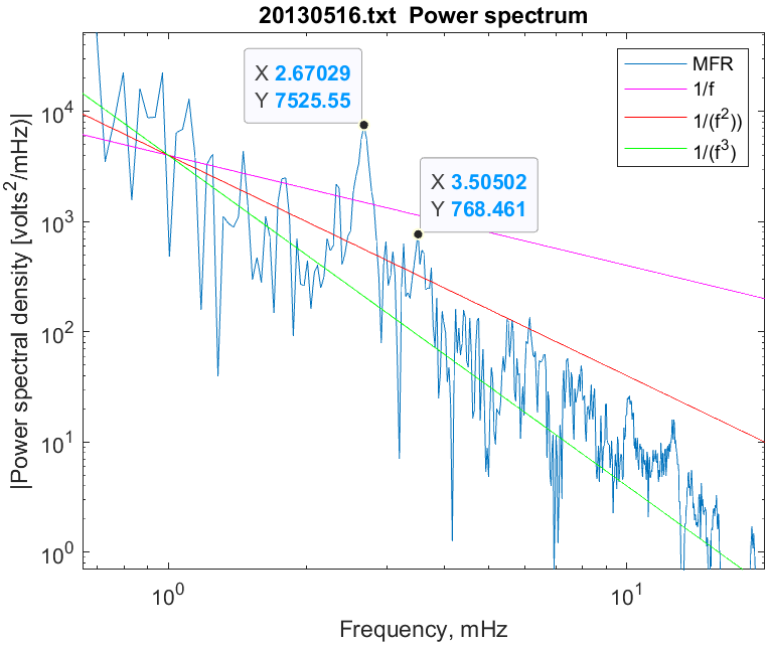

Figure 5-5: Close up of Figure 5-4 showing the two peaks associated with gravity wave frequencies (2.67 mHz and 3.47 mHz)

Figure 5-3 also shows a small amount of infrasound between $25.5 - 26$ UTC in the time-series, and will be discussed in greater detail in Section 5.7 which deals with case studies of infrasonic sources.

A second night showing GW activity is seen in Figure 5-6, with the clear sinusoidal shapes of the waves visible at several intervals during the night of the 4/5 April 2018. Although the GW trains occur at multiple instances, the main wave train of continuous GWs persists for 2 hours between $24 - 26$ UTC. The average period of the GWs in the wave train is approximately 5 minutes, which corresponds to a frequency of 3.33 mHz (which is in the gravity wave range according to Figure 5-2). With regards to the GWs seen after 28 UTC, these show less consistent periods compared to the main wave train, but do have periods within the GW range.

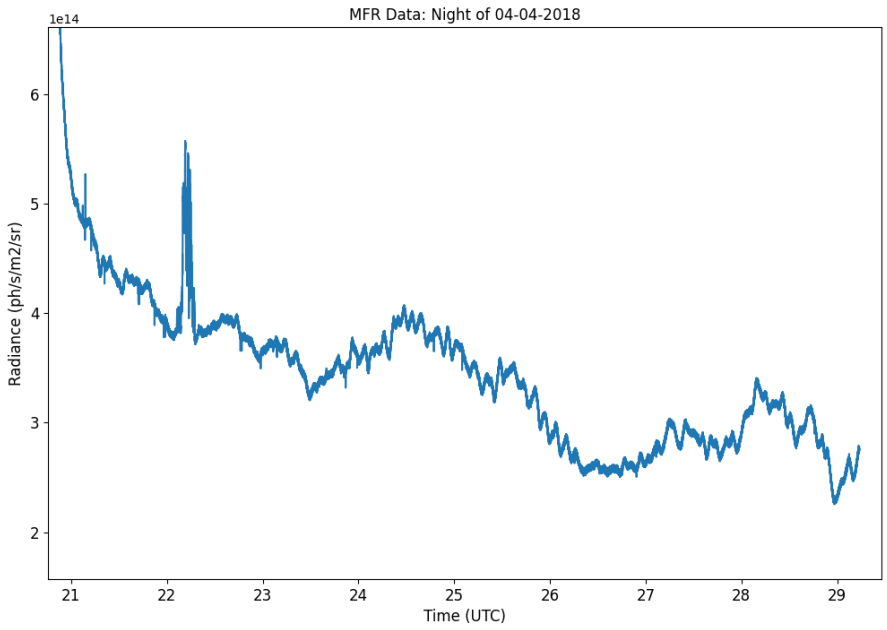

Figure 5-6: The night of 4/5 April 2018, showing long duration gravity wave trains, beginning just after 00:00 (24 UTC) – the peak after 22:00 UTC is associated with cloud.

GWs which consist of periods of approximately 5 minutes appear to be the most common within the datasets, representing the majority of these waves over the Maynooth station. These gravity waves thus have periods close to the lower boundary of gravity wave periods (the Brunt-Väisälä period, or more commonly the corresponding Brunt-Väisälä frequency). More characteristics regarding the GWs can be extracted from the tripartite array data, characteristics which are obtained by plotting the time-series from all three instruments (MFR, MFR2, UWOSCR) as shown in Figure 5-7 and Figure 5-8 for the 4/5 April 2018. These plots show the signatures found during the night of 4/5 April 2018 are also found in the time-series of MFR2 and UWOSCR.

Through directional analysis, already shown in Chapter 4 (Section 4.5) and described in Chapter 2 (Section 2.5), the speed and directional of the GWs can be calculated. As mentioned in previous paragraphs, the main wave train begins at around 24 UTC, and a brief estimate of the speed and direction of the waves from this point gives values of 63.3° west of south and 77.8 m/s. Based on the values found by *Rourke et al.* (2017), the speed of the GWs found in the time-series appear to be fast GWs but of course they are influenced by the prevailing wind speed at the time.

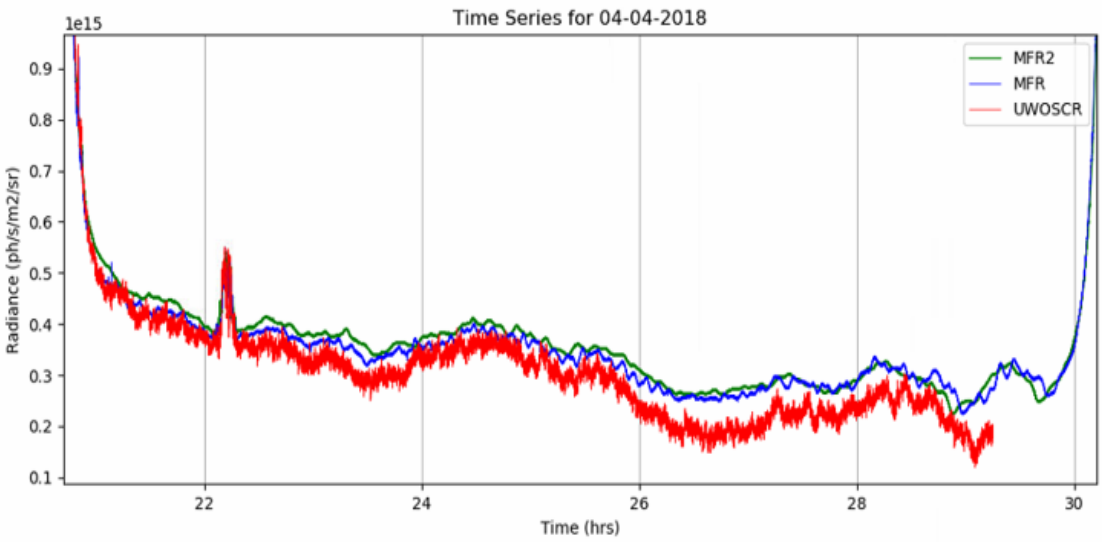

Figure 5-7: Gravity wave trains observed by all three radiometers on the 4/5 April 2018

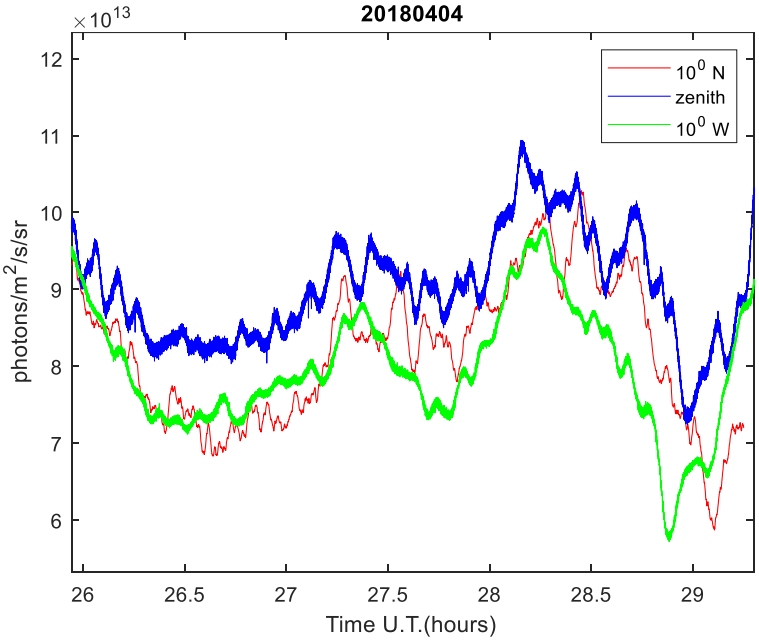

Figure 5-8: Gravity wave train detail observed by all three radiometers on the 4/5 April 2018. Directional and speed information can be obtained through lag analysis as outlined by ElGabry et al. (2017)

These same methods of parameter determination will be used in the following sections to demonstrate the applicability to infrasonic disturbances.

5.3. Infrasound

The main aim of this thesis is to demonstrate the capability of a tripartite array in observing low-frequency infrasonic waves. Infrasonic waves are not constrained to one type of shape or set of characteristics, and instead an infrasound wave's characteristics are based on the source of the infrasound signal. This fact becomes important for the aim of the CTBTO for infrasonic monitoring, to distinguish between infrasound created by different sources. *Bittner et al.* (2010) note many prominent infrasonic sources create one or two types of two wave shapes – continuous trains and/or impulsive signals. These wave shapes can be further differentiated based on the frequency and amplitude of the given signals, which may lead to source identification as shown in Figure 5-9. Both types of wave shape shown in the figure are investigated in the following sections (Section 5.4 – Section 5.7).

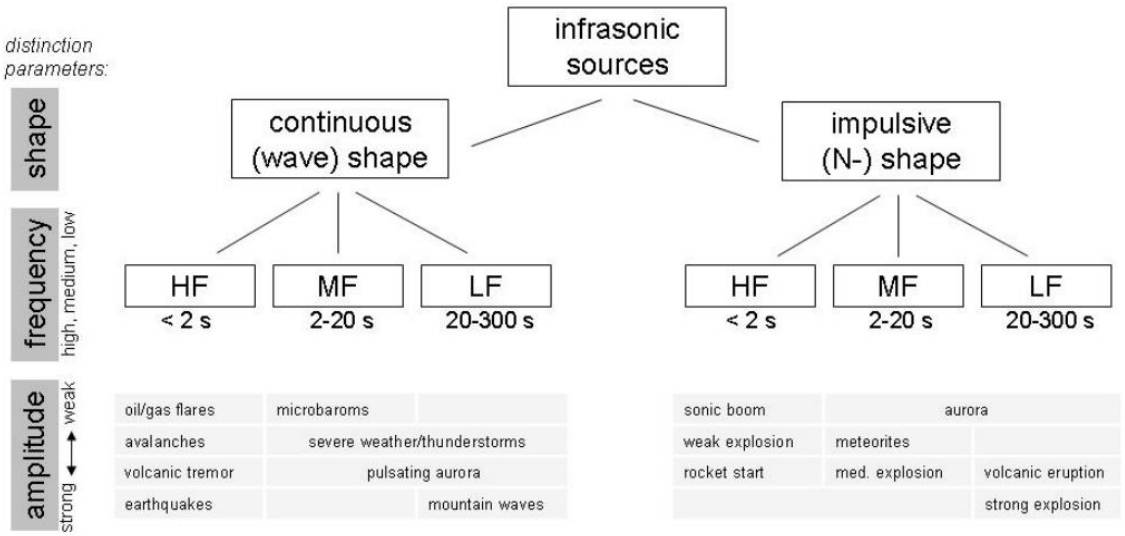

Figure 5-9: Schematic from Bittner et al. (2010) *showing the categorisation of infrasonic signals and how the shape, frequency and amplitude can help determine the source of the signal. Bittner et al.* (2010) *appear to determine these characteristics through modelling*

Section 5.4 discusses the first type of infrasonic wave shape - continuous wave shapes, which in the case of those shown, are a result of microbaroms within the atmosphere. Microbaroms are a ubiquitous source of infrasound in the atmosphere and are regularly

treated as noise in the IMS networks, but due to the fact that they are ever present, they are considered a good target for proving the capability of instruments in the detection of infrasound. The other infrasonic wave type, due to impulsive signals, are then discussed in Section 5.5, where the case study presented relates to a clear and coherent N-shaped signal propagating across the station.

Infrasound is the main focus of the ensuing sections, and it is important to distinguish these waves from those of gravity waves, which can be done using frequency analysis of the signals of interest. As discussed in Section 5.2, infrasound occupies a higher frequency range than that of gravity waves, which has been seen in Figure 5-1 and Figure 5-2, and can also be seen in practice in the wavelet transform for a given time-series. The use of the wavelet transform for frequency analysis has been discussed in Section 2.6, with its usage shown in Section 4.5 regarding NLCs. Figure 5-10 shows an example wavelet transform for the night of the 16/17 May 2013, with the regions of infrasound and gravity waves given. The blue dashed box in the figure shows the region of gravity waves, which is also occupied by the background radiance of the night (lower frequencies), while the red dashed box indicates the region where infrasound frequencies can be found. Figure 5-10 shows an example of an infrasound signal extending into the given region, while also demonstrating the greater level of detail given in the infrasonic region of the wavelet transform, as a result of the $\log_2$ y-axis. Like that of the gravity wave region, the infrasound region contains other signals such as a the pedestrian beacon signal (scattered by clouds and shown in Figure 5-11) seen prior to 2017. Figure 5-11 details the frequency determination of the wavelet transform, where various signals are analysed.

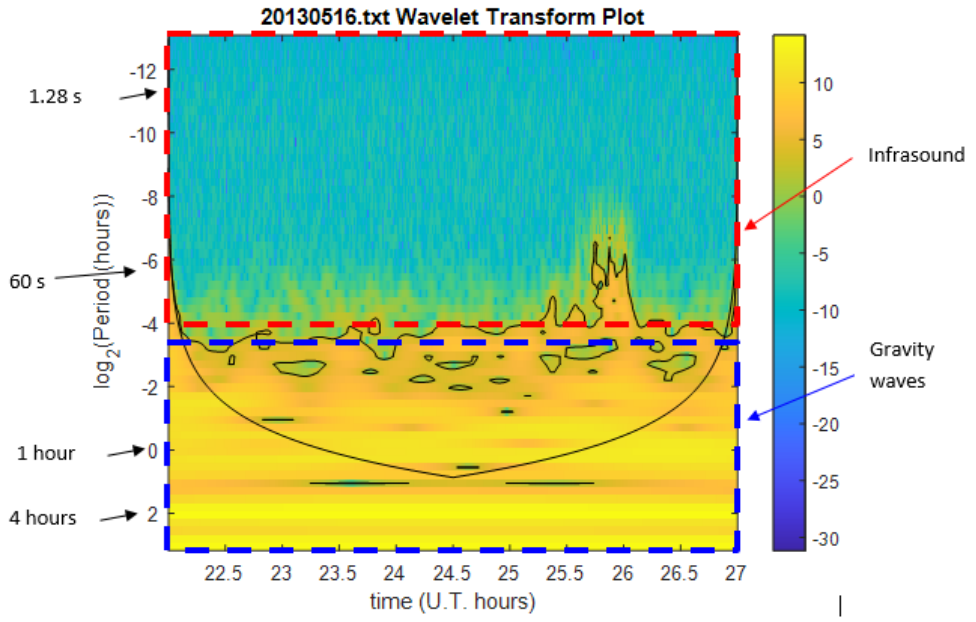

Figure 5-10: Wavelet transform of the night of the 16/17 July 2013, showing the regions containing gravity waves and infrasonic waves. These waves are not alone in the wavelet transform, as other signals, due to clouds, background radiance and sunlight can also occupy the regions. The colour bar demonstrates the power associated with the frequencies on the y-axis, while the black curved line is the boundary of the cone of influence (region closer to the edge of the plot, where the power spectra is distorted)

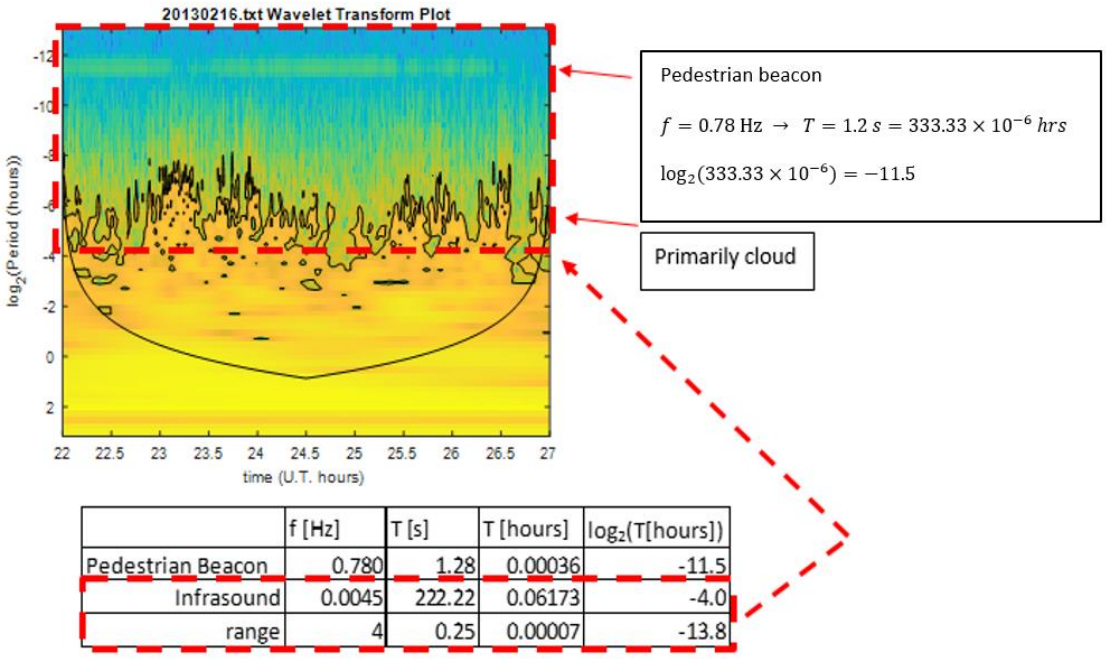

	f [Hz]	T [s]	T [hours]	$\log_2$(T[hours])
Pedestrian Beacon	0.780	1.28	0.00036	-11.5
Infrasound	0.0045	222.22	0.06173	-4.0
range	4	0.25	0.00007	-13.8

Figure 5-11: Frequency determination from the wavelet transform spectrum of an example night (16/17 February 2013) showing signals due to cloud, with the pedestrian beacon signal clear in the data. The colour bar in this plot matches that of Figure 5-10.

5.4. Microbaroms

Microbaroms are a type of infrasound resulting from non-linear ocean wave interactions (*Bowman* and *Lees*, 2017), and possess a range of frequencies within the infrasound band, with dominant frequencies between about $0.12 - 0.35$ Hz. Due to the prevalence of microbaroms in this band, many infrasonic signals emanating from other sources can be masked by their presence. As a result, microbarom signals are considered as noise in the IMS network data (*Landès et al.*, 2012). However, these signals also provide a steady source to test that an infrasound array is capable of detecting its target, an idea recognised by authors such as *Bowman* and *Lees* (2017). This approach is taken here to demonstrate that the array is capable of the detection of infrasound, which is the primary focus of this thesis. In Chapter 2, the instrumentation was introduced showing the parameters required to detect infrasound. Microbaroms have been chosen as the target to prove the capability. One of the advantages of attempting to use microbaroms to prove the capability of the detector is that the spectral peak of microbaroms is most evident during night hours (*Brachet et al.*, 2009).

5.4.1. Microbarom Analysis Software

As mentioned above, microbaroms dominate in the $0.12 - 0.35$ Hz frequency band. In order to obtain frequencies from this passband in the dataset, a suitable high-pass filter or band pass filter must be introduced. This is achieved using the method of analysis from *Le Dû et al.* (2020). *Le Dû et al.* (2020) investigate microbaroms on a single night in south-eastern France by the analysis of the time-series as a sequence of 7-minute intervals. The 7-minute length was chosen to be comfortably above the Brunt-Väisälä frequency (~ 5 minutes period). Once the time-series was split into these intervals, the dominant frequency of each interval was obtained by the authors, and the most common frequency of the night was obtained. *Le Dû et al.* (2020) were forced to adopt these

apparently cumbersome methods because of the miniscule level of power in the microbarom frequency range. In the following paragraphs, the method used on the time-series in this project is outlined.

The time-series is first split into the 7-minute (420 seconds) intervals and then a 3rd order polynomial is fitted to and removed from each interval to eliminate very slow variations arising from gravity waves for example (periods on the order of 5 minutes). This is not done for the entire night at once as that would average out the frequencies of interest. The 3^{rd} order polynomial is reapplied and removed each time a 7-minute interval is analysed to ensure no large step functions are introduced.

A high-pass 5^{th} order Butterworth filter is then applied to find appropriate frequencies corresponding to the dominant microbarom frequencies. The cut-off needed by the Butterworth filter to obtain the given frequencies is a variable of interest here and the microbarom analysis to be shown is broken down based on cut-off frequency. *Le Dû et al.* (2020) use a 1/(60 s) cut-off frequency to investigate OH* signals for microbarom frequencies. A number of test cut-offs were attempted to obtain evidence of microbaroms.

Issues related to noise frequencies occur for smaller cut-off frequencies. Frequencies occurring during cloudy conditions must also be analysed, as these are categorised as a type of noise. Once the Butterworth filter is applied, the signal is tapered by 20% on each end of the interval and then the power spectral density (PSD) is determined. Welch's method (*Welch*, 1967) is used to obtain the power spectral density over 128 frequencies, where the frequencies range from 0 to the Nyquist limit (2.27 Hz –which originates from the recorded sampling rate of 0.22 s). Welch's method determines the frequency with the highest power in the interval based on the 128 frequencies and returns this frequency as the dominant one.

This process of filtering and obtaining the PSD is shown in Figure 5-12 below, where the plots on the left-hand side show various 7-minute intervals with a high-pass filter applied for each (red curve, labelled 'e'). The corresponding PSD for each interval is shown on

the right-hand side of Figure 5-12. The red arrow in these PSDs on the right-hand side indicate the frequency of the filtered 7-minute interval with the highest power. This frequency is returned as the 'dominant frequency' by the program, but does not represent the only frequency returned by the PSD within the given interval. This step shows why the gravity wave frequencies are filtered out, as they have greater amounts of power associated with them compared to infrasonic waves.

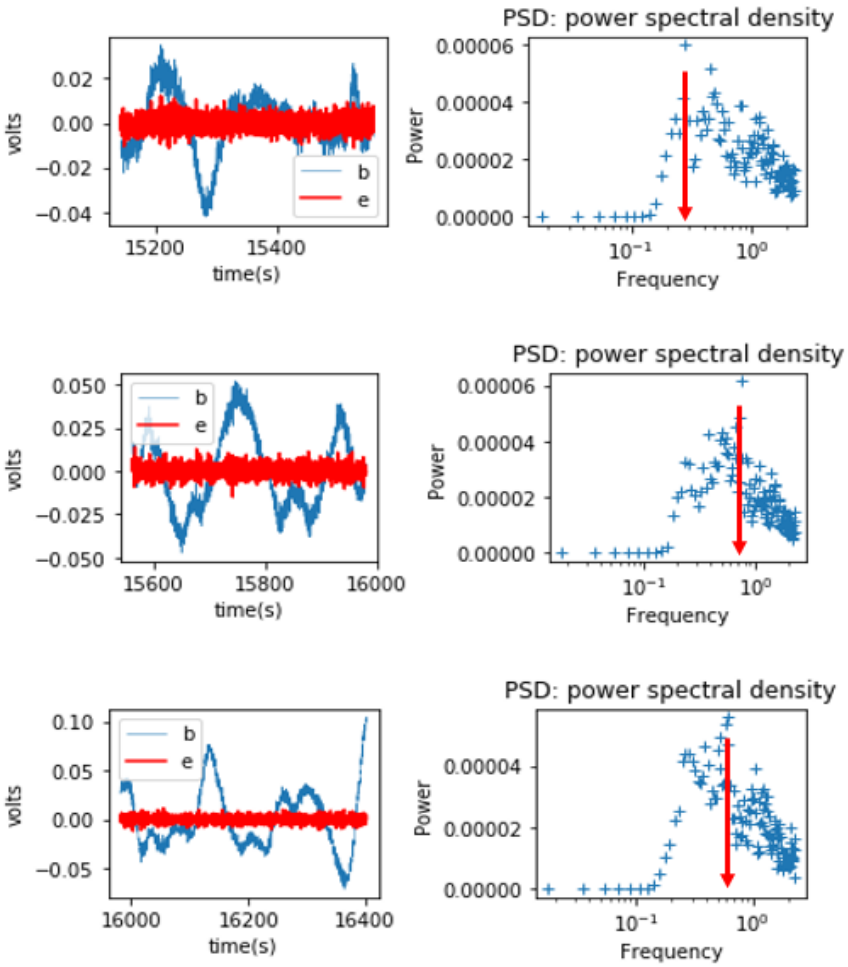

Figure 5-12: Dominant frequency analysis regime for clear nights taken from the Maynooth radiometers. The left-hand side of the figure (top, middle and bottom) shows subsequent 7-minute voltage-time plots (blue, given as b), each filtered using a high-pass filter (the resulting filtered signal is shown by the red trace (given as e). On the right-hand side of the plot, the PSD is taken of each interval (after it is filtered), creating a plot with the blue crosses. The program created determines the dominant frequency from this plot, where the same regime is carried out for the entire time-series. It should be noted here that the labels b *and* e *are arbitrary.*

The lowest frequency obtained by this method is 0.0178 Hz (2.27 Hz by 128 frequencies), and the range of frequencies outputted is between $0.0178 - 2.27$ Hz in steps of 0.0178 Hz. Microbaroms would thus be a subset included in this range. Gravity wave frequencies which are normally below 3.3 mHz are not picked up through this analysis as the lowest frequency possible is larger than the highest gravity wave frequency. These lower frequencies are not of interest in this section and so are not considered for further analysis. These lower frequencies are normally eliminated by the analysis so as to remove slow variations within the $7-$minute analysis intervals. The entire software process is shown in Figure 5-13 below, where the steps described above are summarised briefly.

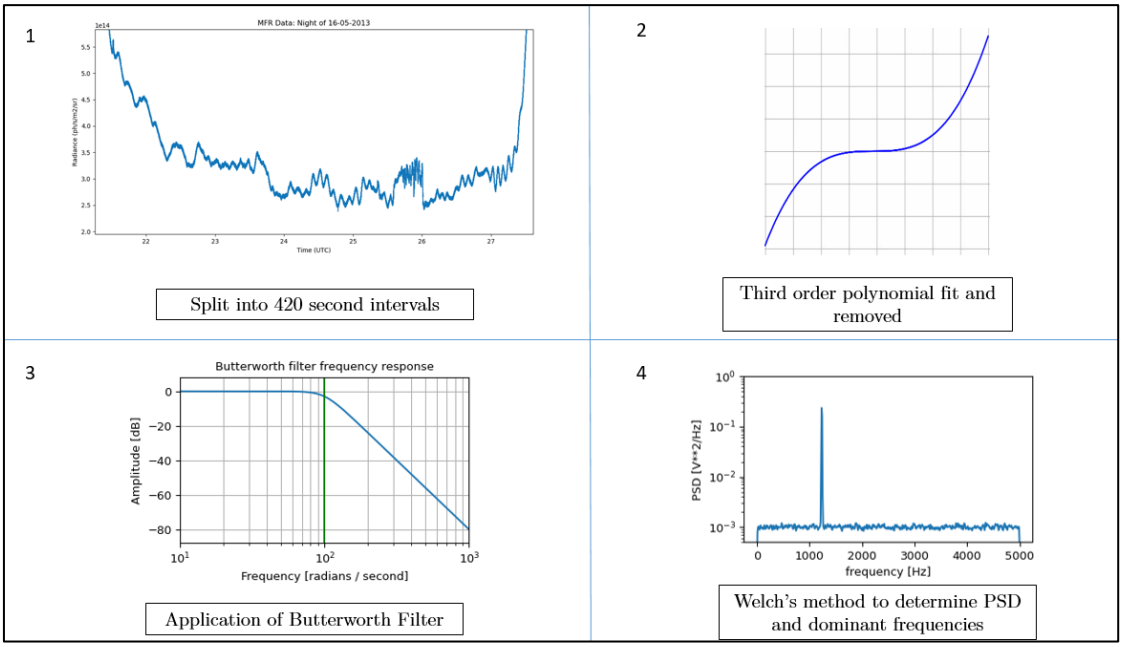

Figure 5-13: Software process for microbarom analysis of the datasets. Four steps are involved in this process: (1) the time-series is split into intervals of 420 seconds (7 minutes), (2) each interval then has a third-order polynomial applied and removed. Once the polynomial is removed, (3) a high-pass 5^{th} order Butterworth filter is applied to the interval and (4) Welch's method is used to obtain the PSD and dominant frequency of the given interval. Steps (3) and (4) are repeated for each interval and the final output of the process is a histogram of all of the dominant frequencies.

5.4.1.1. Le Dû et al. (2020) *software testing*

Before analysis of the clear nights is undertaken, software testing is needed to determine whether the frequencies returned are authentic. This can be completed by analysing the data from *Le Dû et al.* (2020) using the software, but another more efficient way to determine the authenticity of the frequencies exists as a result of cloud detection methods prior to 2017.

Section 4.2.1 discussed the fundamental elements of a typical clear night for a time-series acquired by the detectors. If nights feature a fixed frequency of 0.78 Hz, they are deemed to be cloudy and are removed from consideration. This frequency arose due to the presence of an on-campus pedestrian beacon as discussed in Section 4.2.1, and this same frequency can be used to assess the authenticity of the software used in this section.

An example night containing confirmed instances of clouds is used to determine whether the 0.78 Hz peak occurs within the output of the software. Figure 5-14 (a) shows the night of 13/14 April 2016, when the pedestrian beacon was operational. Several instances of erratic radiance measurements occur during the time-series shown, which indicates the presence of cloudy conditions. This is verified by the power spectrum in Figure 5-14(b), which shows a peak at 0.78 Hz and at ~2.3 Hz (a harmonic of the beacon frequency). The software outputs all the dominant frequencies obtained when the time-series is split into 7 minute intervals.

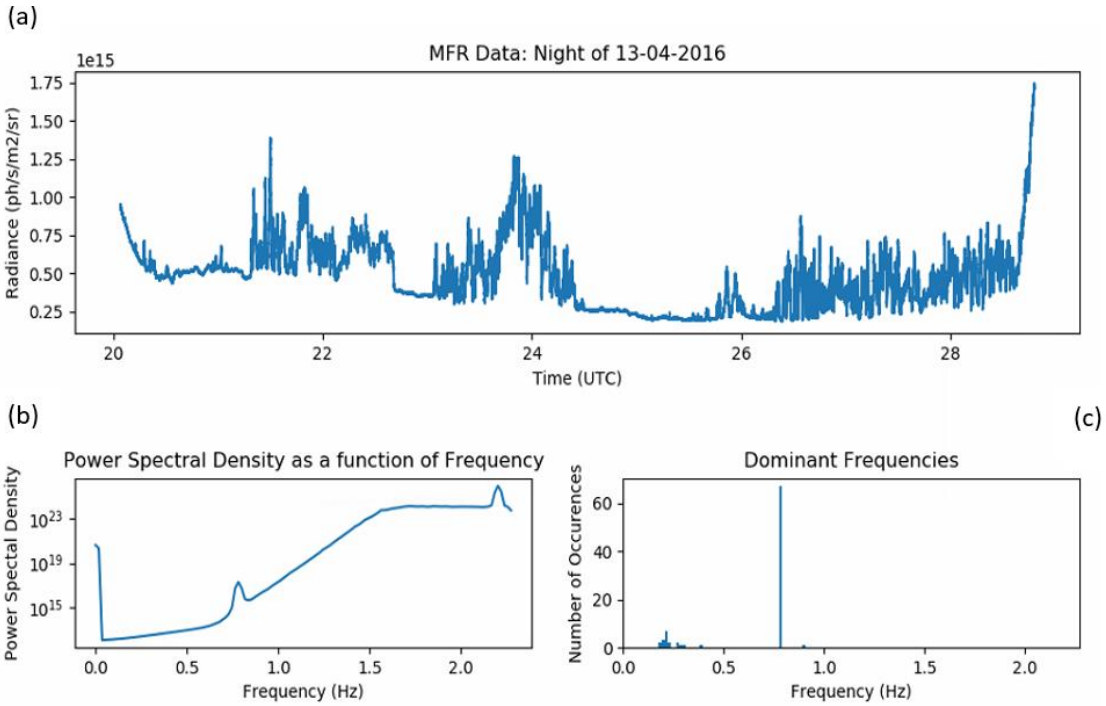

Figure 5-14: Software test applied to a cloudy night prior to 2018. The PSD is shown in (b) with a histogram of all the dominant frequencies for the night shown in (c). The most common dominant frequency throughout the night is within the bin centred on 0.78 *Hz. This coincides with the beacon frequency and appears to confirm cloudy conditions. The beacon frequency can be used to calibrate the histogram outputs.*

These frequencies are then binned and outputted in the form of a histogram, shown in Figure 5-14(c) for the 13/14 April 2016. The most common dominant frequency for the night is centred on 0.78 Hz, indicating that the beacon frequency that appears in the PSD in Figure 5-14(b) is picked up by the software. This appears to confirm that the output frequencies are authentic and the analysis method yields valid results. To ensure that this is the case, a night confirmed to be clear is also presented to confirm the lack of a beacon frequency. Figure 5-15(a) shows a clear night, confirmed by the lack of the 0.78 Hz or harmonics within the PSD in part (b) of the same figure. Based on the dominant frequency histogram in Figure 5-15(c), the lack of the beacon frequency is also apparent.

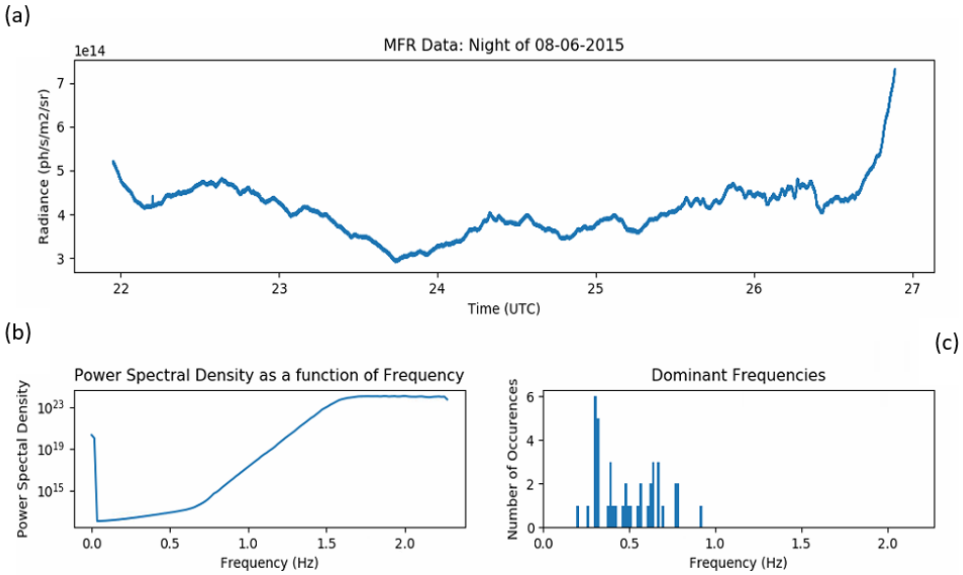

Figure 5-15: Software test applied to a clear night as confirmed by Met Éireann data. As the night is clear, a peak in the 0.78 Hz would not be expected in the output histogram in (c), which in this case is true for the night. Instead the most common dominant frequency for this night was ~0.36 *Hz*

Other examples, not shown here, confirm that the beacon frequency occurs in the dominant frequency histogram for cloudy nights. Through calibration of the software using the beacon frequency, clear nights in the dataset can now be analysed for evidence of microbaroms.

5.4.2. Analysis of Datasets for Evidence of Microbaroms

Section 5.4.1 has discussed the software used in the analysis of the datasets in search of microbaroms. One of the variables that can change the frequencies returned by the software is the cut-off frequency, and the next few sections focus on the effect of a changing cut-off frequency on the frequency ouput.

Various cut-off frequencies were used to analyse the datasets, including the following frequencies, corresponding to 3 minutes (5.5 mHz), 2 minutes (8.3 mHz) and 1 minute (16 mHz). It was found that the 8.3 mHz cut-off frequency gave consistent results which

are shown in this section, compared to other cut-off frequencies which returned frequencies strongly affected by any noise in the recorded signal.

Of the datasets examined for evidence of microbaroms, MFR and MFR2 are primarily discussed. The two datasets are presented together to ensure that any patterns in the frequencies are genuine and are not unique to any one detector. This reduces the possibility of mistaking noise for patterns. UWOSCR data is not considered alongside the data of the other two instruments. UWOSCR, lacking an optical chopper, contains more power in the lower frequencies compared to the other instrument datasets. This leads to larger amounts of output drift in the UWOSCR data which affects the results from these datasets. The frequency range coinciding with the dominant frequency range of microbaroms, namely $0.2 - 0.3$ Hz, is heavily affected, rendering microbaroms difficult to detect among noise. This result demonstrates the importance of including the chopper and lock-in amplifier in the MFR and MFR2 instruments.

The cut-off frequency used to examine frequencies from the datasets is a cut-off frequency of $1/120$ Hz (8.3 mHz) or a period of 2 minutes, which guarantees fewer noise frequencies involved, as opposed to higher cut-off frequencies. The analysis is completed on a month-by-month basis, and an example plot of the frequency distribution for days in February is shown in Figure 5-16. The plot shows the data from MFR (blue) and MFR2 (orange), where two peaks are evident in the 0.25 Hz and 0.35 Hz bins for both instruments. It should be noted that the y-axis in Figure 5-16 refers to the percentage of each frequency bin compared to the total frequency occurrences. For instance, of the frequencies observed by MFR for days in February (between 2018 and 2020), ~ 10 % were between $0.2 - 0.25$ Hz (and thus occurred in the 0.25 Hz bin). MFR2 also found a similar percentage of frequencies within the 0.25 Hz bin.

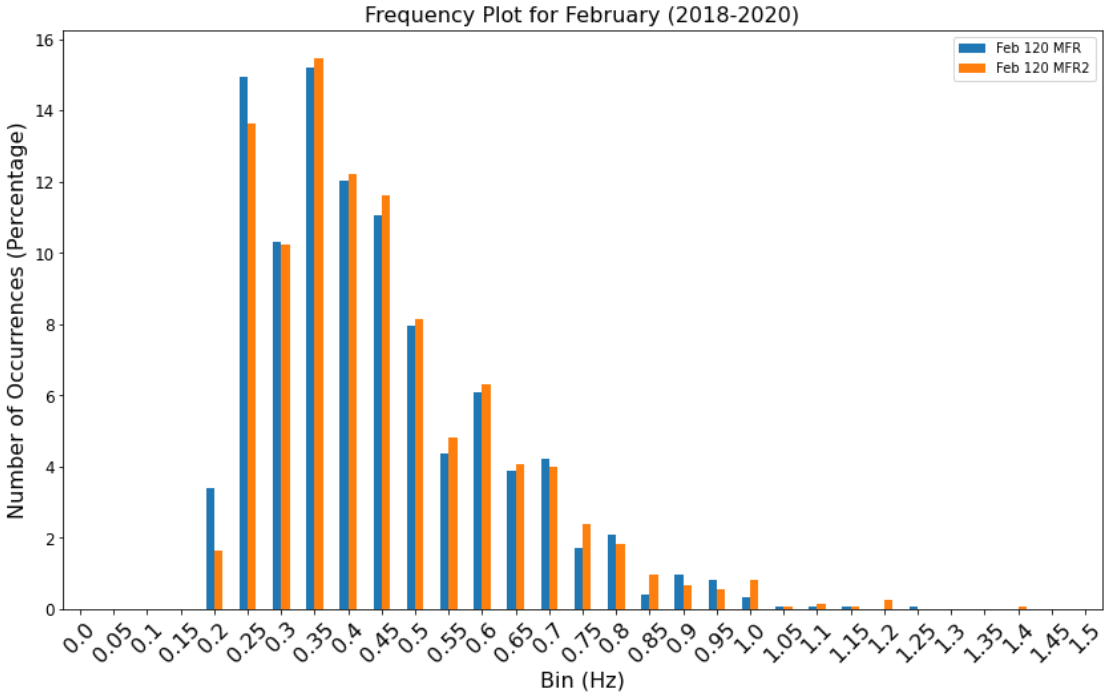

Figure 5-16: Example of the microbarom analysis completed for days in February between 2018 and 2020.

Figure 5-16 demonstrates an example of the month-by-month frequency analysis, while Figure 5-17 shows the same analysis for all months. The frequencies are primarily distributed across a range of $0.2 - 0.8$ Hz (with a smaller number of frequencies occurring in higher bins), with the dominant frequencies mainly occurring between 0.25 Hz and 0.45 Hz. During winter months, particularly between November to February, a clear peak can be seen in the 0.25 Hz bin. This bin also contributes around 10% or more to the total frequency occurrence, for the given month in winter. During summer months the 0.25 Hz bin, although still apparent in some cases, contributes less to the overall total frequency occurrences. August numbers from MFR indicate a frequency distribution more akin to winter numbers rather than the rest of the summer numbers. This may be explained by the small sample size for August, as the rest of the months follow a pattern of a 0.25 Hz peak in winter and no 0.25 Hz peak in summer. MFR2 data was also analysed for the same period. Due to the somewhat larger field-of-view of MFR2, it would be less responsive to frequency variations; however a similar, although less obvious variation between summer and winter can be seen in orange data in Figure

5-17. As in the MFR data, a peak (smaller compared to MFR data) in the 0.25 Hz bin can be seen in winter months as opposed to summer months. This shows a seasonal variation in the frequency distribution. Figure 5-18 shows this same peak in the 0.25 Hz bin but presented in the format of radar plots (where the 'spokes' represent the percentage of the total frequency occurrence (like that on the y-axis of Figure 5-16) and the categories represent the frequency bins).

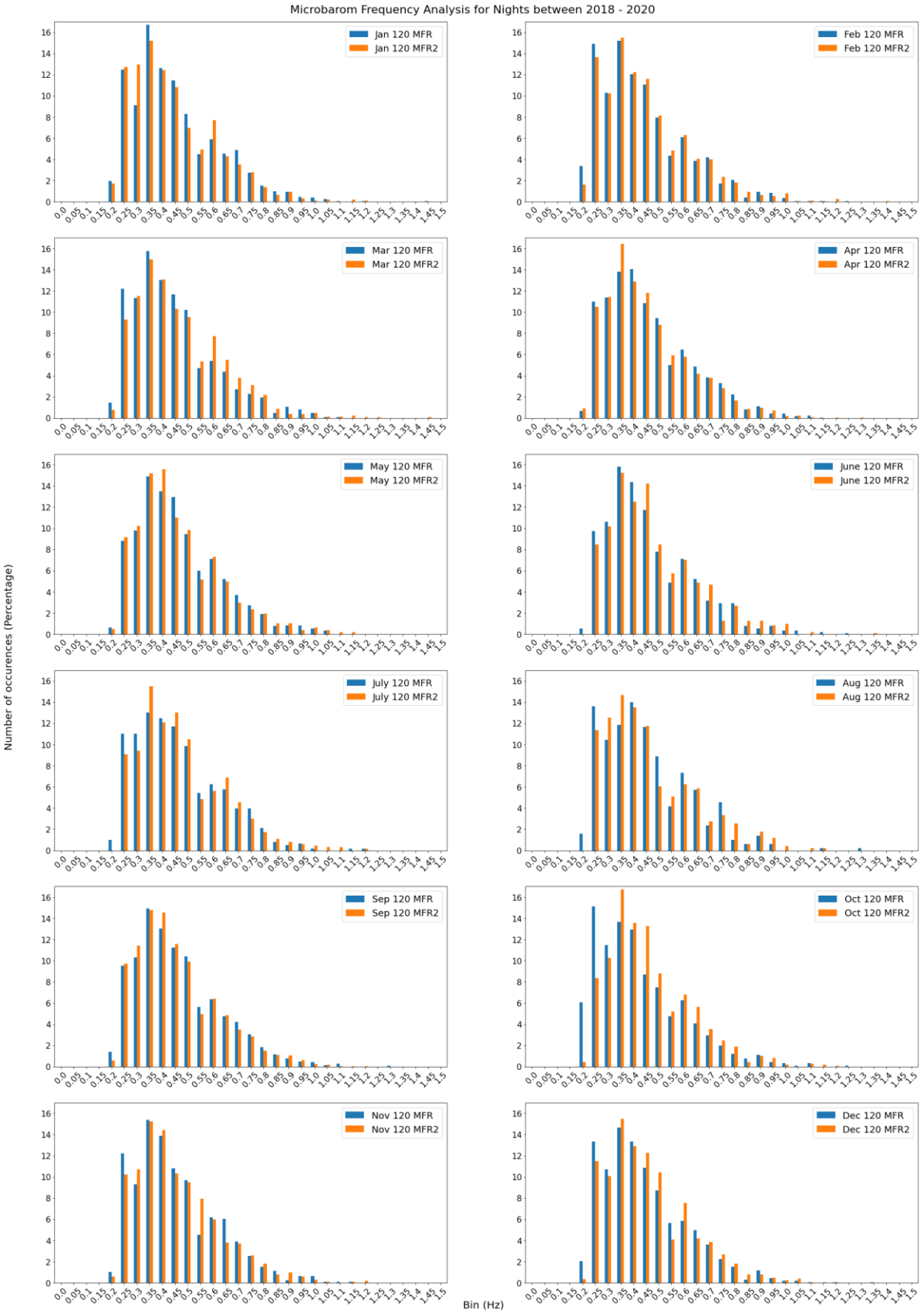

Figure 5-17: Analysis of clear nights after 2018, showing MFR (blue) and MFR2 (orange) analysed using the software from Section 5.4.1 on a month-by-month basis for a cut-off frequency of 1/120 Hz.

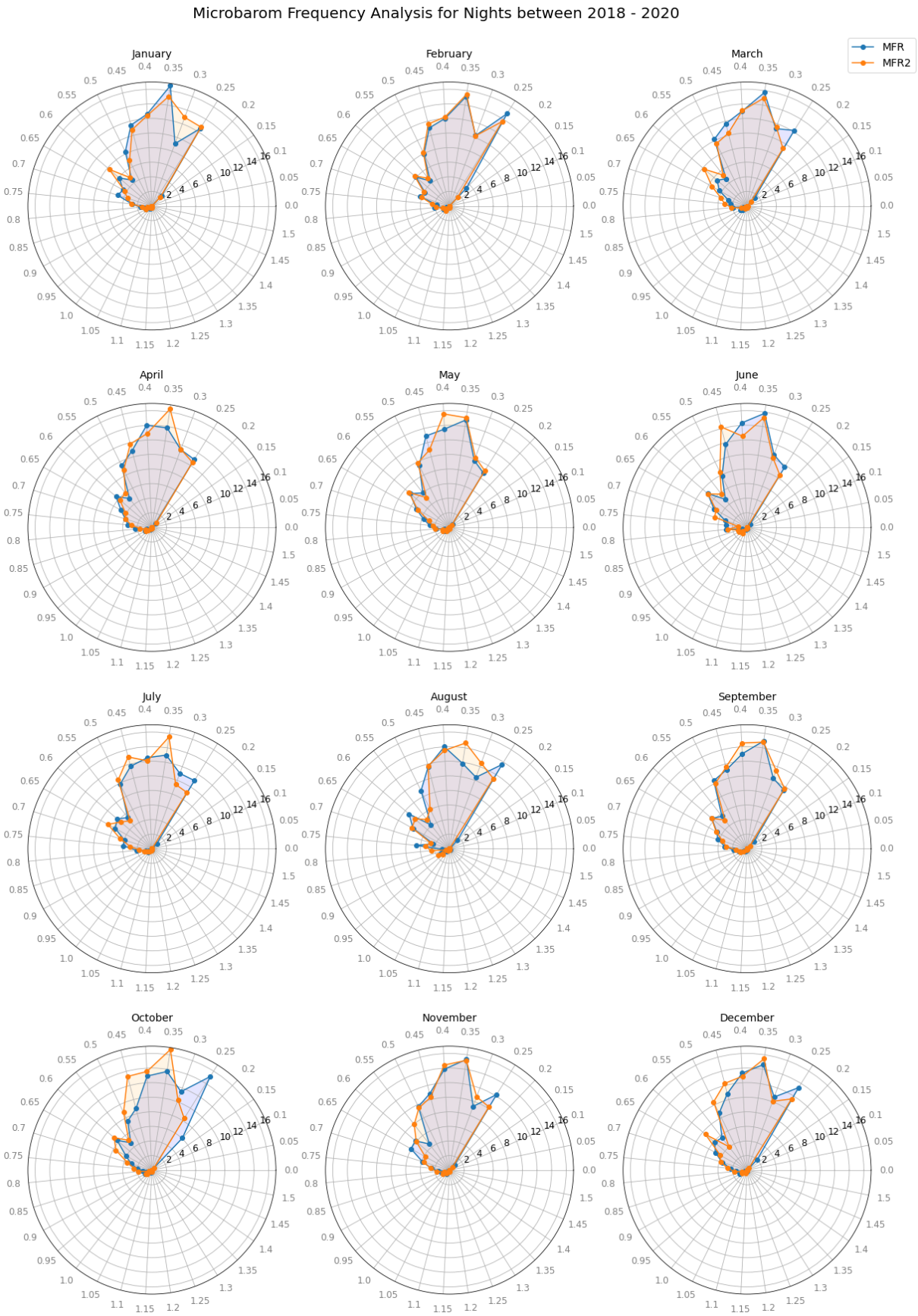

Figure 5-18: Same as Figure 5-17 but presented in the form of radar plots. Although the same information is presented, the 0.25 *Hz bin peak is more apparent.*

5.4.3. Comparison to Microbarom Detections in Northern Europe

Based on data from *Hupe et al.* (2019), this peak in the 0.25 Hz bin ($0.2 - 0.25$ Hz) found throughout Figure 5-17 appears to be expected. *Hupe et al.* (2019) note that the dominant frequency of microbaroms from the North Atlantic occur in the frequency range of $0.2 - 0.3$ Hz. This becomes obvious from the map shown in Figure 5-19 (*Hupe et al.*, 2019), which shows that the dominant frequency originating from the North Atlantic is ~0.2 Hz.

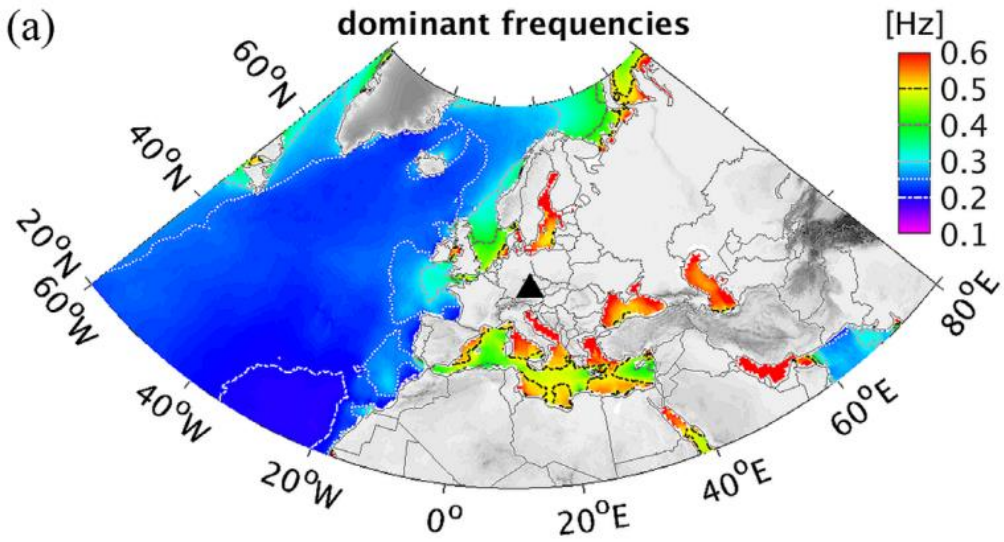

Figure 5-19: Map reproduced from Hupe et al. (2019) *showing the dominant frequencies of the microbaroms as they originate from different areas around the North Atlantic Ocean.*

Landès et al. (2012), in addition to *Hupe et al.* (2019), note that the distribution of microbaroms in the upper atmosphere is not constant throughout the year and instead depends on the season. For instance, *Landès et al.* (2012) notes that the North Atlantic ocean, just south of Greenland, appears as the dominant microbarom source for much of the winter, as seen in Figure 5-20. Although the directional information of the probable microbaroms in the datasets cannot be determined, Figure 5-20 does show the seasonal variability of the North Atlantic Ocean as a source of microbaroms, potentially explaining why the 0.25 Hz frequency band in Figure 5-17 grows larger in winter – due

to a close-by source of microbaroms to the station. Moreover, when discussing the frequencies found in their analysis, *Hupe et al.* (2019) note that the signals that carry such frequencies are more numerous in winter months, rather than summer months, in the Northern Hemisphere.

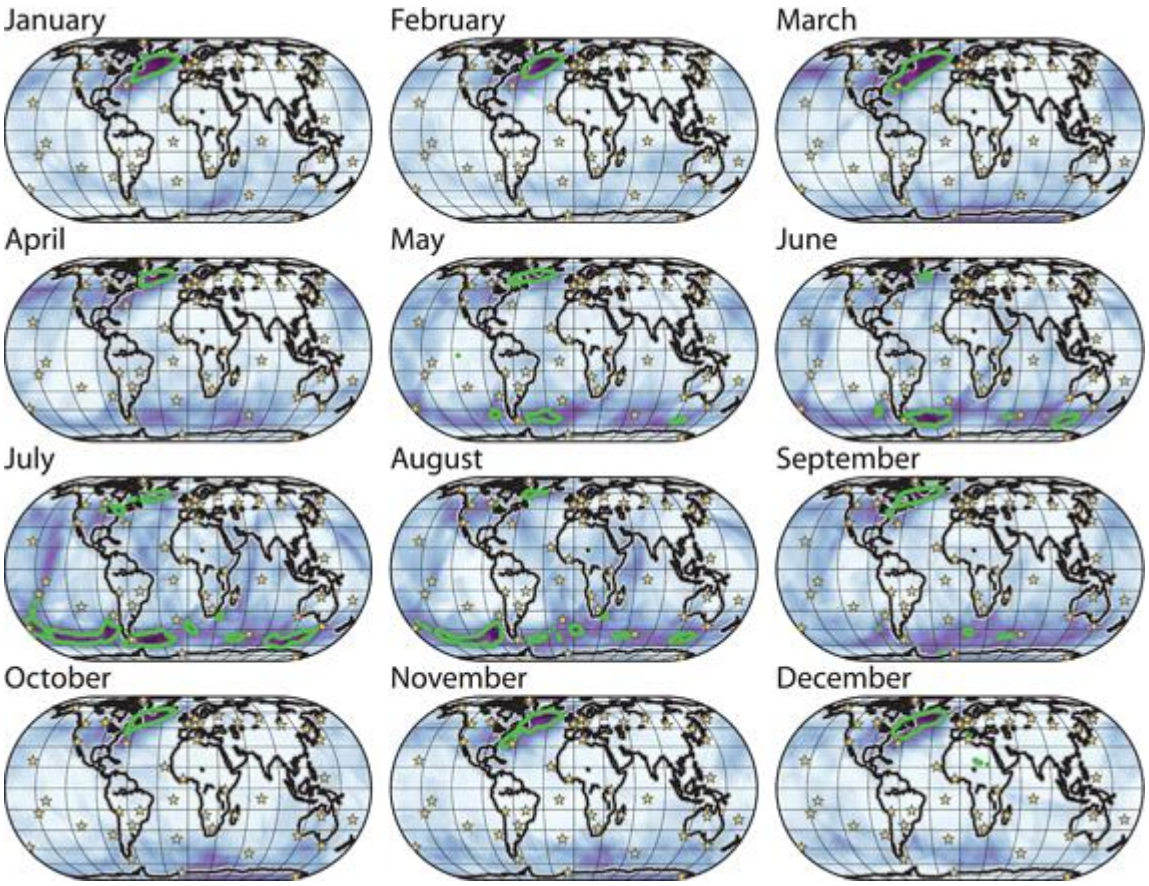

Figure 5-20: Locations of microbarom sources by month, as given by Landès et al. (2012), *showing the dominance of the North Atlantic ocean as a microbarom source during the Northern Hemisphere winter. Purple areas (high densities of which are seen circled in green) of the ocean show areas with a higher probability of producing microbaroms while white areas show a null probability.*

5.5. Infrasound Signal (Case Study of 25/26 July 2018)

Section 5.4 discussed the first sub-category of infrasound as described by *Bittner et al.*, (2010), where evidence of microbaroms was presented. This section illustrates an example of the second sub-category, namely, N-shaped infrasonic signals. On the 25/26 July 2018 an N-shaped signal was observed over Maynooth, which possessed infrasonic

characteristics, and the next sub-sections present these signal characteristics of the observation, such as duration, direction and speed. Based on the characteristics, source determination was undertaken and tentative relationships to sources such as the entry/fragmentation of a fireball over Greenland is shown. Propagation modelling in Section 5.5.4 shows how a theoretical signal from this fireball source would travel. The aspects derived from the signal and propagation modelling are then discussed in relation to expected characteristics from literature in Section 5.5.5.

5.5.1. Background Conditions for 25/26 July 2018

Before analysis of the signal is shown, clear conditions were confirmed using both data from the Met Éireann database taken at Casement Aerodrome and the on-site cloud detector. Figure 5-21 below shows the cloud amount in oktas for the night in question as reported by Met Éireann, and it is seen in the figure that from $21{:}00 - 07{:}00$ UTC at Casement Aerodrome, a maximum cloud amount of 2 oktas was registered. According to Table 4-1, this corresponds to a maximum amount of $2 - 3$ tenths cloud cover of the entire sky.

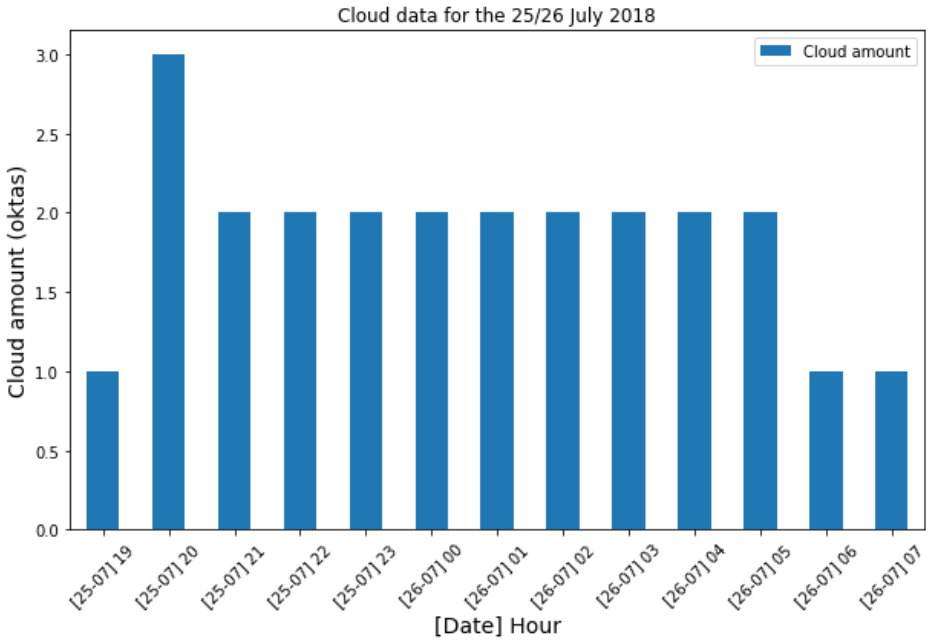

Figure 5-21: Cloud amount (measured in oktas) as reported by Met Éireann from Casement Aerodrome (53.3090° N, 6.4414° W) for the 25/26 July 2018. The cloud amount remains at or below 2 oktas during observation time.

The cloud record from the Maynooth observing station agrees with the Met Éireann cloud observations for the same time. Clarity and other concepts related to detection by the cloud detector have been discussed in Chapter 4 (Section 4.2). The cloud detector information from Maynooth is shown below in Figure 5-22, but based on plots shown in Section 4.2.2, the signal in Figure 5-22 does not represent a typical cloud signal. Other effects which may have influence in this case study, such as moonlight as outlined in Chapter 4, have also been eliminated as possible causes. During the time of the signal, the phase of the moon was waxing gibbous, meaning the moon was close to full, but the moon elevation angle was less than 10 degrees. As such, effects from the moon would make a negligible contribution to the signal intensities, and are therefore disregarded as a source of the signal. NLCs also not explain the signal's nature due to the shape of the waveform.

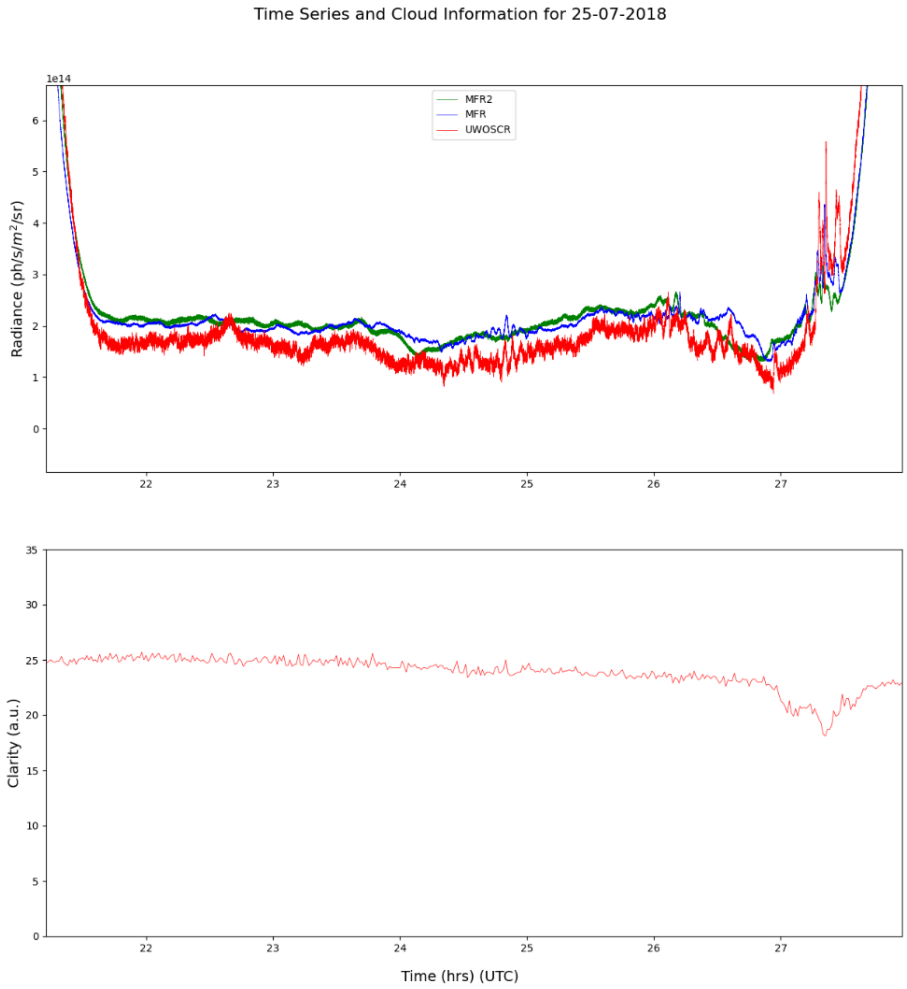

Figure 5-22: Time-series for the night of 25/26 July 2018 with accompanying cloud information. Higher clarity values indicate clearer conditions. A small amount of cloud is indicated after around 03:00 UTC (27 UTC).

5.5.2. Signal Characteristics

This section discusses an N-shaped signature found on the night of 25 July 2018. This signature is shown in Figure 5-23. At approximately 26.25 ($02{:}15$ UTC on the morning of 26 July 2018), a large N-shaped signal was observed by the MFR instrument at Maynooth. This N–shaped signature has a duration of about 100 seconds, with an amplitude of 0.3×10^{14} ph/s/m^2/sr. Compared to the background noise, the signal has a SNR of nearly $15{:}1$, which although is significantly less than that of the NLC signals seen in Section 4.5 of Chapter 4, is larger than that of the gravity waves seen previously (this has been determinable as a result of the calibration efforts detailed in Chapter 3).

Before the main N-shaped signal is registered, a period of wave activity occurs just before 01:00 UTC.

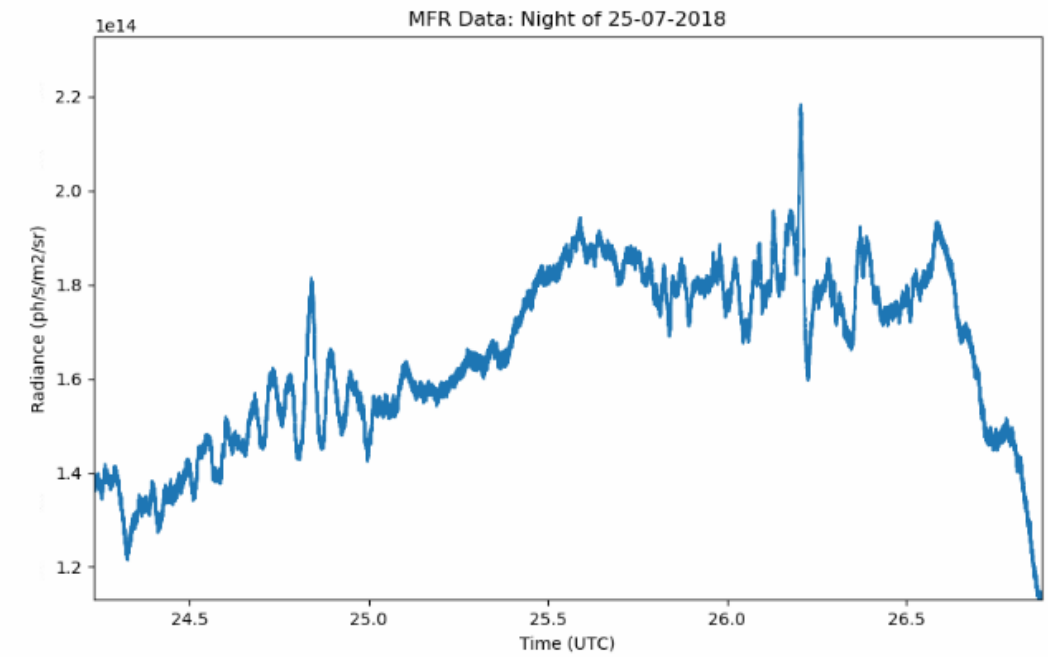

Figure 5-23: N-shaped signal as described in the text. The peak amplitude occurs at approximately 26.25 UTC (02:12 UTC). Amplitude of the signal is ~0.4 ph/s/m²/sr.

As noted in the previous section, the focus here is on an N-shaped signal detected at Maynooth. Figure 5-24 shows the detail for the main part of the signal as detected by MFR, where there is a clear increase followed by a decrease, forming a characteristic N-shape. The whole signal has a duration of 146 seconds (2 minutes 26 seconds), with a time between the maximum and minimum around 75 seconds (1 minute 15 seconds). Based on these durations and the sampling rate of MFR, the whole signal is captured over more than 600 (averaged) samples, whilst the maximum-minimum is captured over ~340 (averaged) samples.

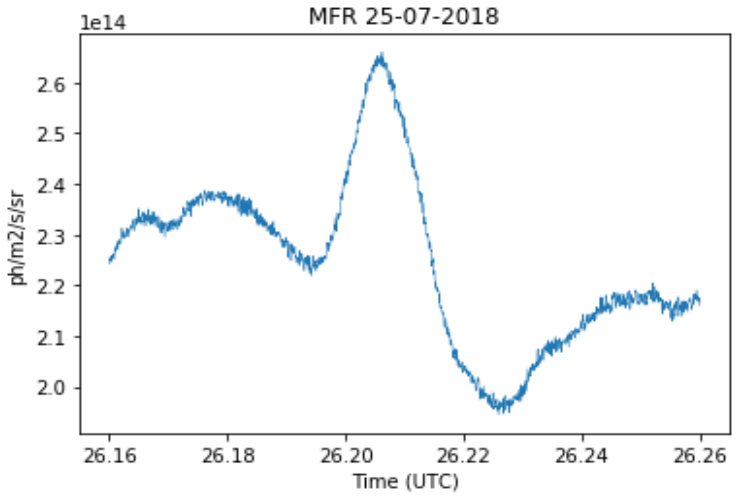

Figure 5-24: Detail of the N-shaped signal seen on the morning of the 26 July 2018. The time lapse between maximum and minimum amplitude is ~75 seconds.

One of the questions regarding this signal is whether it can be correctly identified as an infrasonic signal. The frequency of the signal can be used to confirm its infrasonic nature. Chapter 1 (Section 1.7.4) and Section 5.2 have discussed how acoustic wave frequencies are bounded by the acoustic cut-off frequency, which is shown as a function of altitude in Figure 5-2, along with the Brunt-Väisälä frequency in an isothermal atmosphere. The acoustic cut-off frequency in the region of the hydroxyl layer is ~4 minutes or ~240 seconds (4.17 mHz) according to Figure 5-2, and the signal presented is well below this value, giving a period of about ~146 seconds (6.85 mHz).

The signal is further analysed through a power spectral density estimation, with the power spectrum for the night shown in Figure 5-25. If a large amount of power were associated with the signal discussed, a peak in the power spectrum would be expected around 10^0 mHz. However, no peak is apparent in this part of the power spectrum, meaning that there is little power associated with the signal. Instead, a wavelet transform of the night is used to determine where the power of the signal mainly lies. A discussion on wavelet analysis has already been presented in Chapter 2 but a word on the Morlet wavelet is given here. According to *Lau* and *Weng* (1995), advantages come with the Morlet wavelet transform as it can obtain amplitudes and phases that change

temporally for various frequencies. As the main aim here is to obtain the power contained within different frequencies, the Morlet wavelet was seen to be a good option.

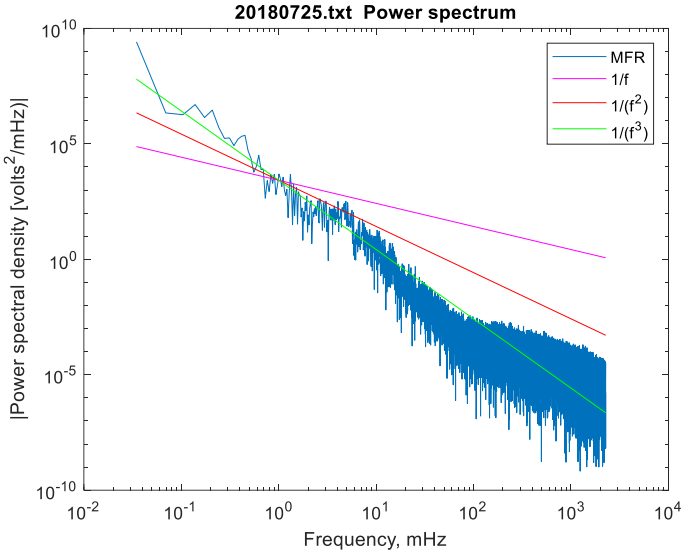

Figure 5-25: Power spectrum for the night of the 25/26 July 2018. The lines given as 1/f, $1/f^2$ and $1/f^3$ are guides for the eye and are associated with buoyancy waves, inertial and turbulence respectively.

The norm of the Morlet Transform is taken for the entire night and so the power associated with various signals is seen on a temporal basis and is shown in Figure 5-26. The majority of the power lies in the background signal, and this is indicated by the yellowish colour that occupies the lower part of the transform plot, while areas of dark blue refer to areas of low power (in terms of frequency). The signal occurs just after 26:00 UTC, shown in the red box, possessing a small amount of power centred on a frequency of 10^{-2} Hz (the figure shows the data from MFR2). The frequency of this signal in the transform correlates with the manually calculated frequency from the time-series of around 0.013 Hz (~ 75 seconds).

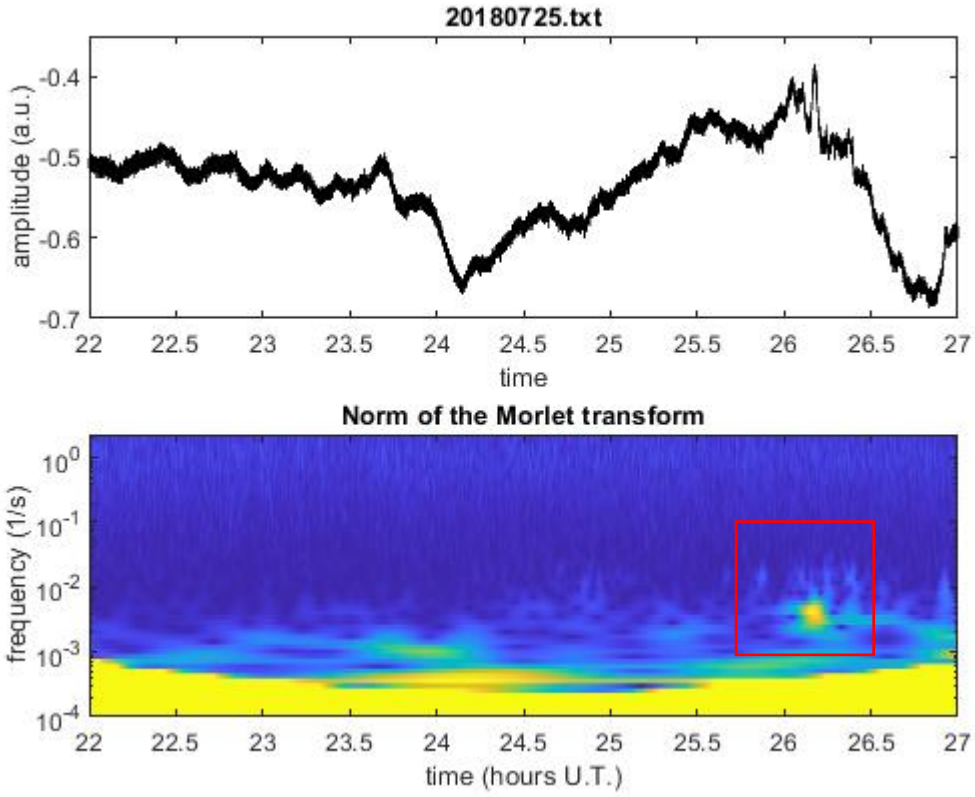

Figure 5-26: Norm of the Morlet Transform for the 25/26 July 2018, as taken from the MFR2 instrument.

More characteristics of the signal can be found by using all three of the instruments. Figure 5-27 shows the combination of all three of the time-series from MFR, MFR2 and UWOSCR for the night. Instrument conditions for the night show higher noise levels in UWOSCR compared to MFR, while the sensitivity of MFR2 is lower due to a non-identical field-of-view compared to UWOSCR and MFR. This affects the overall observations, resulting in MFR having the cleanest signal and best SNR of all three instruments, and is therefore used as the main signal of all three instruments. Lag analysis, based on the work of *Giers et al.* (1997), *Pignatelli et al.* (2008) and *ElGabry et al.* (2017), was performed and the result is shown in Figure 5-28.

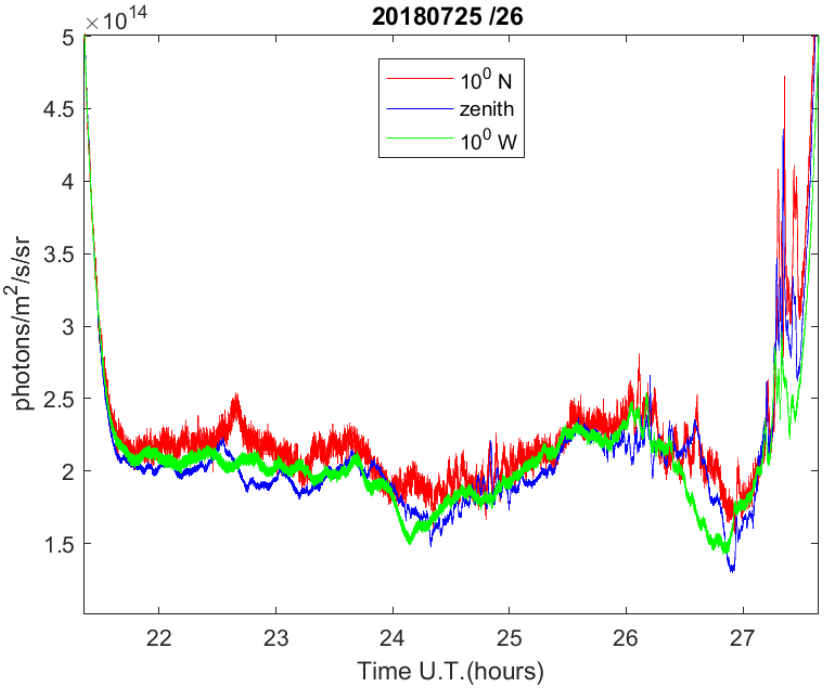

Figure 5-27: All three time-series for the 25/26 July 2018. The signal occurs in all three datasets, where UWOSCR is given in red, MFR in blue and MFR2 in green. A greater amount of detail is seen in Figure 5-28.

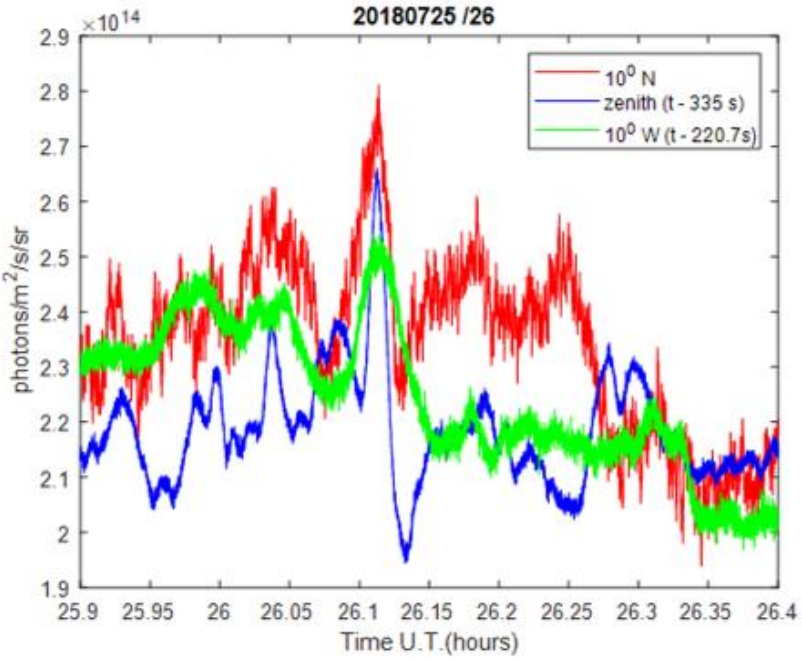

Figure 5-28: Lag analysis of the signal. MFR (zenith, in blue) and MFR2 (10 degrees west) are correlated with respect to UWOSCR (10 degrees north).

Based on the arrival time of the signals, the time delay of MFR and MFR2 are completed with respect to the signal observed in UWOSCR, where the disturbance is observed first. This was decided based on the relative intensities found in all three instruments, where the leading edge of the largest amplitude signal around this time (of similar shape) was used. The signal arrives at MFR2 around 221 seconds after the signal is first observed by UWOSCR, while it passes over MFR 335 seconds after the first observation at UWOSCR. An initial estimate of the direction indicates that the signal originates from the north-west direction.

Using the *ElGabry et al.* (2017) method, the back-azimuth (direction) of the signal was calculated and determined to originate from 19.4° west of north. The speed of the signal was calculated to be 45 m/s. As the use of all three instruments is required to determine the source of the signal (through the direction and speed), the next step was to consider the possibilities that could have resulted in the disturbance based on the calculated parameters.

5.5.3. Source Determination

For source determination, Figure 5-9 pertaining to infrasound source characterisation was used as a benchmark for the possible origins of the signal. Assuming the signal is that of an impulsive infrasound source, based on the N-shape of the signal, the relevant databases (e.g. USGS (United States Geological Survey), GVP (Global Volcanism Program) and CNEOS (Center for Near Earth Object Studies)) were examined for information.

To cover the bases of infrasound sources, the USGS was consulted to determine if the signal could have been due to earthquake-related atmospheric disturbances. From the USGS website, no large earthquakes occurred prior to the signal that could reasonably be assumed to be the source of the disturbance. Earthquakes were thus ruled out as the possible source of the signal.

There were no notable volcanic eruptions that occurred during the time in question or before the signal was observed at Maynooth. According to the weekly report of 25 – 31 July 2018 from the Global Volcanism Program, a number of ash plumes occurred on the 25 July 2018 (*Global Volcanism Program*, 2018), and the only other activity related to volcanoes during this time were tremors that occurred during volcanic activity on the Galapagos Islands on 25 July. These tremors were due to seismic activity associated with the Sierra Negra volcano, which also gave rise to infrasound. The main tremor occurred around 15:47 UTC (*Instituto Geofísico*, 2018), but based on the distance to Maynooth and a sound speed of 230 m/s and up, potential signals arising from these tremors would not arrive in time to conceivably be the source of the disturbances registered at Maynooth.

Another source of impulsive infrasound according to *Bittner et al.* (2010) are due to the entry of meteors into the upper atmosphere. Meteors can also be described as fireballs or bolides, depending on the brightness of the NEO (Near-Earth object). Fireballs are reported and archived by CNEOS – Centre for Near Earth Object Studies - led by NASA, which reports characteristics like altitude, location and velocity for observed objects. Many of the fireballs reported by CNEOS are small in terms of calculated total impact energy (< 1 kT) and would thus be unlikely to generate a large enough signal to be detected by the array. However, a number of fireballs reported by the network have calculated impact energies of over 1 kT, where 1 kT would be comparable to the 2020 Beirut Explosion (*Goldstein*, 2020). Thus, fireballs with these impact energies are investigated to determine whether they could result in the signal found in the data. One of the more famous examples of a fireball/bolide that has caused infrasonic signals is the Chelyabinsk bolide (*Tauzin et al.*, 2013, *de Groot-Hedlin* and *Hedlin*, 2014). This super-bolide produced an air burst over Chelyabinsk, Russia and caused shock waves that were detected globally (shock waves are a feature of ablating meteors (*Silber et al.*, 2018), and are known to cause N-shaped signatures as seen in *Pierce* (1968).

CNEOS publish a list of these fireballs and their locations are shown on the map available from *Chamberlin* (2021). CNEOS report a single fireball event with a calculated

impact energy of over 1 kT on the 25 July 2018, occurring over Western Greenland. The fireball's location is shown on the map in Figure 5-29, showing a location of 76.9 °N, 69.0 °W, with an observation time of 21:55:26 UTC, with fragmentation of the fireball occurring in the stratosphere at around 43.3 km in altitude. A brief calculation of the estimated speed of the wave, based on the distance between the fireball location and Maynooth gives:

$$\frac{3500\ km}{0.27\ km/s} = 3.6\ hours \tag{5-2}$$

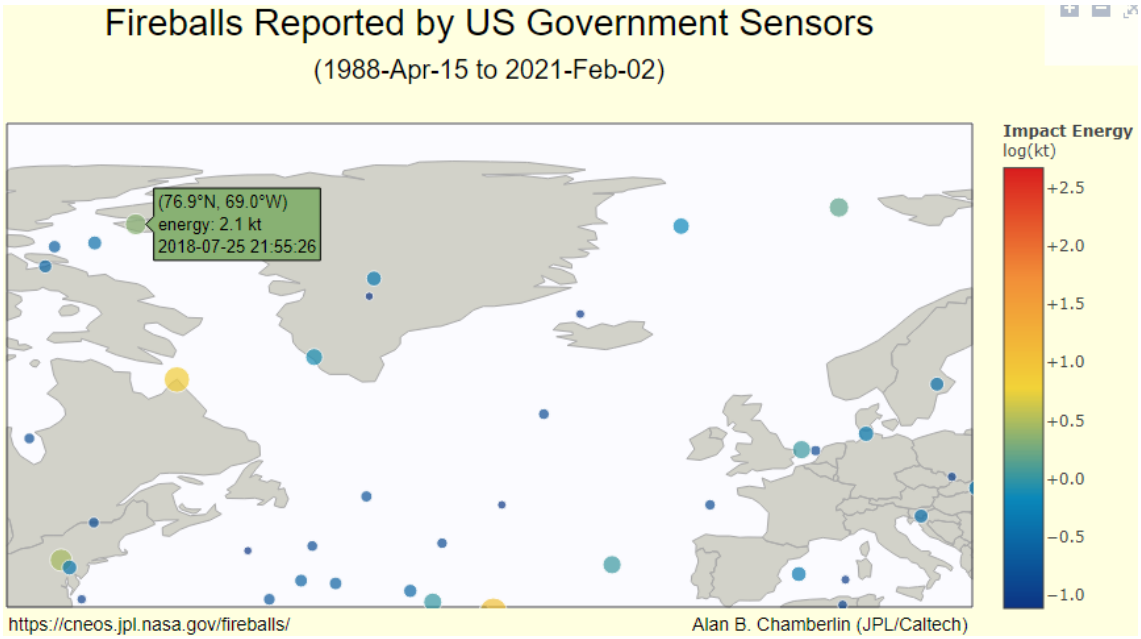

Figure 5-29: Fireball map published by Chamberlin (2021) *showing the potential source of the signal (shown in the green box). The Great Circle path from the fireball to Maynooth has a back azimuth angle of 22° west of north in almost complete agreement with the back-azimuth calculated from the tripartite array signals (19.4°± 3°).*

If a signal emanating from this event propagated to Maynooth, the earliest time it could be detected, based on a general speed of sound in the upper atmosphere of 270 m/s, would be at approximately 01:30 UTC. As the signal is observed at Maynooth at 02:12 UTC, the fireball could reasonably be viewed as the source. Assuming the signal does originate from this event, where the distance to the source and time are fixed, such a

signal would travel at a speed of 234 m/s from source to station (using the distance/speed/time calculation).

The next question to answer is whether infrasound from the fireball underwent long-range propagation and whether it can be recorded at Maynooth. *Pilger et al.* (2020b) answers this using the map shown in Figure 5-30, whereby three IMS network stations recorded a signal associated with the fireball event, with two of these IMS stations over 4000 km from the fireball event (the third IMS station was close-range and only 50 km away from the location of observation).

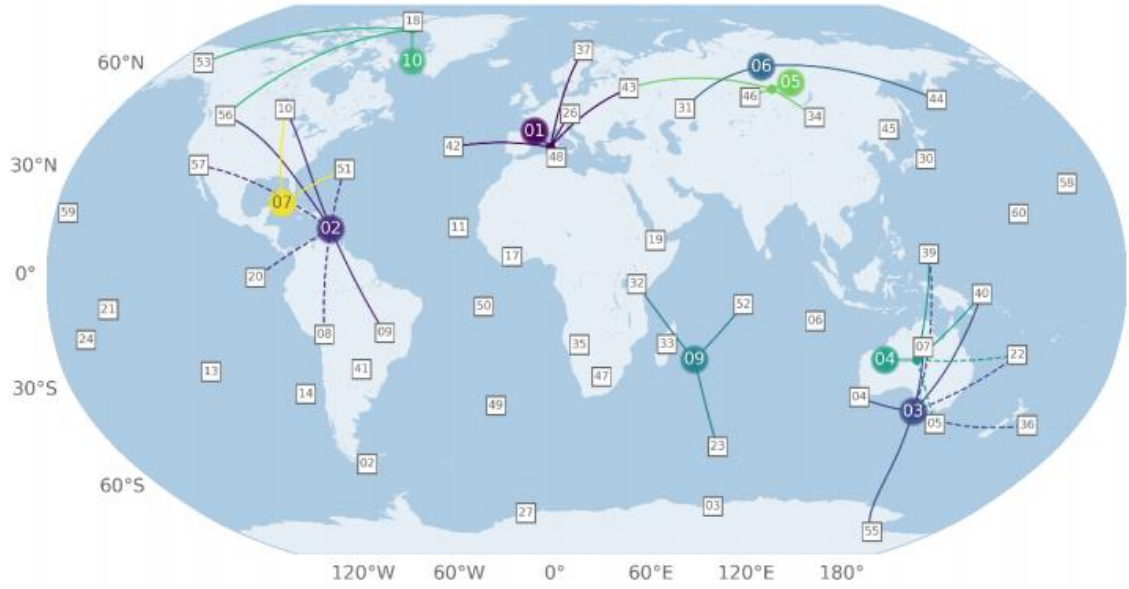

Figure 5-30: IMS network map of stations recording specific fireball events. Event 10 is the fireball discussed in this section (*Pilger et al.*, 2020b)

From the above paragraphs, the timing of the source and the confirmation of long-range propagation indicate the fireball as a possible source of the signal. The fragmentation event (where the fireball exploded) of the Western Greenland fireball is a known source of infrasound as shown by *Pilger et al.* (2020b), however the entry of the fireball into the Earth's atmosphere can also be considered as a source of infrasonic waves. Both or one of these origins may result in the signal appearing over Maynooth. According to Table 5-1, meteorites create singular duration type signals with periods of less than 5 seconds, which does not describe the signal detected. However, if the fragmentation and explosion

of the fireball is considered as a source, Table 5-1 shows that explosions are more diverse in terms of their period of the subsequent infrasonic waves and are more likely to be the origin of the signal seen at Maynooth (assuming the signal emanates from this event). The same table shows the expected amplitudes of the waves induced in the hydroxyl layer from the various sources, in the form of temperature variations. These temperature variations (in Kelvin) show that that medium- and long-period waves from explosions make larger impacts on the hydroxyl layer temperatures (specifically the $OH(3-1)$ Meinel band), compared to short-period waves from explosions or meteorites.

Source	Period	Amplitude (K)	Duration
Severe weather	< 2 s (SP)	< 0.5	Continuous
	2–60 s (MP)	0.05–0.5	Continuous
	60–300 s (LP)	0.05–5	Continuous
	> 300 s (GW)	> 0.5	Continuous
Volcanic activity	0.1–2 s (SP)	0.05–5	Continuous
	2–190 s (MP)	> 5	Continuous
	190–300 s (LP)	> 5	Singular
	> 300 s (GW)	> 5	Singular
Orography	20–60 s (MP)	> 0.05	Continuous
	> 300 s (GW)	> 0.5	Continuous
Explosions	< 20 s (SP/MP)	0.05–5	Singular
	20–60 s (MP)	> 5	Singular
	60–300 s (LP)	> 5	Singular
Microbaroms	5 s (MP)	< 0.5	Continuous
Earthquakes	0.5–2 s (SP)	0.05–1	Continuous
Aurorae	10–60 s (MP)	< 0.5	Continuous
Meteorites	1–5 s (SP/MP)	0.05–5	Singular
Rocket starts	< 2 s (SP)	0.5–5	Singular
Thunder/Sonic boom	< 2 s (SP)	< 0.5	Singular

Table 5-1: (seen previously in Chapter 1, Section 1.8.1) The period of waves produced by a variety of sources according to Pilger et al. (2013b) *along with the amplitude induced in the hydroxyl layer by the waves and the duration of such signals (where singular signals are less than 3 complete wave trains).*

Although Table 5-1 quantifies the amplitude in terms of temperature (in units of Kelvin), based on the instruments used in this study and the calibration procedure of Chapter 3, the same data is needed for radiance values. *Espy et al.* (2007), relating the radiance values of the $OH(3-1)$ band to the temperature, found the conversion factor between the two parameters on a seasonal basis, namely winter and summer. The authors found two conversion factors for each season, where the average for winter is 0.38 ± 0.05 K/kR, and summer is $\sim 0.17 \pm 0.05$ K/kR, and the general relationship between the two is given in Figure 5-31. These values would thus result in a signal with

an amplitude of 5 K, having an equivalent radiance of 25 kR, if only the OH(3 − 1) band is measured. This would only represent a small increase in the context of the response of the detector, as it observes more than the OH(3 − 1), as seen in Figure 2-2 of Chapter 2. Table 3-4 shows how each band covered by the response of the detector contributes to the overall radiance seen by the detector, and the expected response that would be seen by the detector to a 5 K signal change is approximately 84 kR ($\sim 0.66 \times 10^{14}$ ph/s/m^2/sr), if it is assumed that all bands covered react the same as the OH(3 − 1) band.

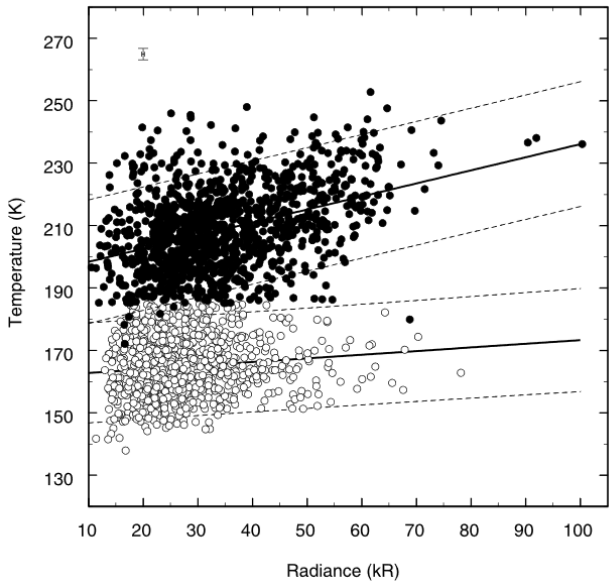

Figure 5-31: Relation between temperature determined by the OH(3-1) band and the associated radiance for winter (closed circles) and summer (open circles) (*Espy et al.*, 2007)

As stated above in Section 5.5.2, the amplitude increase seen by MFR is 0.3×10^{14} ph/s/m^2/sr, and is thus smaller than the expected perturbation ($\sim 0.66 \times 10^{14}$ ph/s/m^2/sr) that would be caused by an explosion (with amplitudes of > 5 K). Although the values are smaller than the expected perturbation, this could be due to a variety of reasons, such as the uncertainty surrounding the correlation between radiance and temperature, the assumption that the temperature data from the OH(3 − 1) band can be appropriately extrapolated, or the signal dissipating in the atmosphere and producing smaller amplitudes in the hydroxyl layer farther from the source. This last

point concerns the propagation of the signal through the atmosphere and whether the time of the signal compared to the source time is reasonable, as well as the amount of loss such a signal would experience (if a wave duct occurs which can facilitate a signal's original amplitude and coherency). Propagation of the signal is discussed in Section 5.5.4 (the following section). The signal characteristics are summarised in Table 5-2 below, showing their relation to the fireball event.

Description	**Parameters**	
Western Greenland Fireball	76.9°N, 69.0°W	2018-07-25 21:55:26 UTC
Observing Station (Maynooth)	53.38°N, 6.6°W	2018-07-26 02:12:00 UTC
Great Circle Distance	3602 km	
Time Difference		04:13:34
Average Speed	234 m/s	
Back Azimuth (degrees) measured from time-lags of the radiometer array	$340.6 \pm 3°$	
Back Azimuth (degrees) measured from geographic coordinates of source and observing station	337.94°	
Time for peak to peak signal of zenith observation	74 seconds	
Period/Frequency of signal	146 s/0.0068 Hz	

Table 5-2: Signal characteristics and comparison to the expected results if the signal originates from the fireball over Western Greenland.

5.5.4. Propagation Modelling

This speed of the signal is dependent on the temperature and wind conditions of the upper atmosphere through which it travels. The approximate speed of sound in the mesosphere is 270 m/s (depending on temperature and wind conditions), and so the speed calculated is lower than this value. To determine whether the temperature and

wind conditions for the time in question could lead to the value calculated, propagation modelling was undertaken by *Pilger* (2021, *private communication*). The modelling utilises ECMWF data, along with MSIS/HWMF models to determine likely propagation paths of signals originating from the fireball. Figure 5-32 shows the initial results of the propagation modelling where the source resulting in infrasonic waves is positioned at an altitude of 43.3 km (the fragmentation altitude (*Chamberlin*, 2021)). The various eigenrays (rays connecting source to receiver) are shown along a corridor from the fragmentation position to Maynooth (covering around 3500 km in distance). Many of the rays that are launched from the fragmentation altitude reflect between the ground and the thermosphere.

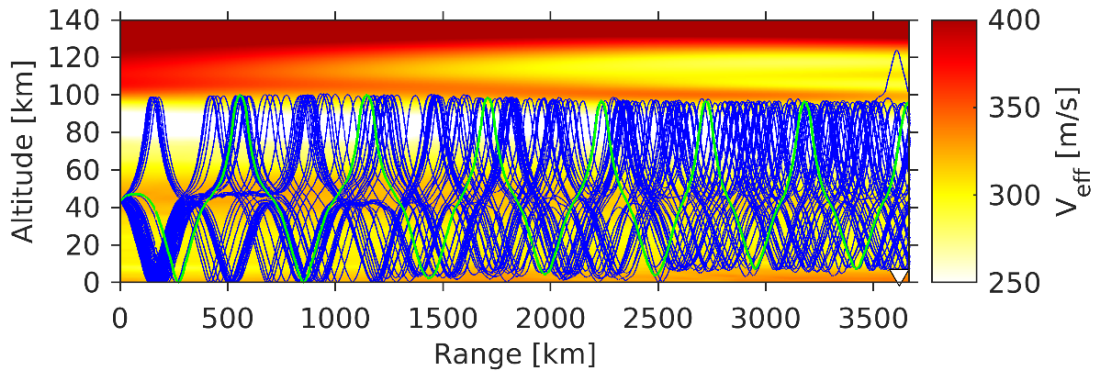

Figure 5-32: Eigenrays launched from the fragmentation altitude of the meteorite. The x-axis represents the full distance between the location of fragmentation (0 km) and Maynooth (~3600 km). Celerity of the green ray is approximately 279 m/s (Pilger, 2021, private communication), where celerity is defined as the speed of sound in relation to ground.

Many of the rays shown would travel too quickly to be considered the source of the signal seen at Maynooth. The eigenray marked in green for instance has a celerity of 279 m/s and would arrive at Maynooth in less than 4.25 hours. When the propagation is modelled instead using a parabolic equation solver to show the energy loss per kilometre, it shows very little amplitude loss for the signal (Figure 5-33). From Figure 5-32, the rays are shown to be considerably steep and may represent the reason that they occupy the entire range between ground and thermosphere. These rays likely do not represent the propagation path of the signal that arrives at Maynooth.

As the signal is detected in the mesopause region in the hydroxyl layer, the source may instead originate from the mesopause region. The fireball passes through this region and the entry of the bolide, as well as its fragmentation, are capable of producing infrasonic waves (*Pilger et al.*, 2020b). Figure 5-34 represents the same propagation modelling as Figure 5-32, but the source is modelled to originate at around 87 km (position of the approximate centre peak of the hydroxyl layer) rather than at the fragmentation altitude.

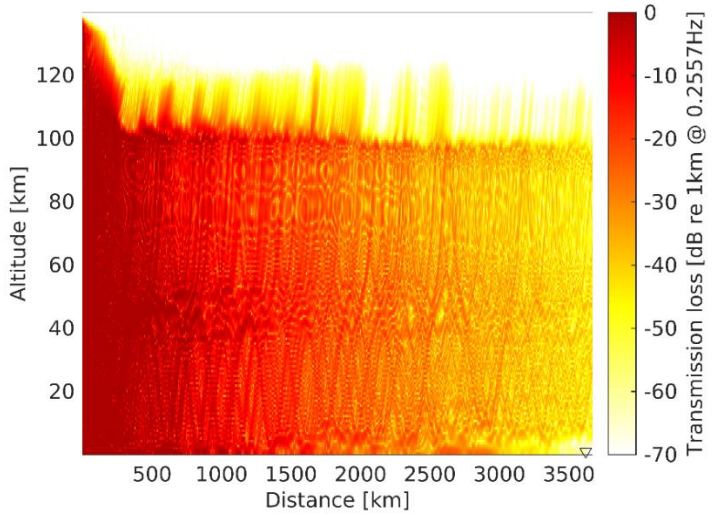

Figure 5-33: Transmission loss of the eigenrays depicted in Figure 5-32 (Pilger, 2021, private communication)

The smaller range of altitudes that the eigenrays occupy is the most apparent difference between Figure 5-34 and Figure 5-32. The eigenrays occupy a region likely coinciding with the hydroxyl layer, and the wave duct present continues for the entire distance between the co-ordinates of the fragmentation event and Maynooth, representing an area of the atmosphere where the effective sound speed is less than or equal to 250 m/s. The duct descends slightly before reaching Maynooth, but is still in close proximity to or likely overlapping the hydroxyl layer on the bottom-side. The celerity of the green eigenray was calculated and gives a value of 233.7 m/s. This speed, derived from the modelling, agrees well with the approximate calculation performed in the previous section.

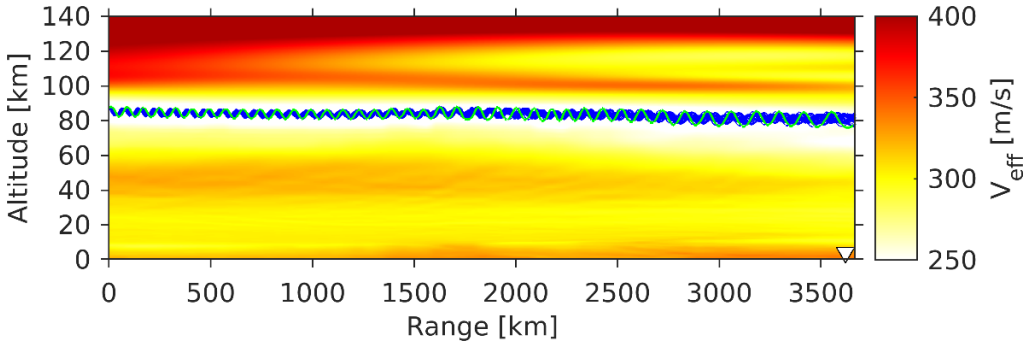

Figure 5-34: Same as Figure 5-32 except the launch altitude is lifted to 87 km (Pilger, 2021, private communication)

Although these values show remarkable agreement, additional uncertainty is introduced due to the likely source occurring further to the west compared to the fragmentation co-ordinates, if it is assumed that the source results from entry rather than the fragmentation.

As before, the transmission loss of the signal can also be derived using the same background model. This is shown in Figure 5-35, where the transmission loss relates to a signal with a frequency of 0.2557 Hz (dominant frequency of the signal from *Pilger et al.* (2020b)). There is very little attenuation in the wave duct, which is apparent from the region around 80 km. The presence of this wave duct may also explain the coherent nature of the signal observed by MFR.

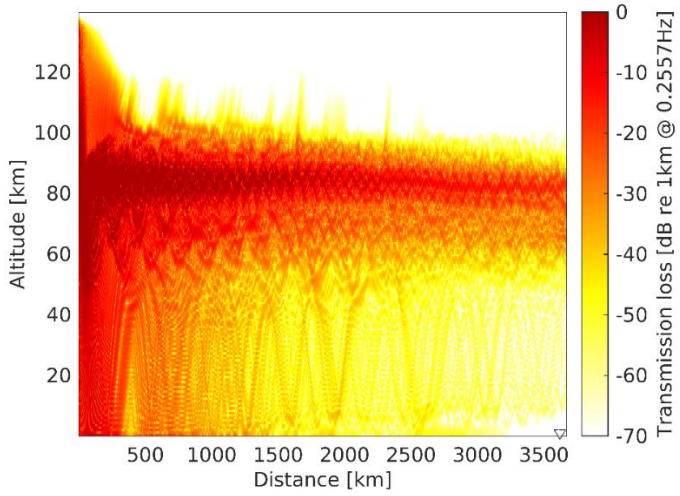

Figure 5-35: Transmission loss of the eigenrays shown in Figure 5-34 (Pilger, 2021, private communication)

5.5.5. Comparison of Signal to Literature

According to *Silber* and *Brown* (2014), the general shape of infrasound from fireballs/bolides comes in the form of N-shaped disturbances, which the authors outline in a proposed classification scheme (see Section 1.8.1.4). The vast majority of the arrivals (57 %) seen by *Silber* and *Brown* (2014) are single N-shaped signals emanating from meteors, the same type of signal seen in the infrasound signal seen in this section. The same type of signal described by *Silber* and *Brown* (2014) is also seen in modelling by *Sabatini et al.* (2019), which is shown in Figure 5-36. From these studies, it is clear that the signal seen on 25 July 2018, especially the signal seen in MFR, presents like an infrasonic disturbance resulting from the entry of a meteor into the Earth's atmosphere. The signal occurs over a longer time frame than signals detected closer to the source, but this fits with modelling found by *Sabatini et al.* (2019) where the signal stretches farther from the origin point (Figure 5-36), while also maintaining the original N-shape. Although *Silber* and *Brown* (2014) and *Sabatini et al.* (2019) present the oscillation of the atmosphere as a function of pressure, this same signature should translate to a similar response from light emissions from the hydroxyl layer (as discussed in Chapter 1, Section 1.5).

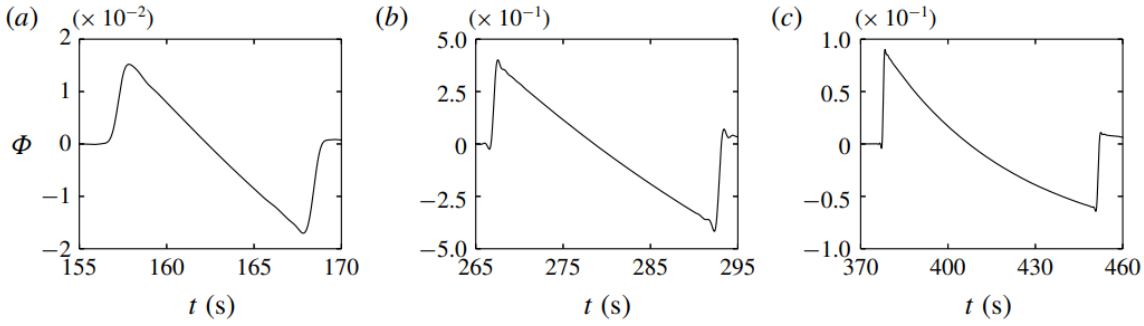

Figure 5-36: Modelled pressure effects of non-linear infrasound propagation on the upper atmosphere at various altitudes (a) 50 km, b) 90 km, c) 130 km) from the source. As the signal propagates into the upper atmosphere, it stretches out over time, which is seen here (*Sabatini et al.*, 2019)

To identify the source of the signal, the speed and the directional information is used to narrow down the number of potential origins. The Great Circle path from the fireball to Maynooth has a back azimuth angle of $22°$ west of north, which is in almost complete agreement with the back-azimuth calculated from the tripartite array signals ($19° \pm 3°$ west of north). This agreement would make the fireball event a likely source of the signal, and the next step is to determine if the speed of the signal is in the range of the speed of sound in the upper atmosphere (~ 270 m/s). Using the same data from the instruments, the speed of the signal across the station was determined to be ~ 45 m/s, significantly lower than the speed of sound in the upper atmosphere. Although the direction of the signal appears to provide evidence that the fireball is the origin point, the speed of the signal across the station does not support this hypothesis. As a result, the fireball cannot be conclusively linked to the disturbance observed in the Maynooth radiometers.

As noted in Section 5.5.3 above, no other large sources that could result in an N-shaped signal have been identified (such as volcanic eruptions or large explosions) that could explain the source of the signal, while also propagating from the north-west. In terms of smaller events, a Falcon 9 launch did occur in Vandenberg Air Force Base in California ($34.74\,°\text{N}, 120.57\,°\text{W}$) (*Mathews et al.*, 2020) at approximately $11{:}39{:}26$ UTC, heading in a southerly direction. It was confirmed by *Mathews et al.* (2020) that infrasound was generated from the rocket launch, and detected at a nearby station. The air force base is located approximately 8360 km from the Maynooth station, and if the signal were as a result of this launch, the disturbance arrived $14\,\text{h}\,45\,\text{m}\,34\,\text{s}$ after ignition. Through a simple distance, speed, time relation, this would point to a non-linear infrasound signal travelling with an average speed of ~ 158 m/s. However, the signal does not match with the direction of the air force base with respect to Maynooth's station.

Although the signals shown so far illustrate the capability of the detectors in observing infrasonic signals, the discussions above regarding the source show the difficulty in determining the likely origin of the signal, and is an issue that will be highlighted again in the subsequent sections of this chapter.

5.6. Infrasound Signal (Case Study 2 - 20/21 July 2014)

5.6.1. Background Conditions and Signal Characteristics

A further example of an infrasonic signal occurred on the night of 20/21 July 2014, and is shown in Figure 5-37, with a zoomed-in version of the same signal seen in Figure 5-38. The signal occurs at around 01:33 UTC (shown as 25:55 UTC) on the morning of 21 July, and lasted for 18.5 minutes.

Weather conditions for the evening have been confirmed (as previous) through Met Éireann and power spectral analysis for the night. It was confirmed by Met Éireann data that the cloud amounts during the course of the signal was only 1 okta, indicating a night of few if any clouds. The power spectral analysis of the night confirms these observations, and shows a night with no apparent 0.78 Hz signal, indicating a cloudless sky over the station. As a result the signal is assumed to originate from the hydroxyl layer, rather than from streetlights affecting the detector input. One of the noticeable trends of the MFR time-series in Figure 5-37 and Figure 5-38 is the regular dipping of the signal throughout the night (where the data contributes a sudden vertical dip, seen more clearly in Figure 5-38, and shown next to the data from MFR2 and UWOSCR in Figure 5-39). This was caused by the lock-in amplifier going out of the "lock" condition. This problem was eliminated in later data sets, but it does not interfere with the frequency determination of the time-series in Figure 5-38, which through manual methods was confirmed to be approximately 0.01 Hz, also seen in the time-series of MFR2, giving a frequency of 0.009 Hz (about once every 2 minutes).

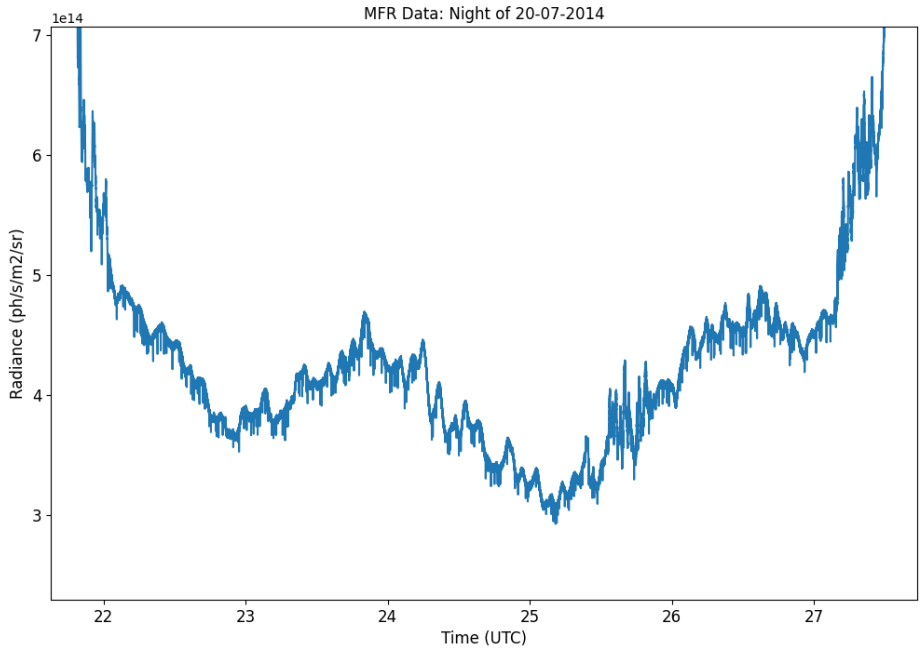

Figure 5-37: Time-series for the night of 20/21 July 2014 from the MFR dataset.

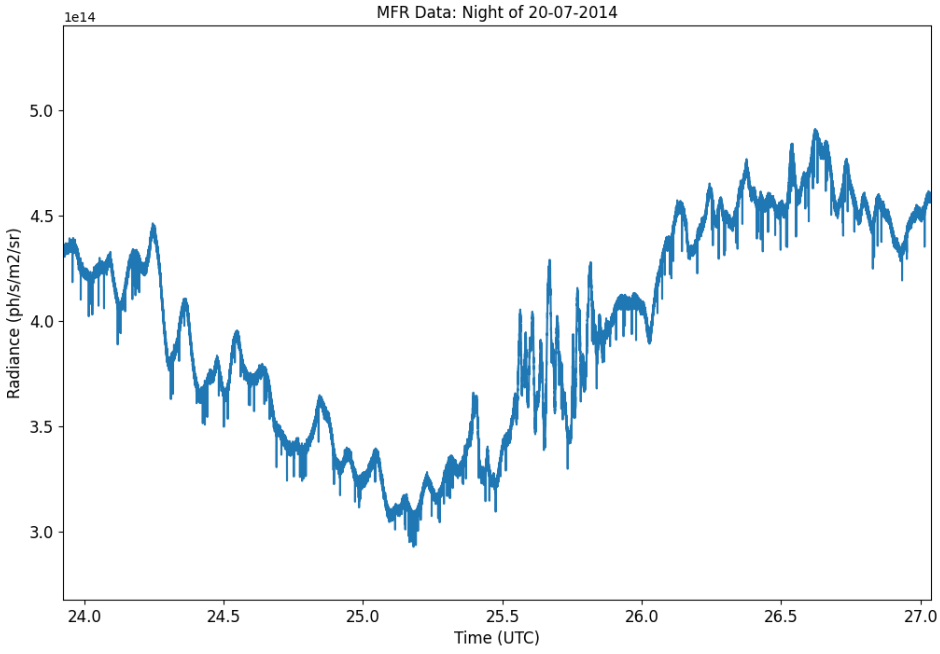

Figure 5-38: Zoomed in plot of Figure 5-37, showing the detail of the signal of interest from MFR. Similar signals are seen in MFR2 and UWOSCR.

Detail from the UWOSCR instrument was difficult to obtain due to the noise the instrument experienced (seen in Figure 5-39) and thus could not be used for further frequency evaluation. The frequency spectrum of the signal is more easily seen from the

Morlet transform of the night, which is shown in Figure 5-40, where the spectrum appears to confirm the manual analysis of the signal frequency, giving a value close to that of 0.01 Hz. A similar Morlet transform was obtained for the MFR2 time-series (not pictured), again showing power associated with frequencies of 0.01 Hz. Both power spectra thus confirm that the frequency of the signal is in the infrasonic range.

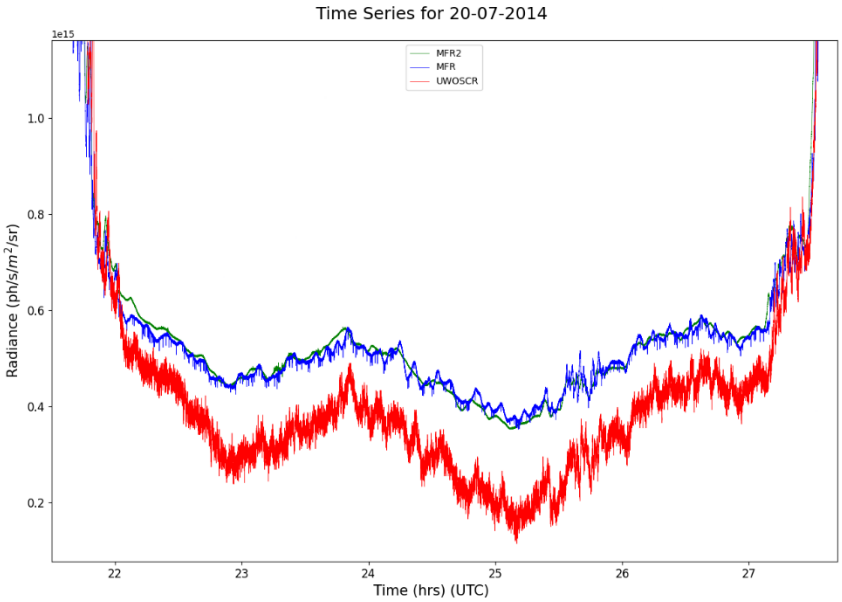

Figure 5-39: Time-series plots for all instruments. The dipping seen in MFR is obvious compared to both MFR2 and UWOSCR.

Accurate speed and directional information could not be gathered in the case of the signal due to the difficulty in determining the onset of the signal in UWOSCR, but it was found that the general direction of the signal was from south-west to north-east.

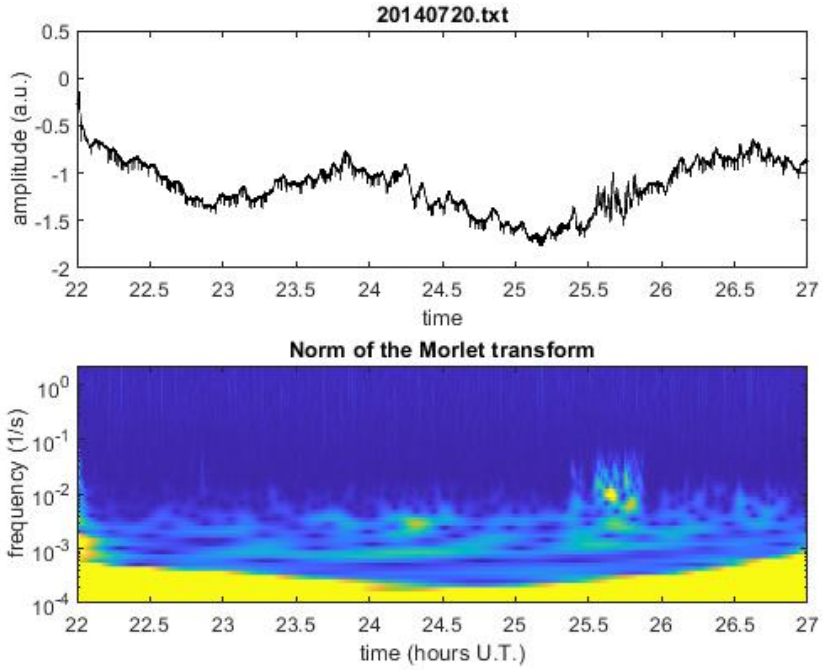

Figure 5-40: Time-series from MFR for the night of the signal (top) and the Morlet transform for the same time-frame (bottom). The signal of interest is apparent in the Morlet transform for the night, showing a majority of the signal power lies in the 0.01 *Hz region of the frequency spectrum.*

5.6.2. Source Determination

Due to data from Met Éireann, and a frequency spectrum confirming that likely no cloud existed over the station during the time of the infrasound signal, source determination was undertaken. The signal represents a short-lived disturbance in the upper atmosphere, but is unlike the previous signal shown in Section 5.5 which was more N-shaped in form. Although short-lived, the signature is continuous in nature and sources producing such signals, shown in Figure 5-9, are considered as candidates. Due to the difficulty in determining the speed and direction of the signal, the source of the signal cannot be determined exactly, but rather, candidates for signal origin are discussed.

Of the sources shown to produce continuous signatures, only one event, an earthquake, was identified that had the capability of producing the signal seen in all three instruments. On the 20 July 2014, an earthquake measuring 6.2 on the Richter scale was registered 98 km south-east of Kuril'sk, Russia at approximately 18:32:48 UTC, and

was detected by a seismometer at Maynooth 12 minutes later (Figure 5-41). Based on the time when the earthquake was registered by the seismometers at Maynooth and the distance between Maynooth and the epicentre, the speed of the disturbance would be ~12.32 km/s, which is in line with the general speed of P-waves emanating from earthquakes (dependent on the material that the waves pass through (*Stein* and *Wysession*, 2009)).

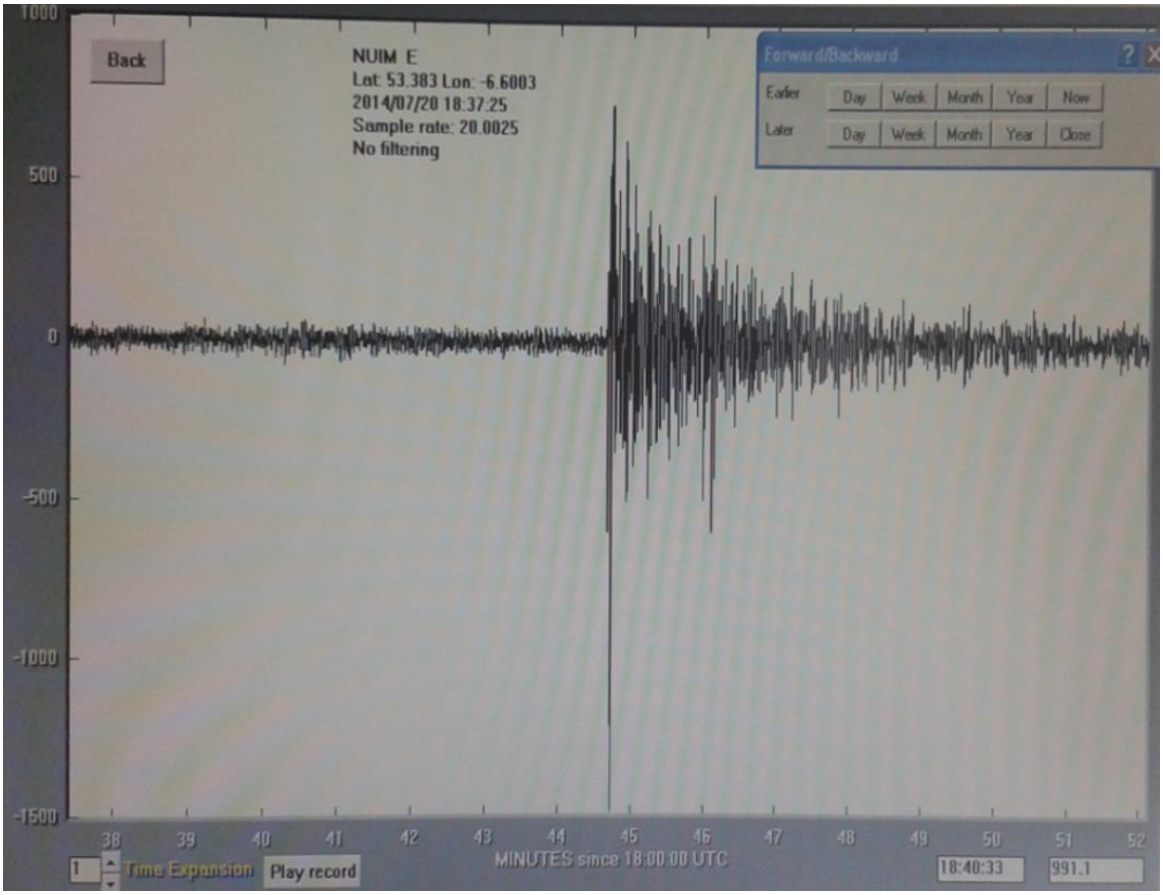

Figure 5-41: Seismograph from Maynooth registering the Kurik'sk earthquake that occurred on 20 July 2014 (Credit: Dr F.J. Mulligan)

Based on the time-series in Figure 5-38, the signal considered here was detected 6.5 hours after the initial earthquake. Based on the distance to the source (~8800 km), the theoretical average speed of the wave is 376 m/s, which is noticeably higher than the general speed of sound in the mesopause (the signal could take a more complicated path by travelling through the Earth and then propagating to the atmosphere from mountainous peaks (as discussed in Section 1.8.1.3), resulting in a higher average

velocity). Along with the direction of the signal (passing over the station from south-west to north-east), the evidence appears to make the earthquake an unlikely source of the signal.

Due to the competing evidence available to tie the signal to the earthquake, other sources were considered as the origin, including NLCs, which have been previously covered in Chapter 4 (Section 4.4 – Section 4.5), and are a summer hemisphere phenomenon which occur at high latitudes. Based on the time of the signal, the disturbance seen in the time-series may be due to the presence of NLCs. Chapter 4 has shown that the general characteristic found with NLC signals in the time-series is a sudden increase in radiance, followed by a sudden decrease (with variation at this higher radiance level sometimes seen), which is an aspect not observed in the case of this signal. Rather, the signal is observed as an oscillation of the background radiance, and no sudden increase or decrease is witnessed. As well as this observation, no visual evidence of NLCs was reported on the evening of the 20/21 July 2014, according to records from NLCNET. This appears to provide a lack of evidence for the structures above the station, however if this signal is due to NLC phenomena, the signal could result from structures too faint to be visually observed, and thus give only a small variation in the background radiance seen at Maynooth.

It is also noted here, in relation to other sources producing continuous signals, no fireballs were reported during the time in question according to data extracted from the CNEOS database (*Chamberlin*, 2021). Severe weather events and volcanic tremors also do not appear to have caused the signal appearing in the datasets. With the current information available, the two most likely sources of the signal appear to be either due to Kuril'sk earthquake mentioned (with the opposing evidence outlined) or NLCs above the station.

5.7. Infrasound Signal (Case Study 3 - 16/17 May 2013)

5.7.1. Background Conditions and Signal Characteristics

The final infrasonic case study signal to be presented is from a time-series already presented on the 16 May 2013, where gravity wave activity was present through the night. The infrasonic signal is seen in Figure 5-42, and more clearly in Figure 5-43, beginning at 25.6 UTC and ending at 26 UTC (02:36 – 03:00 UTC on 17 May 2013). Information from the night's power spectrum and Met Éireann confirms that the night saw little or no clouds (Casement Aerodrome cloud amount level remained constant at 1 okta for the majority of the night while the power spectrum showed no 0.78 Hz peak).

As a result of these clear conditions, data analysis was undertaken and it was found that the disturbance over the station persisted for around 24 minutes, with the detail of the variation becoming increasingly clear after 25.7 UTC. Based on the variation seen after this time, the disturbance had an average period of 86 seconds, giving a frequency of 0.0116 Hz (or 11.6 mHz), which lies well within the infrasonic range of frequencies.

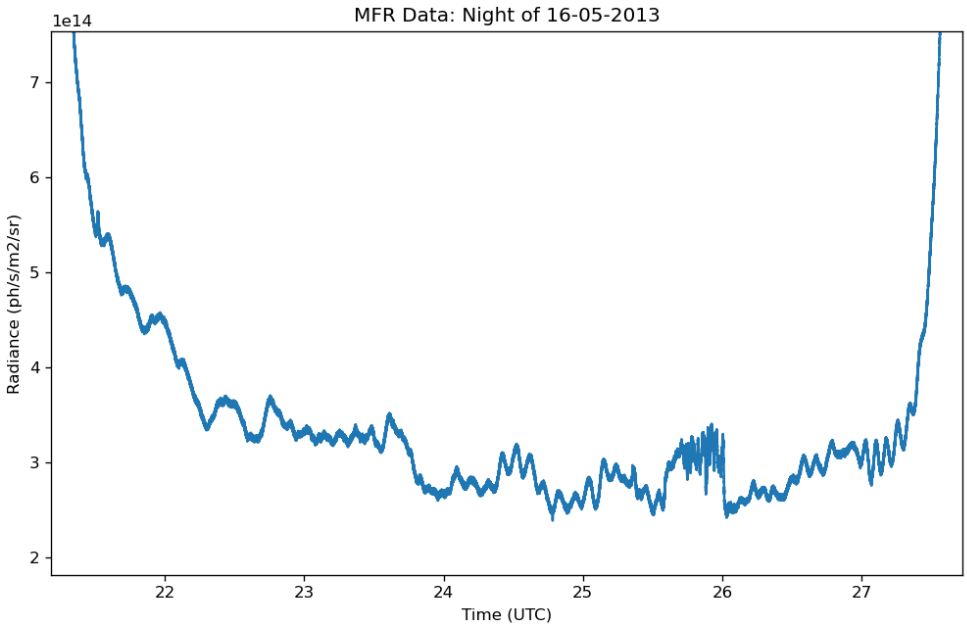

Figure 5-42: Time-series of the 16 May 2013 (MFR) showing gravity wave signatures and the infrasonic signal occurring before 26:00 UTC

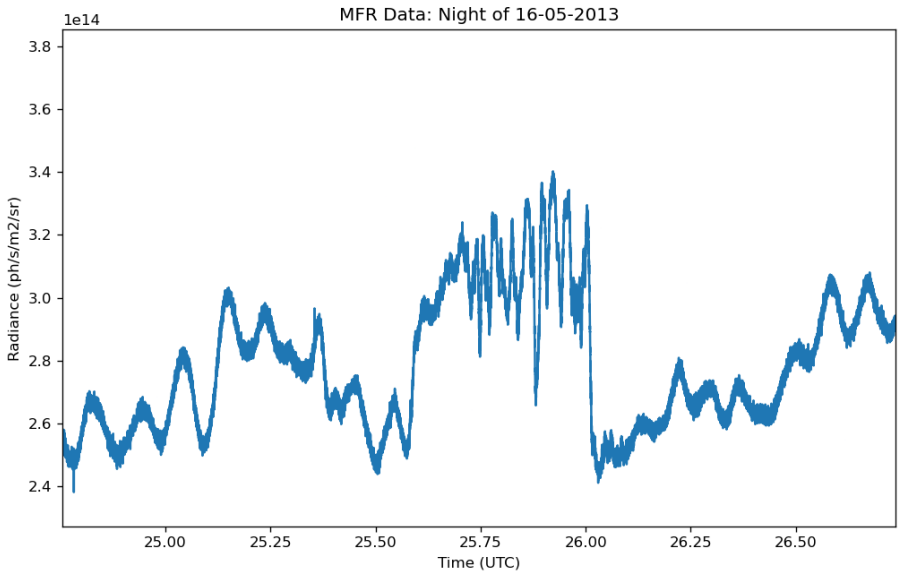

Figure 5-43: Detail of the infrasonic signal discussed in this section, where a noticeable increase above background levels is seen followed by a variation of this new level. Due to the shape of the signal, NLCs were first considered as a source.

To confirm this was the case for the signal, wavelet analysis was performed on the signal, shown previously in Figure 5-10, where the signal occupies a period range up to 60 seconds, or 0.016 Hz. Both manual time-series calculation and the wavelet transform thus confirm the fact that the signal is infrasonic in nature. The amplitude increase of the signal is $1.28 \pm 0.05\, I_0$ above background levels with a average variation around this new amplitude increase of 0.3×10^{14} ph/s/m^2/sr (seen in Figure 5-43).

5.7.2. Source Determination

The only data for the night exists in the MFR dataset, as the MFR2 instrument was only beginning operation during this time while UWOSCR was not operational on the night. As a result of this lack of data, no speed or directional information could be extracted from the signal. As a result, any determination of a source is speculative.

The first source considered in the case of this signal was that of NLCs, due to the similar shape of the signal to the signals shown in Section 4.5, and specifically the sudden

increases and decreases. However, the signal occurs early in the NLC season (early May), rather than during the peak of the NLC season (around the summer solstice), making their presence over the station unlikely. It was also confirmed through measurements from the AIM-CIPS satellite that no PMC activity occurred close to the station, while there were no reports of NLCs from amateur observers on the NLCNET network on the night in question.

In terms of sources such as earthquakes, no notable events (exceeding 5 on the Richter scale) occurred in the relevant time frame on the 16 May 2013. The attempt to connect an earthquake to the signal is hampered by the lack of directional and speed information as the signal source cannot be triangulated (since data only exists for one radiometer). For other sources like volcanoes and explosions, again no notable events have been found that could explain the radiance increase found by MFR on the 16/17 May 2013.

5.8. Chapter 5 Summary

This chapter has summarised the main signals found in the datasets that have originated from hydroxyl emissions in the mesopause region. In particular, the focus (and the aim of the thesis) was on the detection and analysis of infrasonic signals in the dataset. The chapter opened with a discussion of gravity waves propagating through the hydroxyl layer, illustrating the ability of the array to detect waves in the layer, albeit at a lower frequency than infrasonic waves.

Gravity wave analysis is shown in Section 5.2 to demonstrate how characteristics like frequency, duration, speed and directional information can be obtained. Infrasound signals were introduced in Section 5.3, presenting the two main infrasonic wave shapes seen in the upper atmosphere, including those classified as continuous or N-shaped waves. These wave types were explored in the following sections, with an analysis of the datasets after 2018 showing evidence of small continuous infrasonic waves known as microbaroms (Section 5.4). The chapter then dealt with case studies in Sections 5.5 –

5.7, showing one-off events in the datasets that were clear compared to the background (as opposed to microbaroms, which possessing small amplitudes are impossible to distinguish as standalone signals from the background). Each of the case studies, whether N-shaped (Section 5.5) or continuous in wave shape (Section 5.6, 5.7), were examined for their characteristics and were only considered for further analysis if the signals had infrasonic frequencies.

As well as the characteristics, source determination was also attempted for each of the signals presented in Section 5.5, 5.6 and 5.7. This process proved very difficult due to the absence of concurrent measurements, absence of observations or the lack of data from part of the array (particularly in the case study shown in Section 5.7). Section 5.5 showcased the most well-documented and coherent signal found in the infrasonic range and emanating from the hydroxyl layer, and a tentative connection to an explosive fireball event was discussed. Although many features of the signal supported the idea of the fireball as the source, the origin of the signal cannot be conclusive due to the slow speed of the apparent signal across the array. This same issue of conclusive source determination is also true for the case studies of Section 5.6 and Section 5.7. The case studies, and microbarom analysis show that it is possible to detect infrasonic signals originating in the hydroxyl layer using a ground-based tripartite radiometric array, but attributing them to a specific source is difficult.

6. Summary and Conclusions

6.1. Summary of Findings

The primary objective of this thesis was an attempt to prove that it is possible to detect infrasound signals at mesopause altitudes by observing infrared emissions from the OH* layer near the altitude of that layer. A number of previous attempts focussed on detections using these emissions; measuring temperature fluctuations (*Bittner et al.*, 2010, *Pilger et al.*, 2013b), and radiance variations (*Hannawald et al.*, 2016, 2019, *Sedlak et al.*, 2016, *Le Dû et al.*, 2020) with some success. The temperature variations reported by Bittner and Pilger based on spectrometer measurements were at the lower end of the infrasonic frequency range, and might indeed be classified as ripples associated with gravity waves. *Hannawald et al.* (2016, 2019), *Sedlak et al.* (2016) and *Le Dû et al.* (2020) all employed impressive high speed CCD camera systems, but even they were limited to a cadence of 2 images per second, giving a maximum detectable Nyquist frequency of 1 Hz. Detection of infrasound in OH* emissions is not an easy task due to the low levels of signal likely to be generated (*Bellisario et al.*, 2020) and most of the published reports that attempt to do this generally resort to examining gravity waves (*Bellisario et al.*, 2020).

The approach adopted in this work is based on an original radiometer detector (UWOSCR) (*Stockwell* and *Lowe*, 2001) which was designed for detection of gravity waves by raster scanning a region of the sky over the observing station. In order to convert from detection of gravity waves to infrasound, raster scanning was abandoned and a fixed detection viewing geometry was implemented. This allowed the possibility of up to 3000 samples per second, which was more than sufficient to detect infrasound, according to the requirements described in Section 2.2.2 of Chapter 2. Since the maximum frequency of infrasound is about 20 Hz, a large number of samples were averaged to improve the signal-to-noise level of the detected time-series. Tests using a single radiometer operated in this mode showed that infrasound (arising from a

pedestrian beacon) could be detected reliably.

The difficulty with this configuration is that it is in essence a single pixel detector, which does not provide any information on the direction of travel or the speed of the infrasound across the observing station. To address these two problems, two additional radiometers similar to the first were assembled in such a way that the three instruments operating together constituted a three-element array similar to early seismic detection configurations, and described in Chapter 2. Unfortunately, one of the radiometers had entrance optics issues which led to a field-of-view that was approximately twice the FOV of the other two devices. The time-series signal from this instrument showed the averaging effect clearly on the passing infrasound. This problem was addressed by introducing a field-stop which naturally reduced the quantity of light admitted to the detector, thereby introducing a different set of problems.

6.2. The Successes

Using a single radiometer, infrasonic frequencies were detected successfully from a clear reference source (a pedestrian beacon) and the frequency which was at the upper end of the infrasound range (0.78 Hz) was clearly identifiable. Infrasound at much lower frequencies was clearly observed in the individual time-series of this first radiometer, but no direction or speed could be attributed to these sources.

When the three element array was completed, infrasound was detected by all three instruments, and the separation of the fields-of-view of the instruments enabled the time delays between the arrival of similar signals at the different radiometers to be determined, and from which direction and speed information were calculated using the principles outlined by *Briggs* (1968) and *ElGabry et al.* (2017). Infrasound-like signals (in terms of frequency and speed), initially thought to be associated with infrasonic waves, were observed and found instead to be associated with the presence of noctilucent clouds potentially too thin to be detected visually by amateur observers (Section 4.5.1

and 4.5.2, Chapter 4), which suggest the possibility for improved detection of these clouds.

There were many cases of infrasound detected by all three instruments which may have arisen from distant earthquakes or volcanic activity as discussed in Chapter 5. A few case studies have been included where evidence was available to attribute the infrasound signal to major events at very considerable distance from the observing station in Maynooth. Of the main events found in Chapter 5, the signal seen in Section 5.5, which was at first connected to the Greenland fireball (*Pilger et al.*, 2020b) found that no signal from the event occurred in the European IMS stations, but did occur in the North American stations.

The two types of signal observed demonstrate that the original concept could work successfully in cases where the signal level was relatively large and the wave pattern was easily identifiable in the time-series. This is particularly true for the N-shaped signature found in Section 5.5 of Chapter 5. On reading the work published by *Le Dû et al.* (2020) who resorted to a study of microbaroms when they were unsuccessful in detecting infrasound from the Geminids meteor shower in December 2017, a search for evidence of microbaroms in the data using the same approach was undertaken. This approach turned up evidence of microbaroms in the recorded time-series for MFR and MFR2. It was very difficult to extract microbarom information from the original UWOSCR instrument, which did not have a chopper and lock-in amplifier, thereby demonstrating the value of this enhancement in detection method.

The frequency results for microbaroms showed remarkable agreement with the results of *Hupe et al.* (2019) by identifying a peak in the 0.25 Hz region. The successful implementation of the *Le Dû et al.* (2020) analysis approach which easily picked out the 0.78 Hz peak on nights which were known to have cloudy conditions overhead gave confidence in the method. The seasonal variation of 0.25 Hz microbarom peak also agreed with the results of *Landès et al.* (2012) and *Hupe et al.* (2019). The correspondence of the results from two instruments, MFR and MFR2, give assurance in the validity of these measurements.

Along with the measurements achieved by the radiometers, another one of the major successes of the project was the calibration of the detectors to a known light source, as outlined in Chapter 3. Calibration of radiometric instruments is notoriously difficult, but it allows for the comparison of data from this project to other studies of infrasound in the hydroxyl layer. Compared to the level of signal found in projects like *Bellisario et al.* (2020) and *Le Dû et al.* (2020), the level of signal found at Maynooth appears reasonable. The calibration was also used to quantify the signal found on the 25 July 2018 (Section 5.5 of Chapter 5) and compare the signal expected to the signal seen in the time-series and whether it makes sense in the context of the suspected source.

6.3. The Drawbacks

One of the largest issues faced by the instruments is the requirement of darkness, as well as cloud-free conditions over the station. Although a location like Ireland suffers from a substantial amount of cloudy conditions, making observations difficult, it is not isolated in these difficulties compared to any other nightglow spectrometer operated. The CCD based instruments used by other studies (*Sedlak et al.*, 2016; *Hannawald et al.*, 2019) also suffer from these problems. Due to such limitations, a substantial effort was made to ensure that clouds were not mistaken for signals in the time-series taken from the instruments.

The requirement of darkness for the observation of the hydroxyl emissions also inhibited measurements and the detection of potential events over station. One prime example of this inhibition is the lack of data on the infrasonic waves produced in the Beirut Explosion of August 2020 (occurring on the 4 August 2020 (15:08 UTC)). It is shown by *Pilger et al.* (2020a) that this event produced infrasound, where the infrasound travelled several thousands of kilometres (detected at IMS stations in Tunisia, Germany, Azores etc.). As a result, infrasonic signals from the event should be detectable at the Maynooth observing station. Table 6-1 details the potential arrival times of the signal at

the observing station, using data from both *Pilger et al.* (2020a) and *Silber* and *Brown* (2014), giving the latest time of arrival to be **19: 58: 12** UTC (4 August 2020). During this time of year, the solar elevation angle at the observing station is positive at **19: 58: 12** UTC, meaning any potential signals arriving from the explosion would be masked by sunlight (as viewed by the detectors) and thus undetectable.

Locations	***Great Circle Distance***	***Speed of Sound of Various Atmospheric Ducts (Silber and Brown, 2014)***	***Arrival Time at Maynooth Based on Duct Type (UTC)***
Beirut 33.887°N, 35.513°W	3939.63 km	*Tropospheric:* 340 m/s	*Tropospheric:* 2020-08-04 18:13:12
Observing Station: 53.38°N, 6.6°W		*Stratospheric:* 285 m/s	*Stratospheric:* 2020-08-04 18:50:24
		Mesospheric: 220 m/s	*Mesospheric:* 2020-08-04 19:58:12

Table 6-1: Arrival time determination of a theoretical infrasonic wave from the Beirut explosion occurring on 4 August 2020.

The low-light signals available, as discussed in Section 2.2.1 of Chapter 2, demanded a wide wavelength range in order to capture meaningful signals. This introduced problems whereby signals from non-hydroxyl sources such as street lamps scattered from clouds, and solar illumination scattered from noctilucent clouds were detectable by the instruments. Although signals arising from the solar illumination scattered from noctilucent clouds made for an interesting by-product of the detector capability, it does introduce interference and affected the main aim of observing hydroxyl emissions.

Along with the relatively low-light signal originating from the hydroxyl layer, the wavelength associated with infrasound (for example $\sim \frac{300\ \mathrm{m/s}}{0.15\ \mathrm{Hz}} = 2$ km) demands a relatively small field-of-view (~ 1.7 km) as discussed by *Le Dû et al.* (2020), in order to avoid averaging of individual infrasound waves. This further restricts the amount of light observable by the detectors, in order to observe the main target of the thesis.

In terms of the entire array, unfortunately, it consists of only 3 elements. Ground-based arrays tend to have 4 (or more) elements (as seen in the IMS detectors (*Le Pichon et al.* (2010) and references therein) as this allows several independent measurements of direction and speed, which serves as a check of the self-consistency of the data. Given the fact that changes in wavefront may make identification of the specific pattern difficult, such a check of self-consistency would be a very important improvement. Unfortunately, sufficient apparatus was not available to construct a fourth radiometer in this project, leading to a lack of a check on self-consistency of signal direction.

Another distinct drawback of the current system is that each radiometer is controlled by its own computer, leading to independent clocks controlling each radiometer. Since the relative time of each signal is paramount in determining the direction and speed of an infrasound pattern across the station, this required the clocks of each computer to be synchronised to an external time server. Most of the time this worked reasonably well, but on occasions, loss of communication between an individual radiometer and the time server resulted in a lack of synchronisation of the signal from each instrument and therefore called into question the validity of the direction and speed measurements obtained. This process of synchronisation across the computer clocks has been automated in recent years, whereby the external computer checks the instrument clocks each hour and resyncs the instruments if disparities between timing occurs.

At a more fundamental level, the biggest problem is the low amplitude of the signals generated. It is clear that large events such as earthquakes, volcanoes and major bolides produce signal levels in the OH* emissions that can be detected relatively easily. The work of *Bellisario et al.* (2020) in determining expected signal levels is particularly helpful in this regard, but further work is needed along the lines begun of Snively (2013). It has been shown in Section 5.5 of Chapter 5 that the expected temperature increase due to infrasonic waves from various sources can be connected to the equivalent radiance increase, using data from *Pilger et al.* (2013b) and *Espy et al.* (2007). The relationship established is only immediately applicable for temperatures and radiances of the OH$(3-1)$ band, rather than the entire spectrum of the OH Meinel bands. As a result, the

$OH(3-1)$ relationship is extrapolated for the spectrum observed by the Maynooth detectors to determine the expected increase in the temperature of the OH bands given the observed radiance increase. This extrapolation may be inaccurate due to the lack of temperature data for other OH bands, but does allow for an estimate in temperature variation due to signals observed. For a more accurate measurement of the expected signal levels, more data regarding the temperature of the entire OH spectrum is needed.

Another problem is that the infrasound patterns change as they propagate through the atmosphere and it may not always be possible to identify, unambiguously, the pattern at three or more distinct locations in the sky. This issue arose in many of the case studies shown in Chapter 4 (regarding NLCs) and Chapter 5. The viewing angle chosen for the three radiometers (zenith, 10 °N and 10 °W) used in this work was a first approximation in this regard. Of primary concern was to be able to measure clear time delays between the arrival of similar signals at the three instruments. More accurate timing would allow the fields-of-view of the individual radiometers to be closer together, thereby increasing the likelihood of observing self-similar signals.

Many instruments which employ spatially separated detectors have well developed cross-correlation algorithms for detecting time-lags between the time of arrival of these signals. Examples include meteor radar signals (*Briggs*, 1968, 1985), seismic detectors (*Pignatelli et al.*, 2008, *ElGabry et al.*, 2017) and ground-based infrasound (*Le Pichon et al.*, 2010). A simple version of the Pignatelli algorithm was implemented in this project, but it required some operator intervention due to the lack of clear coherence in the time-series, an idea of which is depicted in Figure 6-1. In addition, in many such systems, the algorithm is applied to versions of the original time-series which has been filtered into separate frequency regions. The criteria for a positive detection is tightened by requiring the detection of a specific signal simultaneously in several filtered frequency ranges. There is substantial scope for work on this topic, and indeed, the data that has been recorded during this period may serve as a suitable test for such an effort.

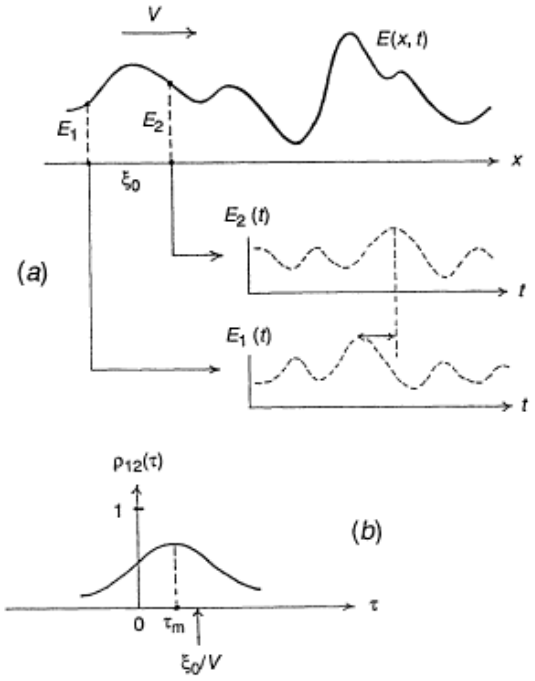

Figure 6-1: Figure taken from Briggs (1968) *showing the variation in coherency of a signal as they propagate past two antennas. As a result of the changing pattern (E(x,t)), two different signals ($E_1(t)$ and $E_2(t)$) are seen by the antennas due to the changing consistency. The cross correlation function ($p_{12}(\tau)$) between these two signals has a maximum value at a lag of τ_m, which is less than the actual lag of ξ_0/V. The radiometers in this study attempt to address this issue by reducing the distance between the radiometer's field-of-views.*

6.4. Future for Instrument Configuration and Technique in General

The tripartite array developed here should be considered as the first iteration of this type of instrument. As is evident in the history of the development of novel measurement approaches, it is envisaged that future versions of the array would overcome some of the limitations or drawbacks which have been identified and described above in Section 6.3. The alternative approach of using fast CCDs is still attractive, but will also require very considerable post-processing as is evident from the reports of *Hannawald et al.* (2016, 2019), *Sedlak et al.* (2016) and *Le Dû et al.* (2020). The study from *Le Dû et al.* (2020) also makes clear the difficulty in detecting impulsive infrasound signatures such as meteors, thus showing similar limitations in this approach.

Experience with ground-based infrasound arrays over the past twenty years has revealed that an array with 8 sensors is far superior to an array with 4 sensors (*Marty*, 2019), which is susceptible to aliasing, and would result in a decrease of detection capability of the array. This problem was found by the CTBTO with regards to the IMS network, where recommendations were made, resulting in newer IMS stations having 8-element rather than 4-element arrays. Such instruments can be seen in the screenshot in Figure 6-2 from the CTBTO.

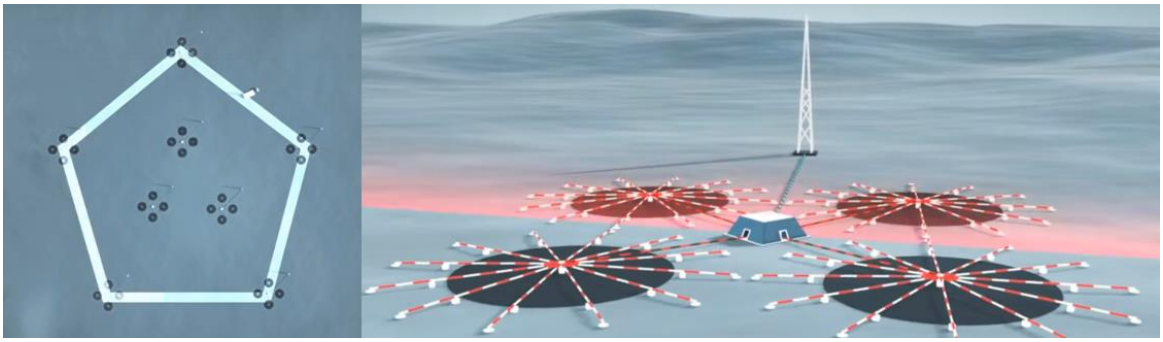

Figure 6-2: Screenshot from (*CTBTO*, 2012a) *(left) showing an example of an 8-element IMS array (3 elements in the middle, and 5 connected by the blue line, and (right) the detection of an acoustic wave by one element in the array.*

One of the biggest improvements to the station would be an increase in the number of elements to the array network. For instance, to have a network of 8 individual radiometers all of which are controlled by a single computer similar to an individual station in the IMS network, would greatly reduce the amount of noise that could be identified as a false signal. More usefully, more array elements would have a smaller impact on the array to detect the speed and direction information from a given signal, as only 3 elements are needed to determine these parameters.

As mentioned in the previous paragraph, one of the issues that the array can face is the validation of the infrasound signals. This is restricted by the lack of elements in the array, which makes validation more difficult. An improvement could be made with more sophisticated processing software, to filter individual time-series into distinctive frequency bands, followed by cross-correlation of the filtered signals leading the

attribution of a back azimuth and speed for the signal (*Cansi*, 1995, *Cansi* and *Pichon*, 2008). An infrasound event would only be accepted as a valid event if there was a particular level of agreement between the results for different frequency bands. Much work remains to be undertaken in this area, but it has been completed successfully in other fields of physics as illustrated in Figure 6-3 from *Ott et al.* (2019). Of course the signal levels at ground stations, like those shown in Figure 6-3, are very large compared with the signal levels expected from the OH* layer.

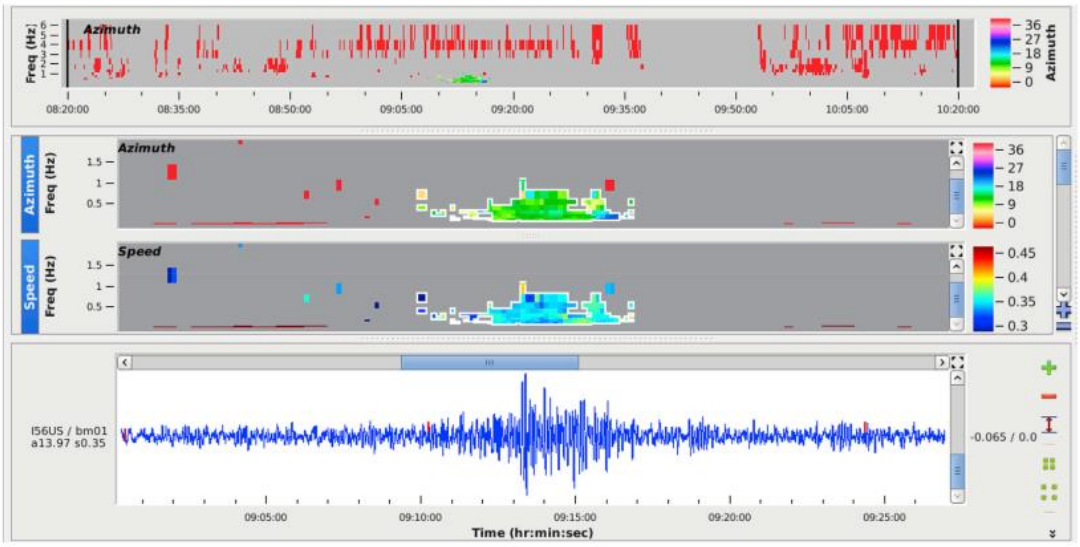

Fig. 2. The infrasound signal received with station I56US (located in Newport, Washington, USA) at a distance of about 8660 km from the event on 21 June 2018 between 08:20 UT and 10:20 UT, processed with PMCC. On the top the result of PMCC is shown for the whole investigated time period, the colors present different wave directions (back azimuths). The middle shows an enlarged part of the analysed signal, the time frame ranges from about 09:00 UT till 09:27 UT. The derived back azimuth of the recorded infrasound signal is shown as well as its speed for the analysed frequency bands. At the bottom the resulting filtered and stacked beam of the station is presented for the same time interval. (For interpretation of the references to color in this figure legend, the reader is referred to the Web version of this article.)

Figure 6-3: Diagram from (Ott et al., 2019) showing their detected infrasound wave on the 21 June 2018, split by frequency band (middle plots). This reduces the ability of noise to be misidentified as signals, as well as validating actual events.

The next step would be the development of software to interrogate the CTBTO database for possible sources of a detected signal. This would, again, rely on cross-correlation, but the number of events to be searched would be limited by the distance to a potential source, and the maximum range of possible sound speeds in any of the tropospheric (340 m/s), stratospheric (280 m/s), mesospheric (270 m/s) or thermospheric (220 m/s) ducts as discussed by *Silber* and *Brown* (2014). Although similar methods were used here, where various databases were interrogated for data, the vDEC (virtual Data

Exploitation Centre - from the IMS) database would serve as a good overall check, especially if the time-series were examined at the end of each night for evidence matching IMS signals based on distance, speed and magnitude. It was envisaged that a detailed study of these events would be correlated with the database of the CTBTO (*CTBTO*, 2012b), and indeed access was granted for this study by the CTBTO. However, the work required to complete this task proved to be much more complex than originally envisaged, and it could not be completed in the time available.

One aspect which would be very helpful in the study of infrasound in the OH* layer would the presence of a nearby regular generator of strong infrasound signals such as a volcano or regular mining explosions (*Hagerty et al.*, 2002, *Koch* and *Pilger*, 2020). This could also serve as a validation technique of signals in the datasets, much like the pedestrian beacon used throughout Chapter 4 and 5 to confirm clear nights prior to 2018, as well as confirming the validity of frequencies found in wavelet analysis.

Finally, further work on modelling the effects of infrasound waves on OH* emissions similar to those begun in the reports of *Tarasick* and *Shepherd* (1992) (which consider the chemistry of the emissions), *Snively* (2013), and *Bellisario et al.* (2020) (which consider both the chemistry and dynamics of the OH* emission process in great detail), could be undertaken. These studies are valuable to observers, by refining the characteristics that might be expected in real world data. Such modelling could be used to theoretically predict the effects on the hydroxyl layer due to acoustic waves and compared against the observations made in Maynooth, serving as a further check and complement to source determination.

Appendix A: The Hydrostatic Equation

This appendix details the full derivation of the hydrostatic equation as shown by authors like *Gossard* and *Hooke* (1975), *Brasseur* and *Solomon* (2006) and *Brune* (2020), and is paramount in the understanding of the evolution of pressure changes in the atmosphere. The hydrostatic equation is derived from the equation of motion, also known as the conservation of momentum (as shown in Section 1.6.2.2) and describes the changing pressure field of the Earth as a function of altitude. By taking the vertical components of Equation (1-10), which describes Newton's second law in a rotating frame of reference, the equation of motion in the vertical direction can be rewritten as:

$$\frac{Dw}{Dt} = 2\Omega \times \mathrm{v} - \mathrm{g} - \frac{1}{\rho}\nabla p \tag{A1-1}$$

Equation (A1-1) considers only the vertical component of acceleration (where w indicates the velocity in the vertical) and the respective forces. In terms of the changing pressure field with height, in Equation (A1-1), the Coriolis force term acts at a much larger scale and for its effects on the smaller scale, can be deemed negligible and set to zero:

$$\frac{Dw}{Dt} = -\mathrm{g} - \frac{1}{\rho}\nabla p \tag{A1-2}$$

The hydrostatic equation represents the balance of forces in the vertical and thus the acceleration is null while the forces balance, as below in Equation (A1-3):

$$\frac{1}{\rho}\nabla p = g \tag{A1-3}$$

Equation (A1-3) can be better described using Figure A1-1, where the three forces which describe the hydrostatic equilibrium are shown for a small, infinitesimal volume of air, that has a height of Δz. In terms of forces acting on the parcel of air, pressure of the atmosphere acts on both the top of the parcel (acting on an area A, pushing down) and

the bottom (pushing up) of the volume of air, represented by pA in Figure A1-1. The force of gravity also acts on the parcel of air, pushing down, and is represented by $\rho A(\Delta z)$g (where $A(\Delta z)$, is the volume of the parcel) and can be described as the weight of the parcel.

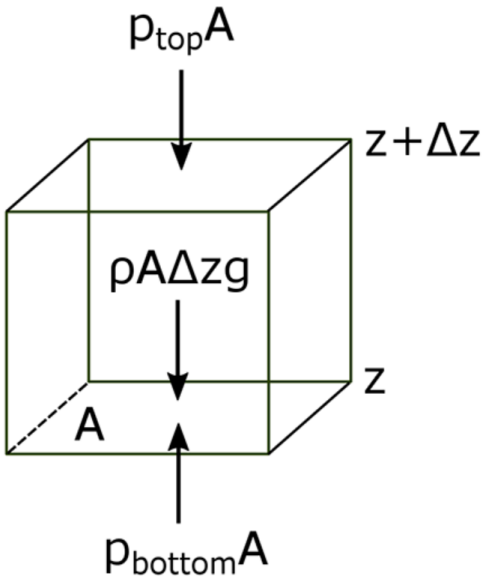

Figure A1-1: The balance of forces which describe the hydrostatic equilibrium of the atmosphere (*Brune*, 2020).

The forces depicted in Figure A1-1 balance one another, which can be written as follows and simplified:

$$p_{bottom}A - p_{top}A - \rho A(\Delta z)g = 0 \tag{A1-4}$$

$$\frac{p_{bottom}A - p_{top}A}{A(\Delta z)} = \rho g \tag{A1-5}$$

$$\frac{p_{top} - p_{bottom}}{(\Delta z)} = -\rho g \tag{A1-6}$$

Equation (A1-6) can be re-written in terms of the height of the parcel:

$$\frac{p(z + \Delta z) - p(z)}{(\Delta z)} = -\rho g \tag{A1-7}$$

It can then be assumed, that as the parcel of air becomes smaller (as it is assumed infinitesimal), the left hand side is that of the partial derivative of pressure as a function of altitude:

$$\frac{\delta p(z)}{\delta z} = -\rho g \tag{A1-8}$$

Equation (A1-8) is thus equivalent to Equation (A1-3) as $\nabla = \delta/\delta z$, which gives the hydrostatic equation. Various derivations of this equation can be seen in works such as *Holton* (1972) and *Salby* (2012).

Appendix B: Data Sheet for InGaAs Photodiodes

PerkinElmer™ optoelectronics

EVERYTHING IN A NEW LIGHT.

Description

The PerkinElmer family of large-area InGaAs PIN photodiodes provide high responsivity from 800 nm to 1700 nm for applications including optical power meters, fiber optic test equipment, near-IR spectoscopy and instrumentation. All devices are planar passivated and feature low capacitance for extended bandwidth, and high shunt resistance for maximum sensitivity. Typical devices feature <1% non-linearity to optical powers >+13 dBm (20 mW), and uniformity within ±2% across the detector active area. Typical responsivity of 0.2 A/W at 850 nm for our large-area InGaAs devices allows use of a single detector in fiber optic test instrumentation designed to operate at 850, 1300, and 1550 nm.

Devices are available with active areas from 0.5 mm to 3.0 mm in TO-type packages or on thermoelectric coolers for increased sensitivity (see below). Photodiodes can also be mounted on customized ceramic sub-mounts to suit specific application requirements. PerkinElmer Optoelectronics Canada is qualified to ISO-9001 and operates to MIL-Q-9858A and AQAP-1 quality standards. All devices undergo extended life-test and periodic process qualification programs to assure high reliability. In addition, all production devices are sourced from a qualified wafer, screened with a 16 hour, 200°C burn-in at -10V bias (C30619 and C30641) or -5V (C30642 and C30665), and tested to meet responsivity, spectral noise, capacitance, shunt resistance and dark current specifications.

Large-Area InGaAs Photodiodes

C30619, C30641, C30642, C30665

Features

- 0.5, 1.0, 2.0, and 3.0 mm diameters
- High responsivity from 850 nm to 1550 nm
- High shunt resistance, low dark current
- TE-cooled package options
- Low capacitance for fast response times

Applications

- Power meters
- Fiber identifiers
- Laser burn-in racks
- Near infrared instrumentation
- F.T.I.R. spectroscopy

PerkinElmer™ optoelectronics

C30619, C30641, C30642, C30665

PerkinElmer optoelectronics

Package Options

TE-Cooled Devices: Large-area detectors are available mounted on a 1-stage or 2-stage thermoelectric (TE) cooler. Cooling increases shunt resistance (see Figure 2) thereby reducing noise for increased sensitivity. Typical detector temperature is -10°C with a 1-stage TE cooler or -35°C using a 2-stage cooler. A TE-cooler option can be specified by adding the extension -TC (1-stage cooler) or -DTC (2-stage cooler) to the standard part number (see ordering guide). More information is available from the "TC-Series Cooled Photodiodes" datasheet from PerkinElmer Optoelectronics Canada.

Detector and Pre-Amplifier: Large-area InGaAs detectors are also available integrated with a preamplifier and TE-cooler. The HTE-series features large-area InGaAs detectors with a high gain hybrid transimpedence amplifier mounted on a 2-stage TE cooler. TE-cooling maximizes sensitivity and stabilizes op-amp offset and output characteristics. This provides an easy-to-use high sensitivity detector platform optimized for good temperature stability over a wide operating temperature range. More information is available from the HTE-series datasheet. The standard HTE-2642 incorporates a C30642E chip.

Specifications (at VR = VOP (typical), 22°C)

Parameter	C30619			C30641			Units
	Min	Typ	Max	Min	Typ	Max	
Active Diameter		0.5			1.0		mm
Responsivity At 850 nm	0.10	0.20		0.10	0.20		A/W
At 1300 nm	0.80	0.90		0.80	0.90		A/W
At 1550 nm	0.85	0.95		0.85	0.95		A/W
Shunt Resistance (VR = 10 mV) [1]	10	250		5	50		MΩ
Dark Current		1	20		5	50	nA
Spectral Noise Current (10 kHz, 1.0 Hz)		0.02	0.10		0.04	0.15	pA/√Hz
Capacitance At VR = 0V		20	25		100	125	pF
At VR = VOP		8 1 0			40	50	pF
Bandwidth (-3 dB, RL = 50Ω)		350			75		MHz
Linearity [2]		> +13			> +13		dBm
Available package types		D2, D14			D2, D14		-

Operating Ratings

Parameter	C30619			C30641			Units
	Min	Typ	Max	Min	Typ	Max	
Operating Voltage	0	5	10	0	2	5	V
Breakdown Voltage	20	80		20	80		V
Maximum Forward Current			10			10	mA
Maximum Photocurrent			100			100	mA
Power Dissipation			100			100	mW
Storage Temperature	-60		125	-80		125	°C
Operating Temperature	-40		85	-40		85	°C

Note 1. Selected higher shunt resistance devices are available to special order.

Note 2. Maximum optical power level for < ±0.04 dB (±1%) responsivity variation under 1300 nm CW illumination, at VR = VOP (typ).

C30619, C30641, C30642, C30665

PerkinElmer optoelectronics

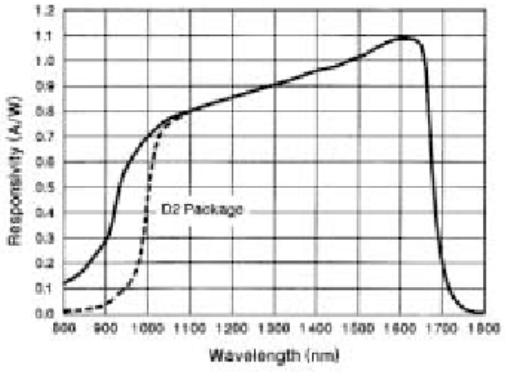

Figure 1. Typical Responsivity vs. Wavelength.

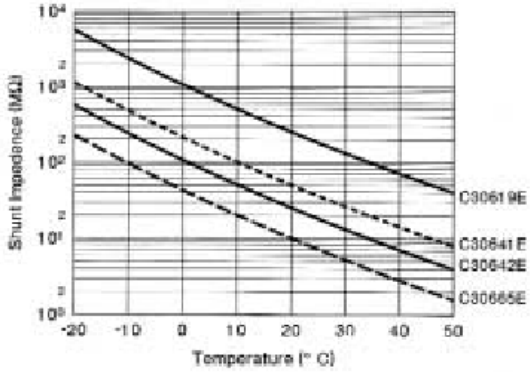

Figure 2. Typical Shunt Resistance as a Function of Temperature.

Specifications (at VR = VOP (typical), 22°C)

Parameter	C30642 Min	C30642 Typ	C30642 Max	C30665 Min	C30665 Typ	C30665 Max	Units
Active Diameter		2.0			3.0		mm
Responsivity At 850 nm	0.10	0.20		0.10	0.20		A/W
At 1300 nm	0.80	0.90		0.80	0.90		A/W
At 1550 nm	0.85	0.95		0.85	0.95		A/W
Shunt Resistance (VR = 10 mV) [1]	2	2 5		1	10		MΩ
Dark Current		1 0 [3]			2 5 [3]		nA
Spectral Noise Current (10 kHz, 1.0 Hz)		0.03	0.15		0.04	0.20	pA/√Hz
Capacitance At VR = 0V		300	500		1000	1250	pF
At VR = 2.0V (typical)		150			400		pF
Bandwidth (-3 dB, RL = 50Ω)		20			3.0		MHz
Linearity [2]		+ 1 1			+ 1 1		dBm
Available package types		D15			D15		-

Operating Ratings

Parameter	C30642 Min	C30642 Typ	C30642 Max	C30665 Min	C30665 Typ	C30665 Max	Units
Operating Voltage		0	5		0	5	V
Breakdown Voltage	15	50		10	50		V
Maximum Forward Current			10			10	mA
Maximum Photocurrent			100			100	mA
Power Dissipation			250			250	mW
Storage Temperature	-60		125	-80		125	°C
Operating Temperature	-40		85	-40		85	°C

Note 1. Selected higher shunt resistance devices are available to special order.

Note 2. Maximum optical power level for < ±0.04 dB (±1%) responsivity variation under 1300 nm CW illumination, at VR = VOP (typ).

Note 3. At VR = 2.0V

PerkinElmer optoelectronics

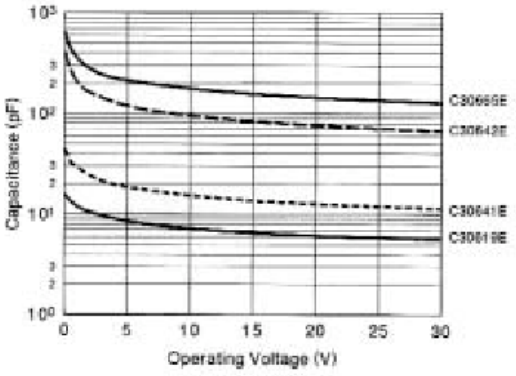

Figure 3. Typical Capacitance vs. Operating Voltage.

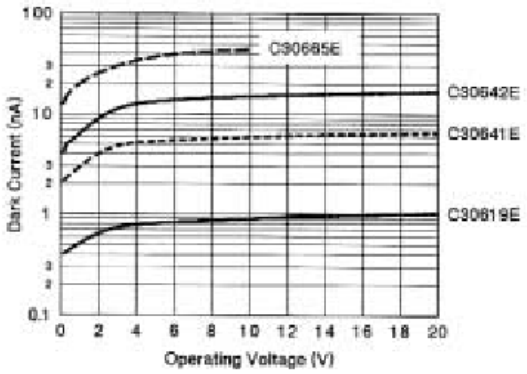

Figure 4. Typical Dark Current vs. Operating Voltage.

Wavelength (nm)	Temperature Coefficient1 (%/°C)	
850	-0.121	
1060	0.039	
1300	0.012	
1550	0.009	
1650	0.085	(20°C to 85°C)
	1.287	(-40°C to 20°C)

Note1: Measured from -40°C to +85°C except 1650nm, as indicated.

Figure 5. Typical Responsivity Temperature Coefficients.

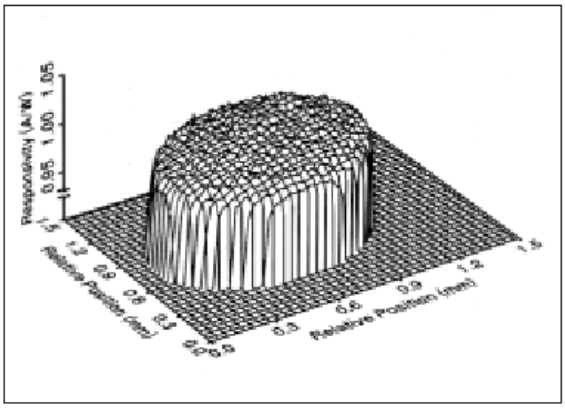

Figure 6. Typical Responsivity Scan of a 1mm Photodiode.

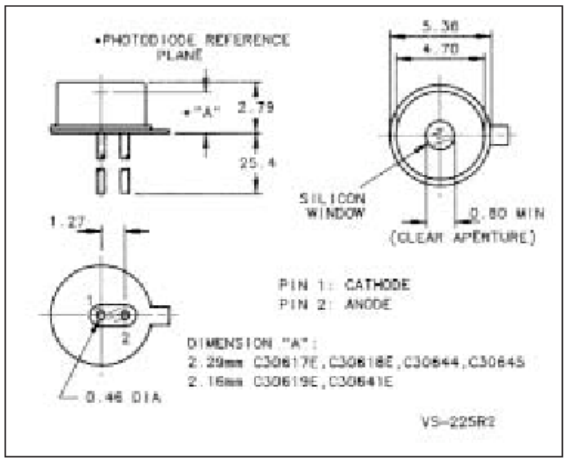

Figure 7. Package D2: TO-18 Low Profile with Silicon Window. To special order.

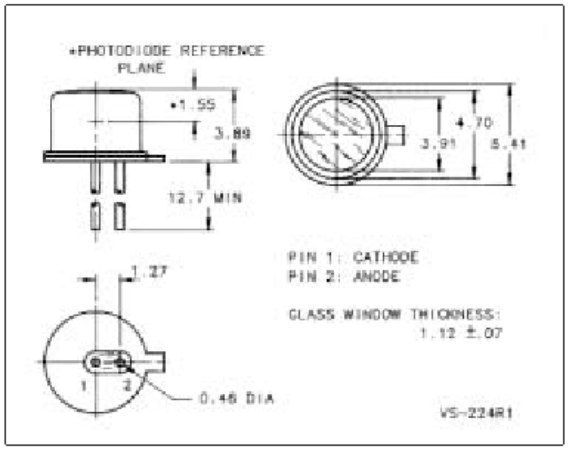

Figure 8. Package D-14: TO-18 with Glass Window.

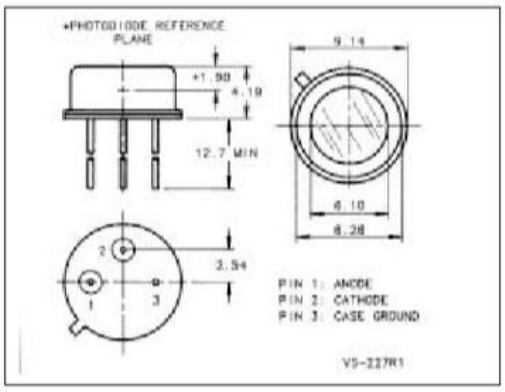

Figure 9. Package D15: TO-5 with Glass Window.

Ordering Guide

C30 # # # L- X X X

TE-Cooler Option:

TC:	1-stage TE cooler
DTC:	2-stage TE cooler (Not yet available for C30665)

Window Option:

E:	Silicon
G:	Glass (See below for availability)

Chip Type:

619:	0.5mm diameter
641:	1.0mm diameter
642:	2.0mm diameter
665:	3.0mm diameter

Device Package Availability

Window Option	Window Type	Package Type C30619	C30641	C30642	C30665
ESilicon		D2.1	D2.1	--	
G	Glass	D14	D14	D15	D15

Note 1: Special Order

For more information e-mail us at upto@perkinelmer.com or visit our web site at www.perkinelmer.com/opto

PerkinElmer Optoelectronics
22001 Dumberry Road,
Vaudreuil, Québec
Canada J7V 8P7
Phone: (450) 424-3300
Fax: (450) 424-3411

©2000 PerkinElmer, Inc.
All rights reserved.
0700

All values are nominal; specifications subject to change without notice.

PerkinElmer™ is a registered trademark of PerkinElmer, Inc.

Appendix C: LabVIEW Software and Data Acquisition

This appendix presents a guide to the LabVIEW program used to process the initial raw data from the instruments known as MFR and MFR2. LabVIEW utilises a visual user interface for programming purposes (called a block diagram), demonstrated by the Figure A3-1, where each part in the below figure works to begin the data acquisition and output the time-series data for each night.

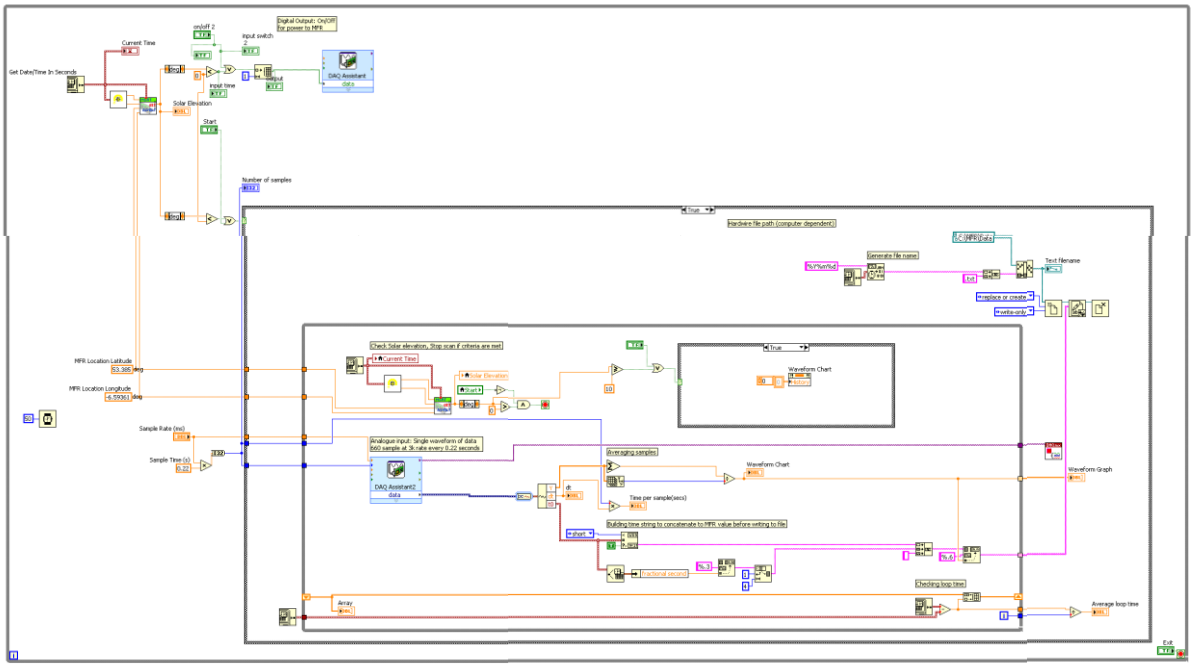

Figure A3-1: Image of the entire LabVIEW program used for data acquisition (for MFR)

The program begins in the top left of Figure A3-1, where this section is shown in a larger format in Figure A3-2. The program computes the current time and date and calculates the solar elevation angle, which depends on the latitude and longitude of the station itself (the figure shows the location of the MFR instrument). This is constantly monitored and only when the solar elevation angle falls into the negative (i.e. the sun descends below the horizon), does the main part of the program begin. The DAQ Assistant in Figure A3-2 acquires the data from the connected DAQ instrument which directly connects to the instrumentation – in this case it provides power to the

instrument once the solar elevation angle turns negative. This assistant only begins to take measurements once the a negative solar elevation is registered by the program.

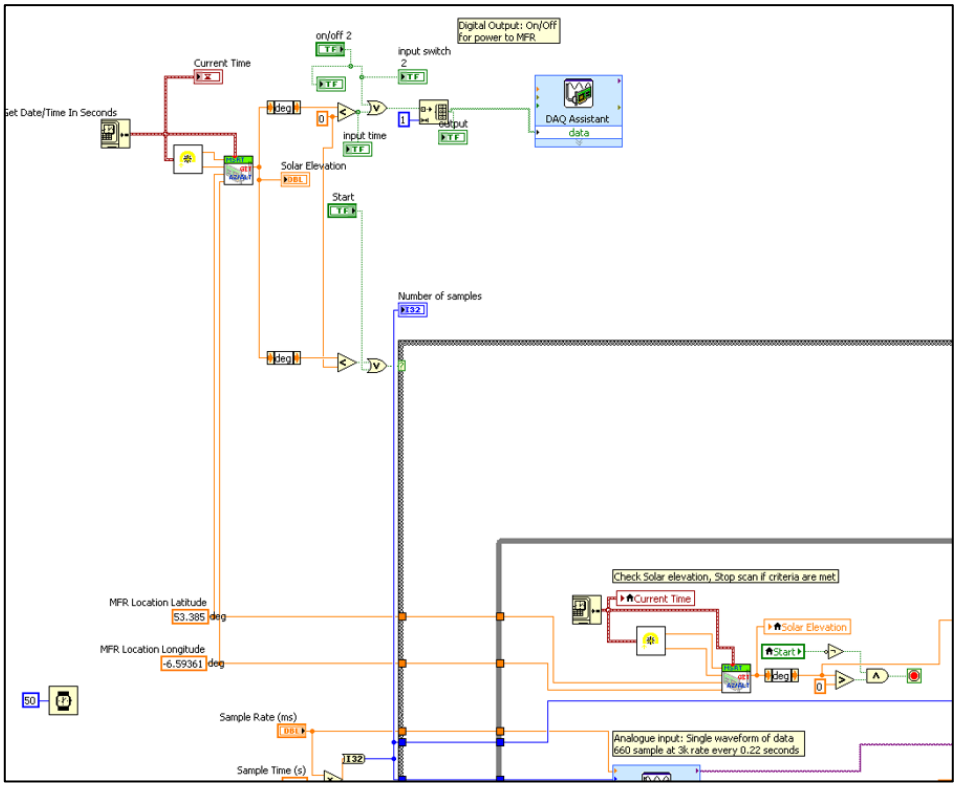

Figure A3-2: Solar elevation calculation and function to turn the DAQ assistant on/off.

The main section of the program is shown in Figure A3-3. The first part, in the top left corner of the figure, constantly monitors the solar elevation angle and in the case where this criteria is met, the program exits the main section. When this case is not met, a data point is registered by the second DAQ Assistant function. This function takes a measurement every 0.22s seconds (660 samples at 3 kHz), where the samples are averaged and plotted on a waveform chart.

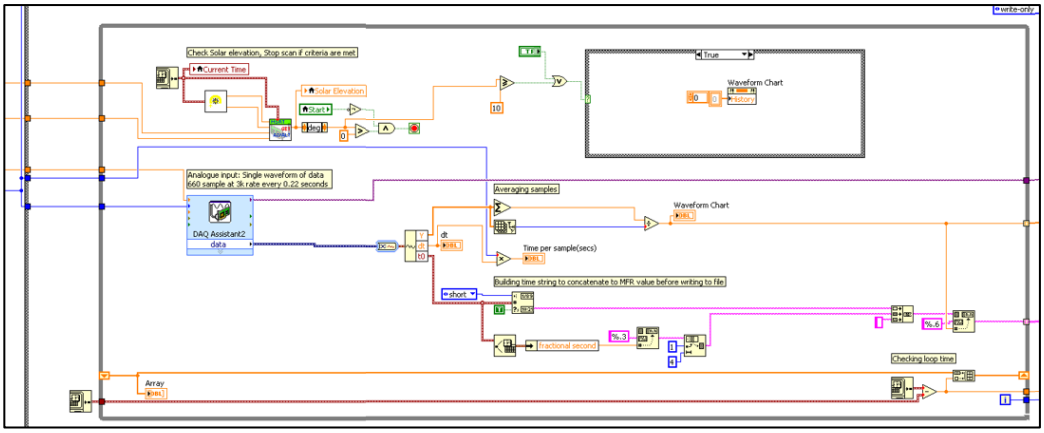

Figure A3-3: Main section of the program where the DAQ assistant registers the data from MFR and constantly updates a waveform graph every 0.22s (average of 660 samples)

Each datapoint on the waveform graph (updated constantly through the night) is plotted every 0.22 seconds, where the time of the datapoint acquisition is recorded. The sample and time arrays are updated through the night, and once the solar elevation angle passes into positive numbers, the program exits this section and plots a second waveform graph of all the samples through the night (Figure A3-4). A file save operation, shown at the top of is also executed where the sample and time arrays are saved into a text file. This file can then be manipulated and analysed by other programs designed in-house (like the Python program mentioned in Chapter 2).

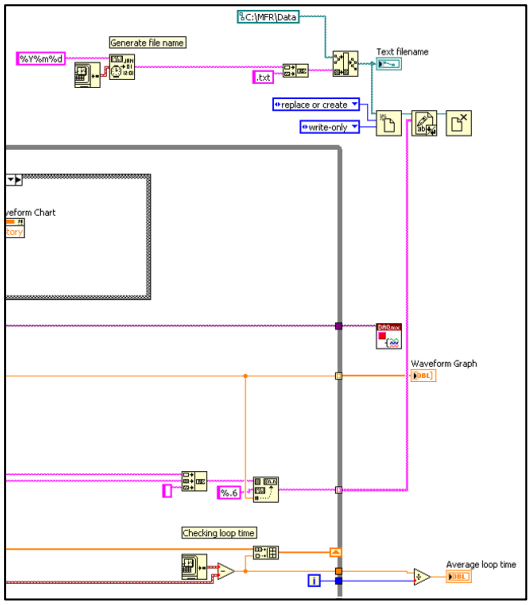

Figure A3-4: Final section of the program where the data and timestamps are saved to a text file and a waveform chart displaying the entire night of data is produced on the user interface.

This program outputs the graphs seen below in Figure A3-5, where the constantly updated waveform graph are shown on the right, and the final waveform shot, which takes the form of the time-voltage graph is shown on the left.

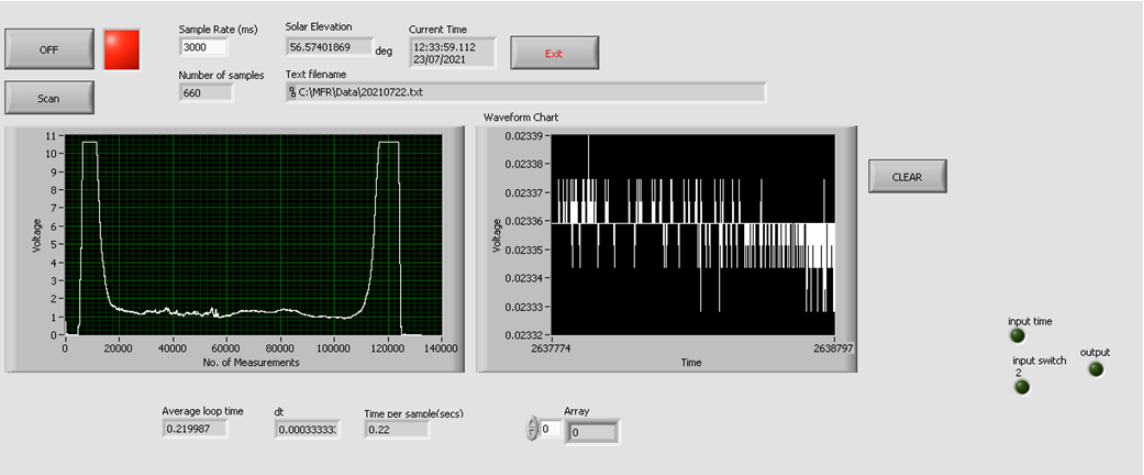

Figure A3-5: Screenshot of the output graphs of the LabVIEW program

References

Adler-Golden, S. (1997). Kinetic parameters for OH nightglow modeling consistent with recent laboratory measurements. *JOURNAL OF GEOPHYSICAL RESEARCH*, *102976*, 969–19, doi: 10.1029/97JA01622.

Afraimovich, E. L. (2008). First GPS-TEC evidence for the wave structure excited by the solar terminator. *Earth, Planets and Space*, *60*, 895–900, doi: 10.1186/BF03352843.

Afraimovich, E. L., E. A. Kosogorov, and A. V. Plotnikov. (2002). Shock–Acoustic Waves Generated during Rocket Launches and Earthquakes. *Cosmic Research*, *40*, 241–254, doi: 10.1023/A:1015925020387.

Ahrens, C. D. (1991). Meteorology Today: St. Paul, Minnesota. *West Publishing Co.*

Andrews, D. G. (2010). An introduction to atmospheric physics. *Cambridge University Press.*

Andrews, D. G., J. R. Holton, and C. B. Leovy. (1987). Middle Atmosphere Dynamics: Issue 40 of International Geophysics. *Academic Press.*

ARISE. (2019). ARISE Project. http://arise-project.eu/arise-project.php.

Arrowsmith, S. J., R. Burlacu, R. Whitaker, and G. Randall. (2009). A repeating secondary source of infrasound from the Wells , Nevada , earthquake sequence, *36*, 2–6, doi: 10.1029/2009GL038363.

Artru, J., T. Farges, and P. Lognonné. (2004). Acoustic waves generated from seismic surface waves: propagation properties determined from Doppler sounding observations and normal-mode modelling. *Geophys. J. Int*, *158*, 1067–1077, doi: 10.1111/j.1365-246X.2004.02377.x.

Assink, J. D., G. Averbuch, P. S. M. Smets, and L. G. Evers. (2016). On the infrasound detected from the 2013 and 2016 DPRK's underground nuclear tests. *Geophysical*

Research Letters, *43*, 3526–3533, doi: 10.1002/2016GL068497.

Assink, J. D., R. Waxler, P. Smets, and L. G. Evers. (2014). Bidirectional infrasonic ducts associated with sudden stratospheric warming events. *Journal of Geophysical Research: Atmospheres*, *119*, 1140–1153, doi: 10.1002/2013JD021062.

Avaste, O. A., A. V. Fedynsky, G. M. Grechko, V. I. Sevastyanov, and C. I. Willmann. (1980). Advances in noctilucent cloud research in the space era. *Pure and Applied Geophysics PAGEOPH*, *118*, 528–580, doi: 10.1007/BF01586466.

Baker, D. J. (1974). Rayleigh, the unit for light radiance. *Applied optics*, *13*, 2160–2163, doi: 10.1364/AO.13.002160.

Baker, D. J., and G. J. Romick. (1976). The Rayleigh: interpretation of the unit in terms of column emission rate or apparent radiance expressed in SI units. *Applied optics*, *15*, 1966–1968, doi: 10.1364/AO.15.001966.

Baker, D. J., and A. T. Stair. (1988). Rocket measurements of the altitude distributions of the hydroxyl airglow. *Physica Scripta*, *37*, 611–622, doi: 10.1088/0031-8949/37/4/021.

Baker, D. J., B. K. Thurgood, W. K. Harrison, M. G. Mlynczak, and J. M. Russell. (2007). Equatorial enhancement of the nighttime OH mesospheric infrared airglow. *Physica Scripta*, *75*, 615–619, doi: 10.1088/0031-8949/75/5/004.

Bass, H. E., C. H. Hetzer, and R. Raspet. (2007). On the speed of sound in the atmosphere as a function of altitude and frequency. *Journal of Geophysical Research Atmospheres*, *112*, 2–9, doi: 10.1029/2006JD007806.

Bates, D. R., and M. Nicolet. (1965). Atmospheric hydrogen. *Planetary and Space Science*, *13*, 905–909, doi: 10.1016/0032-0633(65)90175-3.

Bedard, A., and T. Georges. (2000). Atmospheric infrasound. *Acoustics Australia*, *28*, 47–52.

Beer, T. (1973). Supersonic Generation of Atmospheric Waves. *Nature*, *242*, 34–34, doi:

10.1038/242034a0.

Belikovich, M. V., M. Y. Kulikov, M. Grygalashvyly, G. R. Sonnemann, T. S. Ermakova, A. A. Nechaev, and A. M. Feigin. (2018). Ozone chemical equilibrium in the extended mesopause under the nighttime conditions. *Advances in Space Research*, *61*, 426–432, doi: 10.1016/j.asr.2017.10.010.

Bellisario, C., P. Simoneau, P. Keckhut, and A. Hauchecorne. (2020). Comparisons of spectrally resolved nightglow emission locally simulated with space and ground level observations. *Journal of Space Weather and Space Climate*, *10*, 21, doi: 10.1051/swsc/2020017.

Benioff, H., and B. Gutenberg. (1939). Waves and Currents Recorded by Electromagnetic Barographs. *Bulletin of the American Meteorological Society*, *20*, 421–428, doi: https://doi.org/10.1175/1520-0477-20.10.421.

Bespalova, A. V., A. K. Fedorenko, O. K. Cheremnykh, and I. T. Zhuk. (2016). Satellite observations of wave disturbances caused by moving solar terminator. *Journal of Atmospheric and Solar-Terrestrial Physics*, *140*, 79–85, doi: 10.1016/J.JASTP.2016.02.012.

Bittner, M., K. Höppner, C. Pilger, and C. Schmidt. (2010). Mesopause temperature perturbations caused by infrasonic waves as a potential indicator for the detection of tsunamis and other geo-hazards. *Nat. Hazards Earth Syst. Sci*, *10*, 1431–1442, doi: 10.5194/nhess-10-1431-2010.

Bjerknes, V., E. Volken, and S. Bronnimann. (1904). The problem of weather prediction, considered from the viewpoints of mechanics and physics. *Meteorologische Zeitschrift*, *18*, 663–667, doi: 10.1127/0941-2948/2009/416.

Bowman, D. C., and J. M. Lees. (2015). Infrasound in the middle stratosphere measured with a free-flying acoustic array. *Geophysical Research Letters*, *42*, 10,010-10,017, doi: 10.1002/2015GL066570.

Bowman, D. C., and J. M. Lees. (2017). A Comparison of the Ocean Microbarom

Recorded on the Ground and in the Stratosphere. *Journal of Geophysical Research: Atmospheres*, *122*, 9773–9782, doi: 10.1002/2017JD026474.

Bowman, D., J. Lees, J. Cutts, A. Komjathy, E. Young, K. Seiffert, M. Boslough, and S. Arrowsmith. (2018). Geoacoustic observations on drifting balloon-borne sensors. Pages 125–171 Infrasound Monitoring for Atmospheric Studies: Challenges in Middle Atmosphere Dynamics and Societal Benefits: Second Edition. *Springer International Publishing*.

Brachet, N., D. Brown, R. Le Bras, Y. Cansi, P. Mialle, and J. Coyne. (2009). Monitoring the Earth's atmosphere with the global IMS infrasound network. Pages 77–118 Infrasound Monitoring for Atmospheric Studies. *Springer Netherlands*.

Brändström, B. U. E., C. F. Enell, O. Widell, T. Hansson, D. Whiter, S. Mäkinen, D. Mikhaylova, K. Axelsson, F. Sigernes, N. Gulbrandsen, N. M. Schlatter, A. G. Gjendem, L. Cai, J. P. Reistad, M. Daae, T. D. Demissie, Y. L. Andalsvik, O. Roberts, S. Poluyanov, and S. Chernouss. (2012). Results from the intercalibration of optical low light calibration sources 2011. *Geoscientific Instrumentation, Methods and Data Systems*, *1*, 43–51, doi: 10.5194/GI-1-43-2012.

Brasseur, G., and S. Solomon. (2006). Aeronomy of the Middle Atmosphere: Chemistry and Physics of the Stratosphere and Mesosphere Volume 32 of Atmospheric and Oceanographic Sciences Library. Third edition. *Springer Science & Business Media*.

Briggs, B. H. (1968). On the analysis of moving patterns in geophysics—I. Correlation analysis. *Journal of Atmospheric and Terrestrial Physics*, *30*, 1777–1788, doi: 10.1016/0021-9169(68)90097-4.

Briggs, B. H. (1985). The Analysis of Spaced Sensor Records by Correlation Techniques. Page Middle Atmosphere Program. Handbook for MAP.

Brune, W. H. (2020). The Atmosphere's Pressure Structure: Hydrostatic Equilibrium. https://www.e-education.psu.edu/meteo300/node/7.

Budzier, H., and G. Gerlach. (2011). Thermal infrared sensors: theory, optimisation and

practice. *John Wiley & Sons, Inc.*

Campus, P., and D. R. Christie. (2010). Worldwide observations of infrasonic waves. Pages 185–234 Infrasound Monitoring for Atmospheric Studies. *Springer Netherlands*.

Cansi, Y. (1995). An automatic seismic event processing for detection and location: The P.M.C.C. Method. *Geophysical Research Letters*, *22*, 1021–1024, doi: 10.1029/95GL00468.

Cansi, Y., and A. Le Pichon. (2008). Infrasound Event Detection Using the Progressive Multi-Channel Correlation Algorithm. Pages 1425–1435 Handbook of Signal Processing in Acoustics. *Springer New York*.

Carbary, J. F., D. Morrison, and G. J. Romick. (2001). Latitude variations in light scattered from polar mesospheric clouds. *Geophysical Research Letters*, *28*, 2605–2608, doi: 10.1029/2001GL013086.

Carbary, J. F., D. Morrison, and G. J. Romick. (2003). Ultraviolet imaging and spectrographic imaging of polar mesospheric clouds. *Advances in Space Research*, *31*, 2091–2096, doi: 10.1016/S0273-1177(03)00233-3.

Cazelles, B., M. Chavez, D. Berteaux, F. Ménard, J. O. Vik, S. Jenouvrier, and N. C. Stenseth. (2008), May 6. Wavelet analysis of ecological time series. *Springer*.

Chadney, J. M., D. K. Whiter, and B. S. Lanchester. (2017). Effect of water vapour absorption on hydroxyl temperatures measured from Svalbard. *Annales Geophysicae*, *35*, 481–491, doi: 10.5194/angeo-35-481-2017.

Chamberlain, J. W. (2016). Physics of the Aurora and Airglow. Page Physics of the Aurora and Airglow.

Chamberlin, A. (2021). Fireball and Bolide Data. https://cneos.jpl.nasa.gov/fireballs/.

Chandran, A., D. W. Rusch, S. E. Palo, G. E. Thomas, and M. J. Taylor. (2009). Gravity wave observations in the summertime polar mesosphere from the Cloud

Imaging and Particle Size (CIPS) experiment on the AIM spacecraft. *Journal of Atmospheric and Solar-Terrestrial Physics*, *71*, 392–400, doi: 10.1016/J.JASTP.2008.09.041.

Chapman, S., and R. S. Lindzen. (2012). Atmospheric Tides: Thermal and Gravitational. *Springer Science & Business Medi*.

Che, I. Y., J. Park, I. Kim, T. S. Kim, and H. Il Lee. (2014). Infrasound signals from the underground nuclear explosions of North Korea. *Geophysical Journal International*, *198*, 495–503, doi: 10.1093/gji/ggu150.

Christie, D. R., and P. Campus. (2010). The IMS infrasound network: Design and establishment of infrasound stations. Pages 29–75 Infrasound Monitoring for Atmospheric Studies. *Springer Netherlands*.

Chum, J., J. Laštovička, T. Šindelářová, D. Burešová, and F. Hruška. (2008). Peculiar transient phenomena observed by HF Doppler sounding on infrasound time scales. *Journal of Atmospheric and Solar-Terrestrial Physics*, *70*, 866–878, doi: 10.1016/J.JASTP.2007.06.013.

Coble, P. G., R. G. M. Spencer, A. Baker, and D. M. Reynolds. (2014). Aquatic Organic Matter Fluorescence. *Cambridge University Press.*

CTBTO. (2012a). Infrasound monitoring: CTBTO Preparatory Commission. https://www.ctbto.org/verification-regime/monitoring-technologies-how-they-work/infrasound-monitoring/.

CTBTO. (2012b). vDEC: CTBTO Preparatory Commission. https://www.ctbto.org/specials/vdec/.

Dalin, P., S. Kirkwood, H. Andersen, O. Hansen, N. Pertsev, and V. Romejko. (2006). Comparison of long-term Moscow and Danish NLC observations: statistical results.

Dalin, P., S. Kirkwood, A. Moström, K. Stebel, P. Hoffmann, and W. Singer. (2004). A case study of gravity waves in noctilucent clouds. *Annales Geophysicae*, *22*, 1875–1884, doi: 10.5194/angeo-22-1875-2004.

References

Dalin, P., N. Pertsev, S. Frandsen, O. Hansen, H. Andersen, A. Dubietis, and R. Balciunas. (2010). A case study of the evolution of a Kelvin-Helmholtz wave and turbulence in noctilucent clouds. *Journal of Atmospheric and Solar-Terrestrial Physics*, *72*, 1129–1138, doi: 10.1016/j.jastp.2010.06.011.

Dalin, P., N. Pertsev, V. Perminov, A. Dubietis, A. Zadorozhny, M. Zalcik, I. McEachran, T. McEwan, K. Černis, J. Grønne, T. Taustrup, O. Hansen, H. Andersen, D. Melnikov, A. Manevich, V. Romejko, and D. Lifatova. (2018). Response of noctilucent cloud brightness to daily solar variations. *Journal of Atmospheric and Solar-Terrestrial Physics*, *169*, 83–90, doi: 10.1016/J.JASTP.2018.01.025.

Dalin, P., N. Pertsev, A. Zadorozhny, M. Connors, I. Schofield, I. Shelton, M. Zalcik, T. McEwan, I. McEachran, S. Frandsen, O. Hansen, H. Andersen, V. Sukhodoev, V. Perminov, and V. Romejko. (2008). Ground-based observations of noctilucent clouds with a northern hemisphere network of automatic digital cameras. *Journal of Atmospheric and Solar-Terrestrial Physics*, *70*, 1460–1472, doi: 10.1016/J.JASTP.2008.04.018.

Dandekar, B. S., and D. J. Davis. (1973). Calibrations of the Airglow Photometers and Spectrometers. *Applied Optics*, *12*, 825, doi: 10.1364/AO.12.000825.

Demissie, T. D., P. J. Espy, N. H. Kleinknecht, M. Hatlen, N. Kaifler, and G. Baumgarten. (2014). Characteristics and sources of gravity waves observed in noctilucent cloud over Norway. *Atmospheric Chemistry and Physics*, *14*, 12133–12142, doi: 10.5194/acp-14-12133-2014.

Donn, W. L., and E. S. Posmentier. (1964). Ground-coupled air waves from the Great Alaskan Earthquake. *Journal of Geophysical Research*, *69*, 5357–5361, doi: 10.1029/JZ069i024p05357.

Donn, W. L., and D. Rind. (1971). Natural Infrasound as an Atmospheric Probe. *Geophysical Journal of the Royal Astronomical Society*, *26*, 111–133, doi: 10.1111/j.1365-246X.1971.tb03386.x.

References

Drob, D. P., J. M. Picone, and M. Garc e s. (2003). Global morphology of infrasound propagation. *Journal of Geophysical Research*, *108*, 4680, doi: 10.1029/2002JD003307.

Le Dû, T., P. Simoneau, P. Keckhut, A. Hauchecorne, and A. Le Pichon. (2020). Investigation of infrasound signatures from microbaroms using OH airglow and ground-based microbarometers. *Advances in Space Research*, *65*, 902–908, doi: 10.1016/j.asr.2019.11.026.

Dubietis, A., P. Dalin, R. Balčiūnas, K. Černis, N. Pertsev, V. Sukhodoev, V. Perminov, M. Zalcik, A. Zadorozhny, M. Connors, I. Schofield, T. McEwan, I. McEachran, S. Frandsen, O. Hansen, H. Andersen, J. Grønne, D. Melnikov, A. Manevich, and V. Romejko. (2011). Noctilucent clouds: modern ground-based photographic observations by a digital camera network. *Applied Optics*, *50*, F72, doi: 10.1364/AO.50.000F72.

Dukowicz, J. K. (2013). Evaluation of various approximations in atmosphere and ocean modeling based on an exact treatment of gravity wave dispersion. *Monthly Weather Review*, *141*, 4487–4506, doi: 10.1175/MWR-D-13-00148.1.

Duma, V. F., M. F. Nicolov, M. Kiss, T. Ilca, C. Mnerie, D. Demian, and L. Szantho. (2012). Choppers: Optomechatronic devices for the controlled modulation of light. Pages 125–132 Mechanisms and Machine Science. *Springer Netherlands*.

Edgar, A. (1989). Drift in low-cost lock-in amplifiers. *Journal of Physics E: Scientific Instruments*, *22*, 551–553, doi: 10.1088/0022-3735/22/8/003.

Edwards, W. N. (2009). Meteor generated infrasound: Theory and observation. Pages 361–414 Infrasound Monitoring for Atmospheric Studies. *Springer Netherlands*.

ElGabry, M. N., I. M. Korrat, H. M. Hussein, and I. H. Hamama. (2017). Infrasound detection of meteors. *NRIAG Journal of Astronomy and Geophysics*, *6*, 68–80, doi: 10.1016/j.nrjag.2017.04.004.

EOPC. (2017). Tuning Fork Resonant Choppers. http://www.eopc.com/ch10_ch20.html.

References

Espy, P. J., and J. Stegman. (2002). Trends and variability of mesospheric temperature at high-latitudes. *Physics and Chemistry of the Earth*, *27*, 543–553, doi: 10.1016/S1474-7065(02)00036-0.

Espy, P. J., J. Stegman, P. Forkman, and D. Murtagh. (2007). Seasonal variation in the correlation of airglow temperature and emission rate. *Geophysical Research Letters*, *34*, 17802, doi: 10.1029/2007GL031034.

Eurotech, A. (2015). User Guide Aurora Cloud Sensor III.

Evans, W. F. J., H. C. Wood, and E. J. Llewellyn. (1970). Transmission of the infrared oxygen emission at 1.27 μ in the atmosphere. *Canadian Journal of Physics*, *48*, 747–752, doi: 10.1139/p70-094.

Evers, L., and H. W. Haak. (2010). The Characteristics of Infrasound, its Propagation and Some Early History. Pages 3–27 *in* A. Le Pichon, E. Blanc, and A. Hauchecorne, editors. Infrasound Monitoring for Atmospheric Studies. Illustrate. *Springer Science & Business Media*.

Faivre, M., G. Moreels, D. Pautet, P. Keckhut, and A. Hauchecorne. (2003). Correlated measurements of mesospheric density and near infrared airglow. *Advances in Space Research*, *32*, 777–782, doi: 10.1016/S0273-1177(03)00423-X.

Fee, D., and R. S. Matoza. (2013). An overview of volcano infrasound: From hawaiian to plinian, local to global. *Journal of Volcanology and Geothermal Research*, *249*, 123–139, doi: 10.1016/J.JVOLGEORES.2012.09.002.

Fleagle, R., and J. Businger. (1980). An Introduction to Atmospheric Physics. First Edit. *Academic Press*, Orlando, Florida.

Fogle, B. T. (1966). PhD Thesis: Noctilucent Clouds. *University of Alaska*.

Fogle, B. T., R. K. Soberman, B. T. Fogle, and B. Haurwitz. (1966). Noctilucent Clouds. *Scientific American*, *208*, 178.

Forbes, J. M., S. L. Bruinsma, Y. Miyoshi, and H. Fujiwara. (2008). A solar terminator

wave in thermosphere neutral densities measured by the CHAMP satellite. *Geophysical Research Letters*, *35*, L14802, doi: 10.1029/2008GL034075.

Francis, T. S., and X. Yang. (1997). Introduction to optical engineering. *Cambridge University Press*.

Fritts, D. C., and M. J. Alexander. (2003). Gravity wave dynamics and effects in the middle atmosphere. *Reviews of Geophysics*, *41*, 1003, doi: 10.1029/2001RG000106.

Fritts, D. C., A. D. Miller, C. B. Kjellstrand, C. Geach, B. P. Williams, B. Kaifler, N. Kaifler, G. Jones, M. Rapp, M. Limon, J. Reimuller, L. Wang, S. Hanany, S. Gisinger, Y. Zhao, G. Stober, and C. E. Randall. (2019). PMC Turbo: Studying Gravity Wave and Instability Dynamics in the Summer Mesosphere Using Polar Mesospheric Cloud Imaging and Profiling From a Stratospheric Balloon. *Journal of Geophysical Research: Atmospheres*, *124*, 6423–6443, doi: 10.1029/2019JD030298.

Fujimoto, M., W. Baumjohann, K. Kabin, R. Nakamura, J. A. Slavin, N. Terada, and L. Zelenyi. (2008). Hermean Magnetosphere-Solar Wind Interaction. Pages 347–368. *Springer, New York, NY*.

Gadsden, M. (1989). Review Article: Noctilucent Clouds. *Journal of the British Astronomical Association*, *99*.

Gadsden, M. (1998). Can I see noctilucent clouds? *Journal of the British Astronomical Association*, *108*, 35–38.

Gadsden, M., and P. Parviainen. (1995). Observing noctilucent clouds. *International Association of Geomagnetism & Aeronomy*.

Garcés, M. A., R. A. Hansen, and K. G. Lindquist. (1998). Traveltimes for infrasonic waves propagating in a stratified atmosphere. *Geophys. J. Int*, *135*, 255–263.

Garcés, M., P. Caron, C. Hetzer, A. Le Pichon, H. Bass, D. Drob, and J. Bhattacharyya. (2005). Deep infrasound radiated by the Sumatra earthquake and tsunami. *Eos Trans. AGU*, *86*, 317 & 320, doi: doi: 10.1029/2005EO350002.

References

Garcés, M., M. Iguchi, K. Ishihara, M. Morrissey, Y. Sudo, and T. Tsutsui. (1999). Infrasonic precursors to a Vulcanian Eruption at Sakurajima Volcano, Japan. *Geophysical Research Letters*, *26*, 2537–2540, doi: 10.1029/1998GL005327.

Garcés, M., M. Willis, and A. Le Pichon. (2010). Infrasonic observations of open ocean swells in the pacific: Deciphering the song of the sea. Pages 235–248 Infrasound Monitoring for Atmospheric Studies. *Springer Netherlands*.

Gerding, M., G. Baumgarten, M. Zecha, F. J. Lübken, K. Baumgarten, and R. Latteck. (2021). On the unusually bright and frequent noctilucent clouds in summer 2019 above Northern Germany. *Journal of Atmospheric and Solar-Terrestrial Physics*, *217*, 105577, doi: 10.1016/J.JASTP.2021.105577.

Giers, D. H., Y. Sahai, L. L. Cogger, and E. H. Ryan. (1997). Occurrence characteristics of mesospheric gravity waves at 51 °N. *Journal of Atmospheric and Solar-Terrestrial Physics*, *59*, 1197–1203, doi: 10.1016/S1364-6826(96)00117-4.

Global Volcanism Program. (2018). Report on Sierra Negra (Ecuador) In: Sennert, S K (ed.), Weekly Volcanic Activity Report, 25 July-31 July 2018.

Goldstein, P. (2020). Beirut Explosion Yield and Mushroom Cloud Height - Effects of the Source Environment. Livermore, CA (United States).

Gossard, E. E., and W. H. Hooke. (1975). Developments in Atmospheric Science. First Edit. *Elsevier Scientific Publishing Company*, Amsterdam.

Green, D. N., J. Vergoz, R. Gibson, A. Le Pichon, and L. Ceranna. (2011). Infrasound radiated by the Gerdec and Chelopechene explosions: propagation along unexpected paths. *Geophysical Journal International*, *185*, 890–910, doi: 10.1111/j.1365-246X.2011.04975.x.

Grimnes, S., and Ø. G. Martinsen. (2015). Chapter 8 - Instrumentation and Measurements. Pages 255–328 *in* S. Grimnes and Ø. G. Martinsen, editors. Bioimpedance and Bioelectricity Basics (Third Edition). Third Edit. *Academic Press*, Oxford.

References

de Groot-Hedlin, C. D., M. A. H. Hedlin, and D. P. Drob. (2010). Atmospheric variability and infrasound monitoring. Pages 475–507 Infrasound Monitoring for Atmospheric Studies. *Springer Netherlands*.

de Groot-Hedlin, C. D., and M. A. H. H. Hedlin. (2014). Infrasound detection of the Chelyabinsk meteor at the USArray, *402*, 337–345.

Grygalashvyly, M., G. R. Sonnemann, F.-J. Lübken, P. Hartogh, and U. Berger. (2014). Hydroxyl layer: Mean state and trends at midlatitudes. *Journal of Geophysical Research Atmospheres*, 12391–12419, doi: 10.1002/2014JD022094.

Gumbel, J., L. Megner, O. Martin Christensen, N. Ivchenko, D. P. Murtagh, S. Chang, J. Dillner, T. Ekebrand, G. Giono, A. Hammar, J. Hedin, B. Karlsson, M. Krus, A. Li, S. McCallion, G. Olentšenko, S. Pak, W. Park, J. Rouse, J. Stegman, and G. Witt. (2020). The MATS satellite mission-Gravity wave studies by Mesospheric Airglow/Aerosol Tomography and Spectroscopy. *Atmospheric Chemistry and Physics*, *20*, 431–455, doi: 10.5194/ACP-20-431-2020.

Gumbel, J., and G. Witt. (2001). Rocket-borne photometry of NLC particle populations. *Advances in Space Research*, *28*, 1053–1058, doi: 10.1016/S0273-1177(01)80036-3.

Hagerty, M. T., W.-Y. Kim, and P. Martysevich. (2002). Infrasound Detection of Large Mining Blasts in Kazakstan. Pages 1063–1079 Monitoring the Comprehensive Nuclear-Test-Ban Treaty: Data Processing and Infrasound. *Birkhäuser Basel*, Basel.

Hallinan, J. (1991). Auroras. Pages 741–798 *in* J. A. Jacobs, editor. Geomagnetism. *Academic Press*.

Hammamatsu. (2021). Compound semiconductor photosensors.

Hannawald, P., C. Schmidt, R. Sedlak, S. Wüst, and M. Bittner. (2019). Seasonal and intra-diurnal variability of small-scale gravity waves in OH airglow at two Alpine stations. *Atmospheric Measurement Techniques*, *12*.

Hannawald, P., C. Schmidt, S. Wüst, and M. Bittner. (2016). A fast SWIR imager for observations of transient features in OH airglow. *Atmospheric Measurement*

Techniques, *9*, 1461–1472, doi: 10.5194/amt-9-1461-2016.

Hargreaves, J. K. (1992). The solar-terrestrial environment : an introduction to geospace--the science of the terrestrial upper atmosphere, ionosphere, and magnetosphere. *Cambridge University Press*.

Harrison, A. W. (1973). Spectrophotometric Measurements of Noctilucent Clouds. *Canadian Journal of Physics*, *51*, 373–377, doi: 10.1139/p73-047.

Harrison, A. W., and D. J. W. Kendall. (1973). Airglow hydroxyl intensity measurements $0 \cdot 6$–$2 \cdot 3$ μ. *Planetary and Space Science*, *21*, 1731–1741, doi: 10.1016/0032-0633(73)90164-5.

Hecht, J. H., A. Z. Liu, R. L. Walterscheid, S. J. Franke, R. J. Rudy, M. J. Taylor, and P.-D. Pautet. (2007). Characteristics of short-period wavelike features near 87 km altitude from airglow and lidar observations over Maui. *Journal of Geophysical Research*, *112*, D16101, doi: 10.1029/2006JD008148.

Herrin, E. T., H. E. Bass, B. Andre, R. L. Woodward, D. P. Drob, M. A. Hedlin, M.A., Garcés, P. W. Golden, D. E. Norris, C. de Groot-Hedlin, and K. T. Walker. (2008). High-altitude infrasound calibration experiments. *Acoust. Today*, *4*, 9–17.

Hervig, M. E., M. H. Stevens, L. L. Gordley, L. E. Heaver, J. M. Russell, and S. M. Bailey. (2009). Relationships between polar mesospheric clouds, temperature, and water vapor from Solar Occultation for Ice Experiment (SOFIE) observations. *Journal of Geophysical Research Atmospheres*, *114*, 20203, doi: 10.1029/2009JD012302.

Hervig, M., R. E. Thompson, M. McHugh, L. L. Gordley, J. M. Russell, and M. E. Summers. (2001). First confirmation that water ice is the primary component of polar mesospheric clouds. *Geophysical Research Letters*, *28*, 971–974, doi: 10.1029/2000gl012104.

Hines, C. O. (1960). INTERNAL ATMOSPHERIC GRAVITY WAVES AT IONOSPHERIC HEIGHTS. *Canadian Journal of Physics*, *38*, 1441–1481, doi:

10.1139/p60-146.

Hocking, W. K. (2003). Evidence for viscosity, thermal conduction and diffusion waves in the Earth's atmosphere (invited). Pages 420–426 Review of Scientific Instruments. *American Institute of PhysicsAIP*.

Hocking, W. K., S. Fukao, M. Yamamoto, T. Tsuda, and S. Kato. (1991). Viscosity waves and thermal-conduction waves as a cause of "specular" reflectors in radar studies of the atmosphere. *Radio Science*, *26*, 1281–1303, doi: 10.1029/91RS01661.

Hoffmann, T. (2021). MoonCalc. https://www.mooncalc.org/#/49.495,11.073,3/2021.06.24/10:46/1/0.

Holton, J. R. (1972). An Introduction to Dynamic Meteorology. Page (F. Cynar, Ed.). 3rd Editio. *Academic Press*.

Holton, J. R. (1983). The Influence of Gravity Wave Breaking on the General Circulation of the Middle Atmosphere.

Holton, J. R. (2004). An Introduction to Dynamic Meteorology. 4th Editio. *Elsevier Academic Press*.

Horgan, D. F. (1992). MSc. Thesis: Mesopause Airglow OH Emissions: Rotational Temperatures and Gravity Waves. *St. Patrick's College Maynooth, Ireland*.

Horowitz, P., and W. Hill. (2015). The Art of Electronics. *The Art of Electronics, by Paul Horowitz , Winfield Hill, Cambridge, UK: Cambridge University Press, 2015*.

Huang, Y., J. J. Makela, and G. R. Swenson. (2012). Simulations of imaging Fabry-Perot interferometers for measuring upper-atmospheric temperatures and winds. *Applied Optics*, *51*, 3787–3800, doi: 10.1364/AO.51.003787.

Hunten, D. M. M., F. E. E. Roach, and J. W. W. Chamberlain. (1956). A photometric unit for the airglow and aurora. *Journal of Atmospheric and Terrestrial Physics*, *8*, 345–346, doi: 10.1016/0021-9169(56)90111-8.

Hupe, P., L. Ceranna, and C. Pilger. (2018). Using barometric time series of the IMS

infrasound network for a global analysis of thermally induced atmospheric tides. *Atmospheric Measurement Techniques*, *11*, 2027–2040, doi: 10.5194/amt-11-2027-2018.

Hupe, P., L. Ceranna, C. Pilger, M. de Carlo, A. Le Pichon, B. Kaifler, and M. Rapp. (2019). Assessing middle atmosphere weather models using infrasound detections from microbaroms. *Geophysical Journal International*, *216*, 1761–1767, doi: 10.1093/gji/ggy520.

Inchin, P. A., J. B. Snively, A. Williamson, D. Melgar, J. A. Guerrero, and M. D. Zettergren. (2020). Mesopause Airglow Disturbances Driven by Nonlinear Infrasonic Acoustic Waves Generated by Large Earthquakes. *Journal of Geophysical Research: Space Physics*, *125*, e2019JA027628, doi: 10.1029/2019JA027628.

Instituto Geofísico, E. (2018). SISMOGRAMAS ISLAS GALÁPAGOS. https://www.igepn.edu.ec/islas-galapagos-sismogramas.

Jacobson, M. J. (1999). Fundamentals of Atmospheric Modelling. *Cambridge University Press*.

Johnson, J. B. (2003). Generation and propagation of infrasonic airwaves from volcanic explosions. *Journal of Volcanology and Geothermal Research*, *121*, 1–14, doi: 10.1016/S0377-0273(02)00408-0.

Johnson, J. B., R. C. Aster, and P. R. Kyle. (2004). Volcanic eruptions observed with infrasound. *Geophysical Research Letters*, *31*, 14604, doi: 10.1029/2004GL020020.

Jones, R. M., and A. J. Bedard. (2018). Atmospheric gravity wave ray tracing: Ordinary and extraordinary waves. *Journal of Atmospheric and Solar-Terrestrial Physics*, *179*, 342–357, doi: 10.1016/j.jastp.2018.08.014.

Kaifler, N., G. Baumgarten, J. Fiedler, and F.-J. Lübken. (2013). Quantification of waves in lidar observations of noctilucent clouds at scales from seconds to minutes. *Atmospheric Chemistry and Physics*, *13*, 11757–11768, doi: 10.5194/acp-13-11757-2013.

References

Kaifler, N., B. Kaifler, H. Wilms, M. Rapp, G. Stober, and C. Jacobi. (2018). Mesospheric Temperature During the Extreme Midlatitude Noctilucent Cloud Event on 18/19 July 2016. *Journal of Geophysical Research: Atmospheres*, *123*, doi: 10.1029/2018JD029717.

Kallistratova, M. A. (2002). Acoustic Waves in the Turbulent Atmosphere: A Review. *Journal of Atmospheric and Oceanic Technology*, *19*, 1139–1150, doi: 10.1175/1520-0426(2002)019<1139:AWITTA>2.0.CO;2.

Kalnay, E. (2003). Atmospheric modeling, data assimilation, and predictability. *Cambridge University Press*.

Karlsson, B., H. Körnich, and J. Gumbel. (2007). Evidence for interhemispheric stratosphere-mesosphere coupling derived from noctilucent cloud properties. *Geophysical Research Letters*, *34*, doi: https://doi.org/10.1029/2007GL030282.

Karlsson, B., and T. G. Shepherd. (2018). The improbable clouds at the edge of the atmosphere. *Physics Today*, *71*, 30–36, doi: 10.1063/PT.3.3946.

Kelley, M. C. (2009). The Earth's Ionosphere: Plasma Physics and Electrodynamics. Second Edi. *Academic Press*.

Khomich, V. Y., A. I. Semenov, and N. N. Shefov. (2008). Airglow as an indicator of upper atmospheric structure and dynamics. *Springer*.

Kieffer, H. H., and R. L. Wildey. (1996). Establishing the moon as a spectral radiance standard. *Journal of Atmospheric and Oceanic Technology*, *13*, 360–375, doi: 10.1175/1520-0426(1996)013<0360:ETMAAS>2.0.CO;2.

Kiliani, J., G. Baumgarten, F. J. Lübken, U. Berger, and P. Hoffmann. (2013). Temporal and spatial characteristics of the formation of strong noctilucent clouds. *Journal of Atmospheric and Solar-Terrestrial Physics*, *104*, 151–166, doi: 10.1016/j.jastp.2013.01.005.

Kingslake, R., and R. B. Johnson. (2010). Lens design fundamentals. *Academic Press*.

References

Kirkwood, S. (2007). Polar mesosphere winter echoes - A review of recent results. *Advances in Space Research*, doi: 10.1016/j.asr.2007.01.024.

Kirkwood, S., P. Chilson, E. Belova, P. Dalin, I. Häggström, M. Rietveld, and W. Singer. (2006). Infrasound – the cause of strong Polar Mesosphere Winter Echoes?, *24*, 475–491.

Kirkwood, S., P. Dalin, and A. Réchou. (2008). Noctilucent clouds observed from the UK and Denmark - trends and variations over 43 years. *Annales Geophysicae*, *26*, 1243–1254, doi: 10.5194/angeo-26-1243-2008.

Kirkwood, S., A. Osepian, E. Belova, and Y. Lee. (2015). High-speed solar wind streams and polar mesosphere winter echoes at Troll, Antarctica, *33*, 609–622, doi: 10.5194/angeo-33-609-2015.

Kivelson, M. ., and G. Schubert. (1986). Atmospheres of the terrestrial planets. Pages 116–134 *in* M. G. Kivelson, editor. The Solar System: Observations and Interpretations. Rubey Volu. *Prentice-Hall*.

Koch, K., and C. Pilger. (2020). A Comprehensive Study of Infrasound Signals Detected from the Ingolstadt, Germany, Explosion of 1 September 2018. *Pure and Applied Geophysics*, *177*, 4229–4245, doi: 10.1007/s00024-020-02442-y.

Kokhanovsky, A. A. (2005). Microphysical and optical properties of noctilucent clouds. *Earth-Science Reviews*, *71*, 127–146, doi: 10.1016/j.earscirev.2005.02.005.

Kotake, N., Y. Otsuka, T. Ogawa, T. Tsugawa, and A. Saito. (2007). Statistical study of medium-scale traveling ionospheric disturbances observed with the GPS networks in Southern California. *Earth, Planets and Space*, *59*, 95–102, doi: 10.1186/BF03352681.

Krassovsky, V. I., N. N. Shefov, and V. I. Yarin. (1962). Atlas of the airglow spectrum 3000–12400 Å. *Planetary and Space Science*, *9*, 883–915, doi: 10.1016/0032-0633(62)90008-9.

Kulichkov, S. N. (2004). Long-range propagation and scattering of low-frequency sound

pulses in the middle atmosphere. *Meteorology and Atmospheric Physics*, *85*, 47–60, doi: 10.1007/s00703-003-0033-z.

Lamb, O. D., J. M. Lees, and D. C. Bowman. (2018). Detecting Lightning Infrasound Using a High-Altitude Balloon. *Geophysical Research Letters*, *45*, 7176–7183, doi: 10.1029/2018GL078401.

Landès, M., L. Ceranna, A. Le Pichon, and R. S. Matoza. (2012). Localization of microbarom sources using the IMS infrasound network. *Journal of Geophysical Research: Atmospheres*, *117*, n/a-n/a, doi: 10.1029/2011JD016684.

Lau, K.-M., and H. Weng. (1995). Climate Signal Detection Using Wavelet Transform: How to Make a Time Series Sing. *Bulletin of the American Meteorological Society*, *76*, 2391–2402, doi: 10.1175/1520-0477(1995)076<2391:CSDUWT>2.0.CO;2.

Leick, A., L. Rapoport, and D. Tatarnikov. (2015). GPS satellite surveying. *John Wiley & Sons, Ltd*.

Leinert, C., S. Bowyer, L. K. Haikala, M. S. Hanner, M. G. Hauser, A.-C. Levasseur-Regourd, I. Mann, K. Mattila, W. T. Reach, W. Schlosser, H. J. Staude, G. N. Toller, J. L. Weiland, J. L. Weinberg, and A. N. Witt. (1998). The 1997 reference of diffuse night sky brightness. *Astronomy and Astrophysics Supplement Series*, *127*, 1–99, doi: 10.1051/aas:1998105.

Leslie, R. C. (1885). Sky glows. *Nature*, *32*, 245, doi: 10.1038/032245a0.

Lindsay, R. B. (1964). Lindsay's wheel of acoustics. *The Journal of the Acoustical Society of America*, *36*, 2242.

Lipson, H., and J. Littler. (1966). Tuning Fork Choppers for Infrared Spectrometers (No. 109). *Air Force Cambridge Research Laboratories, Office of Aerospace Research, United States Air Force.*

Lissauer, J. J., and I. de Pater. (2013). Fundamental Planetary Science: Physics, Chemistry and Habitability. *Cambridge University Press*.

References

Liu, A. Z., and G. R. Swenson. (2003). A modeling study of O $_2$ and OH airglow perturbations induced by atmospheric gravity waves. *Journal of Geophysical Research*, *108*, 4151, doi: 10.1029/2002JD002474.

Longuet-Higgins, M. S. (1950). A theory of the origin of microseisms. *Philos. Trans. R. Soc.*, *A*, 1–35, doi: doi:10.1098/rsta.1950.0012.

Lott, F., and C. Millet. (2009). The representation of gravity waves in atmospheric general circulation models (GCMs). Pages 685–699 Infrasound Monitoring for Atmospheric Studies. *Springer Netherlands*.

Lowe, R. P., and E. A. Lytle. (1973). Balloon-Borne Spectroscopic Observation of the Infrared Hydroxyl Airglow. *Applied Optics*, *12*, 579, doi: 10.1364/AO.12.000579.

Lübken, F. J., U. Berger, and G. Baumgarten. (2018). On the Anthropogenic Impact on Long-Term Evolution of Noctilucent Clouds. *Geophysical Research Letters*, *45*, 6681–6689, doi: 10.1029/2018GL077719.

Mackovjak, P. Bobík, J. Baláž, I. Strhárský, M. Putiš, and P. Gorodetzky. (2019). Airglow monitoring by one-pixel detector. *Nuclear Instruments and Methods in Physics Research, Section A: Accelerators, Spectrometers, Detectors and Associated Equipment*, *922*, 150–156, doi: 10.1016/j.nima.2018.12.073.

Maihara, T., F. Iwamuro, T. Yamashita, D. N. B. Hall, L. L. Cowie, A. T. Tokunaga, A. Pickles, D. N. B. Hall, L. L. Cowie, A. T. Tokunaga, and A. Pickles. (1993). Observations of the OH Airglow Emission Published by : Astronomical Society of the Pacific Linked references are available on JSTOR for this article : Observations of the OH Airglow Emission. *Publications of the Astronomical Society of the Pacific*, *105*, 940–944.

Makela, J. J., P. Lognonné, H. Hébert, T. Gehrels, L. Rolland, S. Allgeyer, A. Kherani, G. Occhipinti, E. Astafyeva, P. Coïsson, A. Loevenbruck, E. Clévédé, M. C. Kelley, J. Lamouroux, and R. Lett. (2011). Imaging and modeling the ionospheric airglow response over Hawaii to the tsunami generated by the Tohoku earthquake of 11

March 2011. *Geophysical Research Letters*, doi: 10.1029/2011GL047860.

Makhlouf, U. B., R. H. Picard, and J. R. Winick. (1995). Photochemical-dynamical modeling of the measured response of airglow to gravity waves: 1. Basic model for OH airglow. *Journal of Geophysical Research*, *100*, 11289, doi: 10.1029/94JD03327.

Marchetti, E., M. Ripepe, P. Campus, A. Le Pichon, N. Brachet, E. Blanc, P. Gaillard, P. Mialle, P. Husson, and T. Arnal. (2018). Infrasound monitoring of volcanic eruptions and contribution of ARISE to the volcanic ash advisory centers. Pages 1141–1162 Infrasound Monitoring for Atmospheric Studies: Challenges in Middle Atmosphere Dynamics and Societal Benefits: Second Edition. *Springer International Publishing.*

Marlton, G., A. Charlton-Perez, G. Harrison, and C. Lee. (2018). Calculating atmospheric gravitywave parameters from infrasound measurements. Pages 701–719 Infrasound Monitoring for Atmospheric Studies: Challenges in Middle Atmosphere Dynamics and Societal Benefits: Second Edition. *Springer International Publishing.*

Marsh, D. R., A. K. Smith, M. G. Mlynczak, and J. M. Russell. (2006). SABER observations of the OH Meinel airglow variability near the mesopause. *Journal of Geophysical Research*, *111*, A10S05, doi: 10.1029/2005JA011451.

Marsh, D., A. Smith, G. Brasseur, M. Kaufmann, and K. Grossmann. (2001). The existence of a tertiary ozone maximum in the high-latitude middle mesosphere. *Geophysical Research Letters*, *28*, 4531–4534, doi: 10.1029/2001GL013791.

Marty, J. (2019). The IMS Infrasound Network: Current Status and Technological Developments. *Infrasound Monitoring for Atmospheric Studies: Challenges in Middle Atmosphere Dynamics and Societal Benefits: Second Edition*, 3–62, doi: 10.1007/978-3-319-75140-5_1.

Maruyama, T., and H. Shinagawa. (2014). Infrasonic sounds excited by seismic waves of the 2011 Tohoku-oki earthquake as visualized in ionograms. *Journal of Geophysical Research: Space Physics*, *119*, 4094–4108, doi: 10.1002/2013JA019707.

References

Mathews, L. T., K. L. Gee, G. W. Hart, R. D. Rasband, D. J. Novakovich, F. I. Irarrazabal, A. B. Vaughn, and P. Nelson. (2020). Comparative analysis of noise from three Falcon 9 launches. *The Journal of the Acoustical Society of Korea*, *39*, 322–330, doi: 10.7776/ASK.2020.39.4.322.

McCarthy, D. J. (2015). PhD Thesis: Modelling Mesopause Emissions using a Global Circulation Model.

McClintock, W. E., D. W. Rusch, G. E. Thomas, A. W. Merkel, M. R. Lankton, V. A. Drake, S. M. Bailey, and J. M. Russell. (2009). The cloud imaging and particle size experiment on the Aeronomy of Ice in the mesosphere mission: Instrument concept, design, calibration, and on-orbit performance. *Journal of Atmospheric and Solar-Terrestrial Physics*, *71*, 340–355, doi: 10.1016/j.jastp.2008.10.011.

McDade, I. C., and E. J. Llewellyn. (1987). Kinetic parameters related to sources and sinks of vibrationally excited OH in the nightglow. *Journal of Geophysical Research*, *92*, 7643, doi: 10.1029/JA092iA07p07643.

McKisic, J. M. (1997). Infrasound and the infrasonic monitoring of atmospheric nuclear explosions: A literature review.

van de Meerakker, S. Y. T., N. Vanhaecke, M. P. J. van der Loo, G. C. Groenenboom, and G. Meijer. (2005). Direct Measurement of the Radiative Lifetime of Vibrationally Excited OH Radicals. *Physical Review Letters*.

Meinel. (1950a). OH Emission Bands in the Spectrum of the Night Sky. I. *American Astronomical Soceity*.

Meinel, A. B. (1950b). OH EMISSION BANDS IN THE SPECTRUM OF THE NIGHT SKY. II. *American Astronomical Soceity*.

Melo, S. M. L., R. P. Lowe, and J. P. Russell. (2000). Double-peaked hydroxyl airglow profiles observed from WINDII/UARS. *Journal of Geophysical Research: Atmospheres*, *105*, 12397–12403, doi: 10.1029/1999JD901169.

Miyoshi, Y., H. Fujiwara, J. M. Forbes, and S. L. Bruinsma. (2009). Solar terminator

wave and its relation to the atmospheric tide. *Journal of Geophysical Research: Space Physics*, *114*, doi: 10.1029/2009JA014110.

Mlynczak, M. G. (1997). Energetics of the mesosphere and lower thermosphere and the saber experiment. *Advances in Space Research*, *20*, 1177–1183, doi: 10.1016/S0273-1177(97)00769-2.

Moldwin, M. (2008). An Introduction to Space Weather. *Cambridge University Press*.

Moore, J. H., C. C. Davis, M. A. Coplan, and S. C. Greer. (2009). Building Scientific Apparatus. Illustrate. *Cambridge University Press*.

Moreels, G., J. Clairemidi, M. Faivre, D. Pautet, F. Rubio Da Costa, P. Rousselot, J. W. Meriwether, G. A. Lehmacher, E. Vidal, J. L. Chau, G. Monnet, : D Pautet, J. Meriwether, G. Lehmacher, and J. Chau. (2008). Near-infrared sky background fluctuations at mid-and low latitudes. *Springer*, *22*, 87–107, doi: 10.1007/s10686-008-9089-6.

Mulligan, F. J., and J. M. Galligan. (1995). Mesopause temperatures calculated from the O2(a1 Δg) twilight airglow emission recorded at Maynooth (53.2 ° N, 6.4 ° W).

Mulligan, F. J. J., D. F. F. Horgan, J. G. G. Galligan, and E. M. M. Griffin. (1995). Mesopause temperatures and integrated band brightnesses calculated from airglow OH emissions recorded at Maynooth (53.2°N, 6.4°W) during 1993. *Journal of Atmospheric and Terrestrial Physics*, *57*, 1623–1637, doi: 10.1016/0021-9169(94)00133-9.

Munroe, R. (2019). How To: Absurd Scientific Advice for Common Real-World Problems from Randall Munroe of xkcd. *John Murray*.

Murphy, D. J., W. J. R. French, and R. A. Vincent. (2007). Long-period planetary waves in the mesosphere and lower thermosphere above Davis, Antarctica. *Journal of Atmospheric and Solar-Terrestrial Physics*, *69*, 2118–2138, doi: 10.1016/J.JASTP.2007.06.008.

Muscari, J. A. (1975). Photometer calibration problem for extended astronomical sources.

Applied Optics, *14*, 1491, doi: 10.1364/ao.14.001491.

Mutschlecner, J. P., and R. W. Whitaker. (2005). Infrasound from earthquakes. *Journal of Geophysical Research D: Atmospheres*, *110*, 1–11, doi: 10.1029/2004JD005067.

Mutschlecner, J. P., and R. W. Whitaker. (2009). Some atmospheric effects on infrasound signal amplitudes. Pages 455–474 Infrasound Monitoring for Atmospheric Studies. *Springer Netherlands*.

Nappo, C. J. (2013). An introduction to atmospheric gravity waves. *Academic*.

National Research Council, N. (1977). Upper Atmosphere and Magnetosphere. *The National Academies Press*, Washington D.C.

Nicolet, M. (1970). Ozone and hydrogen reactions. *Annales de Geophysique*, *26*, 531–546.

NLCNET. (2016). 2016 » NLCNET. http://ed-co.net/nlcnet/2016-2.

NLCNET. (2018). 2018 >> NLCNET. http://ed-co.net/nlcnet/2018-3.

NLCNET. (2021). NLCNET. http://ed-co.net/nlcnet/.

NOAA, N. W. S. (2019). NWS JetStream - Long and Short Waves. *NOAA's National Weather Service*.

NWS, N. W. S. (2017). Layers of the Atmosphere. https://www.weather.gov/jetstream/layers.

Ogawa, Y., A. Kadokura, and M. K. Ejiri. (2020). Optical calibration system of NIPR for aurora and airglow observations. *Polar Science*, *26*, 100570, doi: 10.1016/J.POLAR.2020.100570.

Oliva, E., and E. Origlia. (1992). The OH airglow spectrum-a calibration source for infrared spectrometers. *Astronomy and Astrophysics*, *254*, 466.

Oriel, C. (n.d.). Using the 63358 amd 63361 45W Quartz Halogen Lamp Standards of Spectral Irradiance.

Oriel, C. (1991). Radiometric Power Supply Model 68830. Connecticut.

Ortland, D. A., P. B. Hays, W. R. Skinner, and J.-H. Yee. (1998). Remote sensing of mesospheric temperature and O $_2$ ($^1\Sigma$) band volume emission rates with the high-resolution Doppler imager. *Journal of Geophysical Research: Atmospheres*, *103*, 1821–1835, doi: 10.1029/97JD02794.

Otsuka, Y., N. Kotake, T. Tsugawa, K. Shiokawa, T. Ogawa, Effendy, S. Saito, M. Kawamura, T. Maruyama, N. Hemmakorn, and T. Komolmis. (2006). GPS detection of total electron content variations over Indonesia and Thailand following the 26 December 2004 earthquake. *Earth, Planets and Space*, *58*, 159–165, doi: 10.1186/BF03353373.

Ott, T., E. Drolshagen, D. Koschny, P. Mialle, C. Pilger, J. Vaubaillon, G. Drolshagen, and B. Poppe. (2019). Combination of infrasound signals and complementary data for the analysis of bright fireballs. *Planetary and Space Science*, *179*, 104715, doi: 10.1016/J.PSS.2019.104715.

Pautet, P.-D., J. Stegman, C. M. Wrasse, K. Nielsen, H. Takahashi, M. J. Taylor, K. W. Hoppel, and S. D. Eckermann. (2011). Analysis of gravity waves structures visible in noctilucent cloud images. *Journal of Atmospheric and Solar-Terrestrial Physics*, *73*, 2082–2090, doi: 10.1016/J.JASTP.2010.06.001.

Pautet, P.-D., M. J. Taylor, W. R. Pendleton, Y. Zhao, T. Yuan, R. Esplin, and D. McLain. (2014). Advanced mesospheric temperature mapper for high-latitude airglow studies. *Applied Optics*, *53*, 5934, doi: 10.1364/ao.53.005934.

Perkin-Elmer. (2000a). Large-Area InGaAs Photodiodes.

Perkin-Elmer, O. (2000b). Technical Note: What is a Lock-in Amplifier?

Peterson, A. W. (1979). Airglow events visible to the naked eye. *Applied Optics*, *18*, 3390, doi: 10.1364/AO.18.003390.

Le Pichon, A., E. Blanc, and A. Hauchecorne, editors. (2010). Infrasound Monitoring for Atmospheric Studies. First. *Springer*.

Le Pichon, A., E. Blanc, and A. Hauchecorne. (2018). Infrasound Monitoring for

Atmospheric Studies: Challenges and New Perspectives. *Springer*.

Pickett, H. M., W. G. Read, K. K. Lee, and Y. L. Yung. (2006). Observation of night OH in the mesosphere. *Geophysical Research Letters*, *33*, L19808, doi: 10.1029/2006GL026910.

Pierce, A. D. (1968). Spikes on Sonic-Boom Pressure Waveforms. *The Journal of the Acoustical Society of America*, *44*, 1052–1061, doi: 10.1121/1.1911195.

Pignatelli, A., A. Giuntini, and R. Console. (2008). Matlab software for the analysis of seismic waves recorded by three-element arrays. *Computers and Geosciences*, *34*, 792–801, doi: 10.1016/j.cageo.2007.10.003.

Pilger, C. (2021). Private Communication.

Pilger, C., and M. Bittner. (2009). Infrasound from tropospheric sources: Impact on mesopause temperature? *Journal of Atmospheric and Solar-Terrestrial Physics*, *71*, 816–822, doi: 10.1016/j.jastp.2009.03.008.

Pilger, C., L. Ceranna, A. Le Pichon, and P. Brown. (2018). Large meteoroids as global infrasound reference events. Pages 451–470 Infrasound Monitoring for Atmospheric Studies: Challenges in Middle Atmosphere Dynamics and Societal Benefits: Second Edition. *Springer International Publishing*.

Pilger, C., L. Ceranna, J. O. Ross, A. Le Pichon, P. Mialle, M. A. Garcés, A. Le Pichon, P. Mialle, and M. A. Garcés. (2015). CTBT infrasound network performance to detect the 2013 Russian fireball event. *Geophysical Research Letters*, *42*, 2523–2531, doi: 10.1002/2015GL063482.

Pilger, C., P. Gaebler, P. Hupe, A. C. Kalia, F. Schneider, A. Steinberg, H. Sudhaus, and L. Ceranna. (2020a). Yield estimation of the 2020 Beirut explosion using open access waveform and remote sensing data. *Scientific reports - Pre Print*.

Pilger, C., P. Gaebler, P. Hupe, T. Ott, and E. Drolshagen. (2020b). Global Monitoring and Characterization of Infrasound Signatures by Large Fireballs. *Atmosphere*, *11*, 83, doi: 10.3390/atmos11010083.

Pilger, C., C. Schmidt, and M. Bittner. (2013a). Statistical analysis of infrasound signatures in airglow observations: Indications for acoustic resonance. *Journal of Atmospheric and Solar-Terrestrial Physics*, *93*, 70–79, doi: 10.1016/j.jastp.2012.11.011.

Pilger, C., C. Schmidt, F. Streicher, S. Wüst, and M. Bittner. (2013b). Airglow observations of orographic, volcanic and meteorological infrasound signatures. *Journal of Atmospheric and Solar-Terrestrial Physics*, *104*, 55–66, doi: 10.1016/j.jastp.2013.08.008.

Plane, J. M. C. (2000). The role of sodium bicarbonate in the nucleation of noctilucent clouds. *Annales Geophysicae*, *18*, 807–814, doi: 10.1007/s00585-000-0807-2.

Posmentier, E. S. (1967). A Theory of Microbaroms. *Geophysical Journal of the Royal Astronomical Society*, *13*, 487–501, doi: 10.1111/j.1365-246X.1967.tb02301.x.

Rapp, M., and F. J. Lübken. (2004). Polar mesosphere summer echoes (PMSE): Review of observations and current understanding. *Atmospheric Chemistry and Physics*, *4*, 2601–2633.

Rees, W. G. (2001). Physical Principles of Remote Sensing. 2nd editio. *Cambridge University Press*.

Rehm, R. G., and H. s. Radt. (1975). Internal waves generated by a translating oscillating body. *Journal of Fluid Mechanics*, *68*, 235–258.

Revelle, D. O. (1976). On Meteor-Generated Infrasound. *Journal of Geophysical Research*.

Revelle, D. O. (1997). Historical Detection of Atmospheric Impaces by Large Bolides Using Acoustic-Gravity Waves. *Annals of the New York Academy of Sciences*, *822*, 284–302, doi: 10.1111/j.1749-6632.1997.tb48347.x.

Revelle, D. O., and R. W. Whitaker. (1999). infrasonic detection of the Leonid bolide: 1998 November 17. *Meteorics & Planetary Science*, *34*, 995–1005.

References

Rind, D., W. L. Donn, D. Rind, and W. L. Donn. (1975). Further Use of Natural Infrasound as a Continuous Monitor of the Upper Atmosphere. *Journal of the Atmospheric Sciences*, *32*, 1694–1704, doi: 10.1175/1520-0469(1975)032<1694:FUONIA>2.0.CO;2.

Ripepe, M., C. Bonadonna, A. Folch, D. Delle Donne, G. Lacanna, E. Marchetti, and A. Höskuldsson. (2013). Ash-plume dynamics and eruption source parameters by infrasound and thermal imagery: The 2010 Eyjafjallajökull eruption. *Earth and Planetary Science Letters*, *366*, 112–121, doi: 10.1016/j.epsl.2013.02.005.

Ripepe, M., and E. Marchetti. (2019). Infrasound Monitoring of Volcano-Related Hazards for Civil Protection. Pages 1107–1140 *in* A. Le Pichon, E. Blanc, and A. Hauchecorne, editors. Infrasound Monitoring for Atmospheric Studies: Challenges in Middle Atmosphere Dynamics and Societal Benefits. *Springer International Publishing*, Cham.

Roach, F. E., and J. L. Gordon. (1973). The Light of the Night Sky. *Springer Netherlands*, Dordrecht.

Rothwell, P. (1947). Calculation of Sound Rays in the Atmosphere. *Journal of the Acoustical Society of America*, *19*, 205–221, doi: 10.1121/1.1916422.

Rourke, S., F. J. Mulligan, W. J. R. French, and D. J. Murphy. (2017). A climatological study of short-period gravity waves and ripples at Davis Station, Antarctica (68 ° S, 78 ° E) during the (austral winter February-October) period 1999-2013. *Journal of Geophysical Research: Atmospheres*, 1–17, doi: 10.1002/2017JD026998.

Rousselot, P., C. Lidman, J.-G. Cuby, G. Moreels, and G. Monnet. (2000). Night-sky spectral atlas of OH emission lines in the near-infrared. *Astronomy & Astrophysics*, *354*, 1134–1150, doi: 10.1007/s10021-009-9251-7.

Sabatini, R., O. Marsden, C. Bailly, and O. Gainville. (2019). Three-dimensional direct numerical simulation of infrasound propagation in the Earth's atmosphere. *Journal of Fluid Mechanics*, *859*, 754–789, doi: 10.1017/jfm.2018.816.

References

Salby, M. L. (1996). Fundamentals of Atmospheric Physics. *Elsevier*.

Salby, M. L. (2012). Physics of the atmosphere and climate. *Cambridge University Press*.

Sanchez-Lavega, A. (2010). An Introduction to Planetary Atmospheres. *CRC Press*.

Sander, S. P., R. R. Friedl, A. R. Ravishankara, D. M. Golden, C. E. Kolb, M. J. Kurylo, M. J. Molina, G. K. Moortgat, H. Keller-Rudek, B. J. Finlayson-Pitts, P. H. Wine, R. E. Huie, and V. L. Orkin. (2006). Chemical Kinetics and Photochemical Data for Use in Atmospheric Studies Evaluation Number 15 NASA Panel for Data Evaluation.

von Savigny, C. (2015). Variability of OH(3–1) emission altitude from 2003 to 2011: Long-term stability and universality of the emission rate–altitude relationship. *Journal of Atmospheric and Solar-Terrestrial Physics*, *127*, 120–128, doi: 10.1016/J.JASTP.2015.02.001.

von Savigny, C., I. C. Mcdade, K.-U. U. Eichmann, and J. P. Burrows. (2012). On the dependence of the OH* Meinel emission altitude on vibrational level: SCIAMACHY observations and model simulations. *Atmospheic Chemistry and Physics*, *12*, 8813–8828, doi: 10.5194/acp-12-8813-2012.

Scharroo, R., and W. H. F. Smith. (2010). A global positioning system - Based climatology for the total electron content in the ionosphere. *Journal of Geophysical Research: Space Physics*, *115*, 10318, doi: 10.1029/2009JA014719.

Schmidt, C. (2019). Private Communication.

Schmidt, C., K. Höppner, and M. Bittner. (2013). A ground-based spectrometer equipped with an InGaAs array for routine observations of OH(3-1) rotational temperatures in the mesopause region. *Journal of Atmospheric and Solar-Terrestrial Physics*, *102*, 125–139, doi: 10.1016/j.jastp.2013.05.001.

Schröder, W. (2001). Otto Jesse and the Investigation of Noctilucent Clouds 115 Years Ago. *Bulletin of the American Meteorological Society*, *82*, 2457–2468, doi: https://doi.org/10.1175/1520-0477(2001)082<2457:OJATIO>2.3.CO;2.

References

Sedlak, R., P. Hannawald, C. Schmidt, S. Wüst, and M. Bittner. (2016). High-resolution observations of small-scale gravity waves and turbulence features in the OH airglow layer. *Atmospheric Measurement Techniques*, *9*, 5955–5963, doi: 10.5194/amt-9-5955-2016.

Seinfeld, J. H., and S. N. Pandis. (1998). Atmospheric chemistry and physics: from air pollution to climate change. Page Atmospheric chemistry and physics: from air pollution to climate change. *John Wiley & Sons, Inc.*

Siebicke, L., and A. Emad. (2019). True eddy accumulation trace gas flux measurements: proof of concept. *Atmospheric Measurement Techniques*, *12*, 4393–4420, doi: 10.5194/amt-12-4393-2019.

Sigernes, F., J. M. Holmes, M. Dyrland, D. A. Lorentzen, S. A. Chernous, T. Svinyu, J. Moen, and C. S. Deehr. (2007). Absolute calibration of optical devices with a small field of view. *Journal of Optical Technology*, *74*, 669, doi: 10.1364/JOT.74.000669.

Silber, E. A., M. Boslough, W. K. Hocking, M. Gritsevich, and R. W. Whitaker. (2018). Physics of meteor generated shock waves in the Earth's atmosphere – A review. *Advances in Space Research*, *62*, 489–532, doi: 10.1016/J.ASR.2018.05.010.

Silber, E. A., and P. G. Brown. (2014). Optical observations of meteors generating infrasound—I: Acoustic signal identification and phenomenology. *Journal of Atmospheric and Solar-Terrestrial Physics*, *119*, 116–128, doi: 10.1016/j.jastp.2014.07.005.

Simoneau, P. (2020). Private Communication.

Šindelářová, T., D. Burešová, and J. Chum. (2009). Observations of acoustic-gravity waves in the ionosphere generated by severe tropospheric weather. *Studia Geophysica et Geodaetica*, *53*, 403–418, doi: 10.1007/s11200-009-0028-4.

Sivjee, G. G., and R. M. Hamwey. (1987). Temperature and chemistry of the polar mesopause OH. *Journal of Geophysical Research*, *92*, 4663, doi: 10.1029/JA092iA05p04663.

References

Smets, P., J. Assink, and L. Evers. (2017). The study of sudden stratospheric warmings using infrasound. *The Journal of the Acoustical Society of America*, *141*, 3627–3627, doi: 10.1121/1.4987796.

Smets, P. S. M., J. D. Assink, A. Le Pichon, and L. G. Evers. (2016). ECMWF SSW forecast evaluation using infrasound. *Journal of Geophysical Research: Atmospheres*, *121*, 4637–4650, doi: 10.1002/2015JD024251.

Smith, W. J. (2000). Modern Optical Engineering. Third Edit. *McGraw-Hill Book Company*.

Snively, J. B. (2013). Mesospheric hydroxyl airglow signatures of acoustic and gravity waves generated by transient tropospheric forcing. *Geophysical Research Letters*, *40*, 4533–4537, doi: 10.1002/grl.50886.

Somsikov, V. M. (1983). Solar Terminator and Atmospheric Dynamics. *Nauka*.

Somsikov, V. M., and B. Ganguly. (1995). On the formation of atmospheric inhomogeneities in the solar terminator region. *Journal of Atmospheric and Terrestrial Physics*, *57*, 1513–1523, doi: 10.1016/0021-9169(95)00014-S.

Sonnemann, G. R., P. Hartogh, U. Berger, and M. Grygalashvyly. (2015). Hydroxyl layer: trend of number density and intra-annual variability. *Annales Geophysicae*, *33*, 749–767, doi: 10.5194/angeo-33-749-2015.

Stebel, K., V. Barabash, S. Kirkwood, J. Siebert, and K. H. Fricke. (2000). Polar mesosphere summer echoes and noctilucent clouds: Simultaneous and common-volume observations by radar, lidar and CCD camera. *Geophysical Research Letters*, *27*, 661–664, doi: 10.1029/1999GL010844.

Stein, S., and M. Wysession. (2009). An Introduction to Seismology, Earthquakes, and Earth Structure. *Wiley*.

Stewart, I. (2012). Seventeen Equations that Changed the World. Page (J. Davey, Ed.). *Profile Books*.

References

Stockwell, R. G., and R. P. Lowe. (2001). Airglow imaging of gravity waves: 2. Critical layer filtering. *Journal of Geophysical Research: Atmospheres*, *106*, 17205–17220, doi: 10.1029/2001JD900036.

Strangeway, R. J. (2008). How do auroras form? *Physics Today*, *61*, 68–69, doi: 10.1063/1.2963020.

Stull, R. (2015). Practical Meteorology: An Algebra-based Survey of Atmospheric Science. *University of British Columbia*.

Sturdy, E. . (1884), September. The volcanic eruption of Krakatau. *Atlantic Monthly*, 385–391.

Sturman, A. P., and N. J. Tapper. (1996). The weather and climate of Australia and New Zealand. *Oxford University Press*.

Summers, M. E., R. R. Conway, D. E. Siskind, M. H. Stevens, D. Offermann, M. Riese, P. Preusse, D. F. Strobel, and J. M. Russell. (1997). Implications of satellite OH observations for middle atmospheric H2O and ozone. *Science*, *277*, 1967–1970, doi: 10.1126/science.277.5334.1967.

Sutherland, L. C., and H. E. Bass. (2004). Atmospheric absorption in the atmosphere up to 160 km. *The Journal of the Acoustical Society of America*, *115*, 1012–1032, doi: 10.1121/1.1631937.

SWPC. (2021). Earth's magnetosphere | NOAA / NWS Space Weather Prediction Center. https://www.swpc.noaa.gov/phenomena/earths-magnetosphere.

Symons. (1888). The eruption of Krakatoa, and subsequent phenomena. Report of the Krakatoa Committee of the Royal Society. London.

Tarasick, D. W., and C. O. Hines. (1990). The observable effects of gravity waves on airglow emissions. *Planetary and Space Science*, *38*, 1105–1119, doi: 10.1016/0032-0633(90)90019-M.

Tarasick, D. W., and G. G. Shepherd. (1992). Effects of gravity waves on complex

airglow chemistries: 2. OH emission. *Journal of Geophysical Research: Space Physics*, *97*, 3195–3208, doi: 10.1029/91JA02580.

Tauzin, B., E. Debayle, C. Quantin, and N. Coltice. (2013). Seismoacoustic coupling induced by the breakup of the 15 February 2013 Chelyabinsk meteor. *Geophysical Research Letters*, *40*, 3522–3526, doi: 10.1002/grl.50683.

Taylor, F. W. (2010). Planetary Atmospheres. *Oxford University Press.*

Taylor, M. J., and M. J. Hill. (1991). Near infrared imaging of hydroxyl wave structure over an ocean site at low latitudes. *Geophysical Research Letters*, *18*, 1333–1336, doi: 10.1029/91GL01299.

Taylor, M. J., D. N. Turnbull, and R. P. Lowe. (1995). Spectrometric and imaging measurements of a spectacular gravity wave event observed during the ALOHA-93 Campaign. *Geophysical Research Letters*, *22*, 2849–2852, doi: 10.1029/95GL02948.

Taylor, M., P. Pautet, W. R. Pendleton Jr, R. Esplin, and D. McLain. (2010). Development of an advanced mesospheric temperature mapper (AMTM) for high-latitude research. *38th COSPAR Scientific Assembly. Held 18-15 July 2010, in Bremen, Germany, p.6.*

Le Texier, H., S. Solomon, and R. R. Garcia. (1987). Seasonal variability of the OH Meinel bands. *Planetary and Space Science*, *35*, 977–989, doi: 10.1016/0032-0633(87)90002-X.

Thomas, G. E., J. J. Olivero, M. Deland, and E. P. Shettle. (2011). Comment on "Are Noctilucent clouds truly a 'Miner's Canary' for Global change?" *Eos Trans. AGU.*

Thompson, R. D. (2002). Atmospheric Processes and Systems. *Routledge.*

Thorne, A. P. (1988). Spectrophysics. 2nd Ed. *Chapman and Hall Ltd.*

Thuburn, J. (2011). Some Basic Dynamics Relevant to the Design of Atmospheric Model Dynamical Cores. Pages 3–27 Lecture Notes in Computational Science and Engineering. *Springer Verlag.*

References

Torr, M. R., P. B. Hays, B. C. Kennedy, and D. G. Torr. (1976). Photometer calibration error using extended standard sources. *Applied Optics*, *15*, 600, doi: 10.1364/ao.15.000600.

Torrence, C., and G. P. Compo. (1998). A Practical Guide to Wavelet Analysis. *Bulletin of the American Meteorological Society*, *79*, 61–78, doi: 10.1175/1520-0477(1998)079<0061:APGTWA>2.0.CO;2.

Tuchman, I. (1999). Laser scanning and chopping methods using mechanical resonant devices. Pages 165–172 *in* L. Beiser, S. F. Sagan, and G. F. Marshall, editors. Optical Scanning: Design and Application. *SPIE*.

Turnbull, D. N., and R. P. Lowe. (1989). New hydroxyl transition probabilities and their importance in airglow studies. *Planetary and Space Science*, *37*, 723–738, doi: 10.1016/0032-0633(89)90042-1.

Ugolnikov, O. S., A. A. Galkin, S. V. Pilgaev, and A. V. Roldugin. (2017). Noctilucent cloud particle size determination based on multi-wavelength all-sky analysis. *Planetary and Space Science*, *146*, 10–19.

Ugolnikov, O. S., and B. V. Kozelov. (2016). Study of the mesosphere using wide-field twilight polarization measurements: Early results beyond the polar circle. *Cosmic Research*, *54*, 279–284, doi: 10.1134/S0010952516040079.

Vasiljević, N., M. Harris, A. Tegtmeier Pedersen, G. Rolighed Thorsen, M. Pitter, J. Harris, K. Bajpai, and M. Courtney. (2020). Wind sensing with drone-mounted wind lidars: Proof of concept. *Atmospheric Measurement Techniques*, *13*, 521–536, doi: 10.5194/amt-13-521-2020.

Verbeek, R. (1885). The time determination of the biggest explosion of Krakatau on August 27, 1883, 43–55.

Verhulst. (2018). Private Communication.

Verhulst, T. G. W., and S. M. Stankov. (2017). Height-dependent sunrise and sunset: Effects and implications of the varying times of occurrence for local ionospheric

processes and modelling. *Advances in Space Research*, *60*, 1797–1806, doi: 10.1016/J.ASR.2017.05.042.

Viezee, W. (1960). Survey of radiometric quantities and units. *RAND Corporation*.

Vincent, J. D., S. Hodges, J. Vampola, M. Stegall, and G. Pierce. (2015). Fundamentals of infrared and visible detector operation and testing. Second. *John Wiley & Sons, Inc.*

Welch, P. D. (1967). The Use of Fast Fourier Transform for the Estimation of Power Spectra: A Method Based on Time Averaging Over Short, Modified Periodograms. *IEEE Transactions on Audio and Electroacoustics*, *15*, 70–73, doi: 10.1109/TAU.1967.1161901.

Whipple, F. (1930). The great Siberian meteor and the waves, seismic and aerial, which it produced. *Quarterly Journal of the Royal Meteorological Society*, 287–304.

White, I. D., S. J. Harrison, and D. . Mottershead. (1992). Environmental Systems: An Introductory Text. Second Edi. *Chapman & Hall*.

Whiter, D. (2018). Private Communication on Infrasound in relation to Auroral Arcs.

Winston, R., J. C. Miñano, P. Benítez, and W. T. Welford. (2005). Nonimaging optics. *Elsevier Academic Press*.

Witt, G. (1962). Height, structure and displacements of noctilucent clouds. *Tellus*, *14*, 1–18, doi: 10.3402/tellusa.v14i1.9524.

Wüst, S., M. Bittner, J. H. Yee, M. G. Mlynczak, and J. M. Russell. (2017). Variability of the Brunt-Väisälä frequency at the OH∗ layer height. *Atmospheric Measurement Techniques*, *10*, 4895–4903, doi: 10.5194/amt-10-4895-2017.

Xu, J., H. Gao, A. K. Smith, and Y. Zhu. (2012). Using TIMED/SABER nightglow observations to investigate hydroxyl emission mechanisms in the mesopause region. *Journal of Geophysical Research: Atmospheres*, *117*, n/a-n/a, doi: 10.1029/2011JD016342.

References

Yi, W., X. Xue, I. M. Reid, D. J. Murphy, C. M. Hall, M. Tsutsumi, B. Ning, G. Li, G. Yang, N. Li, T. Chen, and X. Dou. (2021). Climatology of Interhemispheric Mesopause Temperatures Using the High-Latitude and Middle-Latitude Meteor Radars. *Journal of Geophysical Research: Atmospheres*, *126*, e2020JD034301, doi: 10.1029/2020JD034301.

Yiğit, E., and A. S. Medvedev. (2019). Obscure waves in planetary atmospheres. *Physics Today*, *72*, doi: doi: 10.1063/PT.3.4226.

von Zahn, U. (2003). Are noctilucent clouds a "Miner's Canary" for global change? *Eos, Transactions American Geophysical Union*, *84*, 261, doi: 10.1029/2003eo280001.

Zettergren, M. D., and J. B. Snively. (2013). Ionospheric signatures of acoustic waves generated by transient tropospheric forcing. *Geophysical Research Letters*, *40*, 5345–5349, doi: 10.1002/2013GL058018.

Zettergren, M. D., J. B. Snively, A. Komjathy, and O. P. Verkhoglyadova. (2017). Nonlinear ionospheric responses to large-amplitude infrasonic-acoustic waves generated by undersea earthquakes. *Journal of Geophysical Research: Space Physics*, *122*, 2272–2291, doi: 10.1002/2016JA023159.

Zhang, Z., Z. Jing, Z. Wang, and D. Kuang. (2012). Comparison of Fourier transform, windowed Fourier transform, and wavelet transform methods for phase calculation at discontinuities in fringe projection prolometry. *Optics and Lasers in Engineering*, *50*, 1152–1160, doi: 10.1016/j.optlaseng.2012.03.004.

Zhou, X. Y., R. J. Strangeway, R. C. Anderson, D. G. Sibeck, B. T. Tsurutani, G. Haërendel, H. U. Frey, and J. K. Arballo. (2003). Shock aurora: FAST arid DMSP observations. *Journal of Geophysical Research: Space Physics*, *108*, 8019, doi: 10.1029/2002JA009701.

Zurich Instruments, Z. (2016). Principles of lock-in detection and the state of the art - Zurich Instruments. http://www.zhinst.com/applications/principles-of-lock-in-detection.